



# An Experimental Investigation of the Flow Physics Associated With End Wall Losses and Large Rotor Tip Clearances as Found in the Rear Stages of a High Pressure Compressor

*Reid A. Berdanier and Nicole L. Key  
Purdue University, West Lafayette, Indiana*

## NASA STI Program . . . in Profile

Since its founding, NASA has been dedicated to the advancement of aeronautics and space science. The NASA Scientific and Technical Information (STI) Program plays a key part in helping NASA maintain this important role.

The NASA STI Program operates under the auspices of the Agency Chief Information Officer. It collects, organizes, provides for archiving, and disseminates NASA's STI. The NASA STI Program provides access to the NASA Technical Report Server—Registered (NTRS Reg) and NASA Technical Report Server—Public (NTRS) thus providing one of the largest collections of aeronautical and space science STI in the world. Results are published in both non-NASA channels and by NASA in the NASA STI Report Series, which includes the following report types:

- **TECHNICAL PUBLICATION.** Reports of completed research or a major significant phase of research that present the results of NASA programs and include extensive data or theoretical analysis. Includes compilations of significant scientific and technical data and information deemed to be of continuing reference value. NASA counter-part of peer-reviewed formal professional papers, but has less stringent limitations on manuscript length and extent of graphic presentations.
- **TECHNICAL MEMORANDUM.** Scientific and technical findings that are preliminary or of specialized interest, e.g., “quick-release” reports, working papers, and bibliographies that contain minimal annotation. Does not contain extensive analysis.
- **CONTRACTOR REPORT.** Scientific and technical findings by NASA-sponsored contractors and grantees.
- **CONFERENCE PUBLICATION.** Collected papers from scientific and technical conferences, symposia, seminars, or other meetings sponsored or co-sponsored by NASA.
- **SPECIAL PUBLICATION.** Scientific, technical, or historical information from NASA programs, projects, and missions, often concerned with subjects having substantial public interest.
- **TECHNICAL TRANSLATION.** English-language translations of foreign scientific and technical material pertinent to NASA's mission.

For more information about the NASA STI program, see the following:

- Access the NASA STI program home page at <http://www.sti.nasa.gov>
- E-mail your question to [help@sti.nasa.gov](mailto:help@sti.nasa.gov)
- Fax your question to the NASA STI Information Desk at 757-864-6500
- Telephone the NASA STI Information Desk at 757-864-9658
- Write to:  
NASA STI Program  
Mail Stop 148  
NASA Langley Research Center  
Hampton, VA 23681-2199



# An Experimental Investigation of the Flow Physics Associated With End Wall Losses and Large Rotor Tip Clearances as Found in the Rear Stages of a High Pressure Compressor

*Reid A. Berdanier and Nicole L. Key  
Purdue University, West Lafayette, Indiana*

Prepared under Contract NNX11AI59A

National Aeronautics and  
Space Administration

Glenn Research Center  
Cleveland, Ohio 44135

## Acknowledgments

This work was supported by the National Aeronautics and Space Administration (NASA) under the ROA-2010 NRA of the Subsonic Fixed Wing project. The technical monitor for this project was Dr. Mark Celestina. Additional support for this project is gratefully acknowledged from Rolls-Royce, Mr. John Fabian, Dr. Aaron King, Dr. Roy Fulayter, Dr. Bronwyn Power, Dr. Tony Strazisar, Dr. John Adamczyk, Dr. Hyoun-Woo Shin, Dr. Anna Young, Dr. Ivor Day, Dr. John Brossman and all other people who have provided helpful insights throughout this project. Significant thanks are also due to Mr. Robert McGuire and the other support staff members at Purdue University who helped to facilitate the success of this project.

Trade names and trademarks are used in this report for identification only. Their usage does not constitute an official endorsement, either expressed or implied, by the National Aeronautics and Space Administration.

This work was sponsored by the Fundamental Aeronautics Program at the NASA Glenn Research Center.

*Level of Review:* This material has been technically reviewed by NASA technical management.

Available from

NASA STI Program  
Mail Stop 148  
NASA Langley Research Center  
Hampton, VA 23681-2199

National Technical Information Service  
5285 Port Royal Road  
Springfield, VA 22161  
703-605-6000

This report is available in electronic form at <http://www.sti.nasa.gov/> and <http://ntrs.nasa.gov/>

# TABLE OF CONTENTS

	Page
LIST OF TABLES .....	v
LIST OF FIGURES .....	vi
LIST OF SYMBOLS .....	xi
LIST OF ABBREVIATIONS.....	xiii
SUMMARY .....	xiv
CHAPTER 1: INTRODUCTION .....	1
<i>Authors: Reid A. Berdanier and Nicole L. Key</i>	
1.1. Background.....	1
1.1.1. Survey of Literature .....	1
1.1.2. Characteristics of Tip Leakage Flows.....	2
1.1.3. Computational Validation Using High-Speed Experimental Data .....	3
1.1.4. Spanwise Mixing .....	4
1.1.5. Blockage and Stage Matching .....	5
1.2. Program Objectives.....	5
CHAPTER 2: EXPERIMENTAL METHODS .....	7
<i>Authors: Reid A. Berdanier, Natalie R. Smith, and Nicole L. Key</i>	
2.1. Research Facility.....	7
2.1.1. Integral Facility Components.....	7
2.1.2. Additional Geometry Considerations.....	9
2.1.3. Variable Tip Clearance Hardware.....	9
2.2. Steady Compressor Performance.....	11
2.2.1. Corrected Operating Conditions for Humidity Effects .....	11
2.2.2. Holistic Performance Measurements .....	13
2.2.3. Isentropic Compressor Efficiency.....	16
2.2.4. Detailed Steady Total Pressure Traverses.....	16
2.3. Flow Visualization Techniques .....	17
2.4. Tip Clearance Measurement System .....	18
2.4.1. Static Tip Clearance Measurements.....	18
2.4.2. Operating Tip Clearance Instrumentation.....	19
2.4.3. Operating Tip Clearance Measurement Uncertainty .....	21
2.5. Time-Resolved Flow Field Measurements .....	21
2.5.1. Over-Rotor Static Pressure Measurements .....	21
2.5.2. Total Pressure Measurements at Rotor Exit.....	23
2.5.3. Thermal Anemometry .....	24
2.6. Particle Image Velocimetry .....	33
2.6.1. Experimental Setup.....	33
2.6.2. Image Processing .....	38
CHAPTER 3: STEADY COMPRESSOR PERFORMANCE .....	41
<i>Authors: Reid A. Berdanier, Natalie R. Smith, and Nicole L. Key</i>	
3.1. Compressor Performance Maps.....	41
3.1.1. Total-to-Total Pressure Rise Characteristics .....	41
3.1.2. Operating Tip Clearance Measurements.....	42

	Page
3.1.3. Effect of Ambient Conditions on Tip Clearance and Total-to-Total Pressure Rise ....	46
3.1.4. Stall Margin .....	49
3.1.5. Total-to-Static Pressure Rise Characteristics .....	50
3.1.6. Isentropic Efficiency .....	52
3.1.7. Stator 3 Seal Leakage Flow Measurements .....	55
3.1.8. Casing Outer Diameter Surface Temperature Measurements.....	56
3.2. Stage Performance Characteristics .....	58
3.3. Inter-Stage Flow Measurements .....	60
3.3.1. Total Pressure.....	60
3.3.2. Total Temperature.....	63
3.4. Flow Visualization.....	66
3.5. Stator Wake Measurements .....	74
3.5.1. Steady Pressure and Temperature Rake Data .....	74
3.5.2. Detailed Steady Total Pressure Traverses.....	79
CHAPTER 4: CHARACTERIZATION OF COMPRESSOR STALL INCEPTION.....	84
<i>Authors: Reid A. Berdanier, Natalie R. Smith, Anna M. Young, and Nicole L. Key</i>	
4.1. Measurement Technique.....	84
4.2. Stall Inception Analysis .....	84
CHAPTER 5: TIME-RESOLVED FLOW FIELD MEASUREMENTS.....	90
<i>Authors: Reid A. Berdanier and Nicole L. Key</i>	
5.1. Over-Rotor Static Pressures.....	90
5.2. Influence of Stator Wakes on Leakage Flow .....	95
5.2.1. Influence of Stator Wakes on Leakage Flow Trajectory .....	98
5.2.2. Rotor Exit Total Pressures .....	107
5.2.3. Quantifying the Size of the Leakage Flow .....	117
5.3. Thermal Anemometry.....	119
5.3.1. Flow Angles and Velocity.....	119
5.3.2. Blockage .....	123
5.3.3. Streamwise Vorticity .....	128
CHAPTER 6: PARTICLE IMAGE VELOCIMETRY .....	132
<i>Authors: Sayantan Bhattacharya and Pavlos P. Vlachos</i>	
6.1. Stereo Results .....	132
6.2. Tomographic Results .....	136
6.3. Summary.....	137
CHAPTER 7: SUMMARY AND CONCLUSIONS.....	138
<i>Authors: Reid A. Berdanier and Nicole L. Key</i>	
7.1. Overview of Methods and Findings.....	138
7.2. Recommendations for Future Research.....	139
LIST OF PUBLICATIONS RESULTING FROM THIS PROJECT.....	140
LIST OF REFERENCES.....	141

## LIST OF TABLES

Table	Page
Table 2.1: Purdue three-stage compressor airfoil design parameters. ....	7
Table 2.2: Tip clearance configurations and design intent clearance heights.....	9
Table 2.3: Radial distributions of rake measurement locations.....	13
Table 2.4: Capacitance probe measurements system specifications.....	21
Table 2.5: Flush-mounted sensor positions for each rotor as a percentage of axial chord. ....	22
Table 2.6: Hot-wire calibration matrix. ....	27
Table 2.7: Average differences across one stator pitch for data processed with two calibration sets. Data collected at Stator 1 exit for TC1. ....	31
Table 5.1: Summary of one-dimensional blockage parameters, listed in percent flow area. ....	127

# LIST OF FIGURES

Figure	Page
Figure 2.1: Purdue three-stage axial compressor research facility. ....	8
Figure 2.2: Compressor tip clearance casing geometry configurations. Sketch not to scale. ....	10
Figure 2.3: Casing recess example photograph (TC2) highlighting 45 degree angles at both ends of recess. Flow is from left to right. ....	10
Figure 2.4: Missing 45 degree ramp upstream of Rotor 2, shown here for TC2. Flow is from left to right. ....	11
Figure 2.5: Humidity effects on measured compressor performance for a hot humid day in the context of the 100% corrected speedlines for the three tip clearance heights presented in this study. ....	12
Figure 2.6: Purdue three-stage compressor facility flowpath cross section. ....	13
Figure 2.7: Rake geometry including Kiel head details. ....	14
Figure 2.8: Rake positions for different tip clearance configurations. ....	15
Figure 2.9: Schematic of flow visualization setup, forward looking aft. ....	17
Figure 2.10: Blade-to-blade variability of tip clearance height with respect to “Blade 1” for all three rotor rows. ....	19
Figure 2.11: Circumferential capacitance probe measurement locations. ....	19
Figure 2.12: Capacitance tip clearance measurement system components. (a) Probe; (b) Oscillator; (c) Demodulator. ....	20
Figure 2.13: Over-rotor static pressure measurement system. (a) Removable sensing block and frame; (b) Calibration chamber. ....	23
Figure 2.14: Fast-response total pressure probe. ....	24
Figure 2.15: Purdue Compressor Research Laboratory hot-wire calibration facility schematic (Morrison, 2013). ....	25
Figure 2.16: Hot-wire calibration facility optional three-dimensional calibration feature. Adapted from Morrison (2013). ....	25
Figure 2.17: Radial profile of inlet turbulence intensity, as measured at the AIP. ....	26
Figure 2.18: Angular definitions for slanted hot-wire sensor. The long prong is denoted by the large circle. ....	28
Figure 2.19: Example slanted hot-wire coefficient fit at 300 ft/s. ....	29
Figure 2.20: Approximate accuracy of hot-wire processing algorithm for test-representative conditions at several known flow angles. ....	30
Figure 2.21: Processed hot-wire data at Stator 1 exit for TC1 using two separate calibrations. ...	32
Figure 2.22: Schematic of PIV setup. ....	34
Figure 2.23: Camera, lens, and tilt adapter setup. ....	35
Figure 2.24: Timing diagram for synchronized image capture. ....	36
Figure 2.25: Calibration plate mounted between blade passages. ....	36
Figure 2.26: Calibration plate images from each of the four cameras. ....	37
Figure 2.27: Laser reflection, lens filter characteristics, and fluorescent dye spectrum. ....	37
Figure 2.28: Laskin nozzle used for seeding particles into upstream flow. ....	38
Figure 2.29: Top two camera overlap region after calibration. ....	39
Figure 3.1: Compressor total pressure ratio map. ....	42
Figure 3.2: Operating tip clearances measured using capacitance probes for TC1. ....	43
Figure 3.3: Operating tip clearances measured using capacitance probes for TC2. ....	45

Figure	Page
Figure 3.4: Operating tip clearances measured using capacitance probes for TC3.....	45
Figure 3.5: Overall compressor total pressure ratio discrepancy between hot and cold test days at a 100% corrected operating speed for TC2 and TC3.....	46
Figure 3.6: Variations of total pressure ratio with ambient temperature for each of the three nominal tip clearance conditions (TC1-TC3). .....	47
Figure 3.7: Overall total pressure ratio trends with rotor tip clearance for three tip clearance configurations (TC1-TC3), each for two separate ambient temperatures at NS. ....	48
Figure 3.8: Radial total pressure profile shapes for the three tip clearance configurations with “hot” and “cold” ambient operating conditions at NS.....	49
Figure 3.9: Stall margin and stalling flow coefficient effects with tip clearance height for specified loading conditions on the 100% corrected speedline. ....	50
Figure 3.10: Total-to-static pressure rise characteristics for three tip clearance configurations. .	51
Figure 3.11: Peak total-to-static pressure rise coefficient as a function of tip clearance height...	52
Figure 3.12: Overall isentropic compressor efficiency at four corrected rotational speeds. ....	53
Figure 3.13: Isentropic compressor efficiency for specified 100% $N_c$ speedline points as a function of tip clearance height. ....	54
Figure 3.14: Stator 3 seal leakage flow path and manifold tubes from (a) the rear bearing plate to (b) an orifice plate run (Brossman, 2012). .....	55
Figure 3.15: Stator 3 seal leakage mass flow rate as a percentage of inlet corrected mass flow rate for each of the traversed data points in Figure 3.1.....	56
Figure 3.16: Normalized surface temperatures for three loading conditions on the 100% corrected speedline. ....	57
Figure 3.17: Normalized surface temperatures for the final “near-stall” traversed operating point at all four operating speeds. ....	58
Figure 3.18: Stage total pressure rise characteristics for the traversed map points. ....	59
Figure 3.19: Radial total pressure profiles at LL. ....	60
Figure 3.20: Radial total pressure profiles at NL.....	61
Figure 3.21: Radial total pressure profiles at PE. ....	61
Figure 3.22: Radial total pressure profiles at HL.....	62
Figure 3.23: Radial total pressure profiles at NS.....	63
Figure 3.24: Radial total temperature profiles at LL. ....	64
Figure 3.25: Radial total temperature profiles at NL.....	64
Figure 3.26: Radial total temperature profiles at PE.....	65
Figure 3.27: Radial total temperature profiles at HL.....	66
Figure 3.28: Radial total temperature profiles at NS. ....	66
Figure 3.29: Basic surface flow topology for Stator 1 at the high loading condition (a) image, (b) corner separations, and (c) drawn flow topology with saddle points (S) and nodes (N) labeled. ....	67
Figure 3.30: Surface flow visualization of corner separations for Stator 1 (left), Stator 2 (middle), and Stator 3 (right) at four loading conditions: NL (a-c), PE (d-f), HL (g-i), and NS (j-l) for TC1. ....	69
Figure 3.31: Stator 1 at NS conditions viewed from the leading edge looking downstream. ....	70
Figure 3.32: Flow visualization of vane corner separations at NL for TC1 (top), TC2 (middle), and TC3 (bottom).....	71

Figure	Page
Figure 3.33: Flow visualization of vane corner separations at HL for TC1 (top), TC2 (middle), and TC3 (bottom).....	73
Figure 3.34: Stator 1 total pressure wakes and pitchwise total temperature distribution. ....	75
Figure 3.35: Stator 2 total pressure wakes and pitchwise total temperature distribution. ....	77
Figure 3.36: Stator 3 total pressure wakes and pitchwise total temperature distribution. ....	78
Figure 3.37: Detailed total pressure traverses at Stator 1 exit, NL. ....	79
Figure 3.38: Detailed total pressure traverses at Stator 1 exit, HL. ....	80
Figure 3.39: Detailed total pressure traverses at Stator 2 exit, NL. ....	81
Figure 3.40: Detailed total pressure traverses at Stator 2 exit, HL. ....	81
Figure 3.41: Detailed total pressure traverses at Stator 3 exit, NL. ....	82
Figure 3.42: Detailed total pressure traverses at Stator 3 exit, HL. ....	83
Figure 4.1: Dynamic pressure traces at the inception of stall for TC1 at 100% $N_c$ . ....	85
Figure 4.2: Dynamic pressure traces at the inception of stall for TC2 at 100% $N_c$ . ....	86
Figure 4.3: Static pressure field unsteadiness over Rotor 1, presented as an RMS with respect to the EA, for each tip clearance configuration at NS. ....	87
Figure 4.4: Dynamic pressure traces at the inception of stall for TC1 at 90% $N_c$ . ....	88
Figure 4.5: Dynamic pressure traces at the inception of stall for TC1 at 68% $N_c$ . ....	88
Figure 4.6: Summary of stall inception trends for all tip clearance configurations at all investigated operating speeds. ....	89
Figure 5.1: Ensemble-average static pressure field over Rotor 1 for each tip clearance configuration at NL. ....	90
Figure 5.2: Static pressure field unsteadiness over Rotor 1, presented as an RMS with respect to the EA, for each tip clearance configuration at NL. ....	91
Figure 5.3: Ensemble-average static pressure field over Rotor 1 for each tip clearance configuration at HL. ....	92
Figure 5.4: Static pressure field unsteadiness over Rotor 1, presented as an RMS with respect to the EA, for each tip clearance configuration at HL. ....	92
Figure 5.5: Rotor 1 tip leakage trajectories for all three tip clearance configurations at three loading conditions on the 100% corrected speedline.....	93
Figure 5.6: Static pressure field unsteadiness, presented as an RMS, over each rotor for TC2 at NL. ....	94
Figure 5.7: Static pressure field unsteadiness, presented as an RMS, over each rotor for TC2 at HL. ....	95
Figure 5.8: Schematic of the interaction between rotor tip leakage flow and upstream stator wake. (a) R2 passing in the middle of the S1 passage, (b) R2 passing through the S1 wake. ....	96
Figure 5.9: Flow visualization on the casing endwall highlighting a modulation of the tip leakage flow for TC1. ....	97
Figure 5.10: Schematic of leakage flow measurements over the rotor for two vane wake-leakage flow interaction positions, (a) and (b). A boxed region identifies a representative snapshot of the leakage flow identified by the static pressure measurements. ....	98
Figure 5.11: Static pressure field over Rotor 1, averaged for all 36 blades, in terms of RMS static pressure, at each pitchwise position across one vane passage (clockwise) for TC1 at NL. ....	100

Figure	Page
Figure 5.12: Static pressure unsteadiness (RMS) over Rotor 1 for vpA (a) and vpB (b) from Figure 5.11, and the trajectories (c). .....	100
Figure 5.13: Static pressure field over Rotor 2, averaged for all 33 blades, in terms of RMS static pressure, at each pitchwise position across one vane passage (clockwise) for TC1 at NL. Only IGV and S1 are moved, S2 and S3 are fixed. ....	102
Figure 5.14: Static pressure unsteadiness (RMS) over Rotor 2 for vpA (a) and vpB (b) from Figure 5.13, and the trajectories (c). ....	102
Figure 5.15: Static pressure field over Rotor 2, averaged for all 33 blades, in terms of RMS static pressure, at each pitchwise position across one vane passage (clockwise) for TC1 at NL. Only S2 and S3 are moved, IGV and S1 are fixed. ....	103
Figure 5.16: Static pressure unsteadiness (RMS) over Rotor 2 for vpA (a) and vpB (b) from Figure 5.15, and the trajectories (c). ....	103
Figure 5.17: Static pressure field over Rotor 3, averaged for all 30 blades, in terms of RMS static pressure, at each pitchwise position across one vane passage (clockwise) for TC1 at NL using two separate vane movement techniques. ....	105
Figure 5.18: Static pressure unsteadiness over Rotor 3 for vpA (a) and vpB (b) from Figure 5.17, and the trajectories (c) (TC1, NL). ....	105
Figure 5.19: Static pressure field over Rotor 3, averaged for all 30 blades, in terms of RMS static pressure, at each pitchwise position across one vane passage (clockwise) for TC1 at HL. ....	106
Figure 5.20: Static pressure unsteadiness over Rotor 3 for vpA (a) and vpB (b) from Figure 5.19, and the trajectories (c) (TC1, HL). ....	106
Figure 5.21: Schematic of leakage flow measurements at rotor exit planes for two vane wake-leakage flow interaction positions, (a) and (b). ....	107
Figure 5.22: Average Rotor 1 exit flow field, in terms of RMS total pressure, at each circumferential location across one vane passage (clockwise) at NL. ....	109
Figure 5.23: Average Rotor 1 exit flow field, in terms of RMS total pressure, at each circumferential location across one vane passage (clockwise) at HL. ....	110
Figure 5.24: Average Rotor 2 exit flow field, in terms of RMS total pressure, at each circumferential location across one vane passage (clockwise) at NL. ....	112
Figure 5.25: Average Rotor 2 exit flow field, in terms of RMS total pressure, at each circumferential location across one vane passage (clockwise) at HL. ....	113
Figure 5.26: Average Rotor 3 exit flow field, in terms of RMS total pressure, at each circumferential location across one vane passage (clockwise) at NL. ....	115
Figure 5.27: Average Rotor 3 exit flow field, in terms of RMS total pressure, at each circumferential location across one vane passage (clockwise) at HL. ....	116
Figure 5.28: Identification of defect region associated with leakage flow unsteadiness.....	117
Figure 5.29: Percentage of rotor passage affected by tip leakage flow: passage-averaged value and range.....	118
Figure 5.30: Radial profiles of absolute yaw angle at NL. ....	120
Figure 5.31: Radial profiles of absolute yaw angle at HL. ....	121
Figure 5.32: Radial profiles of pitch angle at NL. ....	122
Figure 5.33: Radial profiles of pitch angle at HL. ....	122
Figure 5.34: Radial profiles of normalized axial velocity at Rotor 2 and Rotor 3 exit. ....	123
Figure 5.35: Example of defect region identification for Rotor 2 exit (TC1, NL). ....	125

Figure	Page
Figure 5.36: Example of defect region identification for Stator 1 exit (TC1, NL).....	125
Figure 5.37: Radial profiles of blockage at NL. ....	127
Figure 5.38: Radial profiles of blockage at HL. ....	127
Figure 5.39: Contours of streamwise vorticity at Rotor 1 exit for TC1 and TC3.....	129
Figure 5.40: Contours of streamwise vorticity at for TC1 at Rotor 2 and Rotor 3 exit.....	130
Figure 5.41: Passage-averaged maximum streamwise vorticity strength.....	131
Figure 6.1: Schematic of the PIV measurement plane and corresponding coordinate system. ..	132
Figure 6.2: Spanwise volume slices of radial velocity for stereo reconstructed velocity field at two loading conditions.....	133
Figure 6.3: Contours of radial velocity at different span-wise location for NL. A vector field representing the projected velocity in the $r - \theta$ plane is superimposed over the contours. Flow is from right to left.....	134
Figure 6.4: Contours of radial velocity at different span-wise location for HL. A vector field representing the projected velocity in the $r - \theta$ plane is superimposed over the contours. Flow is from right to left.....	135
Figure 6.5: Spanwise volume slices of radial velocity for tomographic reconstructed velocity field at two loading conditions.....	136

## LIST OF SYMBOLS

<u>Symbol</u>	<u>Description</u>
$A$	Geometric Flow Area
$B$	Blockage
$c$	Chord
$D$	Diameter
$E$	Wire Voltage
$h$	Enthalpy
$H$	Blade Span/Annulus Height
$\dot{m}$	Mass Flow Rate
$N$	Rotational Speed
$P$	Pressure
$r$	Radial Coordinate
$R$	Resistance
Re	Reynolds Number
$t$	Blade Thickness
$T$	Temperature
$U_t$	Blade Tip Speed
$V$	Absolute Velocity
$W$	Relative Velocity
$x$	Axial Coordinate
Greek	
$\alpha$	Absolute Flow (Yaw) Angle
$\beta$	Relative Flow (Yaw) Angle
$\gamma$	Ratio of Specific Heats
$\delta^*$	Velocity Density Deficit
$\eta$	Isentropic Efficiency
$\omega$	Vorticity
$\Omega$	Blade Angular Velocity
$\phi$	Pitch Angle
$\Phi$	Flow Coefficient
$\Psi$	Total-to-Static Pressure Rise Coefficient
$\rho$	Density
$\sigma$	Wire Slanting Angle
$\tau$	Tip Clearance Height
$\theta$	Tangential Coordinate
Subscripts	
AA	Radial and Circumferential Area Average
act	Actual Condition
$c$	Corrected Condition
CA	Circumferential Average
eff	Effective
leak	Leakage

<u>Symbol</u>	<u>Description</u>
Subscripts	
LN	Normalized Leakage
<i>m</i>	Meridional Direction
mech	Mechanical
<i>o</i>	Stagnation Condition
<i>r</i>	Radial Direction
RA	Radial Area Average
ref	Reference Condition
<i>s</i>	Isentropic Condition
st	Streamwise Direction
stall	Stall Condition
<i>x</i>	Axial Direction
<i>w</i>	Wire
$\theta$	Tangential Direction

## LIST OF ABBREVIATIONS

<u>Abbreviation</u>	<u>Description</u>
AIP	Aerodynamic Interface Plane
BPP	Blade Passing Period
CFD	Computational Fluid Dynamics
DCA	Double Circular Arc
EA	Ensemble Average
HL	High Loading
HPC	High Pressure Compressor
IBR	Integrally Bladed Rotor
IGV	Inlet Guide Vane
LDV	Laser Doppler Velocimetry
LL	Low Loading
LSRC	Low-Speed Research Compressor
NB	Number of Blades
NL	Nominal Loading
NS	Near Stall
OPR	Overall Pressure Ratio
PE	Peak Efficiency
PIV	Particle Image Velocimetry
RMS	Root-Mean-Square
SFW	Subsonic Fixed Wing
SLE	Special Limits of Error
SM	Stall Margin
TC	Tip Clearance
TPR	Total Pressure Ratio
TTL	Transistor-Transistor-Logic
TTR	Total Temperature Ratio

## SUMMARY

The focus of this work was to characterize the fundamental flow physics and the overall performance effects due to increased rotor tip clearance heights in axial compressors. Data have been collected in the three-stage axial research compressor at Purdue University with a specific focus on analyzing the multistage effects resulting from the tip leakage flow. Three separate rotor tip clearance heights were studied with nominal tip clearance heights of 1.5%, 3.0%, and 4.0% based on a constant annulus height.

Overall compressor performance was investigated at four corrected speedlines (100%, 90%, 80%, and 68%) for each of the three tip clearance configurations using total pressure and total temperature rakes distributed throughout the compressor. The results have confirmed results from previous authors showing a decrease of total pressure rise, isentropic efficiency, and stall margin which is approximately linear with increasing tip clearance height. The stall inception mechanisms have also been evaluated at the same corrected speeds for each of the tip clearance configurations.

Detailed flow field measurements have been collected at two loading conditions, nominal loading (NL) and high loading (HL), on the 100% corrected speedline for the smallest and largest tip clearance heights (1.5% and 4.0%). Steady detailed radial traverses of total pressure at the exit of each stator row have been supported by flow visualization techniques to identify regions of flow recirculation and separation. Furthermore, detailed radial traverses of time-resolved total pressures at the exit of each rotor row have been measured with a fast-response pressure probe. These data have helped to quantify the size of the leakage flow at the exit of each rotor. Thermal anemometry has also been implemented to evaluate the time-resolved three-dimensional components of velocity throughout the compressor and calculate blockage due to the rotor tip leakage flow throughout the compressor. These measurements have also been used to calculate streamwise vorticity.

Time-resolved static pressure measurements have been collected over the rotor tips for all rotors with each of the three tip clearance configurations for up to five loading conditions along the 100% corrected speedline using fast-response piezoresistive pressure sensors. These time-resolved static pressure measurements, as well as the time-resolved total pressures and velocities have helped to reveal a profound influence of the upstream stator vane on the size and shape of the rotor tip leakage flow.

Finally, a novel particle image velocimetry (PIV) technique has been developed as a proof-of-concept. In contrast to PIV methods that have been typically been utilized for turbomachinery applications in the past, the method used for this study introduced the laser light through the same access window that was also used to image the flow. This new method addresses potential concerns related to the intrusive laser-introducing techniques that have typically been utilized by other authors in the past.

Ultimately, the data collected for this project represent a unique data set which contributes to build a better understanding of the tip leakage flow field and its associated loss mechanisms. These data will facilitate future engine design goals leading to small blade heights in the rear stages of high pressure compressors and aid in the development of new blade designs which are desensitized to the performance penalties attributed to rotor tip leakage flows.

# CHAPTER 1: INTRODUCTION

*Reid A. Berdanier and Nicole L. Key*

Rising fuel costs and environmental concerns are continuing to drive gas turbine engine development toward increased overall efficiency and decreased fuel burn. However, achieving these goals will likely lead to smaller gas turbine engine cores for two reasons. First, improvements in materials and cooling schemes allow increased turbine inlet temperatures and, thus, increased overall pressure ratios (OPR) that will allow for higher thermal efficiencies. For a given engine size, an increased OPR is most easily accommodated through added stages. Second, larger bypass ratios lead to increased propulsive efficiencies in turbofan engines. For large aircraft, current under-wing engine mounting arrangements are limited in their ability to accommodate larger fan diameters. For small aircraft, the nacelle is already a significant contributor to overall aircraft drag and an increased fan diameter could have an overall negative effect. As these limits for the outer diameter of a turbofan are encountered, designers are turning their attention to reducing the size of the core as a means for increasing the bypass ratio. Both of these driving factors result in smaller blading, especially in the rear stages of a high-pressure compressor (HPC).

As engine cores become smaller, the flow path area decreases, and the losses in the endwall regions become more significant as they comprise a larger percentage of the total flow field. Additionally, tip clearances will not scale with the decreased blade size because of manufacturing tolerances and the margin needed for transient operation and thermal growth. As a result, a smaller core leads to rotor tip clearance heights which are large relative to the blade size. A larger relative tip clearance height leads to increased blockage due to the associated tip leakage flows, as well as potential issues with stage matching at off-design operating conditions. Previous research has suggested increased tip clearance-to-blade-height ratios causes decreased efficiency and pressure rise capability. Similarly, the ratio of clearance-to-chord may also increase, leading to a decrease in stall margin. Thus, small blade heights with increased relative clearances are expected to have a detrimental impact on HPC efficiency and operability.

However, these concerns with large tip clearance heights relative to blade size are not specific to new engine designs. Existing engine designs are also subject to these potential performance detriments as in-service deterioration results in larger clearances in compressors. The development of designs that are de-sensitized to large tip clearances would provide the ability to avoid the penalties of reduced stall margin and reduced efficiency typically associated with in-service deterioration. However, the flow physics of these tip leakage flows must be better understood in a multistage environment to generate these new designs – an understanding which must extend beyond the design point to also improve off-design compressor performance.

## **1.1. Background**

### **1.1.1. Survey of Literature**

Over the years, several dedicated literature reviews have summarized the body of work focused on tip clearance effects in compressors: Reeder (1968) and Peacock (1982, 1983). Experimental campaigns investigating several rotor tip clearances have typically been limited to

isolated rotors or single stage machines operating in a low-speed regime. In particular, the results published by Hunter and Cumpsty (1982), Inoue et al. (1986), McDougall (1990), and Goto (1992) have helped to understand the overall performance effect of increased rotor tip clearance for idealized environments experiencing a clean inlet flow, free from the effects of an upstream stage. Multistage low-speed four-stage research compressors such as the facility used by Wisler (1985), and a similar facility by Tschirner et al. (2006), provide the important multistage flow environment which is expected to affect the rear stages of an HPC. However, these low-speed measurements often do not accurately represent the Reynolds numbers and Mach numbers present in the rear stages of an HPC, nor do they incorporate appreciable compressibility effects.

Using data collected from multistage compressors of varying designs, Freeman (1985) gives a thorough overview of rotor tip clearance effects in axial compressors. This information provides a valuable summary of overall performance effects for varying rotor tip clearance heights, but it does not address the underlying flow physics and stage-to-stage impact of tip leakage flows.

Of the existing studies considering several rotor tip clearance heights, few have studied the effects of rotor tip clearance heights larger than 3% blade span. Also, many published results have focused efforts toward building a detailed understanding of the fundamental leakage flow physics at a single rotor tip clearance height, instead of combining knowledge gained from several clearance heights: e.g., Lakshminarayana et al. (1982a, 1982b), Shin et al. (2008), and Sans et al. (2013).

Experimental results from cascades have also been beneficial to the growth of knowledge relating to tip clearance flows. Of note, Williams et al. (2010) recently used a cascade to investigate very large tip clearances up to 6% of annulus height, which is representative for the HPC stages of industrial gas turbines. As expected, losses increased with increasing tip clearance, however, losses leveled off for clearances larger than 4% annulus height. The authors hypothesized that for large tip clearances, the effect of the endwall became less important, and the flow through the tip gap behaved more like that of a wing tip vortex since the casing had less impact on the leakage flow.

### **1.1.2. Characteristics of Tip Leakage Flows**

The static pressure difference across the rotor tip clearance is the primary mechanism driving the flow through the tip gap. In addition to the pressure-driven flow, the relative motion between the rotor blade and the stationary casing endwall also creates a shear-driven flow. Without a tip clearance, there exists a separation in the corner between the suction surface of the blade and the endwall as the low-velocity fluid near-wall flow is unable to negotiate the required pressure gradient as the radius of curvature decreases. The presence of a small tip clearance can be beneficial since it will energize the separation-prone fluid. Although some authors have suggested the existence of this optimal clearance height which could lead to a peak efficiency condition, this clearance is typically smaller than what can be achieved for mechanical reasons. In most applications, the tip leakage flows found in compressor rotors are responsible for entropy generation, loss in peak pressure rise, and decreased stall margin (Cumpsty, 2004).

In a canonical study, Wisler (1985) measured a change in overall compressor performance with increased tip gap in a four-stage low-speed research compressor (LSRC) at GE. When the tip clearance was increased from 1.36% to 2.8% of blade height, the overall compressor efficiency dropped by 1.5 points, and peak pressure rise was reduced by 9.7%. Wisler also showed a decrease of operability range by an 11% increase of stalling flow coefficient.

Some authors have discussed the formation of a shear layer and a vortex sheet as a result of the leakage fluid passing through the rotor tip gap interacting with the adjacent blade passage. Storer and Cumpsty (1991) used cascade measurements to show that this so-called tip leakage vortex increased in size and strength as the clearance was increased. Once the leakage vortex separates from the blade surface, it may “burst,” or break down into a high-loss region creating significant blockage to the main throughflow. The diffusive nature of the flow field contributes to this breakdown as the leakage vortex grows circumferentially and radially during its travel through the rotor passage. While passing through the tip gap, however, the clearance flow experiences little loss. Instead, the primary loss mechanism is due to the diffusive mixing that occurs when the jet-like clearance flow issues into the main passage flow. Because the exact location of the vortex breakdown may be disputable, the tip leakage “vortex” will usually be referred to as a tip leakage “flow disturbance” throughout this report.

Using measurements acquired on the same LSRC used by Wisler (1985), Yoon et al. (2006) showed that the tip leakage vortex strengthens and moves upstream as flow coefficient is reduced and also as tip clearance is increased. New findings from this experiment include that the tip vortex was weakened and moved downstream as stagger was increased. At very large clearances (5.5% chord), the vortex exhibited a change in trajectory because of a sudden increase in flow between mid-chord and trailing edge. This pushed the tip vortex toward the neighboring blade.

This circumferential flow trajectory increases the potential existence of a double leakage flow condition, as introduced by Khalsa (1996). Double leakage refers to the case when the tip leakage flow convects across the blade passage at a high trajectory angle and passes through tip clearance of the adjacent blade. In this case, the low-pressure fluid contained in the tip clearance flow faces a potentially compounding loss as it passes through the second clearance gap. The presence or absence of this effect is dependent upon the loading of the blade row through its effect on the trajectory of the vortex and the solidity of the blade row (Dickens and Day, 2011).

The role of the upstream stator is important for the development of the tip leakage flow. In particular, Mailach et al. (2008) used Laser Doppler Anemometry to investigate the tip region of a four-stage low-speed research compressor. The upstream stator wakes had a profound influence on the trajectory of the tip leakage vortex, the intensity of the tip leakage vortex, and the position of maximum tip leakage flow along the chord. This same interaction has also been addressed recently by other authors (Smith et al., 2015b; Krug et al., 2015).

Sirakov and Tan (2003) used time-accurate Reynolds-averaged Navier-Stokes simulations to understand the role of unsteadiness on rotor tip leakage flows by replacing the effect of an upstream stator with representative wake deficits. Two situations were investigated for their study: a steady wake deficit and a pulsing wake deficit – the second representing what would be experienced by a rotating blade row. The authors observed a beneficial unsteady interaction between the rotor and (simulated) stator, which was attributed to the suppression of the double leakage phenomenon.

### **1.1.3. Computational Validation Using High-Speed Experimental Data**

Detailed experimental datasets are critical for validating computational models of tip leakage flow effects on compressor performance. Suder and Celestina (1996) compared computations to experimental data obtained in the single stage transonic compressor (Stage 37) facility at NASA Glenn Research Center. Two loading conditions (peak efficiency and near stall) were investigated at two operating speeds: 60% speed with subsonic flow and 100% speed where the shock structure could be studied. The tip clearance at design speed was 0.5% span (0.7%

chord). Laser anemometer measurements captured the interactions between the tip leakage vortex and the shock structure at high speeds. These authors showed that the radial influence of the tip leakage flows extended over a range up to twenty times the physical clearance at operating speeds for which shocks were present. At the subsonic conditions, however, the radial influence of the leakage flow was reduced to only five times the physical clearance.

These experimental data for Stage 37 allowed Van Zante et al. (1999) to investigate computational models of the tip clearance flow field focusing on the impact of grid topology, the numerical treatment of the tip gap, and their effects on the solution. The authors found that gridding the tip gap did not provide any advantages over using a simple tip clearance model, but the wall-bounded shear layer was an important component to the tip clearance flow, especially when the difference between the relative velocities of the leakage jet and casing was large. Gupta et al. (2003) agreed that sufficient clustering of grid points near the casing, as a method for capturing the shear layer, was critical to a successfully modeling the tip leakage flows. However, these authors were able to achieve the best results by using a square tip and fully resolving the tip gap rather than using approximate methods. A summary of these and other difficulties affecting computational models for turbomachinery applications, including tip clearance gap modeling challenges, is addressed by Denton (2010).

The observations by Van Zante et al. (1999) and Gupta et al. (2003) provide an excellent example of how a quality experimental dataset can be used to calibrate CFD models. However, the isolated rotor and single stage environment does not capture all of the important flow physics present in a multistage compressor. In particular, spanwise mixing and endwall boundary layers are influenced by upstream stages. These, in addition to the tip leakage flow, are major contributors to blockage in the endwall region and can lead to stage matching issues (Cumpsty, 2004).

#### **1.1.4. Spanwise Mixing**

Spanwise mixing is responsible for distributing the high losses associated with the endwall flows toward mid-span. For geometry with low aspect ratios, this spanwise mixing component must be accurately modeled to capture the flow field correctly. Adkins and Smith (1982) developed a spanwise mixing model which suggested secondary flow generated spanwise and cross-passage velocities to enhanced mixing, and it agreed well with several test cases. However, because this model was based on inviscid secondary flows, it was not adequate for cases with significant regions of separated flow, including high loading or other off-design cases.

A different mechanism responsible for spanwise mixing was proposed by Gallimore and Cumpsty (1986). Using an ethylene tracer gas technique, these authors concluded that turbulent diffusion, rather than the radial velocity associated with secondary flows, was the main mechanism for spanwise mixing. For this analysis, the experiments were performed near a peak-efficiency point, but off-design conditions with highly separated flows were not investigated.

In fact, both of the mechanisms identified by Adkins and Smith (1982) and Gallimore and Cumpsty (1986) can be important. Wisler et al. (1987) used the ethylene tracer gas technique and hotwire anemometry to investigate mixing at design loading and high loading operating conditions. In the “free stream region,” they found the primary mechanism for mixing was turbulent diffusion. In the endwall regions and along the blade surfaces, though, secondary flow effects were equally responsible, if not slightly more important than turbulent diffusion. A follow-on computational study by Leylek and Wisler (1991) confirmed the importance of both turbulent diffusion and secondary flows in the spanwise mixing process. However, these authors

noted important considerations to accurately recreate spanwise mixing representative of real engine operating environments. Of note, the turbulence intensity associated with upstream blade and vane wakes must be appropriately introduced, and the blade row inlet endwall boundary layer must be adequately represented to achieve the secondary flow field.

The single stage low-speed study conducted by Goto (1992) at the Whittle Laboratory investigated the effect of different rotor tip clearances (up to 3% chord) on the flow field in the downstream stator, with an emphasis on spanwise mixing. As the tip clearance increased, the blockage in the tip region increased and led to a decrease in wake size near the stator hub and a suppression of the unsteadiness in the hub region.

### **1.1.5. Blockage and Stage Matching**

In compressors, blockage represents the reduction of flow area due to the existence of low momentum fluid. Blockage will increase the velocity in the core flow region, thereby reducing the work done by the rotor on the core flow. As endwall boundary layers grow at off-design operating conditions, stage matching problems may be introduced. However, a lack of understanding for this endwall boundary layer growth in multistage axial compressors also exists at design conditions and typically forces designers to rely on correlations, as explained by Cumpsty (2004).

The most significant body of data on compressor endwall boundary layers was acquired by Smith (1970) in the four-stage LSRC at GE. These data showed that blockage was essentially unchanged across a repeating stage, and blockage was a function of tip clearance and loading condition. However, the repeating-stage model is valid for multistage compressors with large aspect ratios and relatively small clearances. The repeating stage condition was not achieved for an aspect ratio of 1.96, the lowest aspect ratio tested by Smith. The rear stages of high pressure core compressors typically have aspect ratios on the order of unity. Thus, further information must be collected under these conditions to supplement the data published by Smith.

Cumpsty (1986) presented measurements from a four-stage compressor at lower Reynolds numbers. The data indicated that the rotor tip clearance (or stator hub clearance) was a critical parameter for determining the endwall boundary layer thickness. Using a model developed to relate the flow through the tip clearance to the downstream blockage, Khalid et al. (1999) proposed that the total pressure loss in the endwall region resulted from the interaction of tip leakage flows and passage flows, and the vortical structure associated with the leakage vortex was deemed less important. Khalid et al. also correlated endwall blockage with aerodynamic loading on the blade. Data acquired by Suder (1998) on the isolated transonic rotor (Rotor 37) showed that the blockage in the endwall region increased with blade loading in agreement with Khalid's correlation. Further, 3D Particle Image Velocimetry (PIV) measurements collected by Wernet et al. (2005) in a large-scale four-stage low-speed compressor at NASA Glenn Research Center showed that the radial velocity component was important in determining the radial extent of influence of the tip leakage flows and the blockage associated with these flows.

## **1.2. Program Objectives**

NASA led a Turbomachinery Technical Working Group that provided a list of propulsion improvements necessary to meet the Subsonic Fixed Wing (SFW) project goals, specifically allowing the project to meet its N+1 and N+2 reduced fuel burn goals. One of the main topics on

the list was tip leakage flows in high pressure ratio cores. The group anticipates that the smaller cores will result in blade tip clearances of 2% to 4% of blade height, and the resulting compressor efficiency loss due to the leakage flow through the tip gap could be as high as 5 points, corresponding to a specific fuel consumption (SFC) effect on the order of 3% (Heidmann, 2009). Thus, reductions in these endwall and tip leakage losses are absolutely necessary to realize SFC improvements.

The research presented in this report supports NASA's strategic goals of reduced fuel burn in the SFW area by contributing to the understanding of core compressor losses associated with tip leakage flows and other endwall losses. Once the flow physics associated with these losses are understood, CFD models can be generated to accurately predict off-design performance. These data will be instrumental in calibrating predictive tools for multistage compressor performance. Before designs attempting to mitigate or desensitize compressor performance to large tip clearances can be successfully achieved, the flow physics associated with these large tip clearance flows must be well understood and accurately predicted. The data acquired in this project help to illuminate such flow physics.

The objective of this research project was to provide detailed flow field measurements in a three-stage axial compressor typical of the rear stages in an HPC. The availability of these data provides an opportunity to calibrate existing CFD tools for off-design prediction and stage matching. The experimental campaign has measured the flow field for three different rotor tip clearances: a baseline case with a 1.5% tip clearance (with respect to annulus height), a 3% tip clearance, and a large tip clearance of 4%. A comparison of three different tip clearance configurations allows the performance deltas between configurations to be captured. Overall compressor performance maps have been acquired, as well as detailed flow field measurements. A combination of traditional measurement techniques such as Kiel head total pressure probe traverses and hotwire anemometry have been used, in addition to a novel PIV technique, which has proven the ability to non-intrusively interrogate 3D flow field structures in the embedded stage of a multistage compressor. This project represents one of the few complete databases available in the open literature, and it is the only database focused on multistage flow in the rear stages of an HPC with large relative tip clearances.

## CHAPTER 2: EXPERIMENTAL METHODS

Reid A. Berdanier, Natalie R. Smith, and Nicole L. Key

### 2.1. Research Facility

#### 2.1.1. Integral Facility Components

The Purdue University three-stage axial compressor research facility is a geometrically-scaled design which models the rear stages of a high-pressure core compressor. In particular, the facility features engine-representative Reynolds numbers and Mach numbers, which makes it a useful vehicle for research at a high technology readiness level. Furthermore, the intermediate rotational speed regime and the multistage design of the facility create unique opportunities to analyze an “embedded” stage and complex multistage flow effects.

The Purdue three-stage compressor facility features a 6061 aluminum casing and all blading is machined from 17-4 stainless steel. The compressor is comprised of an inlet guide vane (IGV) followed by three stages. The inlet guide vane and the three rotor rows are double-circular arc (DCA) designs, and the three stator vane rows are NACA 65-series airfoils. All three of the rotor rows are integrated bladed rotor (IBR) “blisk” designs, such that each of the three rotor rows represents one solid piece of material. Further, each of the stationary vane rows has been created as a 180-degree monolithic segment, with vanes which are fully-shrouded at the inner and outer diameters. Specific geometric parameters for the blading in the facility are outlined in Table 2.1.

Each of the stationary vane rows are individually circumferentially indexable for up to two full stator vane passages, allowing circumferential flow variations to be measured with stationary instrumentation. Each of the vane rows is moved with a pair of linear actuators during compressor operation, and precision string potentiometers provide feedback control of the vane positions. This two-vane circumferential measurement capability was an expansion beyond previous capabilities which was made possible through the new compressor casing hardware required for this project.

Table 2.1: Purdue three-stage compressor airfoil design parameters.

Blade Row	Camber [°]		Stagger [°]		Chord [in.]		$t/c$	Airfoils		$Ma$ (avg)		$Re_c$ $10^5$
	Hub	Tip	Hub	Tip	Hub	Tip		N	Type	Rel	Abs	
IGV	-12.3	-14.0	8.2	9.0	2.00	2.00	0.065	44	DCA	0.26	0.26	3.0
R1	44.7	25.8	32.6	47.8	2.46	2.81	0.045	36	DCA	0.46	0.32	7.0
S1	49.5	48.3	25.6	24.0	2.11	2.11	0.065	44	65	0.35	0.35	4.4
R2	42.4	24.6	35.4	49.8	2.60	2.96	0.049	33	DCA	0.45	0.31	7.7
S2	49.7	48.4	26.1	24.6	2.22	2.22	0.065	44	65	0.33	0.33	4.6
R3	39.5	22.9	38.2	51.8	2.75	3.13	0.051	30	DCA	0.44	0.31	8.4
S3	62.4	61.2	19.7	18.1	2.35	2.35	0.065	50	65	0.31	0.31	4.8

The research compressor is driven from the rear by a 1400 hp AC motor through a 5:1 speed-increasing gearbox to provide a nominal rotational speed of 5000 rpm at the design point. A liquid-cooled variable frequency drive system paired with an encoder on the motor drive shaft provides the capability to maintain a compressor operating speed within 0.01% of the desired mechanical speed. This capability creates an especially unique opportunity to ensure confidence in the repeatability of measurements as they relate to the rotational speed of the machine. In addition to the motor encoder, an optical laser tachometer aimed at the high-speed output shaft of the gearbox creates a transistor-transistor logic (TTL) signal which is used as a once-per-revolution (1/rev) trigger for the high frequency response data acquisition systems.

The compressor operates with ambient, unconditioned air as the working fluid. As shown in Figure 2.1, the air is first drawn into a large settling chamber before passing through a reducing bellmouth into a two foot diameter duct. A long-form Venturi flow meter designed in accordance with ASME PTC-19.5 (2004) flow measurement standards accurately measures the mass flow rate passing through the compressor.

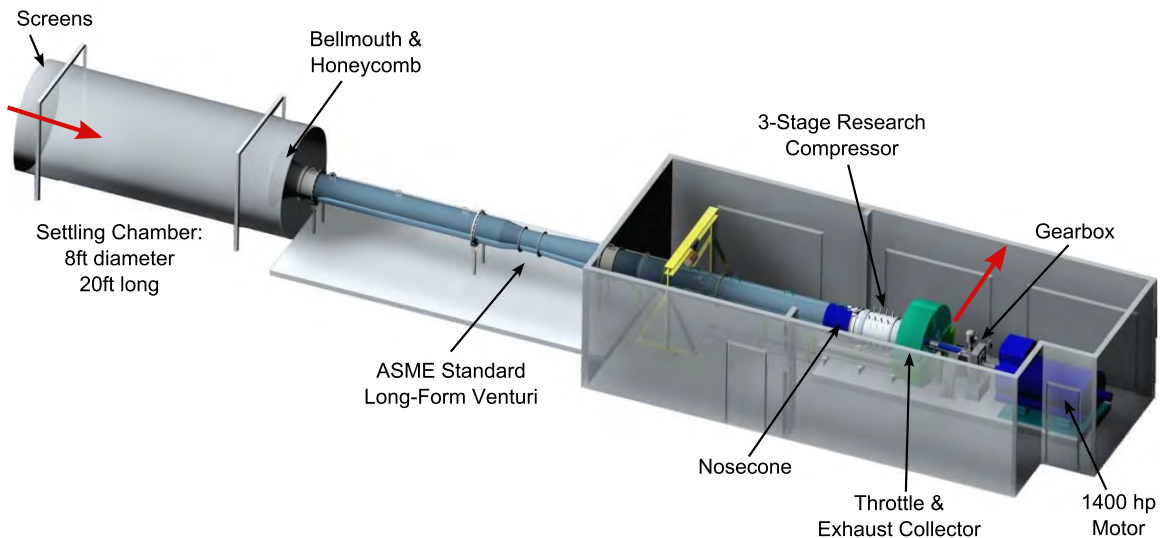


Figure 2.1: Purdue three-stage axial compressor research facility.

Two Rosemount 3051C high-accuracy pressure transmitters are installed for measuring the differential pressure across the Venturi. Because the relative uncertainty of the differential pressure measurement is dependent upon the calibration range, the two 3051C transmitters were calibrated in different pressure ranges (0 to 5 inH<sub>2</sub>O and 0 to 8 inH<sub>2</sub>O) and are connected via a manifold. These ranges were selected to ensure adequate coverage of the entire range of operating conditions (0 to 8 inH<sub>2</sub>O), while maintaining a measurement near the peak efficiency point which utilizes the smallest possible measurement uncertainty. Moreover, in the low flow rate measurement range, the pair of devices provides a redundant measurement for added confidence. As a complement to the differential pressure measurements, a pitot-static pressure probe with an integrated T-type thermocouple is installed just upstream of the Venturi meter, and the measurements from this probe are used to define the density and other thermodynamic properties required for the mass flow rate calculation equations.

After passing through the Venturi meter, the air continues through an insulated duct section that is 11 duct diameters in length. A bullet-nose cone upstream of the compressor directs the airflow to the constant annulus flowpath, which is defined by a two-inch passage height with a hub-to-tip ratio of 5:6. At the exit of the compressor, a sliding-annulus throttle controls the back pressure of the machine, and a scroll collector directs the air to an exhaust plane at ambient pressure. Additional specifics defining the existing facility layout can be found in Ball (2013), and a thorough discussion of facility health monitoring systems is provided by Talalayev (2011).

### 2.1.2. Additional Geometry Considerations

In addition to the typical geometry parameters prescribed for the Purdue three-stage compressor flowpath, other pertinent information may be required to accurately build a computational model of the machine. Of note, the labyrinth (knife) seal clearances under the stator platforms have been measured as “cold” (static) values: 0.022 in. for the IGV, 0.035 in. for Stator 1, 0.037 in. for Stator 2, and 0.024 in. for Stator 3. Operating “hot” clearances for these seals have not been measured. Further, all of the stator vanes have fillet radii at both inner and outer diameter endwalls of 3/32 in., and the rotor hub fillet radii are all 0.150 in. The leading edges of the rotor blades have elliptical shape, and the stators have circular leading edges. An average surface roughness of 30-40  $\mu\text{in.}$  has been prescribed for all of the internal flowpath surfaces, including the blades. A past analysis using an optical scan compared the design intent geometry of the rotor blisks with the as-manufactured geometry and confirmed that all measured dimensions are within the specified design tolerances of the parts. The rotor tip clearances for each defined operating condition have been measured, and the data are presented in this report.

### 2.1.3. Variable Tip Clearance Hardware

A series of compressor casing hardware components were required to support the tip clearance analyses desired for this project. Three tip clearance configurations were used for this study, as outlined by the information in Table 2.2. In each configuration, one discrete tip clearance height exists for all three rotor rows (i.e., no combinations of tip clearance heights were considered). The first tip clearance configuration (TC1) represents the baseline compressor configuration that has been presented by previous investigators with this facility. This baseline configuration represents a nominal 1.5% tip clearance height as a fraction of overall annulus height.

Table 2.2: Tip clearance configurations and design intent clearance heights

Configuration	Nominal Clearance Height, $\tau$ [in]	Normalized Clearance Height, $\tau/H$ [%]	Tip Clearance Representation
TC1	0.030	1.5	Smooth Wall
TC2	0.060	3.0	Casing Recess
TC3	0.080	4.0	Casing Recess

As shown in the cartoon of Figure 2.2, the two larger tip clearance configurations (TC2 and TC3) were achieved through the use of a casing recess over the rotors. These compressor configurations nominally represent 3.0% and 4.0% tip clearance height. Although the differences

between casing recesses and traditional cropped rotors have been documented in the past (Wisler and Beacher, 1989), the parametric analysis discussed by Brossman (2012) showed through computational simulation of the Purdue three-stage axial compressor that the overall performance and the individual stage performances of a compressor with these types of casing recesses – which are introduced as far as possible upstream and downstream of the rotor – sufficiently represent the trends of the same machine with a smooth wall and a cropped rotor. This, combined with the budget constraints involved with a cropped rotor study, led to the choice of using recessed casings to achieve the two larger clearance configurations.

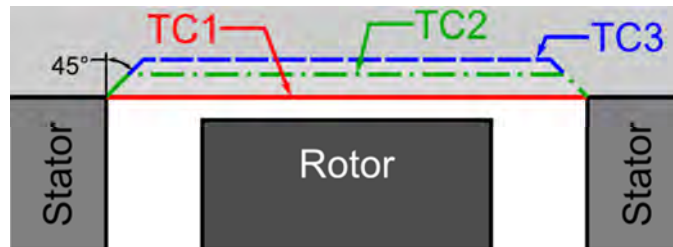


Figure 2.2: Compressor tip clearance casing geometry configurations. Sketch not to scale.

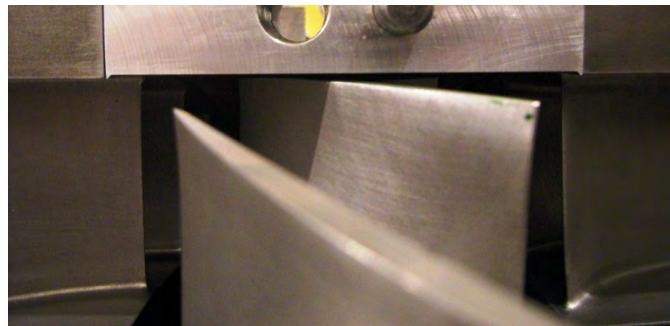


Figure 2.3: Casing recess example photograph (TC2) highlighting 45 degree angles at both ends of recess. Flow is from left to right.

Because the emphasis of this study was not on the effects of trenched casings as discussed by Wisler and Beecher (1989), the axial extent of the trenches was increased as much as allowable to the adjacent stator vanes (approximately 0.4 axial chords upstream and downstream of the rotor blades). Furthermore, 45 degree angles were introduced to ease the transition from the 2-inch annulus height of the baseline compressor defined by the stator vanes and the increased space over the rotors. The introduction of these angle features facilitates grid topology continuity for computational comparison studies. In addition to the cartoon of the casing configurations in Figure 2.2, a photographic example of the casing recess for TC2 is shown in Figure 2.3. It is important to note here that a manufacturing error led to the removal of the 45 degree ramp from the recess at the upstream side for Rotor 2, as shown in Figure 2.4, for both TC2 and TC3.



Figure 2.4: Missing 45 degree ramp upstream of Rotor 2, shown here for TC2. Flow is from left to right.

To ensure that the three separate compressor casings would provide the best possible vehicle for tip clearance performance comparisons, the casing designs incorporated tight manufacturing tolerances. In addition to preventing the introduction of tip clearance non-uniformities for a given casing configuration, these tolerances also helped to ensure consistency between the three casings. The most important of these tolerances pertained to the inner diameter of the casing over the rotor tips, for which the diameter dimension was specified with a tolerance of  $+0.001/0.000$  in., as well as geometric tolerances of 0.005 in. for the overall runout and 0.002 in. for the profile shape. These tolerances, as well as all of the other pertinent dimensions, were verified by coordinate measuring machine (CMM) inspection processes.

## **2.2. Steady Compressor Performance**

### **2.2.1. Corrected Operating Conditions for Humidity Effects**

The definition of a compressor operating point is typically “corrected” to standard day conditions to ensure consistent measurements with changing inlet conditions and comparability with computational simulations. To this end, many facilities operate according to classical corrected speed and corrected mass flow rate definitions defined by turbomachinery textbooks. However, careful examination of these equations shows that they do not appropriate account for the presence of humidity in the air.

Existing compressor test codes and full engine analyses discuss the importance of humidity, and some suggest the use of conditioned or refrigerated air to avoid the potentially negative effects (NACA TN-1138, 1950; Erwin, 1964). Because the Purdue three-stage compressor facility does not have the luxury of a conditioned air supply, a method of appropriately accounting for the presence of humidity is required.

Analysis of the derivation process leading to the classical equations defining corrected speed and corrected mass flow rate for a compressor highlights the assumptions of a thermally- and calorically-perfect gas which are not necessarily appropriate for a humid air mixture. Ultimately, an alternate presentation of these same equations has been derived to circumvent the need for perfect gas assumptions. These alternate equations utilize stagnation speed of sound and stagnation density in place of stagnation temperature and stagnation pressure in the classical equations. By this process, the corrected rotational speed is determined by

$$N_c = \frac{N_{\text{mech}}}{a_{o,\text{act}}/a_{o,\text{ref}}}, \quad (2.1)$$

and the corrected mass flow rate is determined by

$$\dot{m}_c = \dot{m}_{\text{act}} \left( \frac{\rho_{a,\text{ref}} a_{o,\text{ref}}}{\rho_{a,\text{act}} a_{o,\text{act}}} \right). \quad (2.2)$$

A formal derivation of these conditions for humid air considerations is available in Berdanier et al. (2015). The results of this study showed that air conditions which are realizable in the hot and humid midwest United States summers can lead to a miscalculation of required mechanical speed on the order of 0.5% and actual mass flow rate on the order of 1.0%. Even for the intermediate-speed class of compressors encompassing the Purdue three-stage compressor, these effects are well within the measurement capabilities of existing instrumentation. Specifically, a comparison of the results using the classical equations for corrected conditions and the alternate representations of the equations is shown by the humidity zone identified in Figure 2.5.

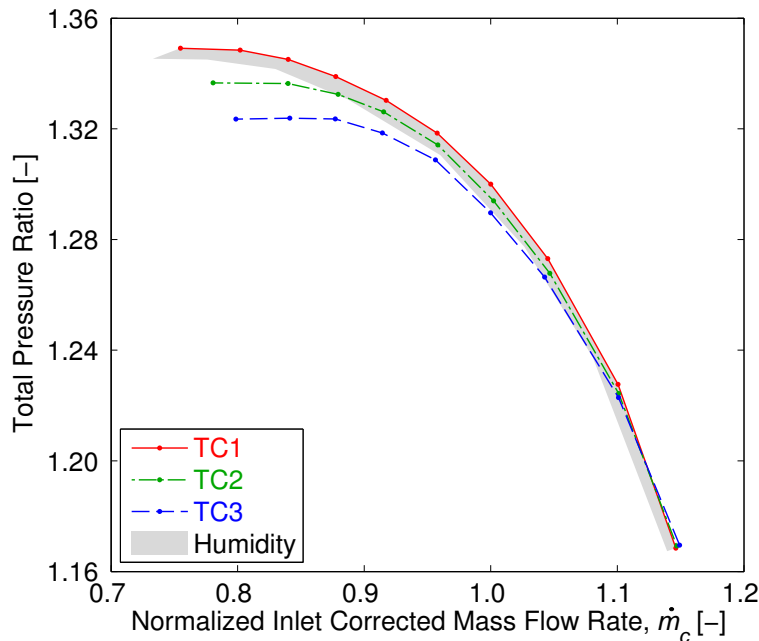


Figure 2.5: Humidity effects on measured compressor performance for a hot humid day in the context of the 100% corrected speedlines for the three tip clearance heights presented in this study.

Figure 2.5 reveals that research facilities which operate with unconditioned ambient air (such as the Purdue three-stage compressor) must carefully consider humidity effects for correcting operating conditions, particularly when measuring small-scale performance changes or attempting to compare results at the same operating condition across several seasons of the year. The desired deliverables of this project match both of these requirements, and therefore, further emphasize the importance of humid air considerations for this project.

### 2.2.2. Holistic Performance Measurements

For the Purdue three-stage compressor, the conditions used to calculate the corrected speed and corrected mass flow rate are measured at the Aerodynamic Interface Plane (AIP), denoted by axial position zero in the flowpath shown in Figure 2.6. At this upstream inlet plane of the compressor, the 50% span measurements from a seven-element total pressure rake and a seven-element total temperature rake are used to represent the bulk one-dimensional flow. The amount of moisture in the air is determined by an Omega HX94 thermo-hygrometer located near the inlet of the compressor, capable of measuring relative humidity with an uncertainty of  $\pm 2\%$ . These measured parameters are used as inputs with the REFPROP thermodynamic equation program (Lemmon et al., 2013) to calculate the pertinent stagnation speed of sound and stagnation density required for Equations (2.1) and (2.2) above.

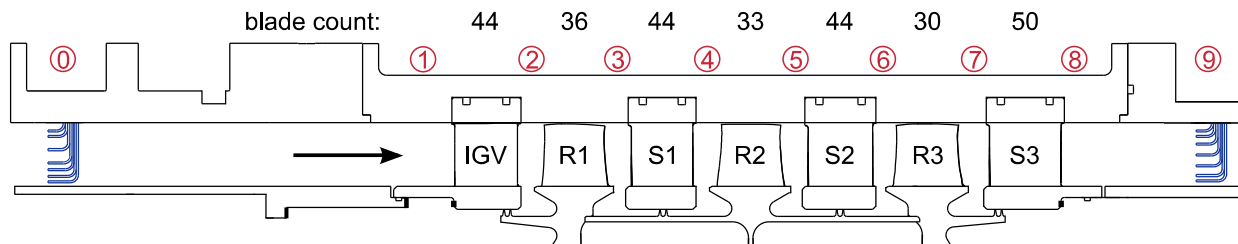


Figure 2.6: Purdue three-stage compressor facility flowpath cross section.

In addition to the seven-element total pressure and total temperature rakes installed at the AIP, 13 circumferentially-distributed static pressure taps evaluate the static pressure for this upstream inlet plane at the outer diameter of the flowpath. Great care has been incorporated to ensure circumferential uniformity of the pressures and temperatures at the inlet of the compressor, as measured by Ball (2013).

Referring again to the flowpath in Figure 2.6, the exit plane of the compressor (axial position 9) is also defined by a set of seven-element total pressure and total temperature rakes and one static pressure measurement. Separate from these upstream and downstream locations, additional seven-element total pressure and total temperature rakes are available at each of the axial positions labeled 1 through 8. Static pressures at these axial positions are evaluated by four circumferentially-distributed static pressure taps on the casing. The combination of these measurements at positions 1 through 9 provide the opportunity to define overall compressor performance and relative performance of each individual blade row or each stage. The radial position of the measurement locations for the seven-element pressure and temperature rakes at each axial position 0 through 9 are provided in Table 2.3.

Table 2.3: Radial distributions of rake measurement locations.

Ax. Pos.	Total Pressure [% annulus height]							Total Temperature [% annulus height]						
0	12	20	30	40	60	80	88	12	20	35	50	70	80	88
1 – 8	12	20	35	50	70	80	88	12	20	35	50	70	80	88
9	12	20	35	50	65	80	88	12	20	30	50	70	80	88

The axial location of the stations labeled in Figure 2.6 is halfway between the blade rows based on the mid-span geometry. Figure 2.7 provides the details of the Kiel head geometries for the total temperature and total pressure rakes. The centerline of the rake coincides with the location of the axial measurement plane. The recovery factor for both the total pressure and total temperature rakes (as provided by the manufacturer) is equal to one, with three significant digits, for an angular acceptance range of  $\pm 30$  degrees. The rakes are aligned with a representative mean flow angle, but this angular acceptance facilitates accurate measurements at off-design operating conditions.

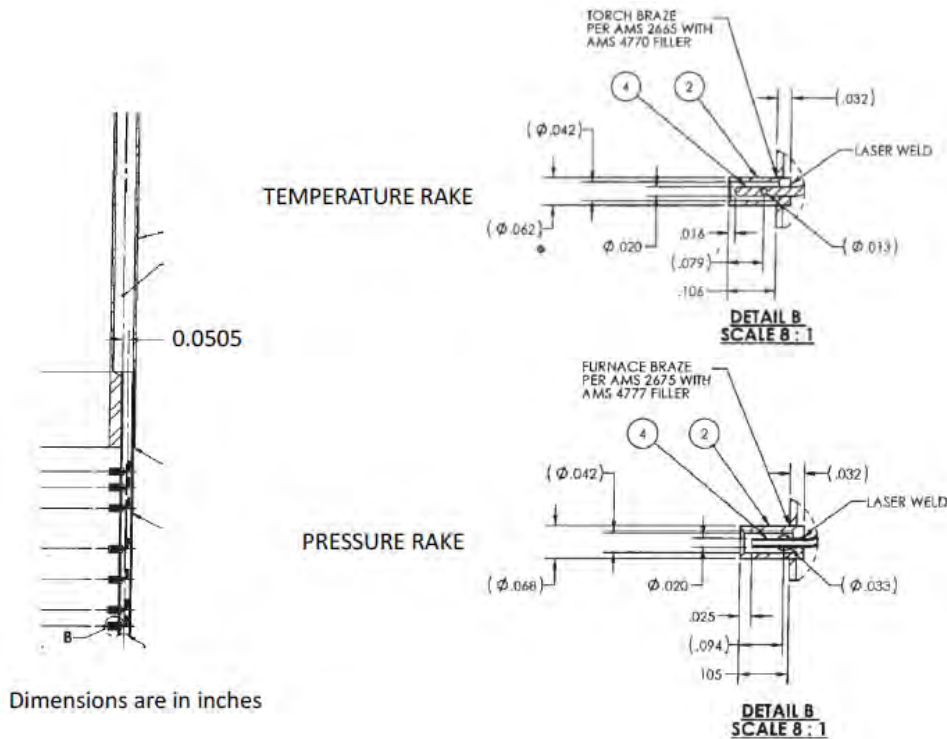


Figure 2.7: Rake geometry including Kiel head details.

Because the recessed casing geometry design (Figure 2.2) extends to the farthest axial extent, when the rakes are inserted with the TC2 or TC3 casing hardware, they are positioned within the tip clearance recess area. For this study, the rakes were radially positioned such that the measurement positions defined in Table 2.3 are consistent with the annulus height of the stator vanes (which are geometrically unaffected by the casing recesses). These rake positions are shown graphically in Figure 2.8, such that the outer edge of the rake was aligned with the 100% annulus height location, regardless of the tip clearance configuration (i.e., whether or not a casing recess was present). By this method, the detailed measurements collected at these same axial positions extend to 101.5% or 102.5% annulus height for the TC2 and TC3 tip clearance configurations, respectively.

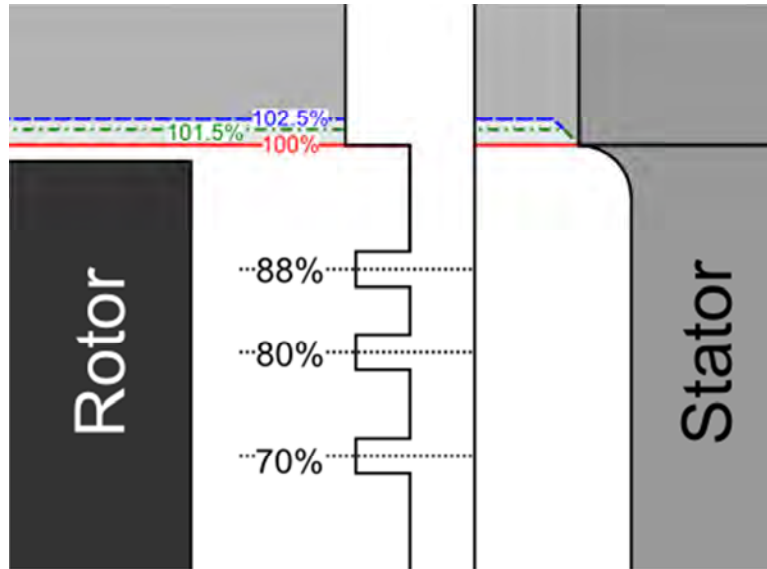


Figure 2.8: Rake positions for different tip clearance configurations.

The new variable tip clearance hardware for this project expanded the capabilities of the facility to accommodate measurement rake insertion at three or five circumferential positions (specifically for measurement plane 6, at the exit of the embedded second stage) for each of the positions 1 through 8 in Figure 2.6. These same rake insertion positions also function as locations for the installation of L.C. Smith precision probe positioners for detailed measurement traverses with a variety of instrumentation technologies.

In addition to the flow measurements, a series of surface-mounted thermocouples are installed on the outer part of the casing over each blade row to yield an axial temperature distribution. These measurements facilitate CFD analyses implementing alternate boundary condition methods, such as the isothermal boundary condition presented by Bruna and Turner (2013) for Rotor 37, instead of the more common, but significantly simplified, adiabatic boundary condition. Because the data collected from this experimental study are expected to aid in the development and calibration of computational models, it is important that these temperatures are collected with the aerodynamic performance data to appropriately define the system boundary conditions.

The total and static pressures for the facility are measured using Scanivalve 3217 and 3016 Digital Sensor Array (DSA) pressure scanner modules, each containing 16 temperature-compensated piezoresistive pressure sensors. Depending on the requirements of the specific measurement, the DSA channels are rated for differential pressure ranges of 1 psid, 2.5 psid, 5 psid, or 15 psid. These devices have been selected for their long-term accuracy ratings of 0.12% FS, 0.12% FS, 0.05% FS, and 0.05% FS, respectively. Thermal measurement drifts from these devices are prevented through regular procedures for an on-line zero calibration prior to and during compressor operation. The differential pressures are referred to an atmospheric reference pressure which is separately measured using a high-accuracy Setra 270 barometric pressure sensor with an accuracy of 0.03% FS.

The temperatures for the facility are evaluated using T-type thermocouples paired with special limits of error (SLE) extension wire. A Keysight Technologies 34980A integrating voltmeter paired with 34921A/T modules and terminal blocks accommodates the measurement

of these thermocouple channels. To achieve significantly reduced uncertainty contributions to the temperature measurements, Keysight Y1138A extension cables separate the terminal blocks from the measurement modules, and a 10 k $\Omega$  thermistor with an interchangeability of  $\pm 0.18$  °R provides the reference temperature for the isothermal terminal block. The temperature data reported for this study have been evaluated by an arithmetic mean of five independent measurements, each of which represents a thermocouple voltage measurement integrated over five power line cycles.

Through the use of a liquid calibration bath, the measurement chain for each of the temperature rake measurement channels was evaluated. By incorporating a high-accuracy thermistor as a reference measurement in the same calibration bath, the overall uncertainty of each individual channel was determined. These calibration results show an overall uncertainty typically less than 0.45 °R for all temperature channels. However, the repeatability of the temperature measurements is an order of magnitude less than this value.

### 2.2.3. Isentropic Compressor Efficiency

For this study, the isentropic compressor efficiency will be evaluated using the formal definition,

$$\eta = \frac{h_{o2s} - h_{o1}}{h_{o2} - h_{o1}}, \quad (2.3)$$

as a function of stagnation enthalpies. Alternatively, a perfect gas assumption allows a simplification of isentropic efficiency,

$$\eta = \frac{\text{TPR}^{((\gamma-1)/\gamma)} - 1}{\text{TTR} - 1}, \quad (2.4)$$

which appears to be preferable due to its definition as a function of measured properties – total pressures and temperatures appearing in the total pressure ratio (TPR) and total temperature ratio (TTR). However, following an effort to minimize perfect gas simplifications, there is an inherent complication with the use of Equation (2.4), as discussed by Lou et al. (2013) and continued by Berdanier et al. (2015). Specifically, Lou et al. (2013) showed that the isentropic efficiency is always over-predicted when using Equation (2.4). This over-prediction may be less than 1 efficiency point for an overall TPR of 1.3, but it increases to over 5 efficiency points for a TPR on the order of 40 or more. The introduction of REFPROP as an integral component of the data processing suite for this study provides the opportunity to calculate isentropic efficiency via the *definition* of the parameter shown in Equation (2.3). As with the calculation of corrected parameters described above, the use of REFPROP also accommodates the inclusion of humidity in the calculation of the stagnation enthalpies required to evaluate efficiency.

### 2.2.4. Detailed Steady Total Pressure Traverses

As described above, the steady compressor pressure rise is defined using a series of seven-element total pressure rakes distributed throughout the machine. However, these measurements inherently lack spatial resolution and a more thorough distribution of measurements closer to the endwalls. Thus, in addition to the total pressure rake measurements, a miniature Kiel head total pressure probe (United Sensor KAC-type) was traversed in small radial increments downstream of each of the stator vane rows. This probe features a 0.063 in. outer diameter Kiel head and was

paired with a L.C. Smith precision probe positioner to incrementally achieve the desired plunge locations with position feedback. The probe accommodates a yaw and pitch acceptance cone of greater than  $\pm 40$  degrees, but the probe was aligned with a representative mean flow angle.

### 2.3. Flow Visualization Techniques

In addition to the detailed total pressure traverses downstream of the stators, a flow visualization method was introduced to investigate the surface flow topologies on the stator vanes and evaluate regions of flow separation. The flow visualization technique was performed using a mixture of kerosene and powder paint. The mixture is inserted at the AIP (axial position 0), as shown in Figure 2.9, while the compressor is running at a steady operating condition. The mixture flows through the compressor, and the kerosene evaporates leaving streaklines of paint on the flowpath surfaces, particularly in regions of flow recirculation. Following a series of preliminary tests, a mixture ratio of 5:2 kerosene-to-paint (based on volume) was selected to provide optimal paint coverage. The position of paint injection in Figure 2.9 was chosen specifically to allow full coverage of each individual vane row. Two colors of fluorescing powder paint were used, blue and orange, to provide high-contrast images.

All flow visualization photographs were acquired with a Canon Rebel XSi DSLR camera with an EF-S 18-55mm f/3.5-5.6 SI lens. Because the paint is deposited in regions of recirculating flow, most of the paint is located near the trailing edge of the vanes. Thus, all pictures were taken aft of the vane, looking forward (unless otherwise noted). The photographs presented herein were all illuminated with a 100 Watt ultraviolet black light lamp, allowing the fluorescent power paint to be more clearly identified. Additional information about the setup procedure and photographic processing methods is available in Smith and Key (2015).

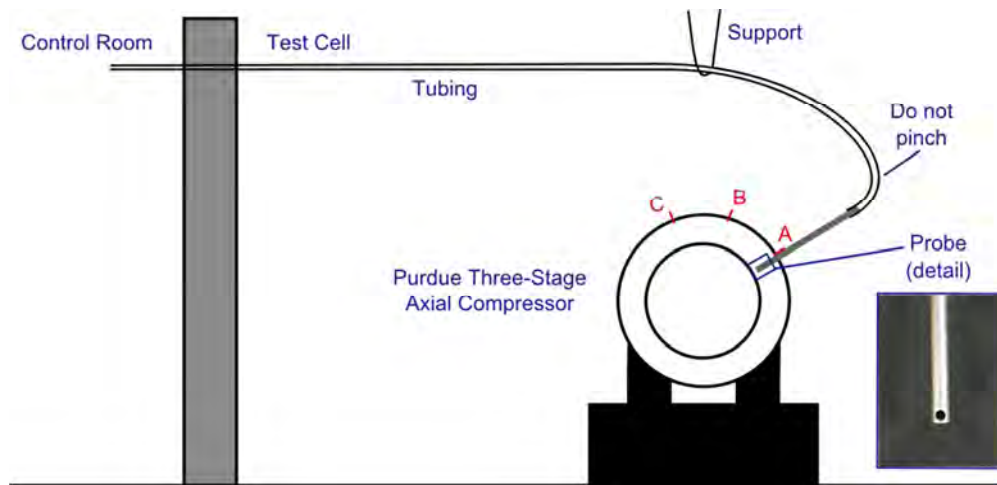


Figure 2.9: Schematic of flow visualization setup, forward looking aft.

## **2.4. Tip Clearance Measurement System**

It is well known that static rotor tip clearances – sometimes referred to as “cold” clearances – do not typically represent the operating, or “hot” running, clearances. In general, thermal growth, pressure forces, and centrifugal effects due to high-speed rotor rotation contribute to blade growth and untwist which leads to difference rotor tip clearances at different operating conditions and for different ambient conditions. The influence of thermal effects on the compressor casing may also contribute significantly to changing rotor tip clearances. As a result, a series of measurements have been collected to evaluate the static and operating tip clearances of the Purdue three-stage compressor.

### **2.4.1. Static Tip Clearance Measurements**

The static “cold” tip clearances have been evaluated for each of the three tip clearance configurations. These measurements were collected by measuring the blade-to-blade variability (i.e., the run-out of the rotor blade tips) using a fixed dial indicator with a rolling tip. The manufacturing tolerances of the rotor blisk show the blade-to-blade variability at any fixed location about the circumference of the compressor, as presented in Figure 2.10. These blade-to-blade measurements were collected several times to calculate the mean values in Figure 2.10. As a result, the uncertainty of the mean value is on the order of  $1 \times 10^{-4}$  in.

The concentricity of the rotor with respect to the casing has also been evaluated using static tip clearance measurements collected at several positions around the circumference of the compressor casing. These measurements have shown for each tip clearance configurations that the concentricity of the rotor with respect to the casing is on the order of 0.004-0.008 in. The smallest tip clearances are measured at a position of 345 degrees from the top of the compressor, in the direction of rotor rotation, as shown in Figure 2.11. The rotor concentricity can be controlled using a set of alignment bolts at both the front and rear bearing assemblies, as prescribed by Talaleyev (2011). This concentricity control is limited to within 0.008-0.012 in. based on bolt thread pitch. Thus, the measured concentricity of the rotor is confirmed to be within the adjustment capabilities of the system.

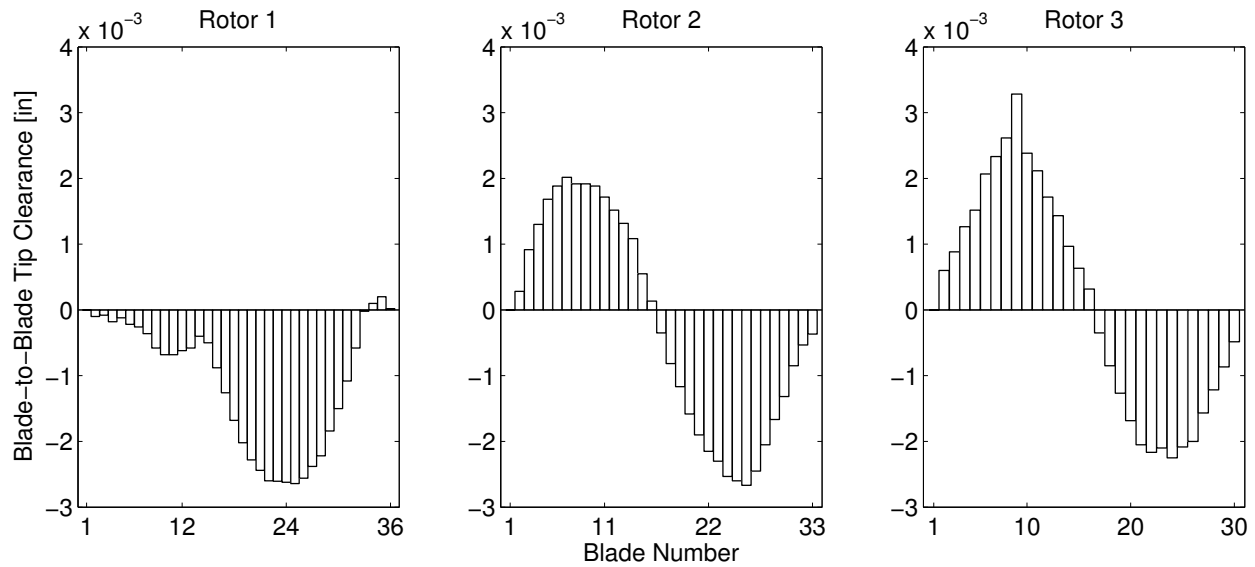


Figure 2.10: Blade-to-blade variability of tip clearance height with respect to “Blade 1” for all three rotor rows.

#### 2.4.2. Operating Tip Clearance Instrumentation

For this study, a facility upgrade included the introduction of a CapaciSense 5-series frequency modulated (FM) capacitance probe tip clearance measurement system (produced by Pentair Thermal Management). The system features nine available channels, allowing three probes to be implemented for each of the three compressor rotors. The three probes are equally-spaced circumferentially, 120 degrees apart, at positions of 105 degrees, 225 degrees, and 345 degrees – all measured from the top of the compressor in the direction of rotor rotation (see Figure 2.11). Each of the nine probes was individually calibrated using a custom-designed calibration disk which represents the tip geometry of the rotor blade through scaling techniques proven by the manufacturer. The probes were all calibrated for operation from a rub condition (0 in. clearance) to a maximum 0.2 in. clearance height.

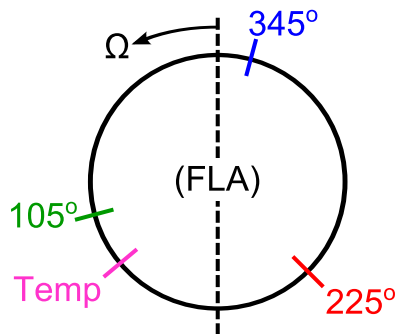


Figure 2.11: Circumferential capacitance probe measurement locations.

The electronics chain for the FM tip clearance measurement system has several key components. The probes, shown in Figure 2.12(a), were designed and built for application in this specific facility; a triaxial cable is permanently attached to the probe and provides enhanced rejection of electromagnetic interference. The use of a non-mineral-insulated cable limits the maximum operating temperature of this system to approximately 260 °C, well above the operating limits of the Purdue three-stage compressor. The oscillator, shown in Figure 2.12(b), drives the cable with an oscillating voltage (nominally 2 MHz). As the blade passes the probe, the measured capacitance modulates the driven frequency from the oscillator. This modulation is sensed by the carrier, and the demodulator (Figure 2.12(c)) converts the modulation frequency due to the blade passing event to a DC voltage. The DC voltage is correlated to a clearance height via the individual channel calibration. This proportionality between measured capacitance, frequency modulation, voltage, and tip clearance is the heart of the FM tip clearance measurement system.

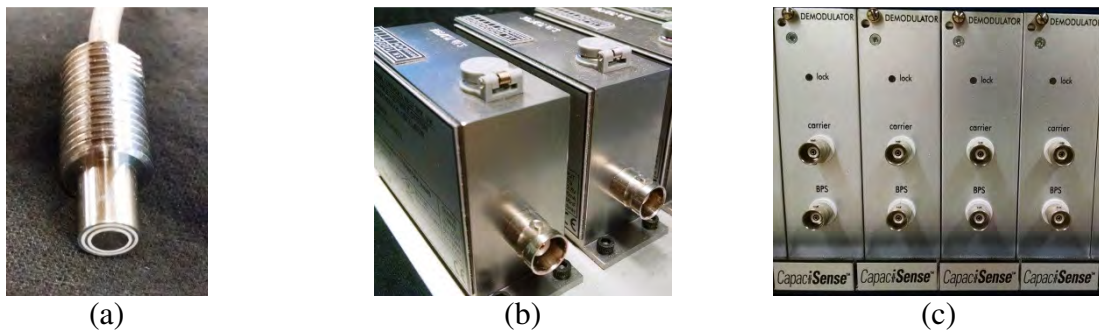


Figure 2.12: Capacitance tip clearance measurement system components.  
 (a) Probe; (b) Oscillator; (c) Demodulator.

The clearance measurement system is controlled from a set of “Control and Processing Module” (CPM) computers operating Slackware 14 Linux. Each of these computers utilizes one Advantech PCI-1714UL data acquisition card to sample four of the nine channels (three total CPMs). The three CPMs are setup in a master-slave-slave configuration communicating via Ethernet, and the master CPM utilizes a proprietary graphical user interface (GUI) to configure and operate the entire probe measurement chain (including the oscillators and demodulators). The data acquisition card is capable of sampling the four analog channels at up to 10 MHz per channel, as well as an external trigger which is linked to the 1/rev signal from the laser tachometer for the compressor. For the measurements presented in this study, all data were collected using the full 10 MHz sampling capability of the data acquisition card. Other specifications for the capacitance probe measurement system are listed in Table 2.4.

The clearance calculation process provides a blade-by-blade clearance output calculated from the peak-to-peak voltage for the typical blade pulse output signal (known as the Blade Passing Signal (BPS)). By synchronizing the measured clearances with the once-per-revolution trigger from the compressor, these calculated clearances from the BPS output can be traced to known blade numbers. As an alternative to this BPS method, the software applies a low-pass filter to the BPS output to create a DC voltage output signal which the manufacturer refers to as a “RMS” signal, although it should be noted that the low-pass filter mechanism does not represent a true root-mean-square calculation procedure. This RMS signal serves as a representative average measurement of the tip clearance for all blades by a particular probe.

Table 2.4: Capacitance probe measurements system specifications.

<b>Parameter</b>	<b>Value</b>
Operating Frequency	2 MHz nominal
Oscillator Sensitivity	100 kHz per pF
Demodulator Sensitivity	500 mV per kHz typical
Measurement Range	0.200 in. calibrated
System Resolution	$< 4 \times 10^{-5}$ in. (at 0.030 in. clearance)
Signal-to-Noise Ratio	30-50 typical

### 2.4.3. Operating Tip Clearance Measurement Uncertainty

The manufacturer of the capacitance probe measurement system claims an umbrella uncertainty on the measurement system of less than  $4 \times 10^{-4}$  in. This value is based on historical comparisons with other measurement techniques, including laser measurements and rub sticks, as well as careful attention to the design, manufacture, and calibration processes to ensure minimal uncertainties. However, no formal uncertainty analysis had yet been performed to validate this claim, which represents more of a repeatability, or comparability, and does not consider uncertainty contributions from the electronics components.

To overcome this limitation, an uncertainty analysis was performed based on known information about the electronic devices in the system and the calibration data. Following a method outlined by Müller et al. (1997) for a similar capacitance probe system, the uncertainty of the individual probes was evaluated to be on the order of 0.001 in. or less over the range of tip clearances investigated for this study. Additional information regarding the tip clearance system uncertainty analysis is available in Berdanier and Key (2015a).

## 2.5. Time-Resolved Flow Field Measurements

### 2.5.1. Over-Rotor Static Pressure Measurements

Time-resolved static pressures over the rotor tips were measured using a custom-designed array implementing flush-mounted fast-response pressure transducers. This array incorporates 25 Kulite XCS-062 subminiature pressure transducers (having an outer diameter of 0.066 in.) with a 5 psig range. These XCS-series transducers feature high-sensitivity piezoresistive sensing elements, maximizing the resolution of the measurements. These sensors were installed with standard B-type screens for protection of the sensing elements, but the new sensors were filled with additional silicon material to reduce the cavity size behind the screen and allow for the greatest allowable frequency response. As a result, a natural frequency on the order of 30 kHz is expected for these new sensors.

During the design process, a specific effort was made to accommodate all sensors in one axial row. Some previous authors have utilized a method of offsetting sensors in two or more

axial rows, separated by some angle in the pitch-wise direction, to accommodate more axial resolution (Yoon et al., 2006; Shin et al., 2008; Courtiade and Ottavy, 2012). However, such sensor orientations can introduce complications in the measurements for multistage machines, as the wakes propagating from upstream stators and potential fields from downstream stators may affect the measurements. Understandably, this effect can be accounted for if the sensors are moved relative to the stator vanes, but it introduces an additional complication to the data acquisition and processing procedures. As an alternative, other authors have achieved maximum axial resolution by implementing a series of sensors at different axial positions, spaced periodically in the circumferential direction with respect to the rotor pitch (Levis, 2006; Sans et al., 2013). However, this method could be also be negatively affected by blade-to-blade non-uniformities, rotor eccentricity, and any associated flow variability.

The small diameter of the XCS-062 devices provided the ability to incorporate as many sensors as possible in one axial row, thereby increasing the spatial resolution of the output results. The sensors are permanently installed in a removable block which can be inserted into any one of nine frames. These nine frames represent one for each of the three rotor blade rows (R1-R3), and each of the three tip clearance configurations (TC1-TC3). The removable sensing block and one of the nine frames are shown in Figure 2.13(a).

The instrumentation block was designed to maximize the number of sensors which can fit within the space defined by the instrumentation access location over Rotor 1, which features the least axial space. Because the same fixed sensor locations are implemented for Rotor 2 and Rotor 3, whereas the axial chord of the rotors increases slightly moving from Rotor 1 to Rotor 3, the positions of the sensors change with respect to the leading and trailing edges of the blades for the three rotor rows. These sensor positions are presented for the three rotors in Table 1 as a percentage of axial chord.

Table 2.5: Flush-mounted sensor positions for each rotor as a percentage of axial chord.

Blade Row	Minimum Sensor Location [% $c_x$ ]	Maximum Sensor Location [% $c_x$ ]	Sensor Separation [% $c_x$ ]
Rotor 1	-14.0	114.0	5.33
Rotor 2	-12.8	113.6	5.26
Rotor 3	-11.9	113.2	5.21

The excitation and amplification for these fast-response pressure sensors were provided by a Precision Filters 28000 chassis with four 28118 full bridge amplification cards, each of which is capable of managing eight channels for a total of 32 simultaneous operating sensors. Each of the channels in the Precision Filters system is independently managed through a manufacturer-designed GUI to adjust the DC offset, gain, and on-board analog filter characteristics. The sensor signals were then digitized using an NI PXIe-1073 chassis utilizing two 16-channel PXIe-6358 modules, each capable of simultaneous sampling of up to 1.25 MHz per channel, via NI BNC-2110 connector blocks.

Immediately prior to installation and operation in the compressor, the fast-response pressure sensors were calibrated in a custom-designed calibration chamber (Figure 2.13(b)) by prescribing a known pressure to the device. For each calibration, up to 15 data points were prescribed over the full sensing range of 0 to 5 psi. From these measurements, a least-squares

linear fit was applied to the calibration data. The channels were zeroed prior to each calibration and again prior to testing, although thermal compensation and a stable measurement system reduce the day-to-day drift of a representative channel to 1 mV or less over (after amplification), which corresponds to a pressure of less than  $8 \times 10^{-4}$  psi.

For each rotor and each tip clearance configuration, data were acquired at several loading conditions on the 100% corrected speedline. In all cases, 500 revolutions of data were simultaneously sampled to allow phase-locked ensemble averaging and other pertinent statistics.

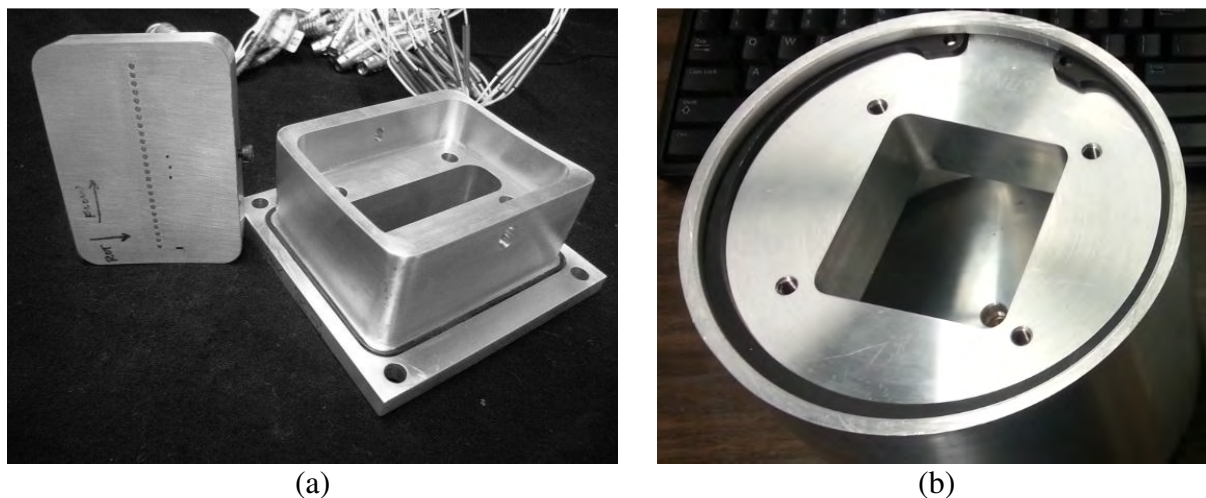


Figure 2.13: Over-rotor static pressure measurement system. (a) Removable sensing block and frame; (b) Calibration chamber.

### 2.5.2. Total Pressure Measurements at Rotor Exit

In addition to the steady total pressures measured at positions downstream of the stator vane rows, time-resolved total pressure measurements were also acquired at the rotor exit planes. A custom-designed fast-response total pressure probe incorporates a Kulite LQ-062 subminiature pressure transducer embedded in a miniature Kiel head with a 0.083 in. outer diameter and a 0.067 in. inner diameter (Figure 2.14). The sensor has a 5 psi maximum range with an electronically sealed gage reference condition. As with the surface-mounted pressure sensors described in Section 2.5.1 above, this transducer also includes a standard B-type protective screen, therefore reducing the natural frequency of the sensors to approximately 20 kHz. A separate pressure chamber designed for this probe provided the ability to calibrate the sensor at prescribed intervals over the 0-5 psi, range and a least-squares linear fit was applied to the calibration results. The sensor was balanced with the acquisition of a zero gage pressure reading prior to each calibration, and similarly before and after each test. As with the detailed steady total pressure measurements, these time-resolved rotor exit total pressures were acquired at two loading conditions on the 100% corrected speedline for the smallest and largest tip clearance configurations (TC1 and TC3).



Figure 2.14: Fast-response total pressure probe.

### 2.5.3. Thermal Anemometry

Hot-wire anemometry was used for this study to acquire time-resolved velocity and flow angle measurements throughout the compressor. For all measurements, a Dantec Dynamics StreamLine Pro frame was used with 91C10 constant temperature anemometer (CTA) bridges. A computer interfaces with the bridge frame through a PC operating the Dantec Dynamics StreamWare software. The sensor voltages output from the CTA bridges are digitized using an NI PXIe-1073 chassis through a NI BNC-2110 connector block and an eight-channel NI PXIe-6356 module. A custom-designed NI LabVIEW GUI operates the L.C. Smith precision probe positioner holding the sensor, as well as the data acquisition procedures.

The hot-wire sensors utilized for this project were calibrated using the hot-wire calibration facility in the Purdue Compressor Research Laboratory, which features a low-turbulence system with three-dimensional directional sensitivity and precision control of flow conditions. The facility, shown schematically in Figure 2.15, is fed from a reservoir of dry compressed air maintained at a nominal pressure of 300 psig. A digital pressure regulator (UP) adjusts the upstream pressure of the system to control the velocity via a proportional-integral-derivative (PID) control loop. The flow passes through two in-line flow heaters (H1, H2), and a separate PID control sequence maintains the jet temperature to within one degree Fahrenheit of the desired set point. The heaters ensure that the hot-wire calibration data are acquired at a constant temperature to remove calibration uncertainties due to temperature changes. After flowing through the two heaters, the air is diverted around a flow spreader and then passes through a series of honeycomb and screens for flow conditioning. A nozzle with a diameter of 1 in. accelerates the flow to the desired velocity, which is determined by a combination of stagnation plenum pressure and static pressure at the nozzle exit. The system maintains the jet exit velocity within 0.2 percent of the desired set point. An attachment to the calibration nozzle (Figure 2.16) provides the capability to vary the position of the probe with respect to the jet, effectively changing the pitch angle of the flow with respect to the probe. Additional information about the calibration jet facility is available from Morrison (2013).

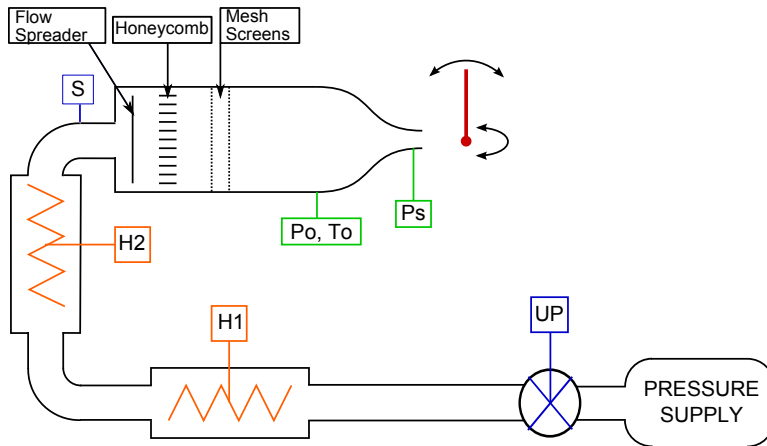


Figure 2.15: Purdue Compressor Research Laboratory hot-wire calibration facility schematic (Morrison, 2013).

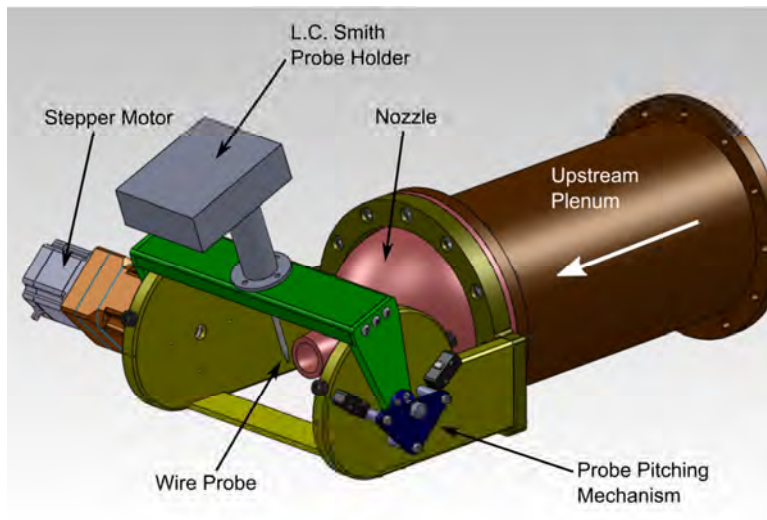


Figure 2.16: Hot-wire calibration facility optional three-dimensional calibration feature. Adapted from Morrison (2013).

### 2.5.3.1. Inlet Turbulence Intensity

The inlet turbulence intensity of the compressor was evaluated by traversing a Dantec Dynamics 55P12 miniature 45 degree slanting wire sensor radially across the flow field at the AIP (plane 0 in Figure 2.6). For these measurements, the sensor was positioned in a normal wire orientation perpendicular to the mean flow in a benign one-dimensional flow region where the slanting wire would not be affected by three-dimensional flows. For these data, the wire bridge was operated in a 1:1 mode to achieve increased frequency response with the CTA system on the order of 200 kHz. In the CTA control software, the overheat ratio (OHR) of the bridge was adjusted to the manufacturer-optimized value of 1.8, as defined the resistance of the wire,  $R_w$ , under heated (“hot”) and ambient (“cold”) conditions:

$$\text{OHR} = \frac{R_{w,\text{hot}}}{R_{w,\text{cold}}} . \quad (2.5)$$

With sufficient frequency response from the hot-wire, the turbulence intensity can be measured as a scale by which to evaluate the amount of turbulent fluctuations in the flow. The turbulence intensity (TI) is evaluated as the ratio of the root-mean-square (RMS) of the velocity fluctuations to the mean velocity:

$$\text{TI} = \frac{v'}{\bar{V}} , \quad (2.6)$$

where the velocity can be defined at any position as the sum of the average,  $\bar{V}$ , and the random fluctuations,  $v'$  (RMS):

$$V = \bar{V} + v' . \quad (2.7)$$

The inlet turbulence intensity, Figure 2.17, has been evaluated for 16 radial measurement positions across the annulus height at the AIP. These results are presented for a loading condition near the peak efficiency point on the 100% corrected speedline. This figure shows the inlet TI is on the order of 1% up to approximately 75% annulus height, where it begins to increase toward the tip. This increase is likely associated to the increased fluctuations in the boundary layer, but the sharp increase close to the wall may be due to an influence from the hole in the outer casing through which the probe is inserted. These same data were collected at ten loading conditions from open throttle to a near stall operating condition, but the standard deviation of TI at each radial position is small (less than 0.05%) across a majority of the speedline, signifying an insensitivity of inlet TI with respect to loading condition. The largest changes are observed approaching the stall point on the 100% corrected speedline, for which the values shown in Figure 2.17 increase by approximately 0.20% across the entire annulus height.

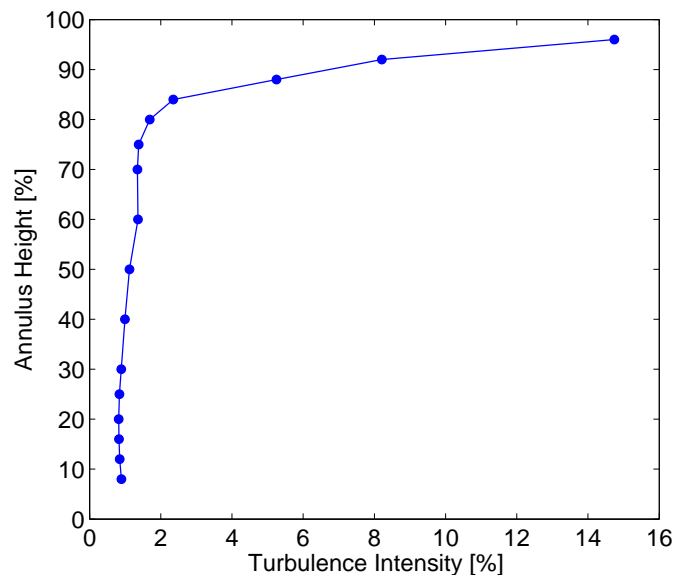


Figure 2.17: Radial profile of inlet turbulence intensity, as measured at the AIP.

### 2.5.3.2. Velocity and Flow Angle Measurements

The velocity and flow angles throughout the compressor were evaluated for axial measurement planes 2 through 8. These data were acquired at two loading conditions on the 100% corrected speedline for the two extreme tip clearance configurations (TC1 and TC3). These tests were conducted using a Dantec Dynamics 55R02 fiber-film sensor with a 45 degree slanting angle. For this sensor, the manufacturer specifies a sensing film length of approximately 0.05 in. and a nickel film diameter of approximately  $5 \times 10^{-5}$  in. The selection of the slanted probe for this project provides the opportunity to investigate three-dimensional flow fields, with a particular emphasis on the tip leakage flow features. For these measurements, the 55R02 sensor was operated in a standard 20:1 CTA bridge mode with a manufacturer-optimized overheat ratio of 1.8, as previously defined by Equation (2.5).

The fiber-film sensor technology is offered as an option which provides a more robust design than traditional thin wires, thereby reducing susceptibility to damage from the high-shear flows present in high-speed compressor applications, without the degradation of frequency response which is typically observed with traditional film sensors. Throughout this document, however, the term ‘wire’ will be used interchangeably to also describe the fiber-film sensor.

The 55R02 sensor was calibrated over a range of velocities and flow angles, as prescribed in Table 2.6. The response of the fiber-film sensor was optimized near the upper end of the velocity calibration range (400 ft/s) using a square wave test signal. Using this method, the frequency response of the sensor was estimated to be approximately 85 kHz – nearly 30 times the blade passing frequency of the rotor blades in the desired compressor application. For each test campaign, a calibration was performed prior to the data collection, and a separate calibration was performed after the completion of the campaign for comparison of measurement drift. The jet temperature for these calibrations was always maintained at a constant 100 °F.

Table 2.6: Hot-wire calibration matrix.

Parameter	Velocity, $V$ [ft/s]	Yaw angle, $\alpha$ [deg]	Pitch angle, $\phi$ [deg]
Min. value	100	-90	-20
Max. value	450	+90	+20
Increment	50	5	5

To evaluate three-dimensional phase-locked ensemble averaged velocity components, three separate wire positions are required with respect to the flow field. At each test condition and measurement location, the sensor was aligned with the approximate mean flow angle, and then yawed to the three desired measurement angles using the precision probe positioner. Following the procedure outlined by Shin and Hu (1986), the sensor angles used for this study were -60 degrees, -20 degrees, and +20 degrees with respect to the null position, as defined by the coordinate system in Figure 2.18.

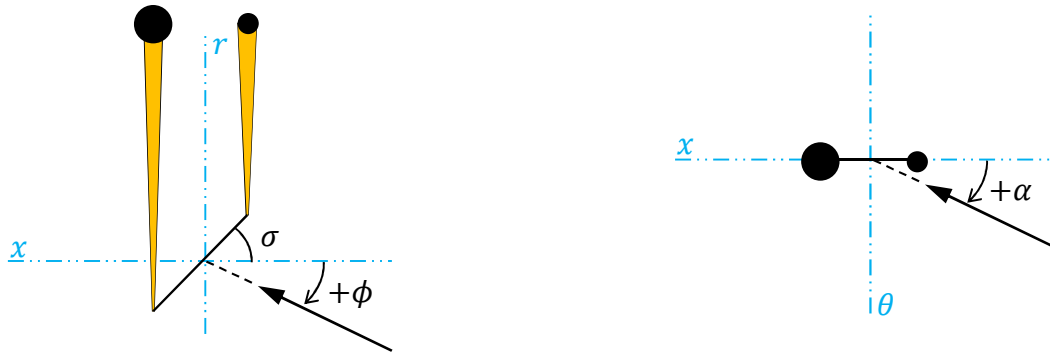


Figure 2.18: Angular definitions for slanted hot-wire sensor. The long prong is denoted by the large circle.

The measured wire voltages were converted to known velocities and flow angles using calibration data with a non-linear solver technique for data reduction. In this case, the Joule heating principle and King's law (1914) are applied to evaluate the voltage-velocity relationship. Next, the relationship between Nusselt number and Reynolds number proposed by Collis and Williams (1959) accounts for variations of flow properties between calibration and test conditions. When required, REFPROP was used to calculate thermodynamic properties for use in the non-dimensional Nusselt and Reynolds numbers. The effective Reynolds number,  $Re_{eff}$ , is determined from the effective velocity, defined as any velocity which does *not* appear as a normal velocity with respect to the wire orientation (i.e.,  $\pm 90$  degrees yaw and 0 degrees pitch). Finally, the desired non-linear relationship:

$$\frac{Re_{eff,j}}{Re} = C_0 + C_1 \alpha + C_2 \phi + C_3 Re + C_4 \alpha \phi + C_5 \alpha Re + C_6 \phi Re + C_7 \alpha^2 + C_8 \phi^2 + C_9 Re^2, \quad (2.8)$$

is developed for ten coefficients  $C_i$  determined from the calibration data, which must apply for all three wire orientations,  $j = 1..3$ . This equation is based on the method utilized by Schmidt and Okiishi (1976).

An example comparison of the non-linear equation fit from Equation (2.8) with the discrete calibration points, Figure 2.19, represents this functional relationship for one of the calibration sets used in this study at a velocity of 300 ft/s. For this study, the slanted wire was found to be asymmetric about the null (zero degrees yaw) position. As a result, a separate coefficient set was defined for each half of the curves in Figure 2.19. The coefficient fit for the example data in Figure 2.19 has an  $R^2$  value greater than 0.98, where  $R^2$  represents the coefficient of determination as calculated from the residual sum of squares and the total sum of squares.

Once wire voltages are measured in the compressor, the effective Reynolds numbers are calculated, and the three equations, Equation (2.8), are solved simultaneously using the pre-determined coefficients to calculate the true Reynolds number and the flow angles, which are geometrically related to the pre-defined wire positions of -60, -20, and +20 degrees.

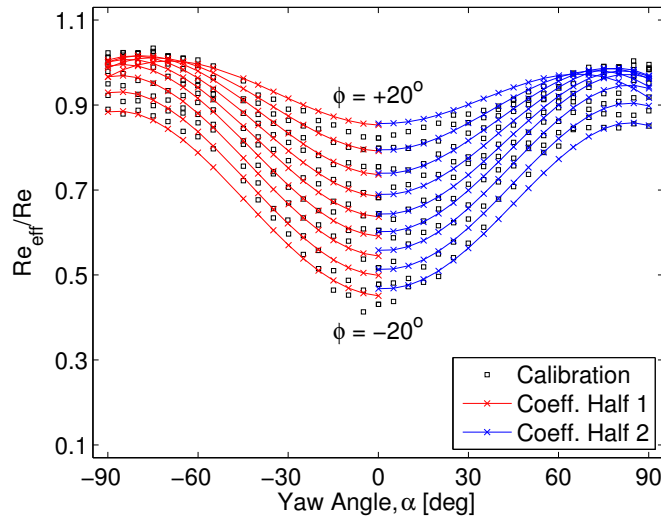


Figure 2.19: Example slanted hot-wire coefficient fit at 300 ft/s.

### 2.5.3.3. Thermal Anemometry Uncertainty

The uncertainty of the calibration data collected from the Purdue calibration jet facility has been evaluated previously by Morrison (2013). To evaluate the accuracy of the processing algorithm implemented for the velocity and flow angles measurements, a series of data were collected at known wire positions, velocities, and conditions in the calibration jet which represent the compressor operating conditions for each test campaign. Specifically, the temperature and density of the jet were adjusted to match the flow conditions determined from the steady total temperature and total pressure rakes (and wall static pressure), as measured simultaneously with the hot-wire. Furthermore, a representative velocity was also calculated from these rake measurements to select the operating velocity of the calibration jet. Using this method, the accuracy of the measurements at each axial measurement position (i.e., Rotor 1 exit, Stator 3 exit, etc.) and compressor loading condition was separately identified, Figure 2.20.

The results in Figure 2.20 show that the calculated velocity from the hot-wire processing algorithm is a strong function of the operating condition in the compressor, whereas the calculated yaw and pitch angles are less dependent on operating conditions. An investigation with alternate processing methods (Berdanier and Key, 2015b) has shown that the velocity can be greatly affected if the conditions of the measured flow vary significantly from the calibration conditions. However, the calculated flow angles are much less sensitive to these temperature effects due to their greater dependence on the geometry of the probe itself. Indeed, analysis of the results in Figure 2.20 shows that the test conditions which yield the most significant velocity difference are the same conditions for which the temperature at the wire location was most different from the calibration temperature. In the same manner, the test conditions which show the least difference (closest to zero) are those for which the temperature at the location of the wire in the compressor was nearly identical to the calibration temperature. For reference, in this figure, the velocity difference on the order of -60 ft/s is representative of a temperature 40 °F lower than calibration conditions, and the velocity difference on the order of +30 ft/s is representative of a temperature 30 °F higher than calibration conditions.

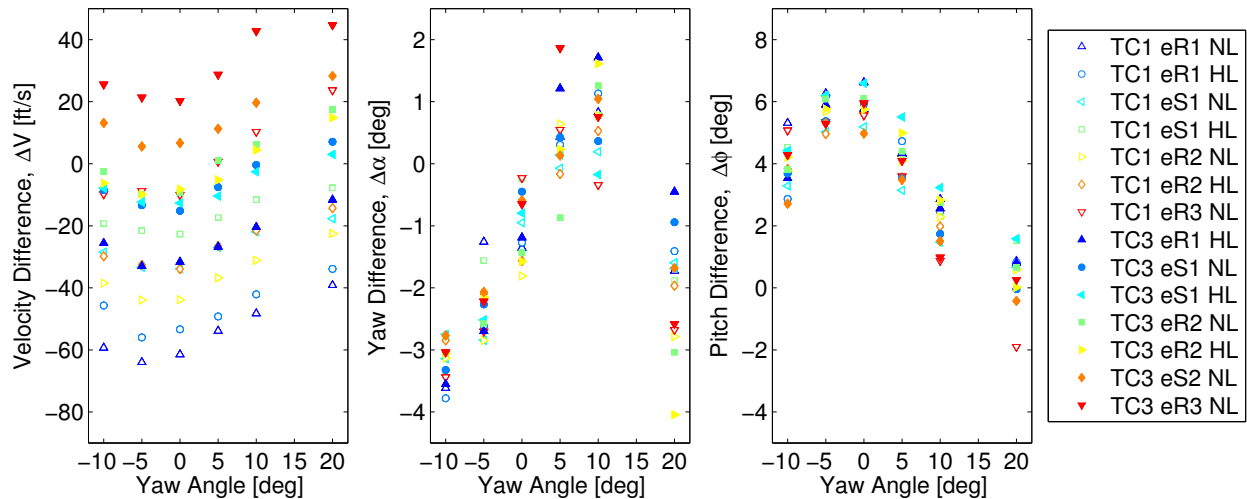


Figure 2.20: Approximate accuracy of hot-wire processing algorithm for test-representative conditions at several known flow angles.

The reason for this discrepancy in velocities is related to the correction proposed by Collis and Williams (1959). Previous studies have shown that the Collis and Williams correction relating the Nusselt number and the Reynolds number deviates for Mach numbers above approximately 0.3. In these cases, compressibility effects begin to become more significant for the hot-wire measurements. Referring again to the results in Figure 2.20, the rotor exit measurements are the locations at which the absolute flow velocity is expected to be the largest (due to the diffusion of flow in the relative reference frame). Furthermore, as the temperature decreases, the Mach number will increase. As a result, the measurements at Rotor 1 exit for TC1 at NL with a velocity difference on the order of -60 ft/s represent a Mach number on the order of 0.35. All of the tested conditions in Figure 2.20 with a velocity difference beyond approximately  $\pm 25$  ft/s represent flow conditions with an average Mach number greater than or equal to 0.30.

Although the velocity differences in Figure 2.20 appear significant, this processing method of solving a set of non-linear equations represents the most accurate of two methods evaluated for these data. The other method implemented a look-up table approach, for which the temperature and density variations are independently accounted using known relationships, as discussed by Berdanier and Key (2015b).

Aside from developing new relationships to accommodate temperature variations with compressibility considerations, future hot-wire measurements such as these may benefit from a more controlled selection of inlet conditions which closely resemble calibration conditions, or several calibration sets for different temperature ranges. However, neither of these recommendations is particularly advantageous: (i) A judicious selection of compressor operating conditions comparable to calibration conditions can only be achieved with temperature-controlled compressor inlet conditions. This is especially true for test campaigns which span several days in the midwest United States, where weather patterns can be particularly difficult to predict. (ii) Extended calibration time poses an increased potential to experience a broken sensor. The fragility of hot-wire sensors makes them particularly prone to breakage, and additional operating time (in a calibration jet, for example) greatly increases this potential for failure.

To further evaluate the robustness of the hot-wire calibration and processing algorithm, two separate calibration data sets (one before the test campaign and another after the test campaign, each approximately one week apart) were used to process the same experimentally-collected data. Specifically, data collected at the exit of Stator 1 for TC1 at two loading conditions were processed using the two sets of coefficients (Equation (2.8)). This axial measurement position at Stator 1 exit was selected because it represents a data set which was collected with approximately equally time between the pre-calibration and the post-calibration data (about four days between the collected data and either calibration). The results from this comparison, Figure 2.21 show the differences between the results processed with the two calibrations are much smaller than the potential differences with respect to operating temperature and density, as shown in Figure 2.20. For the nominal loading (NL) condition in Figure 2.21, the velocities show a constant offset between the two calibrations. The yaw angles are least affected in the wake region, but the pitch angles show the most difference in the wake region. Separately for the high loading (HL) operating condition, the velocities show little effect in the wake region, with a more noticeable change for the undisturbed mean flow. At this same HL condition, the yaw and pitch angles in the mean flow are largely unchanged, but the flow angles in the wake region are most different. The average differences across one vane pitch from Figure 2.21 are summarized in Table 2.7.

Table 2.7: Average differences across one stator pitch for data processed with two calibration sets. Data collected at Stator 1 exit for TC1.

Loading	$\Delta(V/U_t)$ [%]	$\Delta V$ [ft/s]	$\Delta\alpha$ [deg]	$\Delta\phi$ [deg]
NL	2.0	10.3	0.9	0.4
HL	1.7	9.0	0.7	0.1

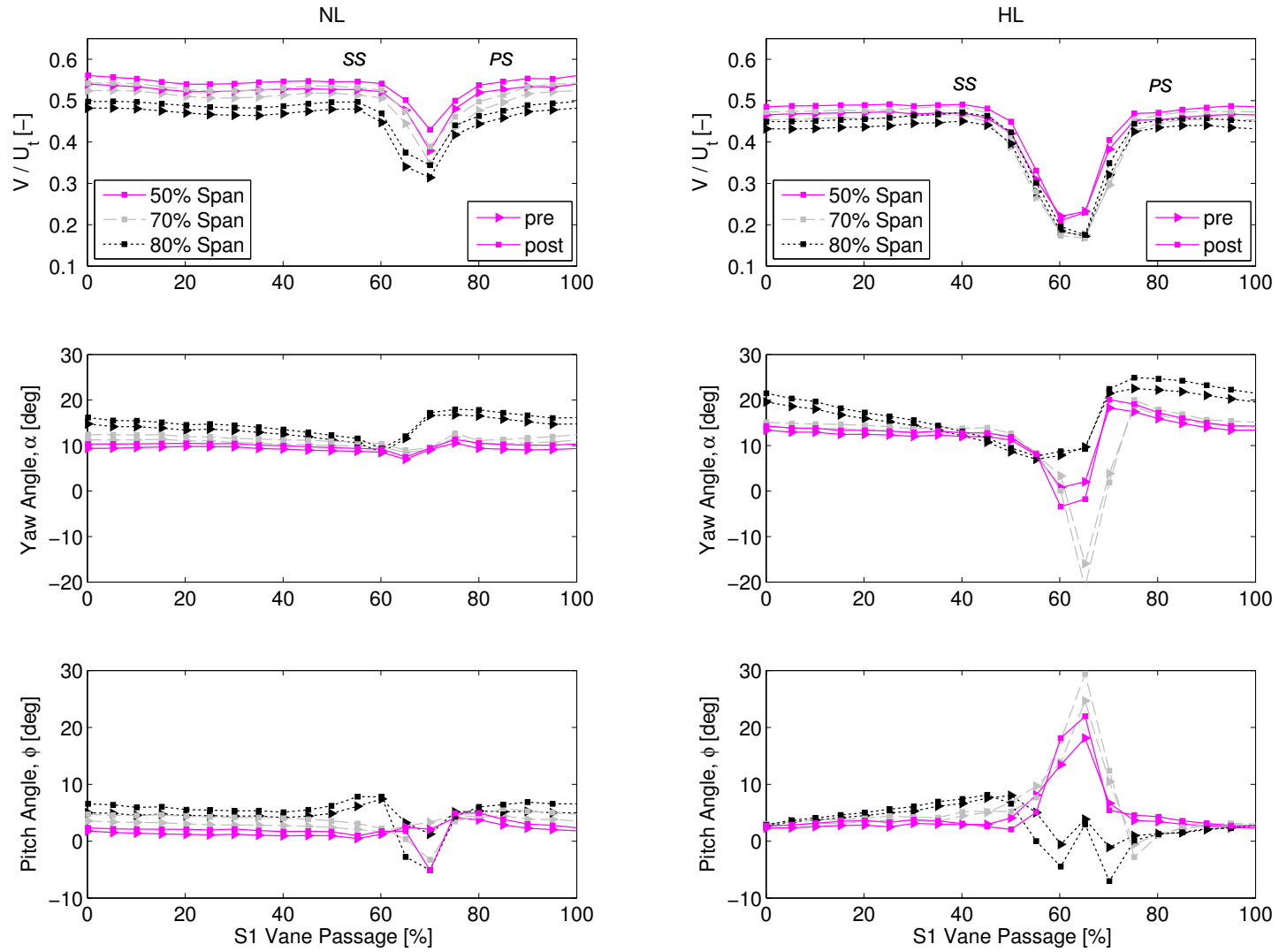


Figure 2.21: Processed hot-wire data at Stator 1 exit for TC1 using two separate calibrations.

## **2.6. Particle Image Velocimetry**

While traditional probe traversing measurement techniques can be used to study compressor performance, their intrusive design will influence the structure of the tip leakage flow. Thus, a non-intrusive method of measuring the tip leakage flow is desirable. To resolve the flow inside the rotor blade passage non-invasive measurement techniques like Laser Doppler Velocimetry (LDV) has been used. Ma (2001) performed 3-component LDV measurements in the axial compressor to reveal the dominant effect of tip corner flow from an inlet guide vane suction surface on the rotor blade passage. Michon et al. (2005) revealed the unsteady flow structures in a single stage compressor rotor blade passage and computed the Reynolds stress distributions using 3-component LDV.

Because LDV is a pointwise measurement, it can be very time-intensive to traverse the flow field with an LDV system. Thus, researchers have turned to Particle Image Velocimetry (PIV) to capture planes of data in the flow field. Balzani et al. (2000) successfully acquired PIV data in a compressor rotor stage. Sanders et al. (2002) first performed PIV measurements in a transonic Compressor stator stage. Stereo-PIV measurements in the rotor blade passage were carried out by Wernet et al. (2001, 2005), and they identified the regions with negative radial velocity and low axial velocity as the tip leakage flow. Voges et al. (2012) studied the flow in the tip clearance region of a transonic compressor rotor with casing treatment. Stereo-PIV measurements were typically performed in large-scale, low speed compressors by Liu et al. (2003).

In all of these studies, periscopic optical probes were introduced to the flow field for light sheet delivery, which renders the measurement invasive. The size of the probe affects the flow, but a small probe results in difficulty in precisely aligning the laser beam to avoid streaking or flare of the beam. Seeding can also damage the probe or require a shutdown to clean the optics. Thus, capability to perform three-dimensional PIV on the embedded stage of a multistage by introducing the laser sheet through the same window used by the cameras to acquire the image has been developed for this project. A window over Rotor 2 was the only optically accessible region through which laser sheet was introduced and also particle images were captured. This work demonstrates, for the first time, the capability of doing three-component, three-dimensional PIV in a multistage compressor, without inserting any invasive imaging or light delivery probes inside the compressor. This section describes the design of the setup and the issues that were overcome to acquire the data in this manner. The following sections describe the experimental set-up and different measurement conditions, PIV processing and analysis of the velocity fields obtained in the blade passage.

### **2.6.1. Experimental Setup**

PIV was performed in the embedded stage rotor passage (Rotor 2) to measure phase-averaged velocity field between the blade passages. All PIV measurements were performed on the TC3 tip clearance configuration. The experimental setup is shown in Figure 2.22. A specially designed glass window with a MgF<sub>2</sub> anti-reflection coating was used to minimize reflections at wavelengths larger than 425nm. This window was the only optically accessible region for PIV measurement. The effective field of view through the window was 2.71 inches in width and 5 inches in height. The measurement plane was located at 2.56 inches from the top inner surface of the window frame (i.e. at 4° circumferential location), which is a radial plane passing through the center of the window.

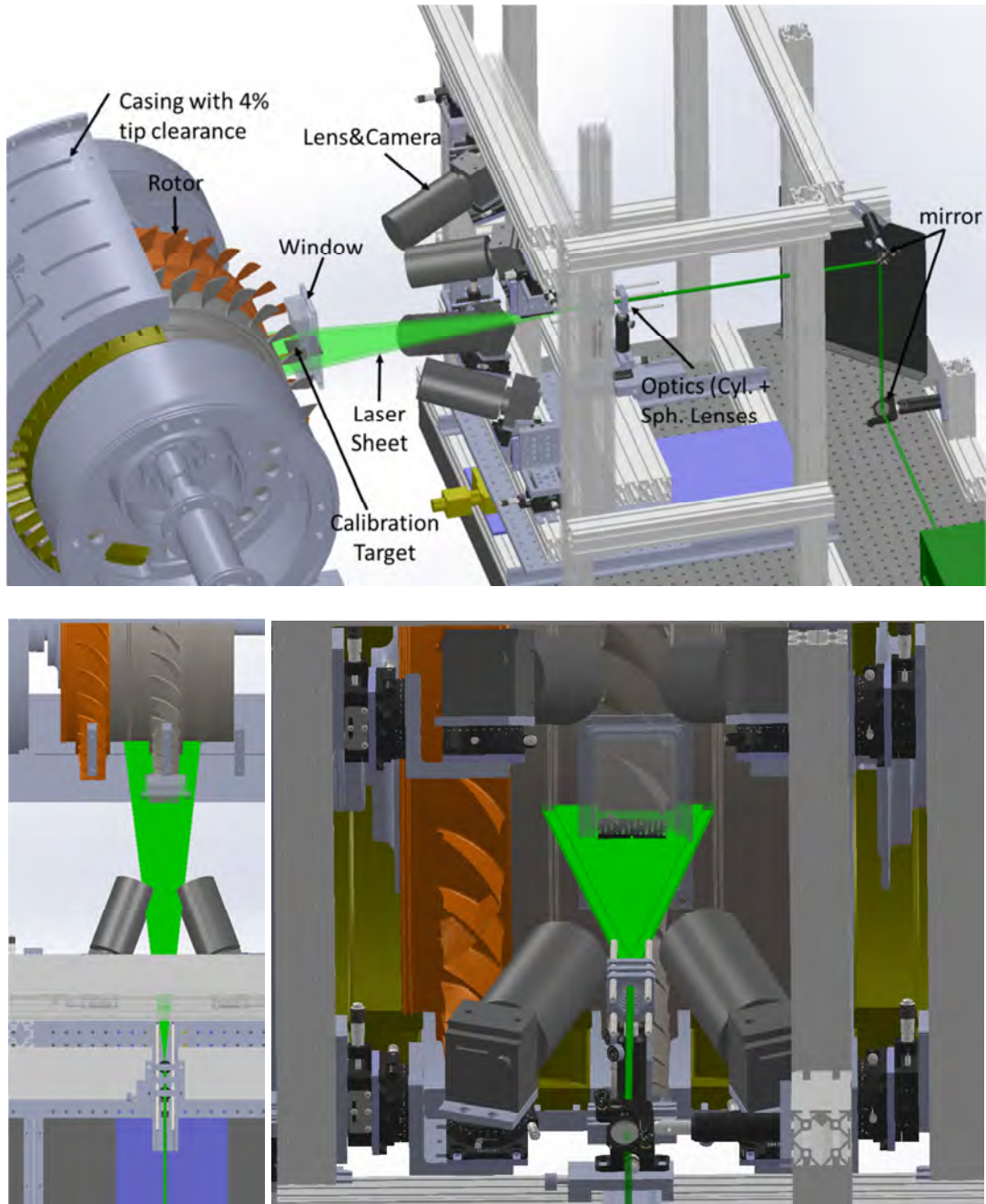


Figure 2.22: Schematic of PIV setup.

The Quantel Evergreen series double pulse NdYAG laser (532 nm) with 211mJ energy per pulse per head and a max repetition rate of 15Hz was used as the illumination source. The laser beam was guided by two mirrors and then passed through a cylindrical lens with  $f=-15$  mm. The expanding beam was passed through a 500mm plano-convex lens placed at a distance of 1.57

inches from the previous cylindrical lens. The resulting light sheet was 4mm thick in the plane of measurement.

Four Imperx 2M30L CCD cameras were used to acquire the images, Figure 2.23. The cameras were operated with external trigger in double exposure mode with a resolution of 1600 by 1200 pixels. The images were recorded at 8 bit depth and at 9.8 frame pairs per second. The desired field of view with a magnification of 27.8  $\mu\text{m}/\text{pixel}$  was obtained using Nikon 105mm AF 1:2.8D lenses. Tilt adapters manufactured by LaVision were placed in between the lens and the cameras to meet Scheimpflug condition and achieve better focus in the plane of measurement. The lens angles were  $70^\circ$  with respect to the laser plane normal. Typically in stereo and tomographic PIV, lens angles of  $30^\circ$  to  $45^\circ$  are optimal, but due to optical access limitations, any further reduction in lens angle was not possible. At this steep viewing angle, the image was out of focus from 60% span towards the hub and thus good measurements were only obtained between the tip and 65% span. Thus, the effective measurement domain was 40mm in the axial direction and 17mm in the radial direction.

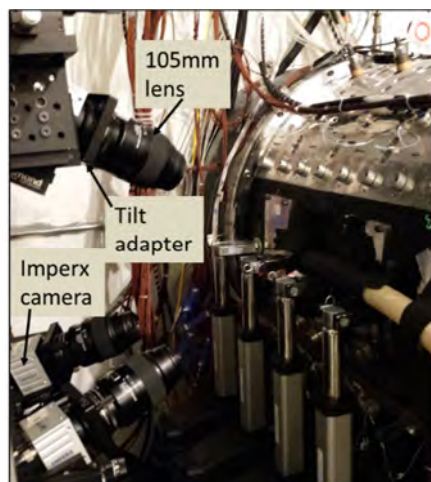


Figure 2.23: Camera, lens, and tilt adapter setup.

The timing and synchronization for the experiment were controlled by a Quantum Composer Plus pulse generator (model 9518). The pulse generator was operated in an external trigger mode, and the individual channels were operated in a duty cycle mode. The tachometer signal generated from the compressor rotor shaft was a square pulse train with a frequency equal to the compressor rotation frequency. This signal was used to trigger the eight channels in the pulse generator which in turn triggered the cameras and the laser heads, Figure 2.24. Thus phase-locked measurements were obtained using the tachometer signal, and data at different circumferential positions were acquired by varying the delay with respect to the tachometer signal. The delay between the two laser pulses was set to  $2 \mu\text{s}$  such that particles with the highest velocity (which was assumed to be the blade tip velocity) would only translate across the measurement plane by no more than a quarter of the laser sheet thickness.

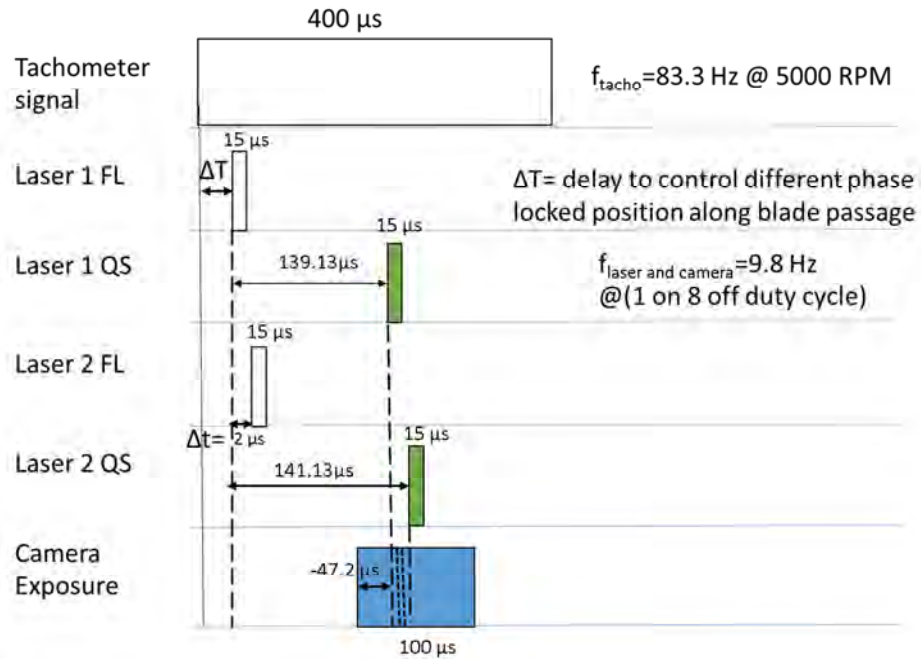


Figure 2.24: Timing diagram for synchronized image capture.

A multi-plane LaVision target was used for calibration, Figure 2.25. The 2.28 inch square target plate was mounted in between the staggered blade passage and the laser sheet was aligned with the top surface of the target. The calibration images for the four cameras are shown in Figure 2.26. The compressor blades blocked different portions of the field of view for each camera.

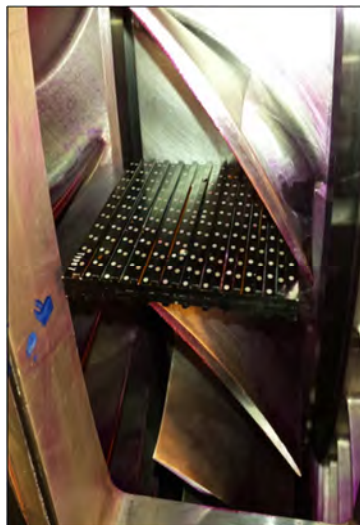


Figure 2.25: Calibration plate mounted between blade passages.

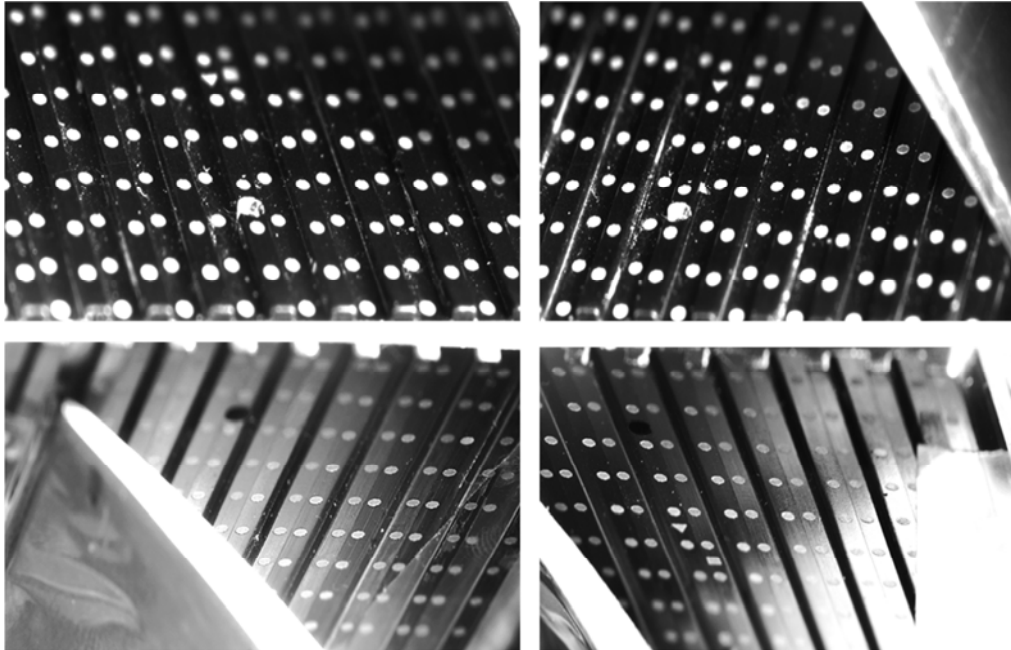


Figure 2.26: Calibration plate images from each of the four cameras.

The laser sheet was introduced through the casing window and initially reflections from blade surface and hub led to saturation of image pixels, and particle image intensities were not discernible, Figure 2.27(a). To overcome the reflection, fluorescent dye was used with the seeding fluid. Lens filters blocking wavelengths below 540nm were used to filter laser reflections, Figure 2.27(b). The fluorescent seeding particles were generated with Rhodamine B 610 chloride (from Exciton Inc.) powder dye. The peak absorption and emission wavelength of this dye are sufficiently separated, Figure 2.27(c), and thus, the recorded images had very low background noise.

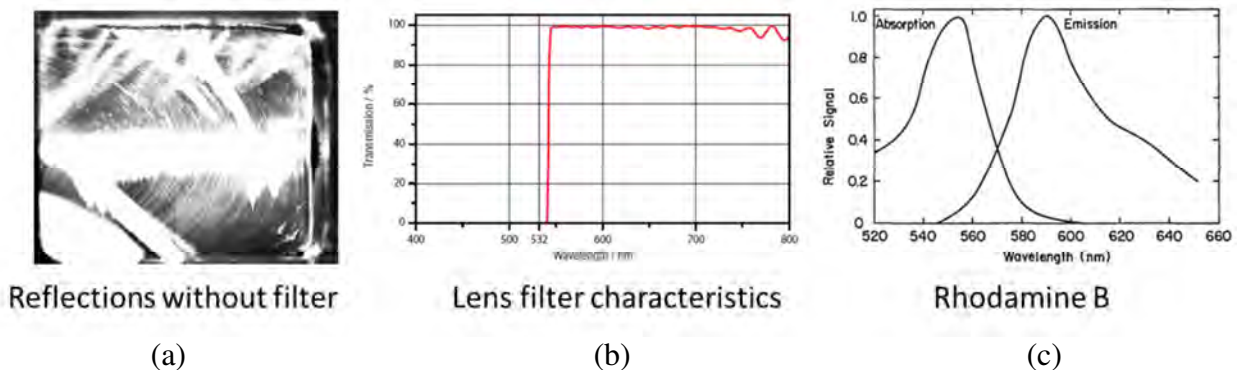


Figure 2.27: Laser reflection, lens filter characteristics, and fluorescent dye spectrum.

Flow seeding was one of the main challenges in this experiment. Typically, PIV experiments conducted in air implement particle seeding through the use of a fogger. However, when fluorescent dye was mixed with the fog fluid for this experiment, the resulting fluid

mixture properties changed, and the particles started depositing on the interior of the window instead of following the flow. As an alternative particle introduction method, a TSI 9307-06 six-jet Laskin nozzle was used to atomize a mixture of fluorescent dye and propylene glycol. The particle generation with Laskin Nozzle was very sensitive to the specific seeding fluid mixture concentration. Successful seeding was achieved for this study using three grams of the dye powder mixed with 1 gallon of propylene glycol and 1.69 oz. of ethanol. The small amount of ethanol reduced the surface tension of the fluid mixture to improve atomization. Any deviation from this mixture prevented the generation of good tracer particles. Air at 75-80 psi pressure was supplied through a one inch tube at the Laskin nozzle inlet to generate micron-sized tracer particles which were seeded in the upstream location through a 0.5 in. hole into the center of the compressor inlet duct, Figure 2.28.

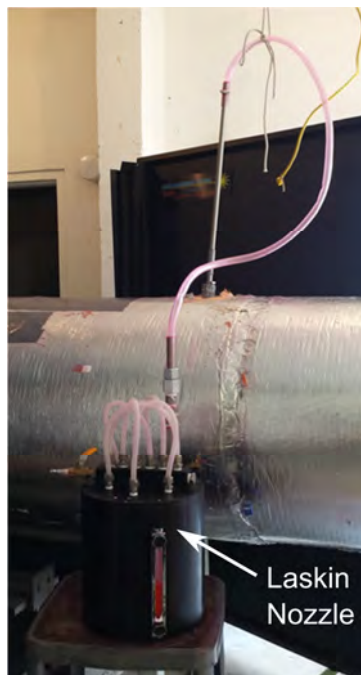


Figure 2.28: Laskin nozzle used for seeding particles into upstream flow.

The output from the seeder was much lower than the flow rate through the compressor, and thus, seeding was sparse. To get sufficient signal for cross correlation in an interrogation window, 1000 image pairs were recorded for each phase locked position, and reasonable particle density was achieved when summing up the phase-locked images. Experiments were carried out using the TC3 tip clearance configuration at two operating conditions on the 100% corrected speedline (nominal loading and high loading), and measurements were acquired at 20 phase-locked positions across one rotor blade passage.

### 2.6.2. Image Processing

The top two camera images were used to reconstruct planar 3-component velocity fields for each phase locked measurement location. In-house PIV software “Prana” was used for all calibration, cross-correlation image processing, and three-component velocity reconstruction. A

polynomial mapping function with cubic order in  $x$  and  $y$  and linear order in  $z$  was used to map the world coordinate system  $(x, y, z)$  in the measurement domain to the image coordinate system  $(X, Y)$  for each camera. The image overlap after applying the calibration is shown in Figure 2.29. The axial overlap between the cameras increases from 100% span to 70% span and then decreases because of the steep viewing angles of the cameras.

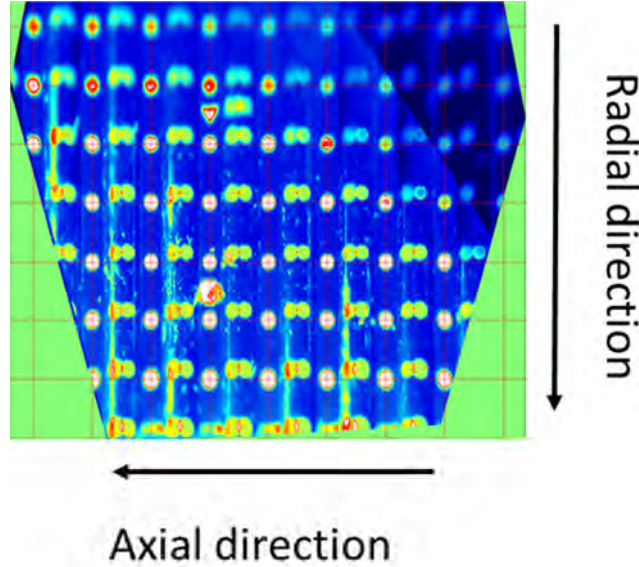


Figure 2.29: Top two camera overlap region after calibration.

The stereo PIV data processing is accomplished using a generalized reconstruction, as described by Soloff et al. (1999), in which the individual camera images are first correlated and then the planar velocity fields from individual cameras ( $U_1, V_1$  for camera 1 and  $U_2, V_2$  for camera 2) are combined with the gradients of the mapping function ( $FX, FY$ ) to obtain the  $U, V$ , and  $W$  velocity components using a least squares fit:

$$\begin{bmatrix} U_1 \\ V_1 \\ U_2 \\ V_2 \end{bmatrix} = \begin{bmatrix} FX_x^1 & FX_y^1 & FX_z^1 \\ FY_x^1 & FY_y^1 & FY_z^1 \\ FX_x^2 & FX_y^2 & FX_z^2 \\ FY_x^2 & FY_y^2 & FY_z^2 \end{bmatrix} \begin{bmatrix} U \\ V \\ W \end{bmatrix}. \quad (2.9)$$

After the individual camera image pairs were summed to identify the region with particles, the rest of the image was masked to remove erroneous contributions from low-quality vectors. Next, the minimum background intensity was subtracted from the images. The summed-up images were then cross-correlated to get planar velocity fields. To obtain a more robust velocity estimate, the individual image pairs were correlated and the correlation planes were summed which results in a higher signal to noise ratio, as shown by Meinhart and Santiago (1999). The cross correlation was performed using two passes: the first pass utilized a window size of 128 pixels, and the second pass utilized the same window size with a 50% Gaussian spatial filter, as recommended by Eckstein and Vlachos (2009a). The grid resolution in first pass was 32 by 32 and in the second pass was 8 by 8. Robust Phase Cross Correlation (RPC), as described in

Eckstein et al. (2008) and Eckstein and Vlachos (2009b), was used to correlate the image pairs. The planar fields were validated using velocity threshold and Universal Outlier Detection (UOD) to remove erroneous vectors. The planar velocity vector fields were then dewarped onto physical coordinate space to determine overlapping region, and the  $U$ ,  $V$ , and  $W$  components were then reconstructed using Equation (2.9). The reconstructed fields were median filtered to remove noisy vectors along the blade edges.

Tomographic PIV analysis (Elsinga et al., 2006) was also performed by combining images collected from all four cameras. For this purpose, the commercially-available software package LaVision DaVis was used. First, a volumetric calibration was performed for all cameras using masked calibration images to remove the portions of the image blocked by the blade. Then, tomographic reconstruction was performed using the sum of the 1000 pairs of images.

The individual camera images were pre-processed with a sliding minimum background subtraction from a local 3 by 3 pixel region. The particle images were then smoothed using a Gaussian filter and a subsequent sharpening filter to remove background noise. These images were used for tomographic reconstruction in which individual particles were back-projected from each camera, and their positions in three dimensional space were determined using a multiplicative line of sight algorithm (Atkinson and Soria, 2009).

The reconstructed 3D particle field was cross correlated using an FFT-based volume cross correlation with 3 passes. A first correlation pass used 50% overlap and a 128 by 128 by 64 voxel window. This was followed by two more passes with 75% overlap and window sizes of 128 by 128 by 32 and 64 by 64 by 32 voxels, respectively. Using calibration information, the reconstruction was performed on a domain with 659 by 330 by 67 voxels. The final cross correlation pass yielded 8 vector planes in the volume of the laser sheet. As a post-processing step for validating the calculated vectors, velocity threshold of 16 pixels was applied, smoothing and UOD techniques were performed, and a software option was selected to interpolate and fill any void regions in the vector field.

## CHAPTER 3: STEADY COMPRESSOR PERFORMANCE

*Reid A. Berdanier, Natalie R. Smith, and Nicole L. Key*

### 3.1. Compressor Performance Maps

For this study, a series of compressor performance data were collected at four corrected operating speeds (100%, 90%, 80%, and 68%) for each of the three tip clearance configurations (TC1-TC3). The 68% corrected speedline was selected instead of the 70% corrected speed to avoid a Campbell diagram crossing corresponding to a rotor first torsion (1T) vibratory mode, as analyzed by Murray (2014). In all cases, the corrected speed and corrected mass flow rate were calculated according to the procedure outlined in Section 2.2.1. For each of the four speedlines, data from different tip clearance configurations were collected at equivalent corrected mass flow rates for direct comparison.

#### 3.1.1. Total-to-Total Pressure Rise Characteristics

Benchmark compressor map data are presented in Figure 3.1. Each measurement point in Figure 3.1 is calculated from area-averaged rake measurements collected from the seven-element total pressure rakes at 20 equally-spaced vane positions across one vane pitch. In this figure, the overall total pressure ratio (TPR) across the compressor is calculated as the ratio of radially and circumferentially area-averaged total pressures from axial planes 1 and 9 in the Figure 2.6 schematic:

$$\text{TPR} = \frac{P_{o,9,AA}}{P_{o,1,AA}}. \quad (3.1)$$

In Figure 3.1, five operating points from the 100% corrected speedlines have been designated for comparison throughout this document: a low loading (LL) condition which represents a high flow rate, negative incidence condition; a nominal loading (NL) condition representing an operating point at a mass flow rate slightly higher than the peak efficiency point; a peak efficient (PE) point; a high loading (HL) condition which represents a low flow rate, high incidence operating point; and a set of conditions near the stall point (NS) which have a stall margin of approximately 5%. For this study, the stall margin (SM) is defined as follows:

$$\text{SM} = \frac{\left(\frac{\text{TPR}}{\dot{m}_c}\right)_{\text{stall}} - \left(\frac{\text{TPR}}{\dot{m}_c}\right)}{\left(\frac{\text{TPR}}{\dot{m}_c}\right)} \times 100\%. \quad (3.2)$$

On the abscissa of Figure 3.1, the corrected inlet mass flow rates have been normalized by the value at the nominal loading point. For reference, the calculated relative uncertainty of the overall total pressure ratio in Figure 3.1 is 0.16% (within the symbol size in the figure). The maximum relative uncertainty of the normalized inlet corrected mass flow rate using the ASME-standard (ASME PTC 19.5, 2004) set of equations is 1.4% and occurs at the near-stall loading condition. Nearly 60% of this calculated measurement uncertainty is contributed by the ASME-standard uncertainty for discharge coefficient, which will be reduced in the future upon calibration of the Venturi flow meter. However, the repeatability of the mass flow rate

measurements for a fixed throttle position at the same loading condition is typically on the order of 0.2%.

In Figure 3.1, the final point at the top of each speedline (the lowest flow rate condition) is not a 20-point traversed point, but rather a representative location of the stall point for the compressor at that operating speed. Once the stall point is identified in a preliminary run, it is subsequently approached slowly through incremental throttle movements to determine the mass flow rate and pressure rise locating the stall point. An approximate representation of the stall point with respect to the traversed points on the rest of the speedline can be determined by a comparison with the last (NS) traversed point and by stalling the compressor in several stator vane positions with respect to the fixed rake positions. The dotted line connecting these points represents a stall line for the specific tip clearance configuration. Comparing these results, an increase of rotor tip clearance leads to a decrease of overall total pressure rise and moves the stall point to a higher flow rate (the stall margin is reduced). Additional discussion about the stall characteristics of the compressor is given in Chapter 4.

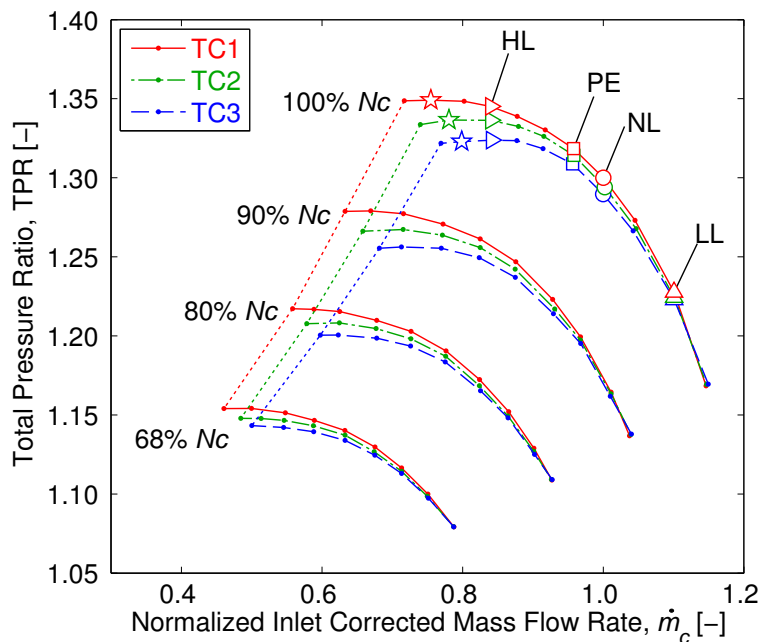


Figure 3.1: Compressor total pressure ratio map.

### 3.1.2. Operating Tip Clearance Measurements

The operating points defined in Figure 3.1 can be characterized by their nominal (design intent) rotor tip clearance height, as listed in Table 2.2. However, several environmental factors can influence the physical components of the facility and, in turn, introduce variations of the operating tip clearance. These factors include, but are not limited to, centrifugal effects related to rotational speed changes and corresponding blade elongation, thermal effects due to temperature rise through the compressor, and pressure forces resulting from the pressure rise through the compressor. In a previous study guided toward modeling tip clearance changes in a multistage

axial compressor, Dong et al. (2014) separated the potential contributions of operating tip clearance changes into several categories, as suggested above:

$$\tau_{\text{model}} = \tau_{\text{static}} - [(\Delta\tau)_{B,\text{thermal}} + (\Delta\tau)_{B,\text{centrif}}] + [(\Delta\tau)_{S,\text{thermal}} + (\Delta\tau)_{S,\text{pressure}}] - [(\Delta\tau)_{D,\text{thermal}} + (\Delta\tau)_{D,\text{centrif}}] \quad (3.3)$$

where the subscripts  $B$ ,  $S$ , and  $D$  represent tip clearance change contributions from the blade, shroud (casing), and disk, respectively. This equation calculates the operating “model” clearances,  $\tau_{\text{model}}$ , based on the static (cold) build clearance,  $\tau_{\text{static}}$ . Equation (3.3) shows a thermal expansion or centrifugal growth of the blade or disk will decrease the clearance height, whereas a thermal expansion or pressure force acting on the shroud will increase the clearance height.

This model has been applied specifically to the Purdue three-stage axial compressor to compare measured tip clearances with model predictions (Berdanier and Key, 2015a), and the outcome showed that the predicted model clearances are driven primarily by the thermal growth terms, which yield clearance change contributions several orders of magnitude larger than the pressure or centrifugal components. Ultimately, this previous study (Berdanier and Key, 2015a), in combination with the original model analysis presented by Dong et al. (2014), has confirmed that considerable changes in operating tip clearance height can be achieved as the loading condition is changed along a given speedline or between speeds.

The operating tip clearances for this project were measured using the capacitance probe system outlined in Section 2.4. Beginning with the baseline tip clearance configuration (TC1), the measured operating tip clearances for the steady operating points defined in Figure 3.1 are presented in Figure 3.2 as a function of the normalized inlet corrected mass flow rate for each of the four identified speeds. These clearance data have been determined using the RMS calculation method, although an arithmetic mean of the blade-by-blade DNS data is similar. In Figure 3.2, the three circumferentially-distributed probes for each rotor row have been averaged to yield one representative tip clearance value for each rotor row.

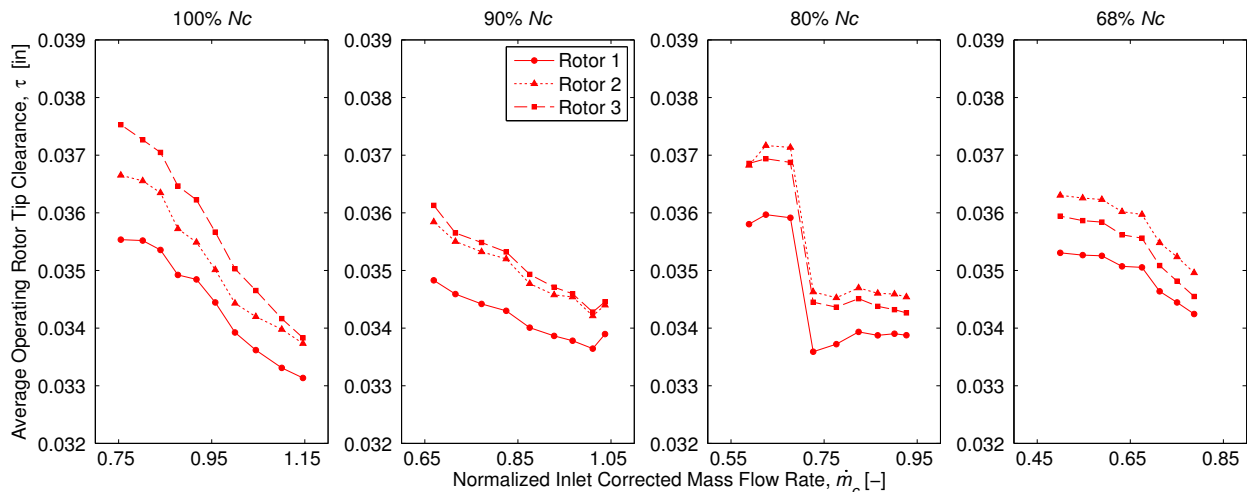


Figure 3.2: Operating tip clearances measured using capacitance probes for TC1.

Considering Figure 3.2, these operating points were collected in immediate succession moving from left to right across the four parts of the figure. In this way, the results display the variation of rotor tip clearance height as the operating point changes with minimal point-to-point effect from ambient temperature changes. However, there are several noticeable effects of changes in ambient conditions. First, the final high flow rate condition for the 90% corrected speedline moving into the 80% corrected speed conditions represents a period of time at the beginning of a day when the ambient temperature was increasing; Second, there is a significant drop of measured tip clearances between the third and fourth points (from left to right) in the 80% speedline. A stretch of looming severe weather forced a stop of the experimental campaign after the completion of the third point in this line, and the data collection process resumed beginning with the fourth point on the following day. This discontinuity represents a change of approximately  $2.5 \times 10^{-3}$  in., which represents an 8% change of operating tip clearance for the nominal value of 0.030 in., and it is attributable to a change in ambient temperature of approximately 28 °F. It is important to note here that there is no measureable change of performance parameters at this speed and for this loading condition (away from the stall point at part-speed) due to this small measured tip clearance change, whereas a high loading point on the 100% corrected speedline may be more likely to show a measurable performance change (see Section 3.1.3). Third, the 80% and 68% operating speed curves in Figure 3.2 show less relationship between measured tip clearance and loading condition (compared to 100%, e.g.) as the temperature rise through the compressor is significantly reduced in this part-speed operating regime. Thus, a majority of the observed decrease of tip clearance with loading conditions in the 68% corrected speed range is due to a decrease in ambient temperature that occurred in the evening.

Similar measurements are presented for the two larger tip clearance configurations, TC2 and TC3 in Figure 3.3 and Figure 3.4. As with the TC1 results in Figure 3.2, these larger tip clearance measurements were also collected in succession, but without the discontinuity in the 80% speedline discussed for TC1. Although the mean weather conditions were extremely similar between measurements collected for the three different tip clearances, the TC2 and TC3 data collection processes began at a different time of day than TC1. As a result, a comparison of the results in Figure 3.3 and Figure 3.4 show a very similar trend which is slightly different than the observed trends for TC1. In particular, the 100% speedline data for TC2 and TC3 began in the early morning hours prior to sunrise and, therefore, the high-loading, low flow rate operating points which showed the highest tip clearance values for TC1 display a less discernable trend as the highest static temperature rise conditions are affected slightly by the slow temporal variation of temperature through the day.

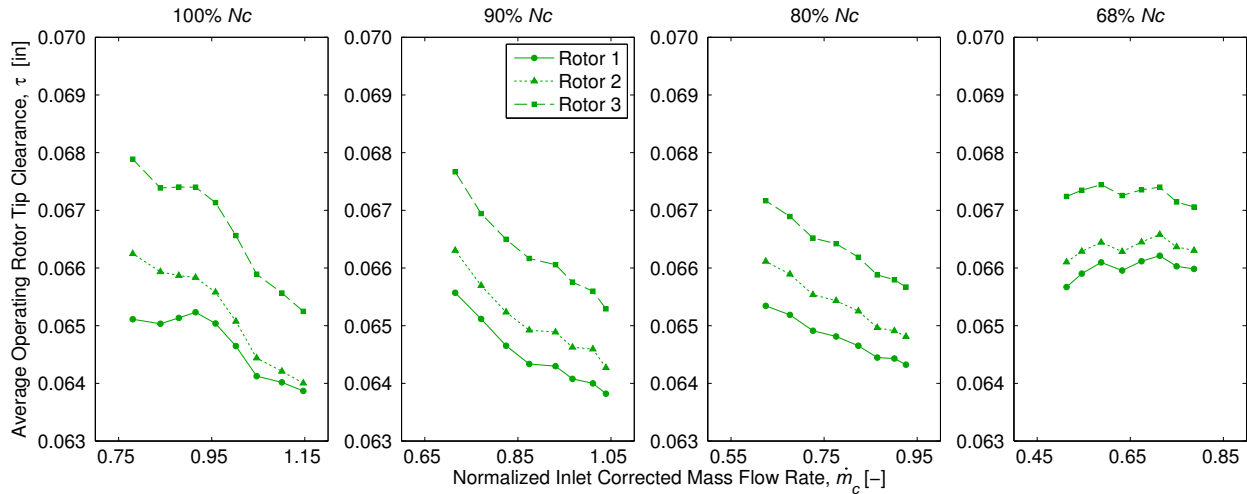


Figure 3.3: Operating tip clearances measured using capacitance probes for TC2.

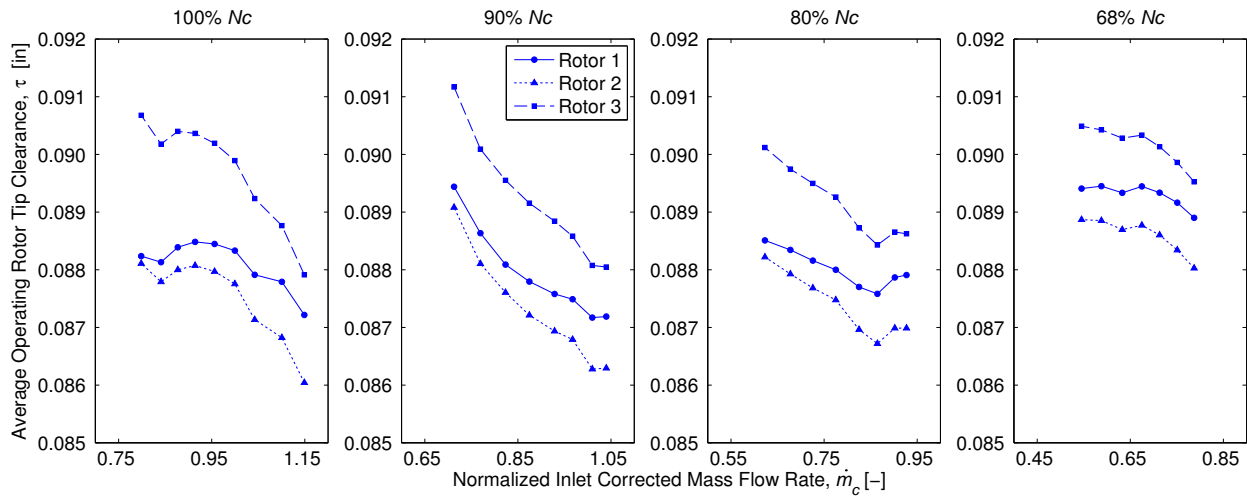


Figure 3.4: Operating tip clearances measured using capacitance probes for TC3.

The operating tip clearance measurements in Figure 3.2, Figure 3.3, and Figure 3.4 are a crucial component of this overall measurement campaign. In particular, these results have shown the potential extent to which even a small variation of ambient temperature can impact the tip clearance height. Furthermore, it is entirely insufficient to report the design intent tip clearance heights, as in Table 2.2, as a result of the potential variations in clearance height between operating conditions alone. For absolute consistency, these measured operating tip clearance values are used throughout the remainder of the document whenever clearance values at a specific operating condition are required. The following section explores the potential influence that these tip clearance height changes can pose for overall performance measurements.

### 3.1.3. Effect of Ambient Conditions on Tip Clearance and Total-to-Total Pressure Rise

Changes of mechanical speed necessary to match corrected speed conditions, as well as thermal blade growth, can cause rotor tip clearance heights to change. The effect of changing tip clearances due to ambient conditions, as introduced in Section 3.1.2 may seem to be a negligible difference in the scale of the overall clearance height. In fact, Walsh and Fletcher (2008) explain that these corresponding differences are usually ignored. However, if great care is taken to reduce measurement uncertainty, and all known corrected conditions are appropriately accounted for, then the variations due to these very small tip clearance changes are measurable and repeatable.

As part of this study, a series of corrected speedlines were collected for different tip clearance configurations (TC2 and TC3) for two different ambient temperature conditions. These results, Figure 3.5, show that measurable changes may exist. In this case, a “hot” day represents an average ambient temperature of 77 °F and a “cold” day represents an average ambient temperature of 24 °F for measurements collected with both TC2 and TC3. As with the data shown in Figure 3.1, these results represent area-averaged rake measurements collected at 20 equally-spaced vane positions across one vane pitch. The performance discrepancies highlighted by Figure 3.5 are most significant at high loading (low flow rate) conditions approaching the stall point. At these high loading conditions, the two operating points are up to 0.42% different in overall total pressure ratio (nearly four times the uncertainty of the same quantity).

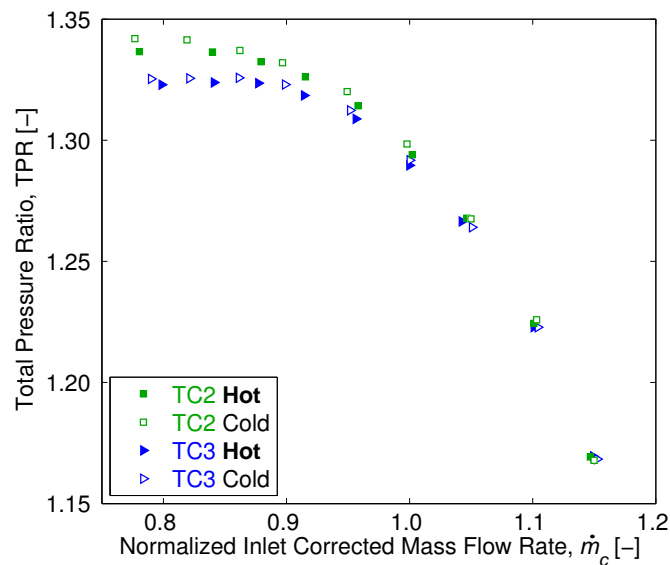


Figure 3.5: Overall compressor total pressure ratio discrepancy between hot and cold test days at a 100% corrected operating speed for TC2 and TC3.

The differences highlighted in Figure 3.5 are consistent with untraversed data (i.e., measurements collected at one discrete position with respect to the stationary vanes) acquired over the course of a full calendar year in the same facility, as presented in Figure 3.6 for all three tip clearance configurations (TC1-TC3). Over the same range of ambient temperatures, TC3 is less affected (approximately 0.15% different in overall total pressure ratio at the near stall operating conditions in Figure 3.5), compared to the TC1 and TC2 configurations. Specifically, Figure 3.6 highlights a negatively-sloping trend of total pressure ratio with increasing inlet temperature, whereas TC3 does not display the same distinct trend.

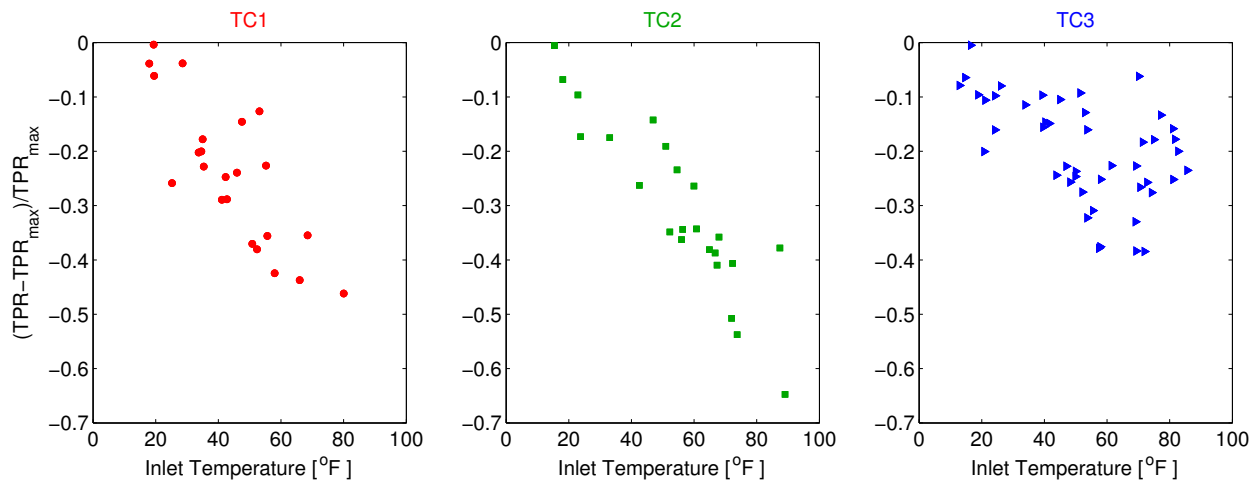


Figure 3.6: Variations of total pressure ratio with ambient temperature for each of the three nominal tip clearance conditions (TC1-TC3).

The overall compressor total pressure rise is assessed for each of the three tip clearance configurations with hot and cold inlet conditions at a near stall (NS) operating condition in Figure 3.7 as a function of the average Rotor 1 tip clearance height. The results in Figure 3.7 show that tip clearance changes with ambient temperature may not be negligible (e.g.,  $2.5 \times 10^{-3}$  in. for a 25 °F change of ambient temperature) as some authors suggest. For the three-stage axial compressor facility utilized in this study, the aluminum compressor casing has a coefficient of thermal expansion which is more than two times larger than that of the stainless steel blades. As a result, changes of ambient inlet temperature introduce corresponding tip clearance changes which can be significant (on the order of 0.1% annulus height). These observations, along with the data presented from Section 3.1.2, suggest that it is a necessity to measure operating tip clearance for studies such as this which desire to clearly evaluate tip clearance effects on compressor performance.

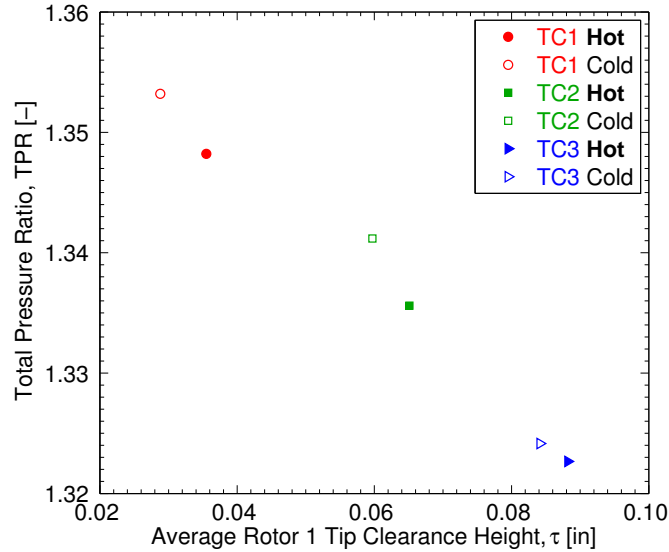


Figure 3.7: Overall total pressure ratio trends with rotor tip clearance for three tip clearance configurations (TC1-TC3), each for two separate ambient temperatures at NS.

To further investigate the observed performance deltas with ambient temperature changes due to clearance height, the normalized total pressure ( $NRP_o$ ) is defined to represent the circumferential average at each radial position, normalized by the radial and circumferential area average at the same axial position:

$$NRP_{o,i} = \frac{P_{o,i,CA}}{P_{o,i,AA}}. \quad (3.4)$$

Using this definition affords the ability to compare the relative shapes of the radial total pressure profiles without the inherent offset due to changes in overall pressure rise with increased rotor tip clearance height. Investigation of the radial total pressure ratio shapes for all three tip clearance configurations, Figure 3.8, shows an increased total pressure loss in the tip region for hot days, suggesting a change in the rotor tip leakage flow which leads to a measurable performance change. The uncertainty of the quantities presented in Figure 3.8 is within the symbol size of the figure. Only the results at Rotor 1 exit and Stator 2 exit are shown in Figure 3.8 because they represent the most significant differences between the two temperature conditions. As expected, the profiles shapes for TC2 fall between the results for TC1 and TC3.

In agreement with the results in Figure 3.5, the cold data generally exhibit less total pressure loss at the tip (except for TC3). The less distinct differences observed for TC3 compared to TC1 or TC2 are consistent with the less noticeable trend in Figure 3.6(c). This may be explained by considering that a  $2.5 \times 10^{-3}$  in. change in tip clearance is less significant for a 0.080 in. nominal tip clearance than for a 0.030 or 0.060 in. nominal tip clearance height. The trends for TC2 are nearly as strong as those for TC1, an observation which could suggest TC2 represents a critical point in the loss development with increased tip clearance. For example, TC2 is near the point where the hub and tip losses switch trends in the Stator 2 exit profiles, as shown in Figure 3.8. Additional specifics regarding these observed performance differences with ambient conditions are discussed by Smith et al. (2015a).

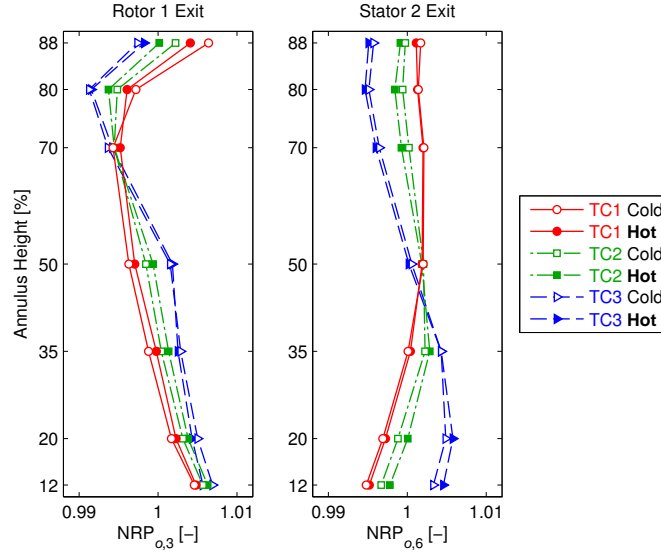


Figure 3.8: Radial total pressure profile shapes for the three tip clearance configurations with “hot” and “cold” ambient operating conditions at NS.

### 3.1.4. Stall Margin

Using Equation (3.2), the stall margin has been calculated for each of the primary identified points on the 100% corrected speedline. These results, Figure 3.9, are presented with the average measured tip clearance on the abscissa, as described in Section 3.1.2. Based on the results in Figure 3.9, the stall margin follows a non-linear trend with increasing tip clearance for each of the four chosen loading conditions: the decrease of stall margin is more significant moving from TC2 to TC3 than from TC1 to TC2 at the same corrected mass flow rate. This difference increases more noticeably at higher flow rates (lower loading conditions) than at the lower flow rates (higher loading conditions). This observed trend also exists for other definitions of stall margin (i.e., based solely on corrected mass flow rates or based on the total pressure ratios in Equation (3.1)).

Previous studies of tip clearance effects on overall compressor performance have identified the loss of operability range using a percent loss of flow coefficient instead of stall margin (Wisler, 1985; McDougall et al., 1990), for which the flow coefficient is defined by the ratio of the axial flow velocity,  $V_x$ , to the rotor tip speed,  $U_t$ :

$$\Phi = \frac{V_x}{U_t}. \quad (3.5)$$

The same quantities can be compared with these data, using a percent difference of the flow coefficient at the stall point as a percent difference from the baseline tip clearance (TC1):

$$\Delta\Phi_{\text{stall}} = \frac{\Phi_{\text{stall}} - \Phi_{\text{stall,TC1}}}{\Phi_{\text{stall,TC1}}} \times 100\%. \quad (3.6)$$

Using this definition with a four-stage low-speed research compressor, Wisler shows an 11% increase of stalling flow coefficient for a rotor tip clearance height increase of 1.4% to 2.8%

based on annulus height; the data from McDougall et al. show approximately 10% increase for a tip clearance height increase of 0.9% to 2.2% based on annulus height in a single-stage low-speed compressor. If the same method is applied to these data, the results in Figure 3.9 show a 3.0% increase of stalling flow coefficient between TC1 and TC2 and a 4.7% increase between TC2 and TC3. These stalling flow coefficient data show that the performance of this three-stage axial compressor is less sensitive to tip clearance changes than has been previously reported for single-stages, isolated rotors, and repeating stage low-speed axial compressors. In this case, it is possible that the multistage compressor design with non-repeating stages provides the opportunity for stage matching adjustments which may postpone stall.

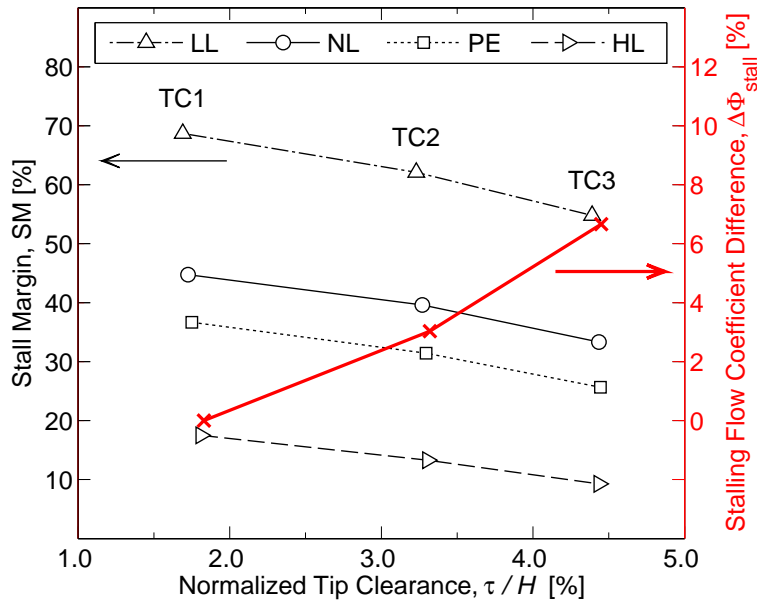


Figure 3.9: Stall margin and stalling flow coefficient effects with tip clearance height for specified loading conditions on the 100% corrected speedline.

### 3.1.5. Total-to-Static Pressure Rise Characteristics

As an alternative to the total pressure ratio as a metric for achieved pressure rise, some authors (Hutton, 1956; Wisler, 1985; McDougall, 1990) have discussed the total-to-static pressure rise coefficient, defined as:

$$\Psi = \frac{P_9 - P_{o1}}{\frac{1}{2}\rho U_t^2}. \quad (3.7)$$

Figure 3.10 shows this total-to-static pressure rise coefficient, presented as a function of the flow coefficient,  $\Phi$ , for each of the three tip clearance configurations at all four corrected operating speeds. As with Figure 3.1, the point at the lowest inlet mass flow rate for each of the curves represents the stall point of the compressor. The results in Figure 3.10 show the expected result of decreasing total-to-static pressure rise coefficient as the tip clearance is increased. Another observations from Figure 3.10 is for the 100% corrected speedline of TC3, which has a location

in the characteristic at a flow coefficient of approximately 0.5 where the slope of the curve changes sharply to be less negative (approaching zero). This location of the characteristic also corresponds to a region of the curve which has a slight positive slope in the speedline from Figure 3.1. This is the only speedline from the 12 presented lines which features a total pressure rise decrease prior to the stall point, which may explain the unique feature of this characteristic in Figure 3.10. Also in this figure, the results for different speeds with a given tip clearance configuration do not collapse to one single line, alluding to the significance of compressibility effects in the Purdue three-stage compressor.

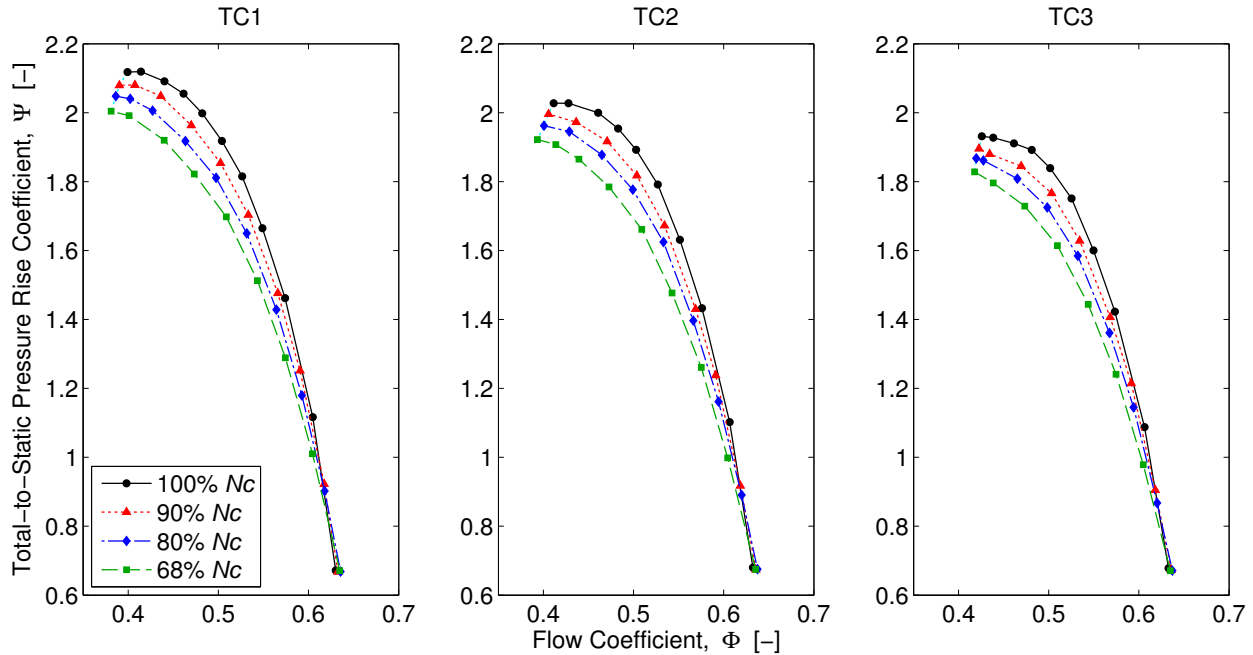


Figure 3.10: Total-to-static pressure rise characteristics for three tip clearance configurations.

Using the definition from Equation (3.6), previous authors have shown a decrease of peak total-to-static pressure rise coefficient on the order of 9.7% (Wisler, 1985) and 12.5% (McDougall, 1990) for a tip clearance change on the order of TC1 to TC2 (nominally 1.5% to 3.0%). Figure 3.11 shows this same comparison using a percent difference of the total-to-static pressure rise coefficient with respect to the 1.5% nominal tip clearance (TC1):

$$\Delta\Psi = \frac{\Psi - \Psi_{TC1}}{\Psi_{TC1}} \times 100\% , \quad (3.8)$$

presented as a function of average measured tip clearance. In contrast to the results discussed by previous authors, the data in Figure 3.11 show that the three-stage compressor studied here has a total-to-static pressure rise coefficient decrease of approximately 4.0% for a similar tip clearance change from TC1 to TC2. In fact, even a change from TC1 to TC3 (nearly twice the change introduced by Wisler or McDougall et al.) only results in an 8.5% decrease in total-to-static pressure rise coefficient compared to the baseline configuration TC1.

However, the results of Figure 3.11 also show an important difference that a clearance change from TC2 to TC3 follows a markedly different trend than that between TC1 and TC2.

Thus, the assumed linearity suggested by many previous authors may not be valid for this compressor application or for large ranges of tip clearance heights. Despite this observation, it can be noted that the trends of  $\Delta\psi$  appear to be relatively insensitive to rotational speed, as shown by the nearly collapsed results in Figure 3.11.

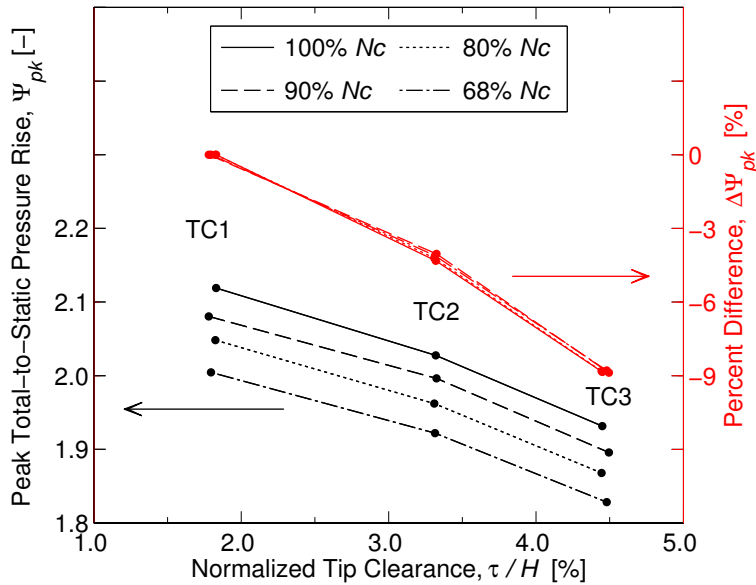


Figure 3.11: Peak total-to-static pressure rise coefficient as a function of tip clearance height.

### 3.1.6. Isentropic Efficiency

As explained earlier, the isentropic efficiency of the compressor has been evaluated using the formal definition from Equation (2.3). The required stagnation enthalpies for this equation are calculated using the thermodynamic equation program REFPROP (Lemmon et al., 2013) through the use of measured conditions (stagnation temperature, stagnation pressure, static pressure, and relative humidity) at axial positions 1 and 9 – in agreement with the measurement planes used to define total pressure ratio in Equation (3.1). Using Equation (2.3), the isentropic compressor efficiency has been calculated for each of the measurement points shown in the overall compressor total pressure ratio map of Figure 3.1 (neglecting the stall points). These efficiencies, shown in Figure 3.12, are presented for each of the four corrected rotational speeds as a function of the normalized inlet corrected mass flow rate.

The uncertainty of the efficiency values in Figure 3.12 can be influenced by uncertainty contributions from measured pressures, temperatures, and humidity. Great care has been taken to ensure that the respective uncertainty for each of these measured parameters is as small as possible (see Section 2.2). With this in mind, the efficiency uncertainty has been carefully evaluated using the  $T$ - $s$  region technique implemented by Lou et al. (2013). The uncertainty values for the 100% corrected speedlines in Figure 3.12 are on the order of 5 points across the entire flow range for all tip clearances. Similarly, the 90% corrected speedline data have efficiency uncertainties of approximately 6 points across the entire flow range. At the lower

speeds of 80% and 68% corrected speed, however, the reduced pressure rise leads to a reduced temperature rise (although still measurable and appreciable), especially at high flow rate conditions. As a result, the uncertainties for the 80% corrected speedline data vary from approximately 6 points at low flow, high loading conditions to as much as ten points for the high flow, low loading conditions. At the 68% speed conditions, the uncertainties vary from approximately 8 points at low flow conditions to more than 15 points at high flow conditions.

These relatively large uncertainty values are primarily due to the propagation of measurement uncertainty when calculating enthalpies, especially  $h_{095}$ , as explained by Lou et al. (2013). Indeed, the data for this project also show that  $h_{095}$  is the largest component of the efficiency uncertainty. Despite the large measurement uncertainties, however, the repeatability of the efficiencies shown in Figure 3.12 is typically on the order of 0.5 points – an order of magnitude improvement over the calculated uncertainty.

As an additional consideration, measurement variability due to machining tolerances, blade row interactions, and more, can also influence calculated performance parameters such as isentropic efficiency. The measurement locations for data presented here were carefully selected to avoid these effects as much as possible based on prior knowledge of the machine. Nonetheless, a vane wake variability study characterizing the circumferential variation in the wakes shed from a particular stator row was recently conducted by Methel et al. (2015). The results from this study, combined with a similar investigation of passage-to-passage variations in total temperature, have shown that the circumferential variation in the flow field is small (on the order of measurement uncertainty) yet repeatable. Thus, efficiencies calculated by combining pressure and temperature measurements from different sectors of the machine can be influenced by this variation. The only way to avoid this error in the absolute value of efficiency would be to use a measurement rake with combined total pressure and total temperature sensors. However, the measured changes in efficiency between different configurations are valid and meaningful.

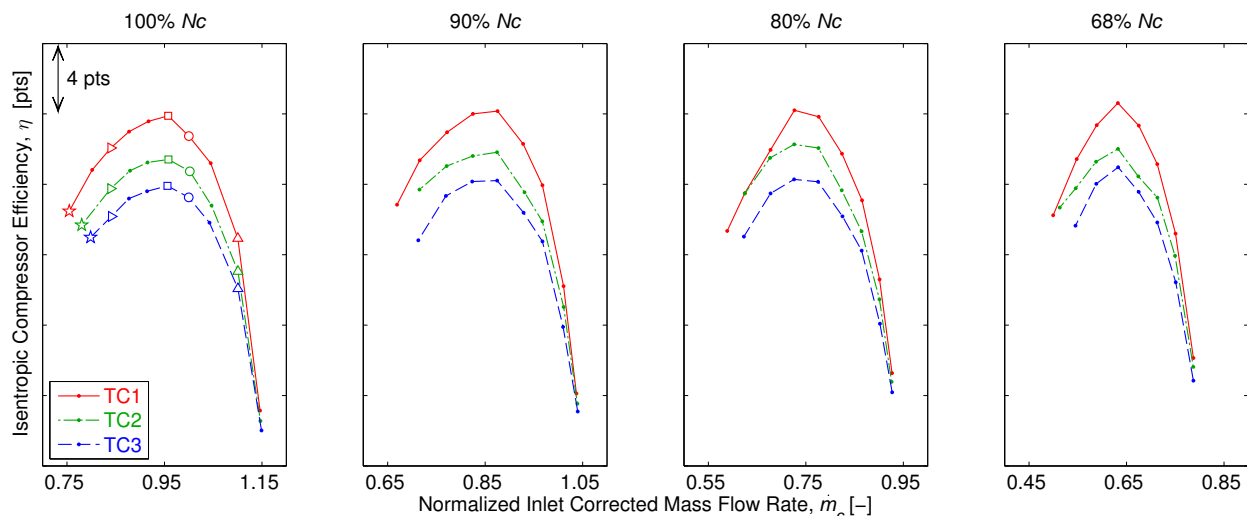


Figure 3.12: Overall isentropic compressor efficiency at four corrected rotational speeds.

Beginning with the data presented in Figure 3.13, the compressor efficiency is separately considered for each of the three tip clearance configurations at the four operating conditions of primary interest on the 100% corrected speedline: LL, NL, PE, and HL. Figure 3.13 shows the

expected result of decreased compressor efficiency with increased rotor tip clearance, as discussed in earlier studies for isolated rotors and multistage machines. At each of the four operating points, the efficiency decreases linearly with increasing tip clearance. Furthermore, the constant of linearity is nearly identical for all four operating points (certainly within the repeatability of the measurements).

Figure 3.13 presents a decrease of approximately 2.5 points at the peak efficiency point between TC1 and TC2 as compared to Wisler’s (1985) canonical observation of 1.5 points for the same change in clearance size. In a four-stage low-speed compressor similar to the design used by Wisler, Tschirner et al. (2006) showed an efficiency decrease of 3.6 points between TC1 and TC2 (also 1.5% and 3.0% with respect to annulus height) at the design point. However, because Tschirner et al. used cantilevered stators, and the stator hub clearances were increased at the same rate as the rotor tip clearances, the resulting decreases in pressure rise and efficiency are larger than a study which studies rotor tip clearances exclusively.

The compressor performance data presented by Freeman (1985) suggest a rule-of-thumb of approximately 3% to 5% stall margin lost per 1% increase of tip clearance and approximately 1.4 to 2 efficiency points lost per 1% increase of tip clearance height. These results are based on linear fits of data collected from several engine tests and research compressor studies. Applying Freeman’s suggestions to these tip clearance values would suggest an efficiency loss on the order of 2 to 3 points and a stall margin loss on the order of 5 to 8 percent comparing TC1 and TC2. The results presented herein are certainly in agreement with this rule of thumb, but a comparison of these data with results from other authors discussed so far also emphasize Freeman’s important observation that the appreciable scatter of data about a general trend shows discernable differences between different machines, airfoil families, levels of aerodynamic loading, and rotational speed regimes.

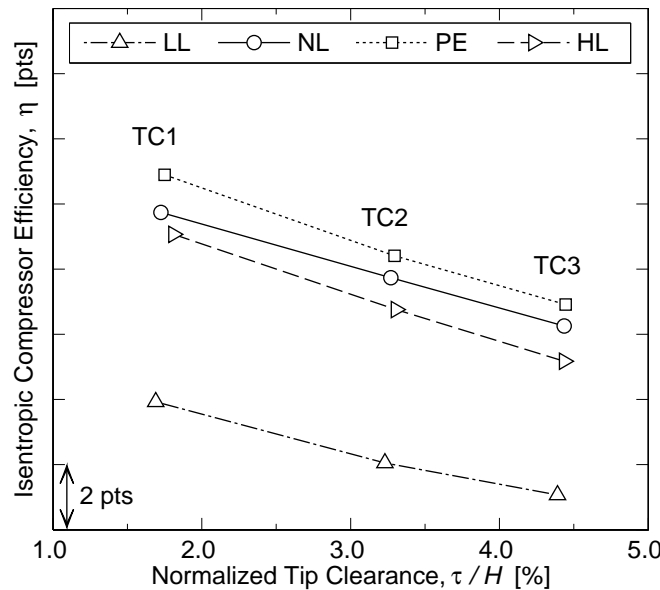


Figure 3.13: Isentropic compressor efficiency for specified 100%  $N_c$  speedline points as a function of tip clearance height.

### 3.1.7. Stator 3 Seal Leakage Flow Measurements

To adequately define boundary conditions for computational models, the leakage flow paths for the compressor have been carefully evaluated. At the inlet of the compressor, the air paths are all sealed, but a potential leakage path exists under the Stator 3 labyrinth (knife) seals to atmospheric pressure. Ball (2013) considered these leakage flow paths and the related knife seal geometry for computational models. Ball determined that whether the Stator 3 seal flow was allowed to exit to ambient pressure, or if the respective flow paths were plugged, the effect on overall compressor pressure rise was negligible. However, a measureable change of overall compressor efficiency was observed, likely due to a localized heating of the rear bearing and other components at the rear of the compressor in the absence of the Stator 3 leakage flow path.

For this study, the leakage pathways remained open to the atmosphere, but the air was connected to a manifold through four tubes at the rear of the compressor, Figure 3.14, to capture the leakage flow. These tubes delivered the leakage flow to a Wyatt Engineering orifice plate with a discharge coefficient of 0.6042 and a diameter ratio of 2.294 (as provided by the manufacturer). The pressure drop across the orifice plate was measured by a Rosemount 3051C differential pressure transmitter with a calibrated range of 0-13 inH<sub>2</sub>O. The representative overall uncertainty of mass flow rate measurement for this orifice plate meter setup is less than 2.4% of the calculated value for mass flow rate.

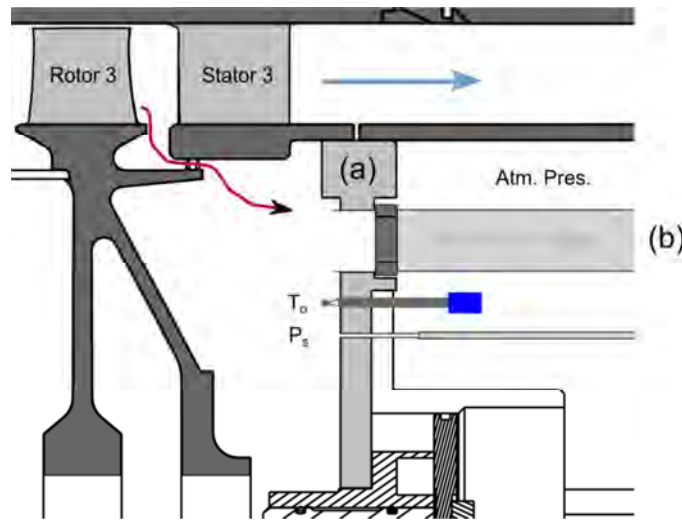


Figure 3.14: Stator 3 seal leakage flow path and manifold tubes from (a) the rear bearing plate to (b) an orifice plate run (Brossman, 2012).

The measured Stator 3 seal leakage mass flow rates for each of the measured points in Figure 3.1 (seal leakage flow rate data for the stall point were not collected) are shown in Figure 3.15, normalized as a percentage of the inlet corrected mass flow rate:

$$\dot{m}_{LN} = \frac{\dot{m}_{leak,c}}{\dot{m}_c} \times 100\% , \quad (3.9)$$

for which the measured leakage mass flow rate is first corrected using the inlet conditions of the compressor using Equation (2.2). The increase of leakage flow rate at lower inlet mass flow rate conditions in Figure 3.15 suggests that the leakage mass flow rate is affected by the pressure rise

through the compressor (increased loading and pressure rise at low flow rates leads to increased leakage flow rate as the pressure differential with respect to ambient pressure increases). However, the curves in Figure 3.15 are independent of tip clearance configuration, showing that the leakage flow rate is influenced more by the flow rate through the compressor than the overall pressure rise through the machine (in which case, the leakage flow rates would change more significantly for different tip clearance configurations). The one potential exception to this is the final two to three points on the 100% speedline for TC3, which appear to roll over unlike the two smaller tip clearances TC1 and TC2. This observation aligns with the previous discussions about total pressure ratio and total-to-static pressure rise characteristics.

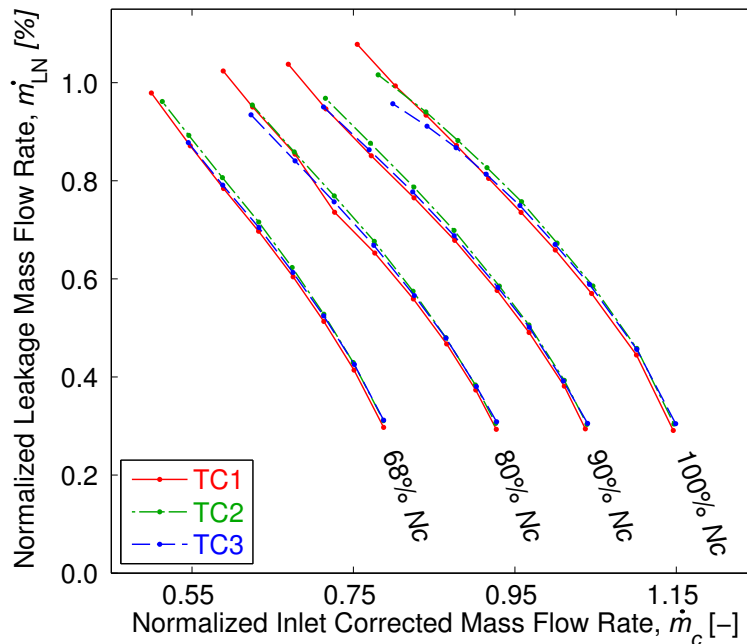


Figure 3.15: Stator 3 seal leakage mass flow rate as a percentage of inlet corrected mass flow rate for each of the traversed data points in Figure 3.1.

### 3.1.8. Casing Outer Diameter Surface Temperature Measurements

Often, turbomachinery system analyses assume that the machine operates adiabatically. This assumption is based on the difference in order of magnitude between the work done by the rotor on the flow and that of the heat flux from the device. However, an analysis of the total temperature profiles through the compressor (see Section 3.3.2) show an increase of the fluid total temperature in the tip region near the compressor casing, especially for the front stages. In this case, the more significant temperature of the aft section of the compressor conducts through the aluminum casing and influences the flow at the front of the machine. As a result, alternative boundary condition techniques may be better suited for computational analyses, such as the isothermal wall boundary condition discussed by Bruna and Turner (2013) or a conjugate heat transfer analysis.

Several surface-mounted T-type thermocouples were installed on the outside of the compressor casing to isolate these temperature measurements. One thermocouple was installed over each of the seven blade rows at a position noted in Figure 2.11. A separate analysis of the circumferential uniformity of the casing temperatures showed the circumferential variations are less than 1.8 °R. Prior to collecting data at each operating point, an additional surface-mounted K-type thermocouple installed over Rotor 3 was allowed to reach a steady operating condition to prevent any transient temperature effects in the collected data.

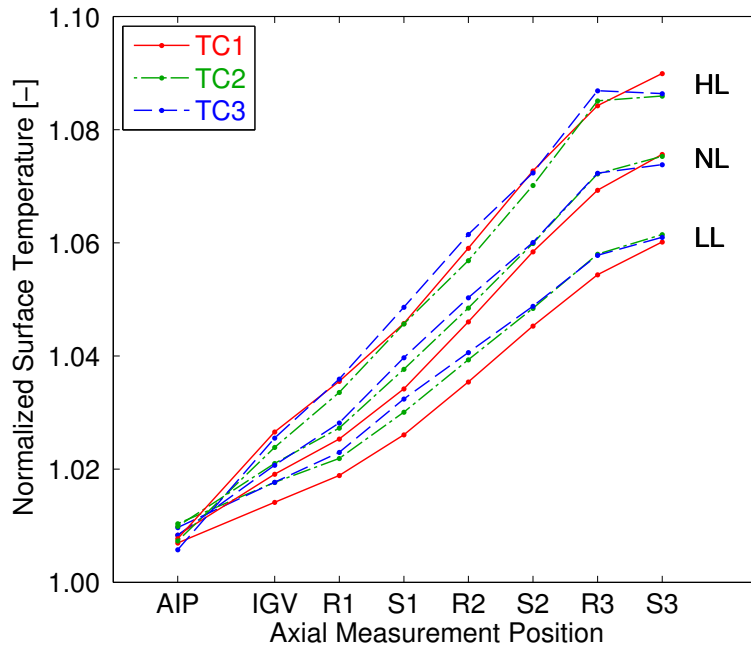


Figure 3.16: Normalized surface temperatures for three loading conditions on the 100% corrected speedline.

Beginning with Figure 3.16, the casing outer diameter surface temperature trends are shown at three selected loading conditions (LL, NL, and HL) for all three tip clearance configurations. These temperatures are presented as a normalized temperature ratio with respect to the area-averaged temperature measured by the total temperature rakes at the AIP (plane 0 in Figure 2.6). As the work imparted by the rotor on the fluid increases with loading condition, the temperature of the outer compressor casing also increases through the compressor. Figure 3.17 shows the same normalized temperature ratio, but for the final “near-stall” traversed operating point, at each of the four speeds and all three tip clearance configurations. Figure 3.16 and Figure 3.17 both show that the TC1 data continue to experience temperature rise, even at the Stator 3 measurement position, whereas the larger tip clearance configurations (TC2 and TC3) appear to level off more significantly comparing the surface temperatures over Rotor 3 and Stator 3.

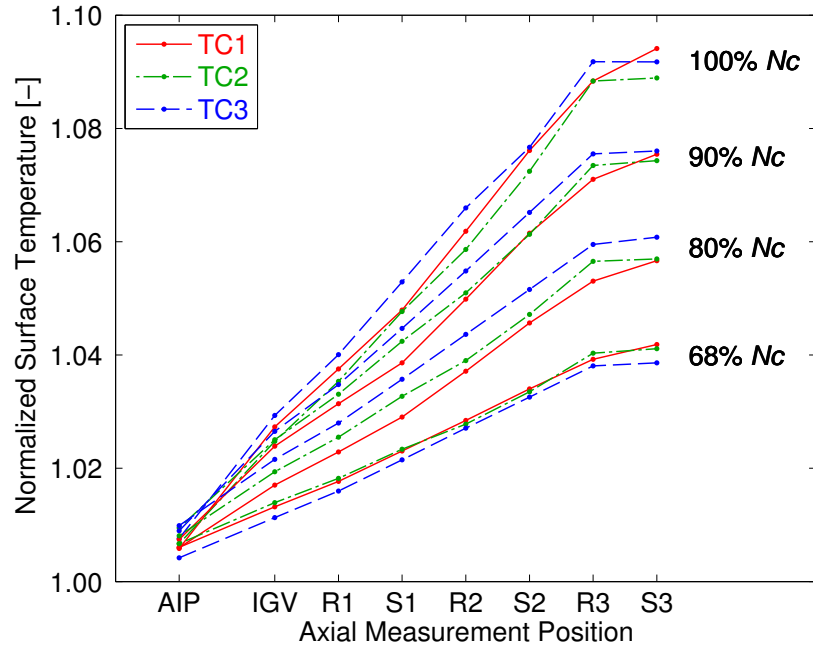


Figure 3.17: Normalized surface temperatures for the final “near-stall” traversed operating point at all four operating speeds.

### 3.2. Stage Performance Characteristics

In addition to the overall performance, the stage-by-stage compressor performance has also been considered for this study. The stage total pressure ratios are shown in Figure 3.18 as a function of the stage inlet corrected mass flow rate. For this figure, the stage inlet corrected mass flow rate uses the same equation for the inlet corrected mass flow rate, Equation (2.2), but the values for stagnation density and stagnation speed of sound are selected to represent the measured parameters at the inlet to the stage. Stage 1 is defined for axial positions 1 to 4, Stage 2 is defined for axial positions 4 to 6, and Stage 3 is defined for axial positions 6 to 9. By these definitions, the combination all three stages results in the overall total pressure ratios from Figure 3.1.

Figure 3.18 allows several important observations regarding the performance of the three-stage compressor, particularly relating to off-design performance and stage matching. Of note, each of the three stages has distinctly different characteristic shapes at all speeds and tip clearance configurations. The Stage 1 characteristics show the total pressure rise turns to a positive slope near the top of the curve as the compressor approaches stall. The Stage 2 curves all show a position where the slope of the curve changes sharply. This location appears at the peak efficiency point of the compressor for each curve – these characteristics could be approximated by two linear regions. Finally, the Stage 3 curves have a curvature which more closely resembles Stage 1 than Stage 2, but with less total pressure rise.

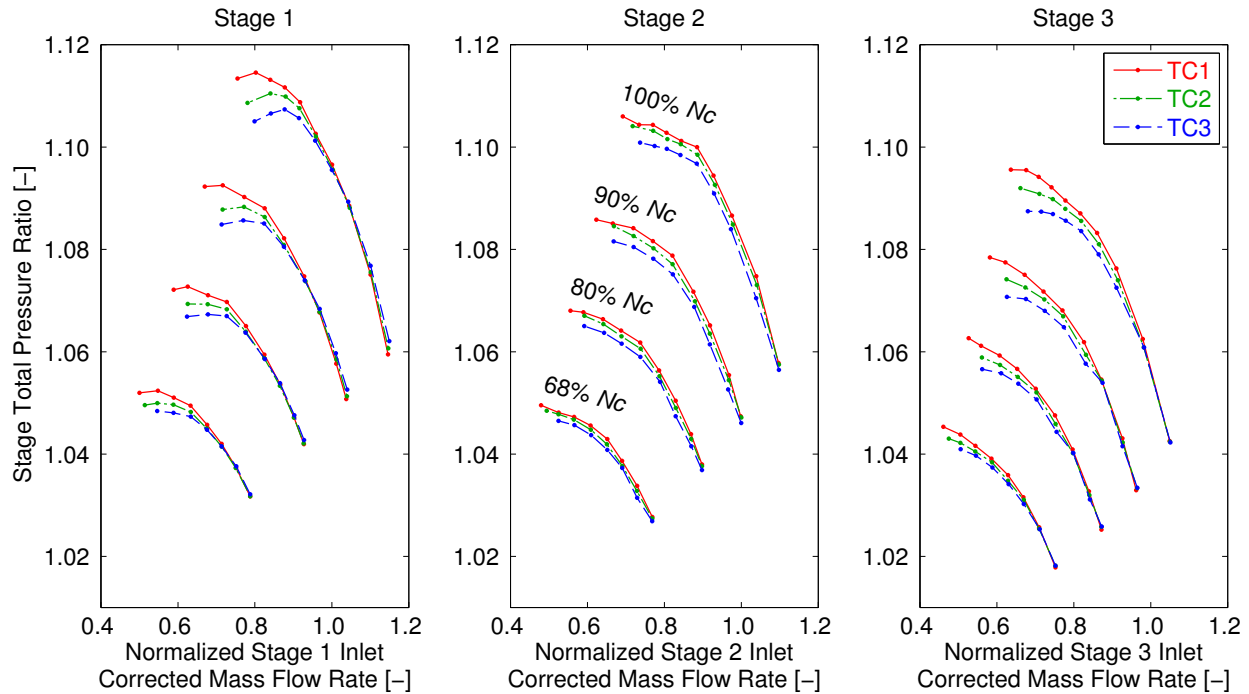


Figure 3.18: Stage total pressure rise characteristics for the traversed map points.

For Stage 1 and Stage 3, the operating points closest to the stall point (the actual stall points are not shown in Figure 3.18) show a noticeable and consistent decrease of total pressure rise with increased tip clearance height. This same observation may be made for the 100% corrected speedline of Stage 2, but the part-speed operating conditions (90%, 80%  $N_c$ , and 68%  $N_c$ ) for Stage 2 show a more consistent offset of results across the entire speedline. Figure 3.18 also shows that the individual stage total pressure rise may actually increase by a small amount for the larger tip clearance configurations (TC2 and TC3) at the highest flow rate position on the 100% speedline for Stage 1. An analysis of the individual rake pressure measurements which combine to create the area-averaged total pressure ratios shown in Figure 3.18 reveals that the lower 60% annulus height performs at a slightly higher total pressure exiting Stator 1 – at the expense of a more significant endwall blockage and total pressure loss in the tip region. Although the magnitudes of these differences are greater than the repeatability of the measurements, they are on the order of the uncertainty of the measurements, so no conclusions can be attributed to the observations.

These stage pressure rise characteristics bring rise to a consideration of stage matching effects in the compressor. It is expected that the Purdue three-stage axial compressor is well-matched at the design speed with the design tip clearance configuration (TC1). Comparing the TC1 performance with TC2 throughout Figure 3.18, the trends of the curves are very similar – many of the characteristics overlap for significant portions of the flow range. This suggests that the stage matching of the compressor may not be significantly altered by a change from 1.5% to 3.0% rotor tip clearance height. However, more distinct differences exist for the largest tip clearance configuration (TC3).

### 3.3. Inter-Stage Flow Measurements

In addition to the performance metrics discussed thus far, the inter-stage total pressure and total temperature measurements collected from the seven-element rakes also provide valuable information regarding the radial distributions of measured flow properties. A direct comparison of these radial distributions for each of the three tip clearance configurations may be affected by the overall pressure rise (or temperature rise) through the compressor, therefore making it difficult to draw meaningful conclusions about the comparisons, especially near the rear of the compressor where discrepancies between tip clearance configurations may be large. As a result, these spanwise measurements must be normalized by some chosen value to accommodate comparison of the radial total pressure and total temperature profile shapes. The five selected loading conditions on the 100% corrected speedline have been chosen for comparison between the three tip clearance configurations.

#### 3.3.1. Total Pressure

As defined in Section 3.1.3, the normalized radial total pressure, Equation (3.4), is again considered here for comparison of the pressure profiles through the compressor. Figure 3.19 shows this normalized radial total pressure shape comparison at the LL operating condition for each of the three tip clearances, TC1-TC3, at axial measurement planes 3 through 8 (as denoted by the schematic in Figure 2.6). For reference, the uncertainty of measurements presented in Figure 3.19 is smaller than the symbol size in the figure. Using Equation (3.4), any reductions in pressure rise due to an increase of rotor tip clearance at the same axial measurement plane are avoided, and the radial stagnation pressure profile shapes remain for comparison.

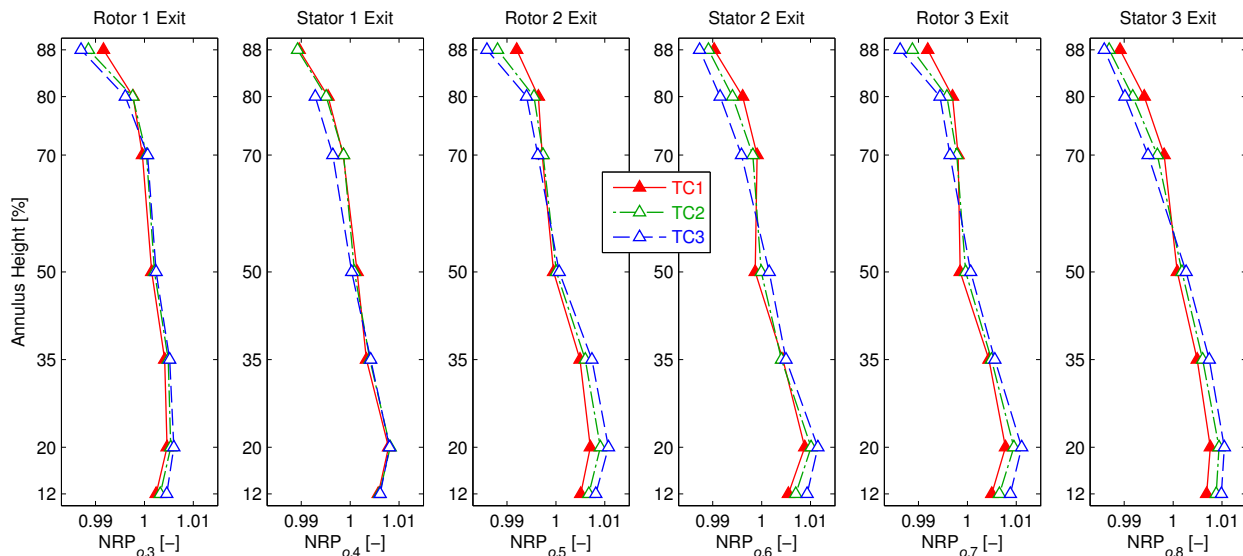


Figure 3.19: Radial total pressure profiles at LL.

As the tip clearance height is increased in Figure 3.19, the tip leakage flow increases and the tip leakage flow disturbance grows in size and strength. This effect is not significant for the low loading (LL) condition, which is expected from the lack of distinct difference in compressor overall total pressure ratio between tip clearance heights for high flow rate conditions in Figure

3.1. However, this effect begins to become more apparent as the loading condition is increased up the speedline to the nominal loading (NL) and peak efficiency (PE) points in Figure 3.20 and Figure 3.21, respectively. In these figures, the increased blockage created by the tip leakage flow disturbance growth redistributes a portion of the flow from the tip region toward the hub region, as distinguished by the reduction of  $NRP_o$  at the tip and increase near the hub for all axial measurement positions. Also in these figures, it is possible to distinguish a set of similar profile shapes at the three rotor exit planes (axial positions 3, 5, and 7), which differ from a separate set of similar profile shapes at the stator exit planes (axial positions 4, 6, and 8).

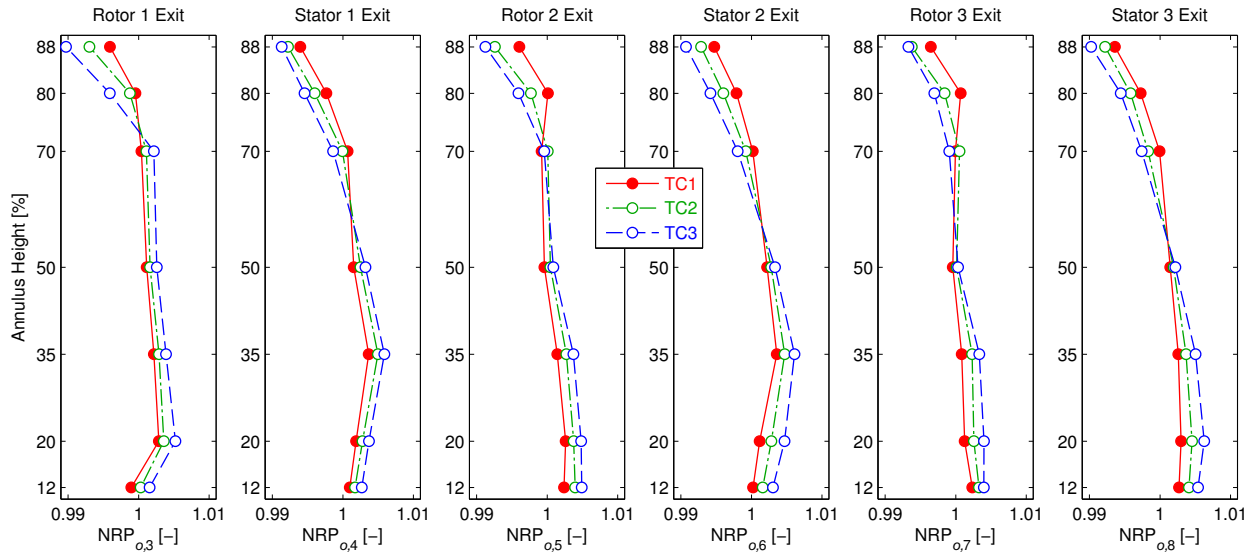


Figure 3.20: Radial total pressure profiles at NL.

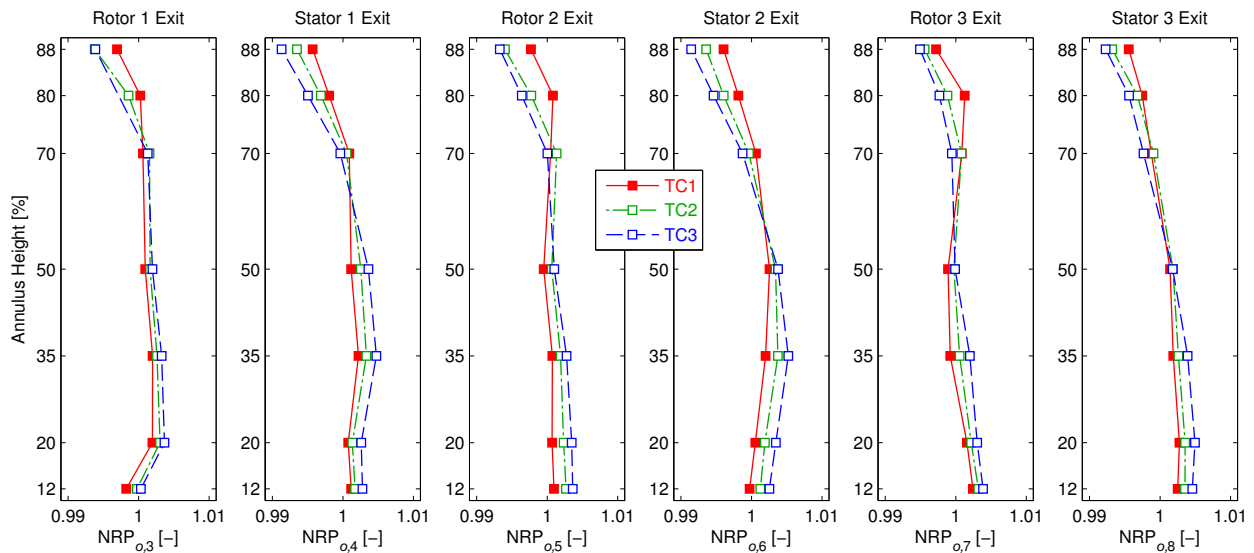


Figure 3.21: Radial total pressure profiles at PE.

As the loading condition is increased further up the speedline toward the stall point, these trends become more distinct. In particular, Figure 3.22 shows the same normalized radial pressure profile shapes at a high loading (HL) condition for the three tip clearance configurations. The same general trends of redistributed flow from the tip toward the hub with increased tip clearance persist in Figure 3.22, but there are more distinguishable characteristics between the axial positions. Of note, the difference between radial pressure profiles for the TC1 and TC3 configurations at Stator 2 Exit are more pronounced than for Stator 1 Exit or Stator 2 Exit. Specifically, a corner separation condition exists at the hub of Stator 2, which is energized by the redistributed flow from the tip region toward the hub to prevent the flow separation tendencies of the vane row. This observation will be further explained with detailed measurements and flow visualization pictures later.

Also in Figure 3.22, the tip region at Rotor 1 Exit portrays a repositioning of the minimum pressure from 88% span to 80% span as the tip leakage vortex core extends radially downward into the flow path with increased tip clearance. This leaning-over of the radial profile in the tip region for TC2 and TC3 is indicative of a close proximity to the stall point which has not yet been reached for TC1 at the same corrected mass flow rate (see Figure 3.1). However, the same distinguishing characteristic is not present at Rotor 2 Exit or Rotor 3 Exit, suggesting a difference in overall performance for the embedded stages, which ingest the increased blockage from the upstream stage(s), compared to the first stage which is always met with the same clean inlet flow from the IGV.

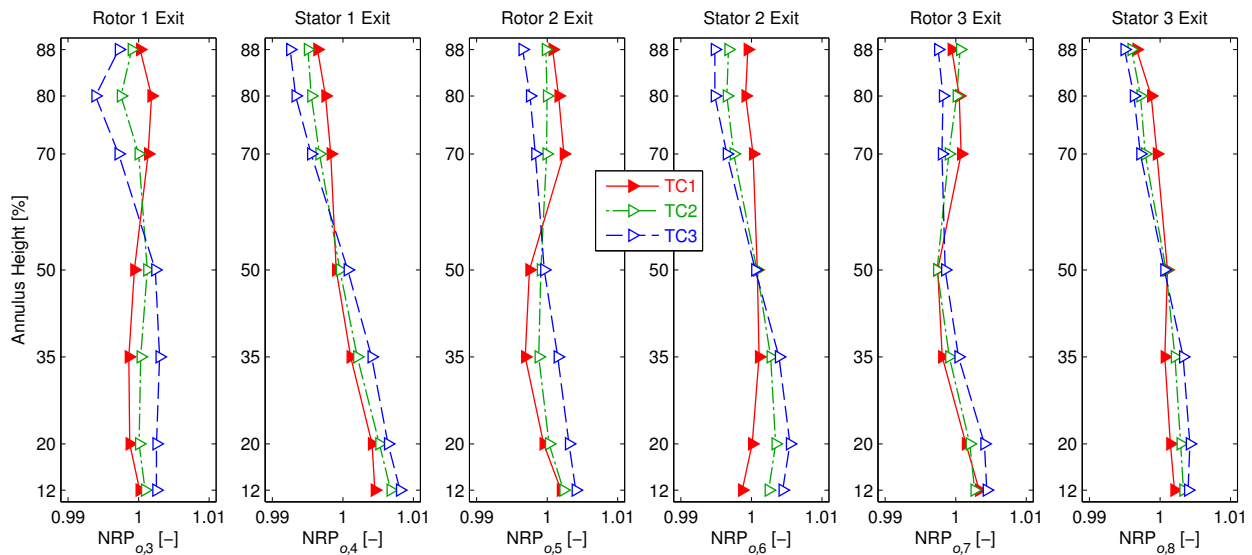


Figure 3.22: Radial total pressure profiles at HL.

As suggested earlier, the HL condition points compared in Figure 3.22 are located at proximities to the stall point which vary with tip clearance. Thus, an additional loading condition is considered which helps to overcome this inherent difference. The near-stall (NS) points denoted by the five-pointed stars in Figure 3.1 are representative of approximately 5% stall margin, as defined by Equation (3.2). By matching stall margin, the data comparison between the three tip clearance configurations should be more appropriate.

This comparison, shown in Figure 3.23, yields some interesting results: the Rotor 1 Exit profile shape for TC1 has leaned over in the same manner as TC2 and TC3; also, the normalized radial pressure profile shapes for the three tip clearance configurations appear to coalesce at Rotor 2 Exit and Rotor 3 Exit. These data at Rotor 2 Exit and Rotor 3 exit show a very slight difference for the TC3 results, but this is explained by the fact that the data for TC3 actually represent a stall margin closer to 4% instead of the desired 5% which was achieved for TC1 and TC2. Therefore, the TC3 data are expected to achieve slightly less pressure near the tip and slightly higher pressure near the hub, as shown in Figure 3.23. Despite this apparent insensitivity of profile shape with respect to clearance size at Rotor 2 Exit and Rotor 3 Exit in Figure 3.23, there is a more noticeable difference at Rotor 1 Exit, and the discrepancy between TC1 and TC3 at Stator 2 Exit is even more significant than in Figure 3.22.

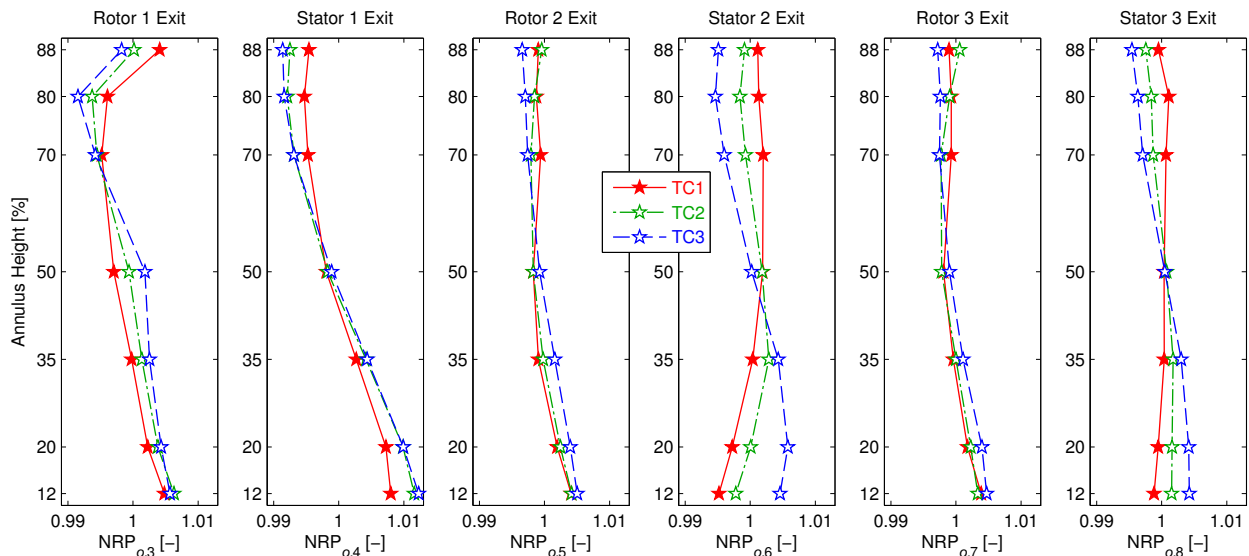


Figure 3.23: Radial total pressure profiles at NS.

### 3.3.2. Total Temperature

In the same fashion as the radial total pressure profiles, the normalized total temperature ( $NRT_o$ ) represents the circumferential average at each radial position, normalized by the area average (radial and circumferential) at the same axial position:

$$NRT_{o,i} = \frac{T_{o,i,CA}}{T_{o,i,AA}}. \quad (3.10)$$

Figure 3.24 presents this normalized radial temperature distribution for the low loading (LL) condition on the 100% corrected speedline. At this operating point, the similarity of the pressure rise for the three tip clearance configurations leads to a largely insignificant difference between the three cases, with only minor differences downstream of each rotor row. For reference, the uncertainty of measurements presented in these figures is smaller than the symbol size in the figure.

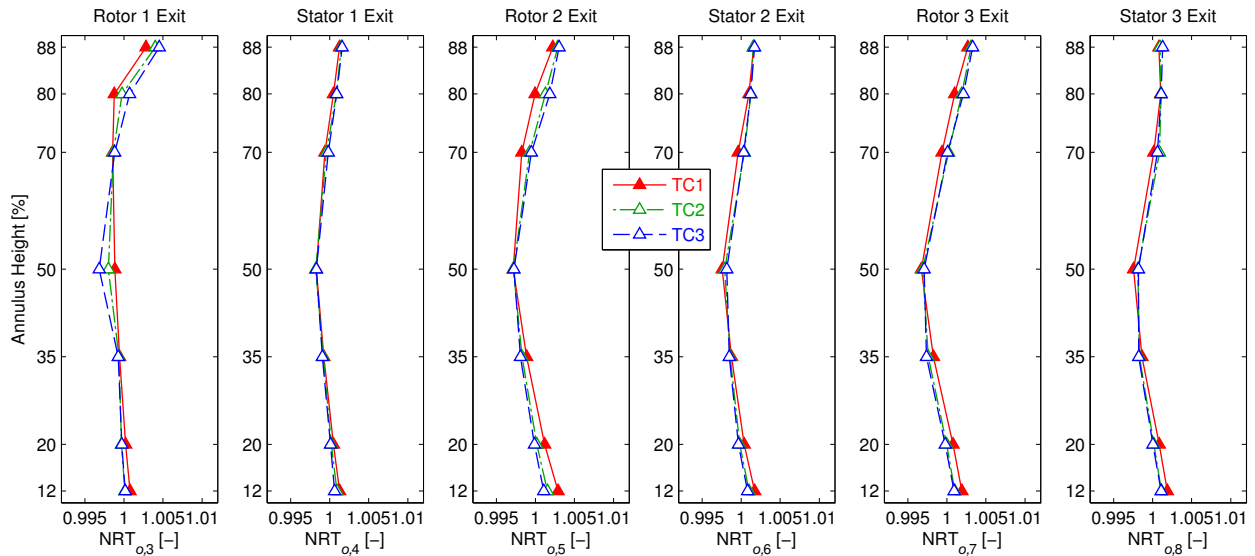


Figure 3.24: Radial total temperature profiles at LL.

As the loading of the compressor is increased, more significant differences appear in these normalized radial temperature profiles. Of note, the NL and PE operating points (Figure 3.25 and Figure 3.26, respectively) begin to show slight differences of the temperature distribution in the tip region at Rotor 1 Exit, denoting the difference of work distribution as the tip leakage flow affects the rotor performance. Also at these loading conditions, the Stator 1 Exit total temperature distributions are largely unaffected by the tip clearance changes, but Stator 2 Exit and Stator 3 Exit begin to show slight shape changes in these radial distributions.

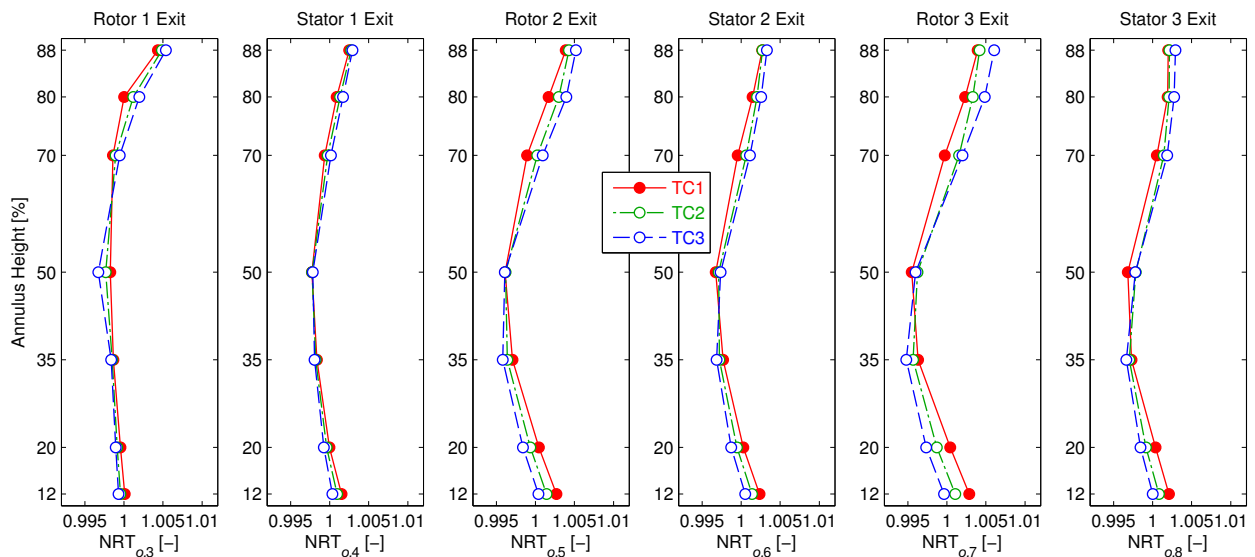


Figure 3.25: Radial total temperature profiles at NL.

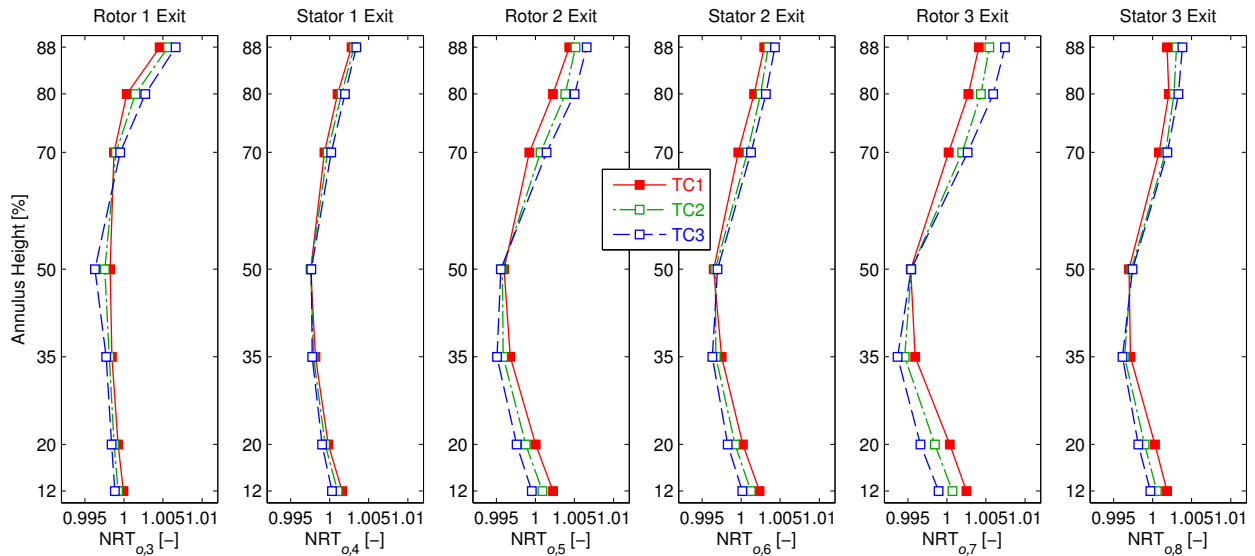


Figure 3.26: Radial total temperature profiles at PE.

As the compressor is further throttled toward stall, the HL (Figure 3.27) and NS (Figure 3.28) normalized radial total temperature distributions show the differences at the rotor exit planes identified for the other loading conditions persist. The Stator 1 Exit profiles remain relatively unaffected by tip clearance changes across the entirety of the 100% corrected speedline. The Stator 2 Exit profiles are largely unchanged from the NL condition to the NS condition, with only slight differences at the LL condition. However, the Stator 3 Exit profiles highlight a slight difference in work distribution for the TC1 configurations compared to the larger tip clearances (TC2 and TC3) at the near stall (NS) operating condition. In particular, the TC1 configuration shows more work distributed in the hub region of Stator 3, compared to TC2 and TC3 which are nearly identical for this normalized total temperature distribution shape.

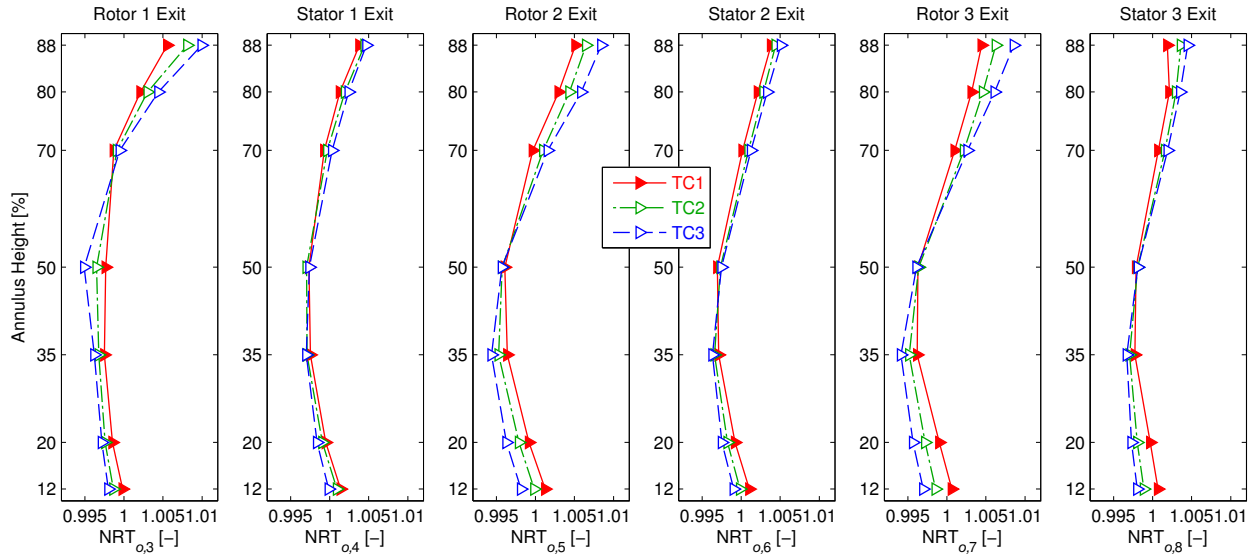


Figure 3.27: Radial total temperature profiles at HL.

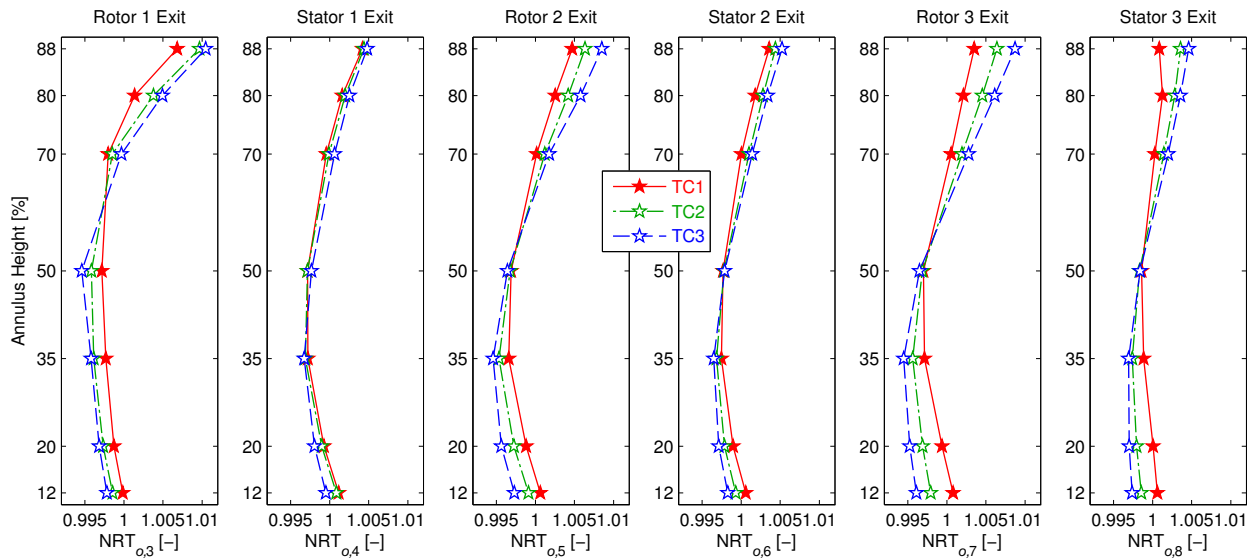


Figure 3.28: Radial total temperature profiles at NS.

### 3.4. Flow Visualization

In addition to the quantitative measurement techniques presented so far, a flow visualization method was introduced to investigate the surface flow topologies on the stator vanes and evaluate regions of flow separation. These flow visualization tests were conducted at two loading conditions, NL and HL, for all three tip clearances, and an additional datasets were also collected at the peak efficiency and near stall operating points for the baseline tip clearance

(TC1). All nominal loading tests feature orange paint, while blue paint was used for the peak efficiency and high loading conditions. A combination of paint colors was used at the near stall condition. Further description of the measurement technique can be found in Smith and Key (2015).

Figure 3.29(a) shows an example image of a stator with corner separations at both the hub and tip endwall junctions on the suction side of a Stator 1 vane. Flow goes from left to right in the figure; the stator hub is at the bottom of the image and the tip is at the top as noted. This vane is positioned at the compressor casing splitline, and therefore may be imaged straight-on, whereas all later images presented were acquired from the trailing edge looking upstream. The corner separations are marked in Figure 3.29(b) and appear as semi-triangular patterns. For this Stator 1 vane at the high loading condition, the tip has a larger corner separation than the hub, as a result of many design factors including but not limited to flow angles, diffusion factor, and Rotor 1 performance. The streaklines in the separated regions reveal the recirculation patterns in the flow, as sketched in Figure 3.29(c).

Several critical points are identifiable in the surface flow topology. At least four saddle points (S) and four nodes (N) are present, which follows the rule given by Flegg (1974) that the number of saddle points and nodes must be equal for a vane row with no tip gap. It should be noted that there are regions that may have indistinguishable critical points due to resolution of paint or flow pattern complexities, like the region where the tip and hub meet and near the endwalls. When comparing many Stator 1 vane images from the same dataset, there is another possible node location near the saddle point at the tip. This type of detailed analysis of the surface flow topology is useful to comparisons with computational models, particularly with respect to the acceptability of turbulence models.

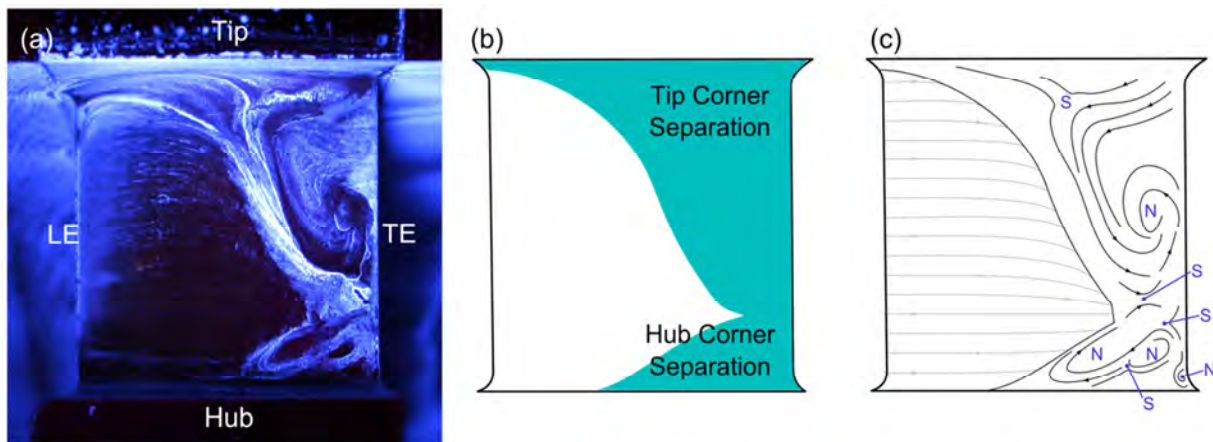


Figure 3.29: Basic surface flow topology for Stator 1 at the high loading condition (a) image, (b) corner separations, and (c) drawn flow topology with saddle points (S) and nodes (N) labeled.

Figure 3.30 provides an overview of the suction side surface flow visualization images on Stator 1, Stator 2, and Stator 3 (left to right) at the four loading conditions (increasing loading top to bottom) for TC1. The image of Stator 1 at peak efficiency loading is labeled, indicating the vane hub, tip, leading edge (LE) and trailing edge (TE). This orientation remains the same for all following images. On the suction surface of each stator, the regions with paint surface flow patterns are regions with recirculating flow and separations. The corner separations increase in size further downstream through the compressor, where Stator 3 has larger separations than Stator 1. The flow conditions in the rear stages contain increased turbulence and more unsteady disturbances due to wakes from upstream blade rows resulting in earlier vane boundary layer separation. Furthermore, as loading increases, the vanes experience a stronger adverse pressure gradient making the boundary layer more susceptible to separations, and thus, the corner separations grow in size.

At the nominal loading (NL) condition, Figure 3.30(a-c), all three stators have larger recirculation regions at the tip compared to the respective hub regions. The amount of separated area increases with each downstream stator, though Stator 1 and Stator 2 are quite similar. These trends fall within expectations of this relatively low loss operating condition, but are also specific to the design of the compressor. When loading is increased from nominal loading to the peak efficiency loading condition, this trend changes and each stator's separation pattern is unique. Changes in the radial distribution of the flow with increased loading are specific to the compressor design, and are governed by various aspects of stage matching (Cumpsty 2004). The flow patterns on Stator 1 are similar at nominal and peak efficiency conditions, whereas the Stator 2 and Stator 3 hub corner separations grow more and both have boundary layer separation along the entire span.

At peak efficiency, the Stator 2 tip still has a larger separated region than the hub, while the Stator 3 hub and tip separations are nearly equivalent. For this PE case, shown in Figure 3.30(d-f), Stator 1 experiences similar inlet conditions as in Figure 3.30(a) at NL, but the effects of increased loading, stronger wakes and adverse pressure gradient are more substantial to the inlet conditions for Stator 2 and Stator 3. All three vanes have large increases in corner separation size at the hub and tip between the peak efficiency point and the high loading condition (Figure 3.30(g-i)), which is consistent with the increased losses expected at high loading conditions. By the point at which the high loading operating condition is reached, Stator 1 shows full spanwise boundary layer separation, and Stator 2 and Stator 3 have separations extending much further upstream on the vane surface. The final set of images, Figure 3.30(j-l), are at the near stall loading condition. The flow visualization at NS shows that all three stators have significant suction side boundary layer separation. The tip region (approximately 75% span and above) of Stator 1 is completely separated, beginning from the leading edge. This is difficult to see in Figure 3.30(j), but can be identified more easily in Figure 3.31, looking downstream at the leading edge.

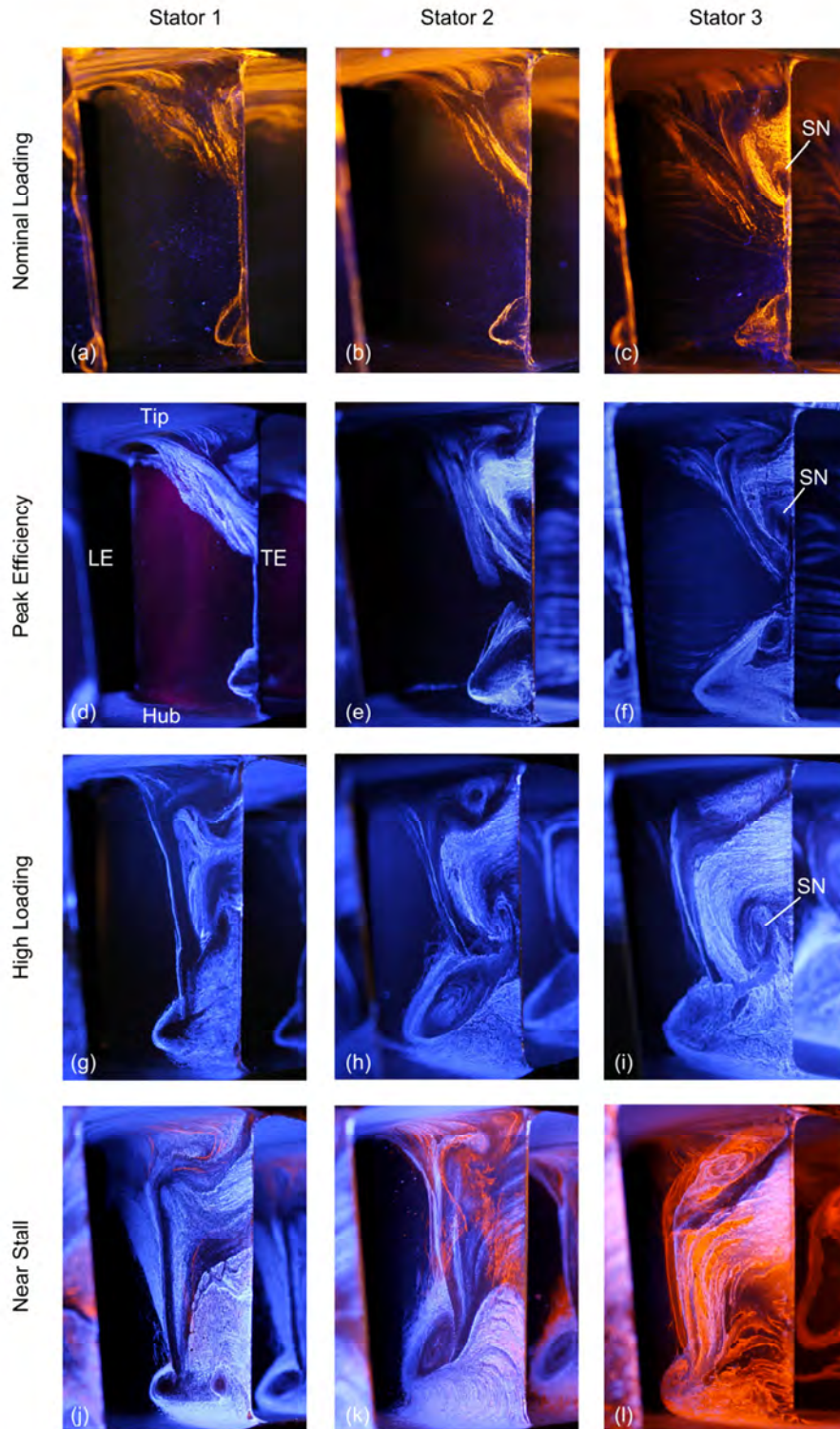


Figure 3.30: Surface flow visualization of corner separations for Stator 1 (left), Stator 2 (middle), and Stator 3 (right) at four loading conditions: NL (a-c), PE (d-f), HL (g-i), and NS (j-l) for TC1.

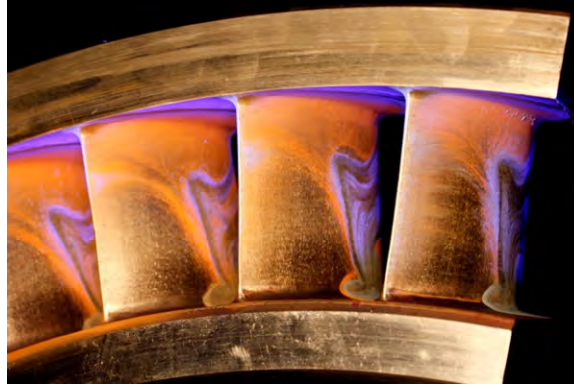


Figure 3.31: Stator 1 at NS conditions viewed from the leading edge looking downstream.

The surface flow patterns in Figure 3.30 have several identifiable nodal points and saddle points in the surface topology of all three stators. Specifically, the spiral node in the tip recirculation region at the trailing edge of Stator 3 is visible in all three loading conditions. For the nominal loading and peak efficiency conditions, it is similar in size and is located at 60% span, but at the high loading condition, the spiral node grows in size and moves toward the hub to approximately midspan.

Increased rotor tip clearance causes larger tip leakage flows, thereby resulting in additional blockage near the tip endwall at the inlet of each stator. This blockage redistributes the flow causing more fluid to travel through the lower half of the vane span. This locally increases the mass flow rate and unloads the hub, resulting in reduced corner separations at the hub. Meanwhile the large blockage at the tip due to the increased tip leakage flow disturbance weakens the tip and increases the amount of separation on the downstream vane. These trends can be observed on all three stators and are presented for NL and HL, at the three rotor tip clearances TC1, TC2, and TC3.

Figure 3.32 shows surface flow patterns at NL for all three stators and increasing rotor tip clearance, with TC1 at the top of the figure and TC3 at the bottom. Even at this relatively low loss loading condition, the increase in size of the rotor tip leakage flow disturbance is significant enough to shift the flow in the downstream stator from the tip to the hub. All three stators experience an increase in loss at the tip as rotor tip clearance increases, resulting in an apparent increase of tip corner separations. The increased size of the tip corner separation is particularly apparent between the TC1 and TC2 cases, for which the tip corner separation begins further upstream along the vane suction surface and extends deeper along the spanwise direction. The hub corner separations of Stator 1 and Stator 2 reduce in size from TC1 to TC2, but their size does not appear to reduce further when the clearance is increased to TC3. In fact, the Stator 3 hub corner separation remains similar in size for all three rotor tip clearances. Based on these observations, the increase in rotor tip clearance has a larger effect from TC1 to TC2 at NL. The growth in blockage from the tip leakage flow disturbance from TC2 to TC3 does not significantly change the radial distribution of the flow.

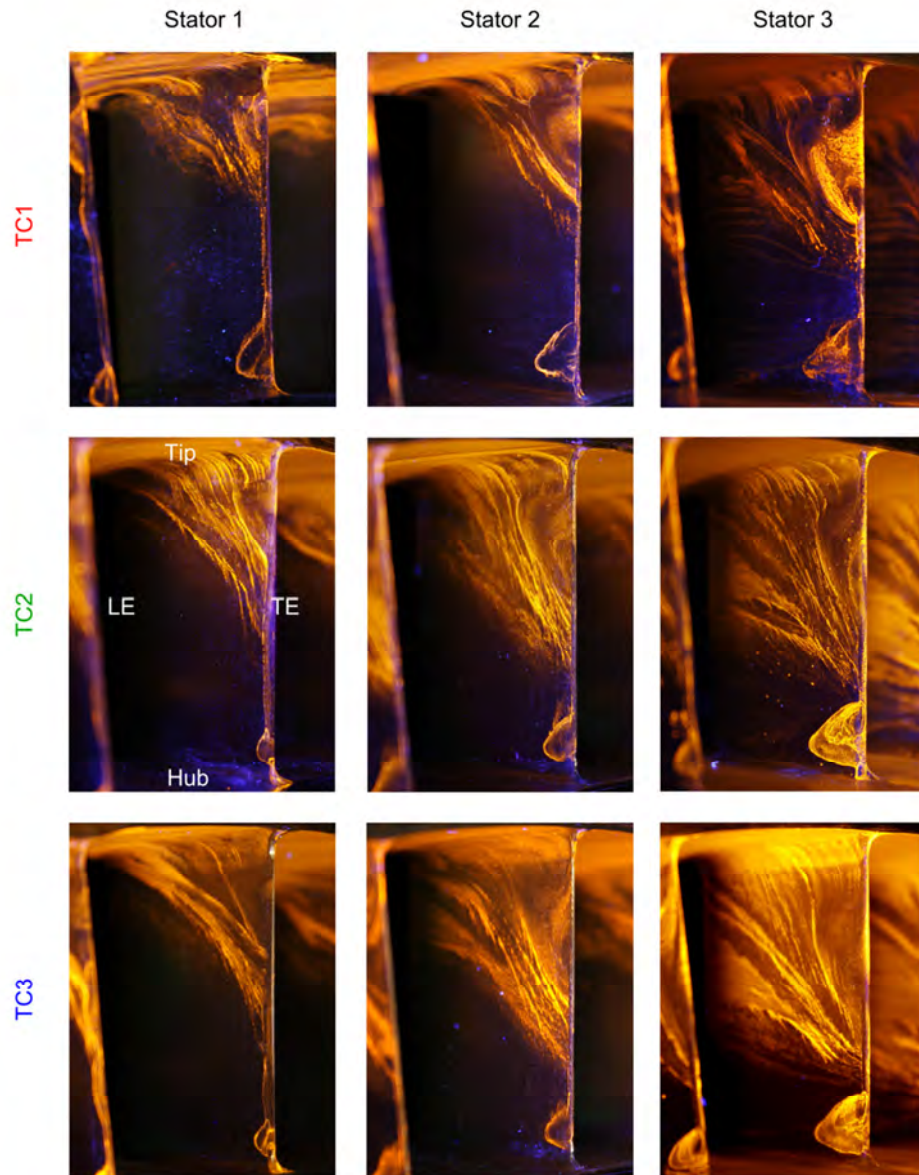


Figure 3.32: Flow visualization of vane corner separations at NL for TC1 (top), TC2 (middle), and TC3 (bottom).

The high loading (HL) operating condition is presented in Figure 3.33 using the same format for three tip clearance configurations. This HL operating condition is further from the design point of the compressor and shows more loss compared to the nominal loading (NL) condition. As a result, the rotor tip clearance effects on stator loss are more dramatic. The higher pressure ratios increases the leakage flow through the clearance gap and results in larger stator separation regions. The amount of boundary layer separation on Stator 1 is nearly unchanged between TC1 and TC2, but there is evidence of a stronger rotor tip leakage flow disturbance in the streamlines near the tip. Of note, TC2 has significant radial shift of streamlines at the top 14% span of the separated region. When the rotor tip clearance is increased to TC3, the effects of

increased flow blockage at the tip are far more significant. The stator tip corner separation originates from a position near the vane leading edge, and the radial streamlines extend down through the outer 22% span. In contrast, the hub region has been strengthened by the redistributed flow, resulting in a smaller hub corner separation.

The surface topology of Stator 2 changes the most of the three stator vane for the high loading (HL) condition in Figure 3.33. At the baseline tip clearance (TC1), there is a large spiral node in the hub corner separation, the tip region has a smaller node, and the two separations intersect at about 42% span. As the rotor tip clearance is increased to TC2, the fluid is redistributed through the Stator 2 passage due to the increased blockage from the Rotor 2 tip leakage flow disturbance, as evidenced by the shifts of the two nodes. Also for this TC2 tip clearance configuration, the spiral node at the hub is reduced in size and originates further downstream in comparison to TC1. The small node at the tip is less defined and is surrounded by more radial streamlines. The point where the two corner separations merge has moved toward the hub to about 37% span. Finally, at the largest tip clearance (TC3), the spiral node at the hub of Stator 2 is smaller and only extends to about 23% span. For this tip clearance condition, the Stator 2 surface flow near the tip region shows strong radial streamlines which extend down to about 72% span.

Similar to both Stator 1 and Stator 2, Stator 3 experiences a shift in radial location of losses with increased tip clearance. The hub corner separation decreases in size, indicating the hub is strengthened as the tip clearance increases. Furthermore, the tip region contains large amounts of blockage with significant radial flow apparent in the surface streaklines.

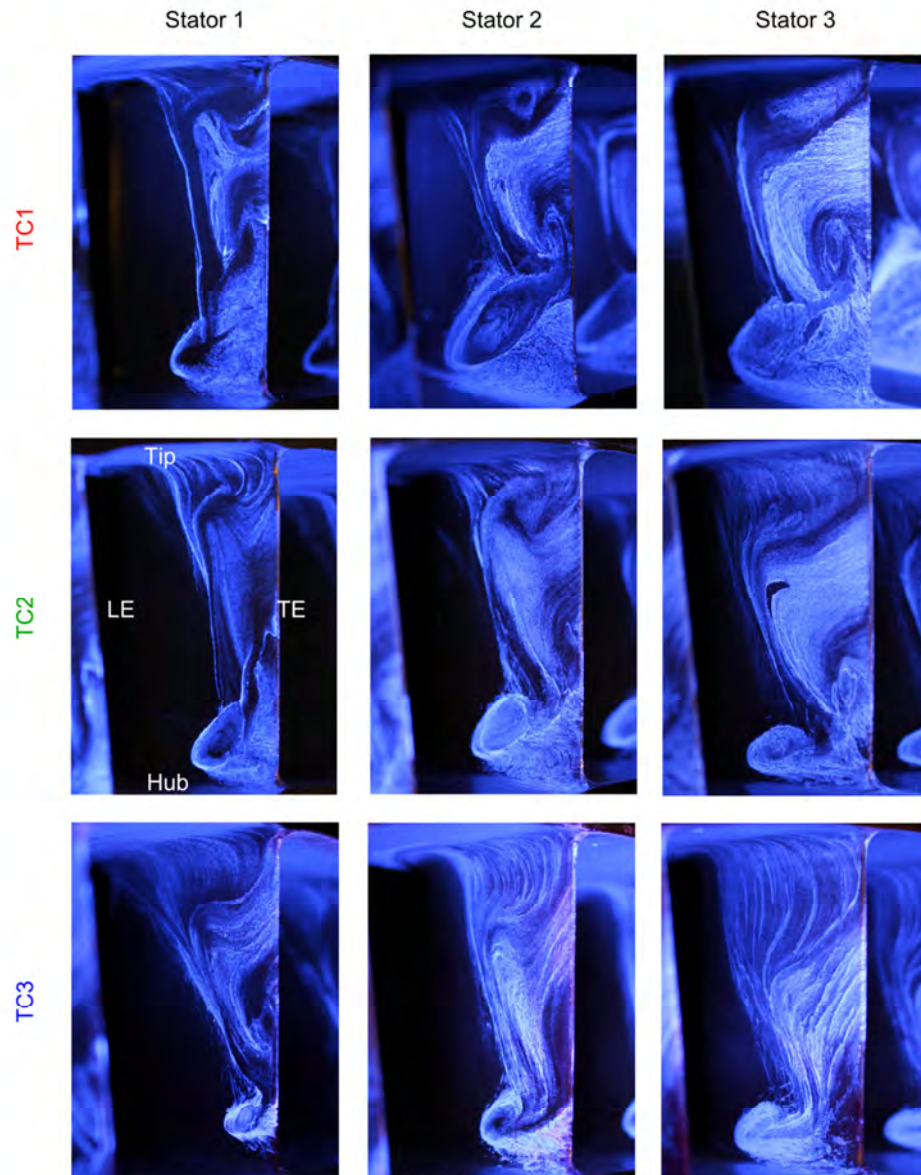


Figure 3.33: Flow visualization of vane corner separations at HL for TC1 (top), TC2 (middle), and TC3 (bottom).

### **3.5. Stator Wake Measurements**

#### **3.5.1. Steady Pressure and Temperature Rake Data**

In addition to the circumferentially-averaged data presented in Section 3.3, the discrete measurements from the total pressure and total temperature rakes have also been considered in the circumferential direction across one vane pitch at the exit of each stator vane row. Beginning with data collected at Stator 1 exit, Figure 3.34 highlights measurements collected at three of the radial measurement positions: 50%, 70%, and 88% annulus height. These data have been normalized by the circumferential average of the data collected at 50% annulus height for each of the tip clearances.

At each of the three loading conditions in Figure 3.34, the Stator 1 total pressure wake shapes at 50% and 70% annulus height are relatively unchanged with tip clearance height. However, there are slight variations in the measurements collected at the 88% span position, where the flow is most directly affected by the tip leakage flow disturbance. At the low loading (LL) condition, the suction side of the wake increases in width at 70% and 88% annulus height.

The Stator 1 Exit wake shapes at nominal loading (NL) appear unaffected by rotor tip clearance height changes at 50% annulus height. The wake depths and widths at 70% are unchanged, but there is a slight decrease of pressure rise off the pressure surface edge of the vane – an effect which is greatest between the TC2 and TC3 tip clearance configurations. At this loading condition, however, the greatest effect is at 88% annulus height, where the change of rotor tip clearance from TC1 to TC3 shows a decrease of the normalized wake shape off the suction surface (near 40% vane passage) on the order of one percent.

At the high loading (HL) condition, the Stator 1 data in Figure 3.34 also show the thickness and minimum normalized pressure of the wake regions are unaffected by the change of rotor tip clearance. However, the pressure in the primary throughflow at 88% annulus height shows a constant offset in the section off the suction surface of the vane. The one percent change observed in the small circumferential region from 30 to 50% vane passage at NL extends across the rest of the vane passage at the HL condition.

The normalized total temperature behind Stator 1 in Figure 3.34 shows the accumulation of high total temperature fluid off the pressure surface of the vanes. This region represents the fluid from the rotor wake which collects on the stator pressure surface, as described by Kerrebrock and Mikolajczak (1970). This same effect has been previously documented at the baseline tip clearance, TC1, by Key (2014). At the LL and NL conditions, Figure 3.34 shows no discernable change of the normalized circumferential total temperature distribution. However, the HL condition shows an increase of the peak normalized total temperature in the region off the vane pressure surface (associated with rotor wake fluid) with increased rotor tip clearance – the most significant of which is observed at 70% annulus height.

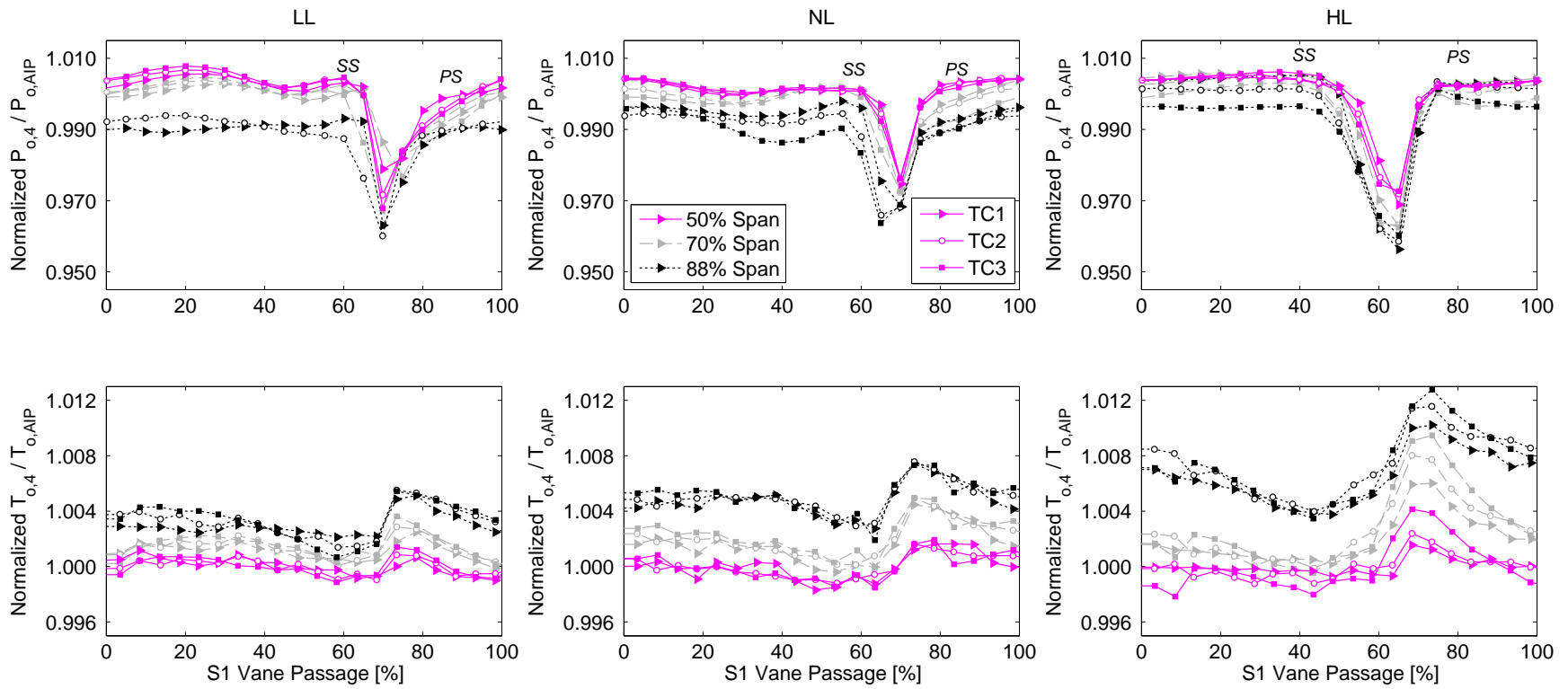


Figure 3.34: Stator 1 total pressure wakes and pitchwise total temperature distribution.

Measurements comparing total pressure and total temperature rake data are also included at Stator 2 exit for three rotor tip clearance configurations and three loading conditions, Figure 3.35. Whereas the Stator 1 exit results showed minimal effect at the LL operating condition, Stator 2 displays a more significant impact at the 88% measurement location: a nearly constant pressure across the bulk throughflow at 88% for TC1 develops into a pressure trough extending approximately 60% vane passage at a maximum depth of approximately two percent with respect to the bulk throughflow. The total temperature variations observed at HL for Stator 1 exit data are not present for the Stator 2 exit data.

The circumferential variations of Stator 3 exit pressures and temperature are shown in Figure 3.36. As with Stator 2, the most distinct effect of the pressure wake shapes with rotor tip clearance changes is observed at the low loading (LL) condition. At this condition, the increase from TC1 to TC2 creates a depression on the order of one percent with respect to the bulk throughflow, in a circumferential region extending across the majority of the throughflow area. In contrast, the increase from TC2 to TC3 shows the same depression depth, but the location of minimum pressure has moved approximately 20% vane passage toward the vane pressure surface.

Similar to the other stators, the Stator 3 results in Figure 3.36 show circumferential total temperature distributions which are largely unaffected by increased rotor tip clearance at LL and NL. At the high loading (HL) condition, there is an increase of normalized total temperature across the entire circumference at 88% span; this observation is in contrast to the slight increase of the peak rotor fluid accumulation which was observed only near the pressure surface of Stator 1 (and most significantly at 70% span), and the Stator 2 measurements which were largely unaffected by rotor tip clearance.

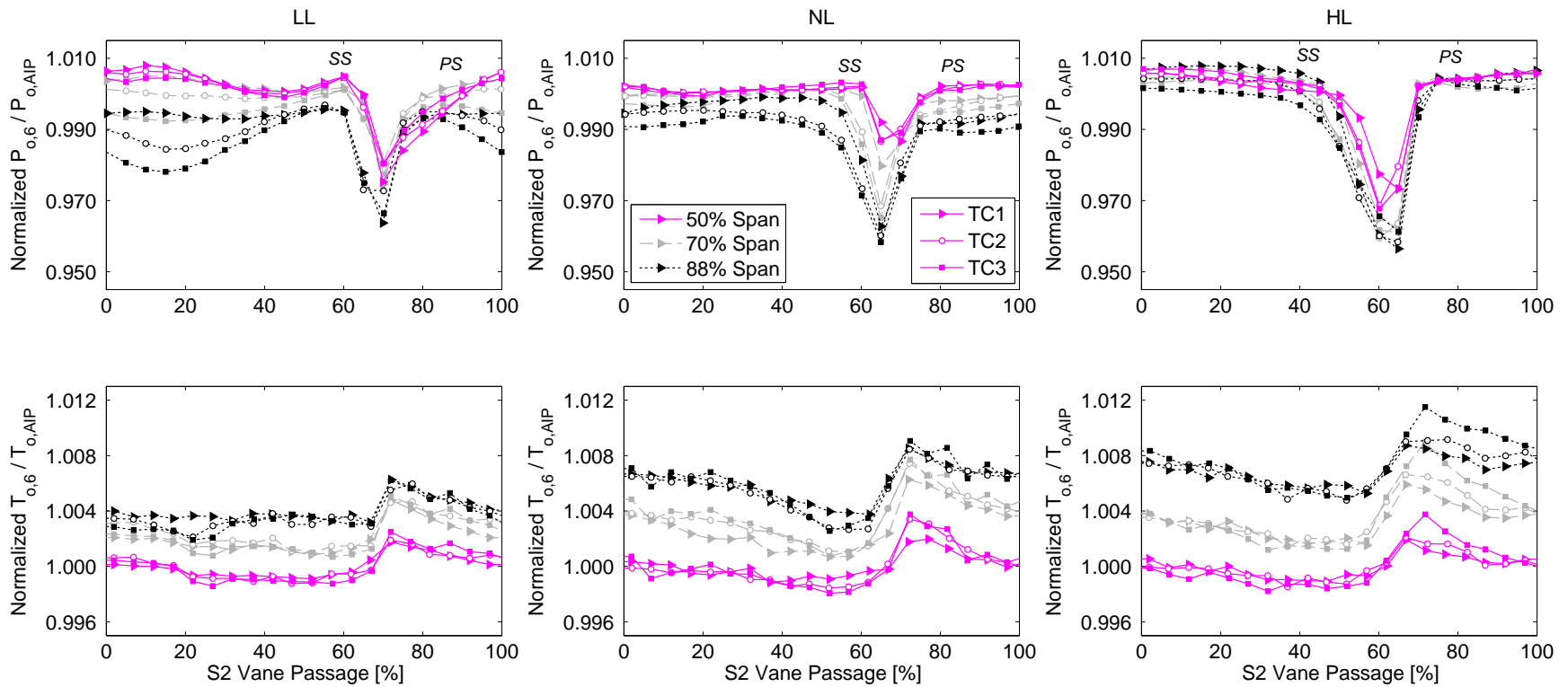


Figure 3.35: Stator 2 total pressure wakes and pitchwise total temperature distribution.

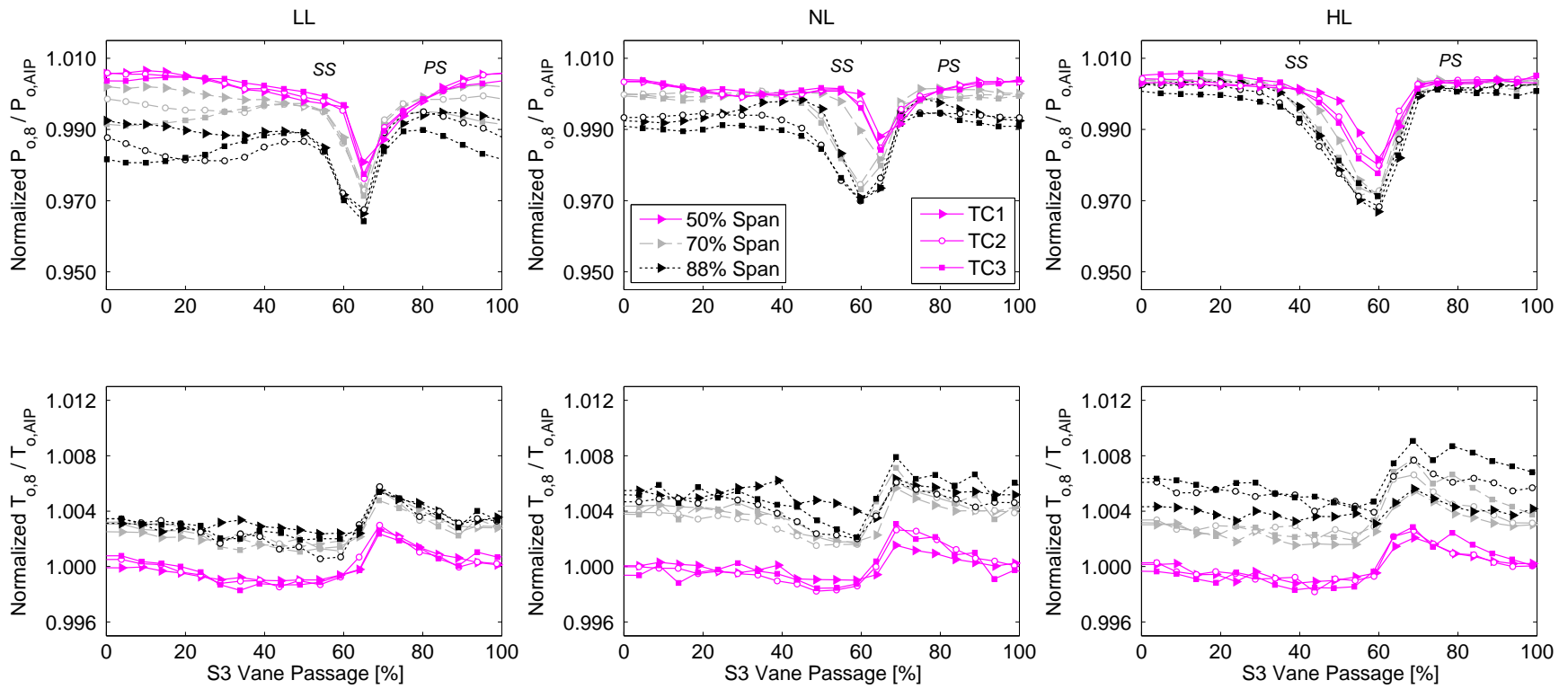


Figure 3.36: Stator 3 total pressure wakes and pitchwise total temperature distribution.

### 3.5.2. Detailed Steady Total Pressure Traverses

To supplement the measurements collected downstream of the stator vanes using the total pressure rakes, a series of detailed traverses were conducted with a miniature Kiel head total pressure probe. These measurements consisted of up to 30 radial plunge positions (at least four times the resolutions from the rake), with an emphasis on capturing the flow features in the endwall regions, as well as a higher resolution of 25 pitch-wise positions with respect to the stationary vanes. Due to the long-duration runs required for this measurement technique, these detailed measurement campaigns were conducted at the exit of each of the three stator vane rows, at two loading conditions (NL and HL), for the smallest and largest tip clearance configurations (TC1 and TC3).

As alluded to by the radial profiles in Section 3.3.1, an increase rotor tip clearance height has the effect of producing increased blockage due to the leakage flow disturbance in the outer regions of the annulus. This corresponding redistribution of mass flow from the tip region toward the hub region unloads the hub region of the downstream stator to reduce the wake thickness in the lower region of the annulus and reduce the corner separation regions in the hub corner, as shown in Section 3.4. However, the reduced flow in the tip region leads to increased flow separation at the outer diameter of the stator vane. For measurements collected at Stator 1 exit for a nominal loading (NL) condition, Figure 3.37 shows this slight decrease of wake thickness at approximately 30% annulus height as the rotor tip clearance is increased from TC1 to TC3. In this same figure, the reduction of flow (and corresponding reduced total pressure) in the tip region is also apparent due the presence of the leakage flow from Rotor 1.

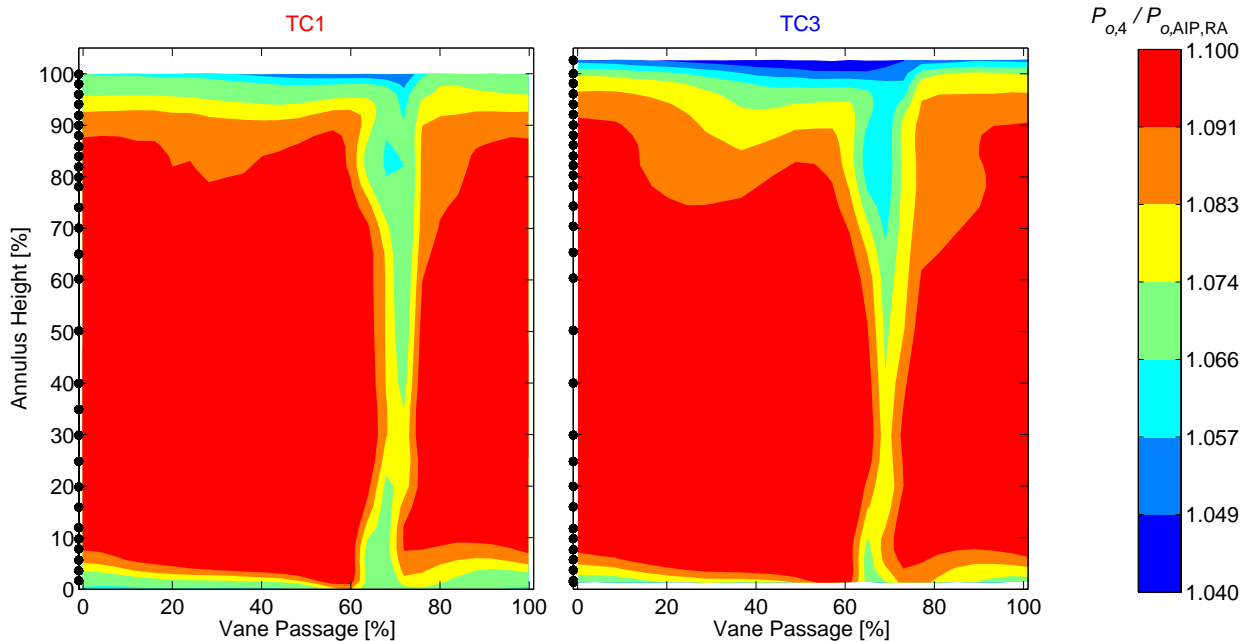


Figure 3.37: Detailed total pressure traverses at Stator 1 exit, NL.

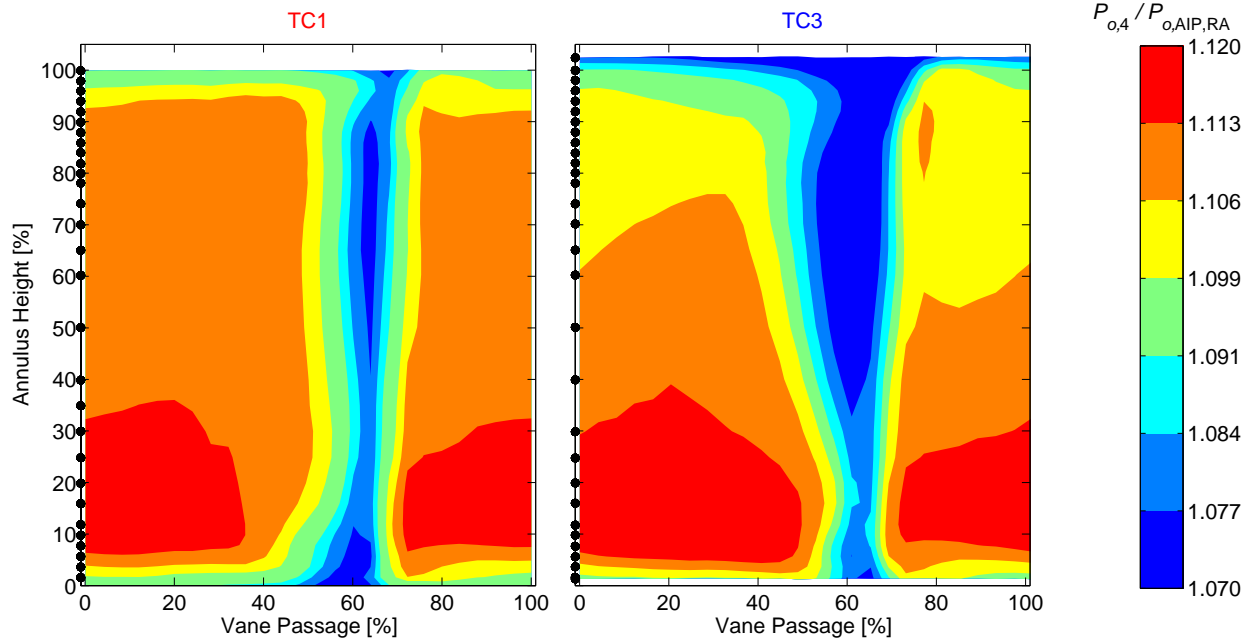


Figure 3.38: Detailed total pressure traverses at Stator 1 exit, HL.

For the same Stator 1 exit measurement plane, but at a high loading (HL) operating condition, Figure 3.38 portrays this same, but more noticeable effect. At this position closer to the stall point, the lower 30% of the annulus shows a benefit from the increased tip clearance, but the outer 70% annulus height presents a significant increase of stator wake width and depth. In this figure, the bulk flow outside the wake also shows a significant decrease of total pressure rise extending down to approximately 70% annulus height.

Similar comparisons can also be made between two tip clearance configurations at the exit of Stator 2. At the NL operating condition, Figure 3.39 shows a significant decrease of total pressure in the tip region as the increased tip leakage disturbance from Rotor 2 is ingested by the stator vane. The compounding effect of the increased tip clearance height is displayed by this embedded stage, making it more difficult to directly compare contour levels between the two tip clearance configurations. However, the effect of the increased blockage appears to affect the flow most significantly in the outer 20% of the annulus height.

At the high loading (HL) condition at Stator 2 exit, Figure 3.40, the most noticeable effect of the increased tip clearance height is observed. Referring back to the radial total pressure profiles at this same operating condition, Figure 3.22, a distinct shape difference is observed for the change from TC1 to TC3. The data in Figure 3.40 show that TC1 exhibits a significant hub corner separation at this high loading condition which extends up to approximately 30% annulus height; however, the wake thickness remains relatively constant across the remainder of the annulus. As the rotor tip clearance height is increased, the redistribution of mass flow from the tip toward the hub region has the expected result of energizing the hub region and decreasing the likelihood of flow separation, thereby reducing the hub corner separation zone. However, this benefit comes at the expense of a drastic increase of wake thickness, as observed for the upper 50% annulus height.

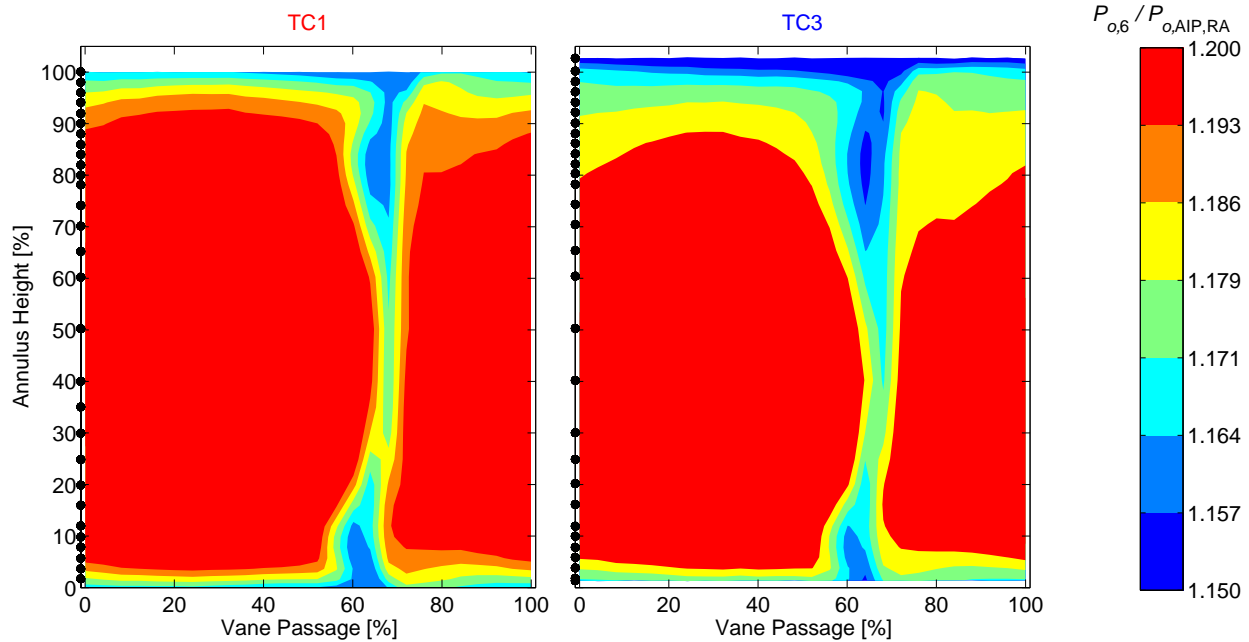


Figure 3.39: Detailed total pressure traverses at Stator 2 exit, NL.

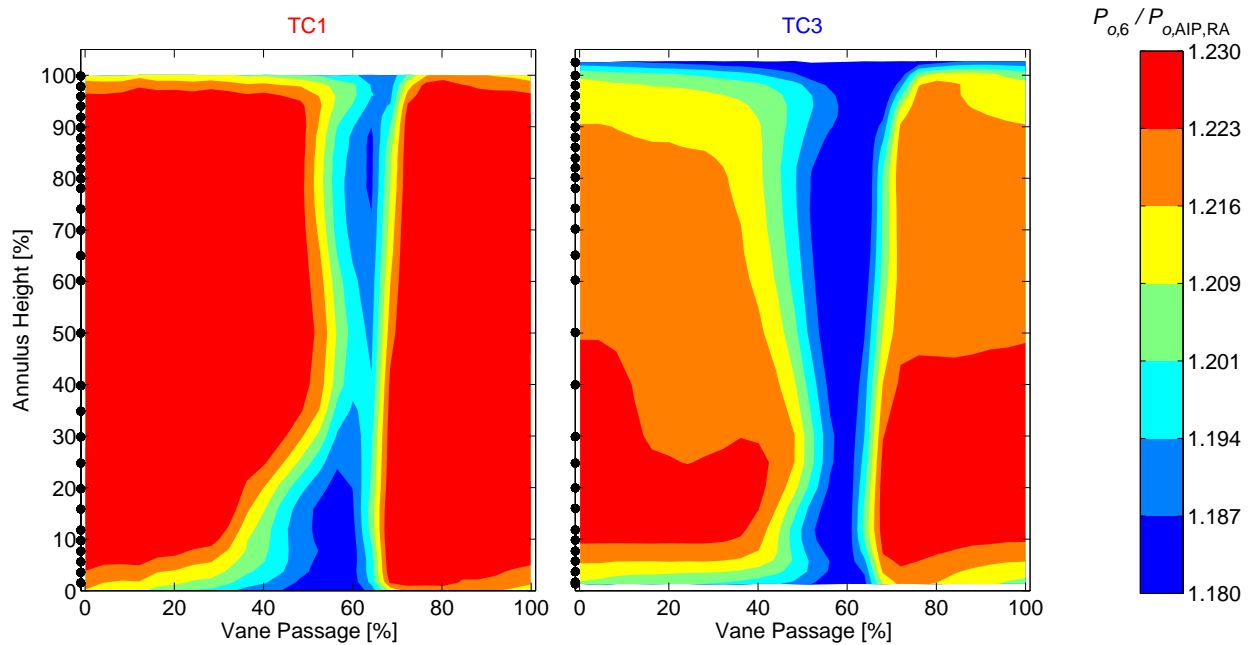


Figure 3.40: Detailed total pressure traverses at Stator 2 exit, HL.

The detailed total pressure measurements collected at Stator 3 exit are also shown for the same NL and HL operating conditions on the 100% corrected speedline in Figure 3.41 and Figure 3.42, respectively. At the high loading condition, Figure 3.42, the TC1 rotor tip clearance configuration exhibits the thickest wake of all three stators (relatively), but with the shallowest

depth (see also Figure 3.36). As the tip clearance is increased to TC3, the observed effect is the same for Stator 3 as it was for the other two vane rows: the hub region (up to approximately 30% annulus height) shows a decreased wake thickness, but the outer 70% annulus height is negatively affected by the decreased flow in the tip region that has been redistributed toward the hub.

In addition to the high resolution of measurements, the increased quantity of data points from these detailed radial traverses provide the ability to compare with the calculated total pressure ratio determined from the seven-element total pressure rakes. On average, the total pressure ratios calculated as an area average of the detailed radial traverse data agree with the values calculated from the pressure rakes within 0.04%, less than one-fourth of the uncertainty for the total pressure ratio.

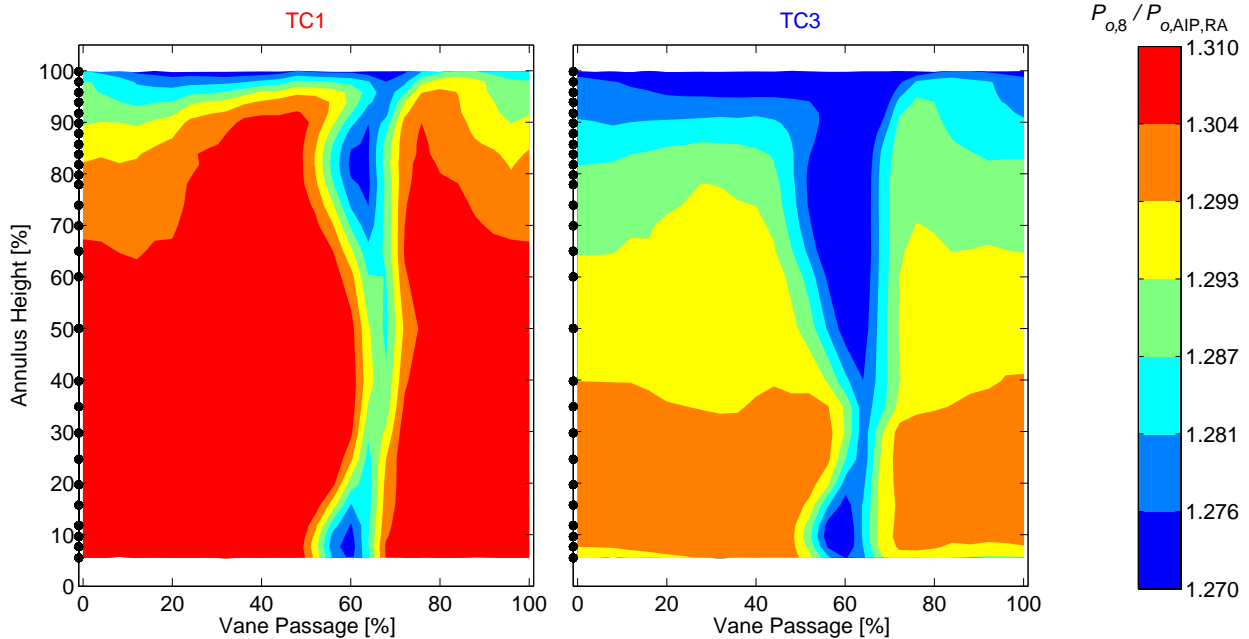


Figure 3.41: Detailed total pressure traverses at Stator 3 exit, NL.

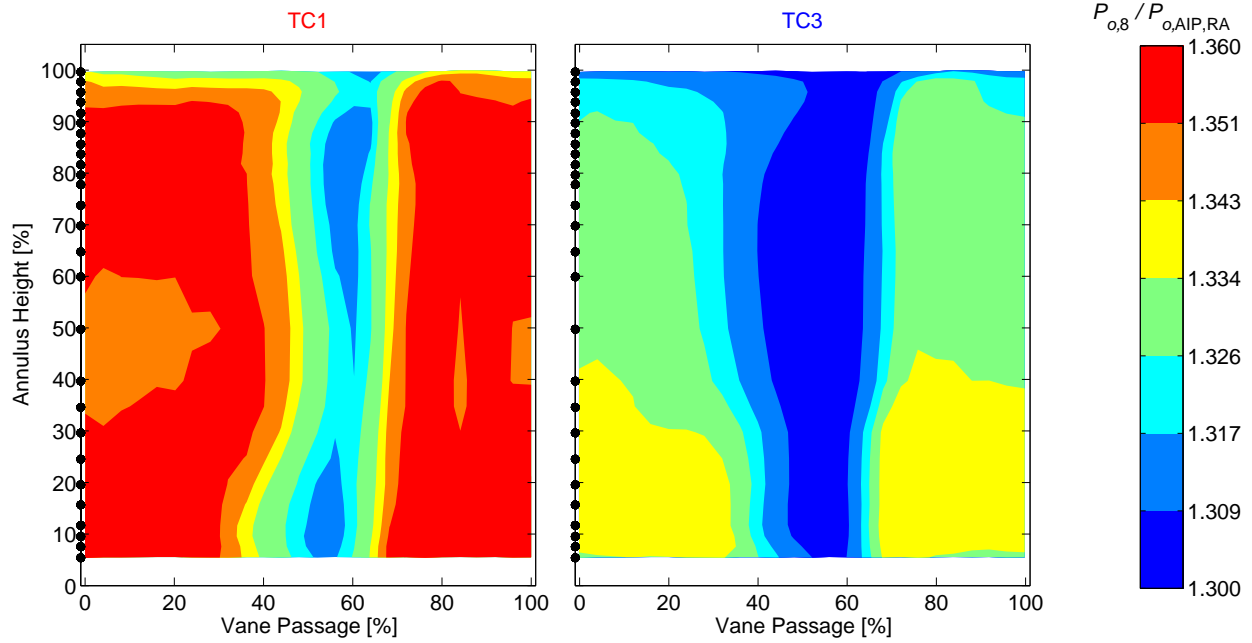


Figure 3.42: Detailed total pressure traverses at Stator 3 exit, HL.

# CHAPTER 4: CHARACTERIZATION OF COMPRESSOR STALL INCEPTION

*Reid A. Berdanier, Natalie R. Smith, Anna M. Young, and Nicole L. Key*

## **4.1. Measurement Technique**

For this study, the stall inception mechanism for the compressor was systematically assessed for each of the three tip clearance configurations. In addition to the four corrected speedlines shown in Figure 3.1, the compressor stall behavior was also investigated for the 60% and 52% corrected speedlines. In each case, the stall point was determined by closing the throttle in incremental steps to slowly increase the loading of the compressor. At the onset of stall, a human-interface control mechanism was initiated to open the throttle and allow recovery to a stable operating condition. This process was repeated several times to determine a representative average of corrected mass flow rate and total pressure ratio for each test case. The previous statements regarding uncertainty of mass flow rate and overall total pressure ratio apply for these measurements as well. For a given operating speed and tip clearance configuration, the compressor was also stalled in up to five different vane positions with respect to the stationary instrumentation to develop a representative average for the overall map. During the stall inception tests, the full set of inter-stage measurement rakes was removed and only the inlet and exit conditions of the compressor (axial measurement planes 0, 1, and 9 in Figure 2.6) were monitored for overall pressure rise information.

To detect the formation of stall events in the compressor, a series of high-frequency response Kulite XTL-140 pressure transducers were installed throughout the compressor. These piezoresistive pressure transducers each have an outer diameter of 0.101 in. with a threaded mounting system to accommodate insertion and removal at several unique positions. As with the other fast-response pressure transducers used in this study, these XTL-140 sensors also featured a standard protective B-screen, reducing the natural frequency of the sensor to approximately 20 kHz. For these stall tests, six circumferentially-distributed sensors were positioned approximately 15% axial chord upstream of each rotor blade row, following the design outlined by Houghton and Day (2010), for 18 total sensors. The measurements from these sensors were collected through the same data acquisition chain described in Section 2.5.1.

## **4.2. Stall Inception Analysis**

Over the years, researchers (McDougall et al., 1990; Day, 1993) have identified two different stall inception mechanisms in axial compressors. The first type, modal oscillations, or “modes,” represents long length-scale disturbances which affect the entire compressor. These modal oscillations are often observed for some time prior to the definitive stall point for the compressor. The second type, “spikes,” appears as a short length-scale disturbance which develops as a result of a localized stalling, typically in one blade row. These spike signals may appear in high frequency response data collected from hot-wire velocity measurements or dynamic pressure transducers.

Camp and Day (1998) continued the discussion of these stall inception types and developed a model for predicting the stall inception mechanism of a given compressor, based on the shape

of the total-to-static pressure rise characteristic for the machine. These authors concluded modal stall inception characteristics are expected to appear if the compressor reaches a peak total-to-static pressure rise prior to entering stall (i.e., a zero slope condition). On the other hand, if the compressor stalls prior to reaching a peak total-to-static pressure rise value, the corresponding stall inception mechanism will likely be a spike-type stall event.

The total-to-static pressure rise characteristics are shown for the Purdue three-stage compressor, with each of three tip clearance configurations at four operating speeds, in Figure 3.10. The characteristics in this figure show that there are three lines which potentially show a peak value has been reached: the 100% corrected speedlines for TC1 and TC2, and the 90% corrected speedline for TC1. Based on the model presented by Camp and Day (1998), it is expected that these three speedlines are the most likely candidates to portray modal stall inception traits. The other nine speedlines all appear to be continuing to rise at the stall point (the lowest flow rate point on each line) – typical signs of spike-type stall inception.

Beyond the predictive capabilities of the characteristics in Figure 3.10, dynamic static pressure traces at several of these operating conditions are presented. First, measurements collected with the baseline tip clearance (TC1) are shown for the 100% corrected speedline, Figure 4.1. This figure presents the offset dynamic pressure traces collected at each of the eighteen locations around the compressor (six circumferentially-distributed sensors at each rotor). As expected from the total-to-static characteristic, this speed and tip clearance configuration exhibits modal stall inception traits. Of note, the long length-scale disturbances are observed for several rotor revolutions prior to the onset of stall (approximately identified by the zero location on the abscissa). Tracking these “modal” oscillations through the compressor shows the mode speed is approximately one-fourth of the rotor rotational speed. At the onset of stall, the stall cell rotates at approximately one-half the rotor rotational speed.

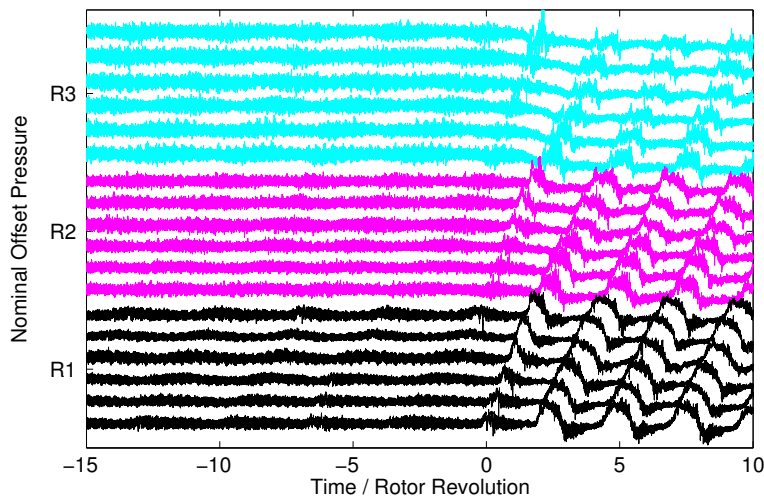


Figure 4.1: Dynamic pressure traces at the inception of stall for TC1 at 100%  $N_c$ .

Day (1993) showed that a change of rotor tip clearance may affect the stall inception mechanism of the machine. As previously discussed, the 100% corrected speed for the intermediate clearance height (TC2) also suggests the existence of modal stall. The dynamic static pressure traces for this speed and tip clearance configuration are presented in Figure 4.2. This figure may show weak long length-scale modal propagations (also at a rotational rate on the

order of one-fourth the rotor speed) in the measurements upstream of Rotor 1, as suggested from the total-to-static pressure rise characteristic. However, the distinct modal traits from Figure 4.1 are certainly less apparent (and nearly absent in the Rotor 2 or Rotor 3 data). Further, some spikes can also be identified in the Rotor 1 pressure traces. Of note, one spike develops in the first sensor upstream of Rotor 1 at eight revolutions prior to the onset of stall, and it rotates approximately at the rotor rotational speed. The traces in Figure 4.2 confirm Camp and Day's (1998) observations that these two stall inception mechanisms can occur simultaneously in the same machine. In this case, however, Figure 4.2 appears to be dominated more by spikes than the long length-scale modal fluctuations.

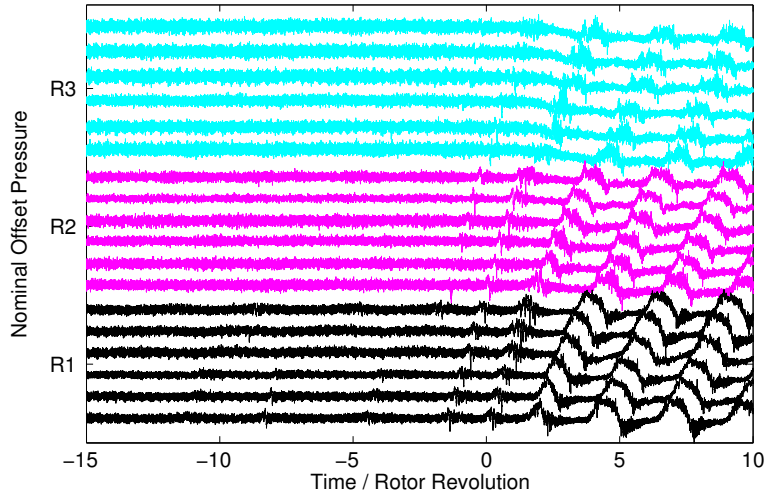


Figure 4.2: Dynamic pressure traces at the inception of stall for TC2 at 100%  $N_c$ .

Hoying et al. (1999) has previously identified that the trajectory of the tip leakage flow approaches a tangential angle as the blade loading increases, influencing the potential for an unstable condition in which the leakage flow may jump upstream of the adjacent rotor blade and cause spike-type stall behavior. This diagnosis from Hoying et al. would predict that the TC3 tip clearance configuration (and possibly also TC2) may display a near-tangential leakage flow trajectory for the near stall operating conditions on the 100% corrected speedline (based on the spikes observed emanating from the Rotor 1 dynamic pressure traces in Figure 4.2, e.g.), whereas the TC1 trajectory would be less inclined due to its modal stall tendencies (Figure 4.1). To investigate this further, dynamic static pressures were measured over Rotor 1 using the removal instrumentation block described in Section 2.5.1. These data were collected at the near stall (NS) operating condition, defined by a position of 5% stall margin using Equation (3.2), as explained in Section 3.1.1. The results are analyzed in terms of root-mean-square (RMS) unsteadiness with respect to the ensemble average:

$$P_{\text{RMS}}(t_i) = \sqrt{\frac{1}{N} \sum_{k=1}^N [P(t_i) - \langle P(t_i) \rangle]^2_k}, \quad (4.1)$$

for which the phase-locked ensemble average (EA) is defined by:

$$\langle P(t_i) \rangle = \frac{1}{N} \sum_{k=1}^N [P(t_i)]_k . \quad (4.2)$$

These NS results, Figure 4.3, show this predicted result by considering the flow field unsteadiness in terms of normalized RMS pressures.

More recent studies continuing the evaluation of spike-type stall inception suggested by Hoying et al. (1999) have suggested the development of spike-type stall may not be strictly dependent on the leakage flow, but rather a radial vortex which develops as a result of leading edge separation (Weichert and Day, 2014; Pullan et al., 2015). It is this radial vortex structure which propagates in front of the adjacent blade and leads to the spike. However, the increased incidence at the tip due to the leakage flow, especially with larger tip clearance heights, as shown in Figure 4.3, is expected to increase the likelihood of such leading edge separation.

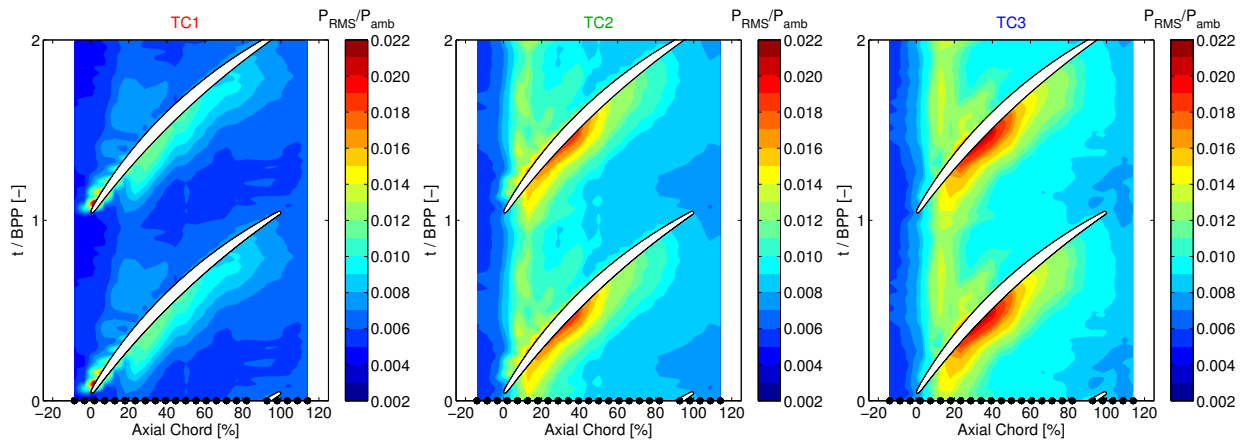


Figure 4.3: Static pressure field unsteadiness over Rotor 1, presented as an RMS with respect to the EA, for each tip clearance configuration at NS.

Considering again the total-to-static pressure rise characteristics for the baseline tip clearance configuration (TC1), Figure 3.10, the 90% corrected speedline also appears to reach a maximum and begin to decrease – a sign of potential modal stall inception traits. The dynamic pressure traces for this case, Figure 4.4, reveal results which are more similar to TC1 at 100% corrected speed than TC2. In particular, Figure 4.4 presents long length-scale modal tendencies which persist through all three rotor rows. However, the spike-type signals are still present in the Rotor 1 pressure traces. Of note, there are spikes propagating from the first sensor of Rotor 1 at 13, 11, and five revolutions prior to the onset of stall, all of which fall in the troughs of the modal waves. Relative to Figure 4.2, these results for TC1 at 90% corrected speed represent more modal stall inception traits than spikes; however, both mechanisms are certainly present for this condition as well.

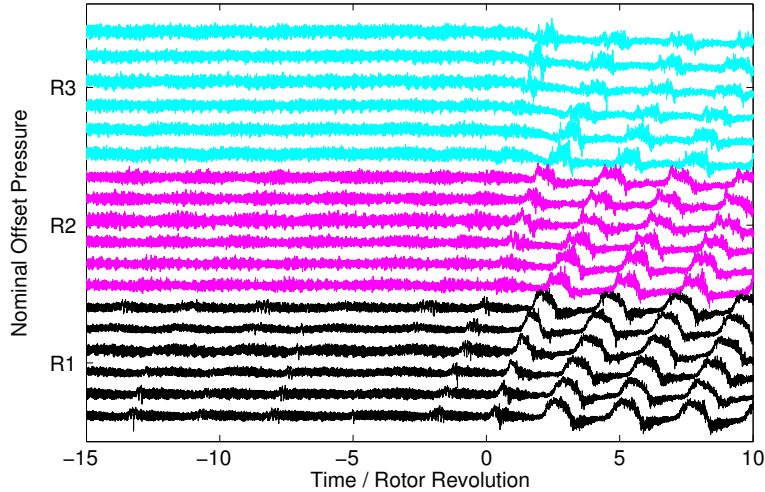


Figure 4.4: Dynamic pressure traces at the inception of stall for TC1 at 90%  $N_c$ .

In contrast with the results presented thus far, the part-speed results for TC1 (68% corrected speed) are shown in Figure 4.5. These dynamic pressure traces are dominated by spike-type stall inception traits propagating from Rotor 1. These spikes travel circumferentially around Rotor 1 at a rate approximately equal to the rotor rotational speed, and they are likely the result of localized separation regions related to high incidence angles for Rotor 1. However, it is interesting to note in this case that it appears to be Rotor 2 which first trips the compressor into stall, suggesting that the rear stages of the compressor could be attempting to “assist” Rotor 1 until they are no longer capable of doing so. The data in Figure 4.5 are shown on the same scale as the previous 100% and 90% speedline traces for consistency. Although it may not be clear from the scale, if the results in Figure 4.5 were shown on a larger scale, modal stall characteristics would still not be present.

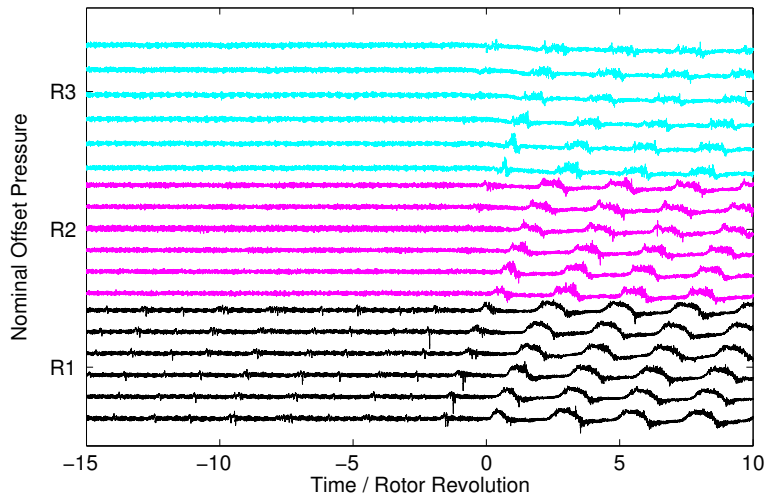


Figure 4.5: Dynamic pressure traces at the inception of stall for TC1 at 68%  $N_c$ .

Although not all of the test cases have been presented here, these four selected results represent the observed trends in the compressor at different speeds and with different tip clearance configurations. A summary of the test cases, Figure 4.6, highlights several regions of a tip clearance vs. speed matrix; the four cases presented thus far are noted by black dots in Figure 4.6. As suggested by Figure 3.10 and shown in Figure 4.1, the 100% corrected speedline for TC1 portrays distinctly modal stall inception traits. This test case is representative of the original design conditions for the compressor, suggesting the compressor is likely well-matched, and it stalls via long length-scale perturbations. The 90% corrected speedline for TC1 and the 100% corrected speedline for TC2 exemplify a transitional range away from the distinct modes to also incorporate spike-type stall inception traits. Ultimately, though, the compressor exhibits clear spike-type stall inception mechanisms (i.e., Figure 4.5) for the conditions which depart most significantly from the original design intent of the machine.

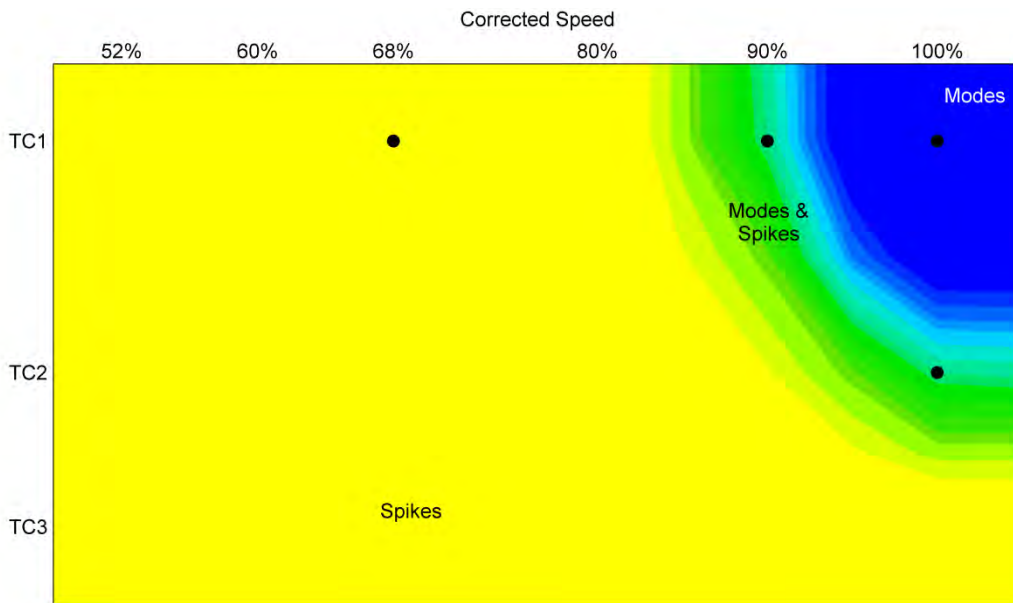


Figure 4.6: Summary of stall inception trends for all tip clearance configurations at all investigated operating speeds.

# CHAPTER 5: TIME-RESOLVED FLOW FIELD MEASUREMENTS

Reid A. Berdanier and Nicole L. Key

## 5.1. Over-Rotor Static Pressures

The tip leakage flow trajectory can be tracked using the dynamic static pressure measurement system described in Section 2.5.1. These data have been collected at a sampling frequency of 100 kHz with a low-pass filter cut-off frequency of 40 kHz for a total of 500 revolutions, as defined by the 1/rev signal from the laser tachometer. The large number of revolutions makes it possible to represent an average flow field using the phase-locked ensemble averaging (EA) technique:

$$\langle P(t_i) \rangle = \frac{1}{N} \sum_{k=1}^N [P(t_i)]_k, \quad (5.1)$$

defined for each revolution  $k$  and each time  $i$ . Using Equation (5.1), the ensemble average static pressure field over Rotor 1 at NL is shown for each of the three tip clearance configurations in Figure 5.1. The data presented in Figure 5.1 represent a mean rotor tip flow, calculated by dividing the ensemble-averaged signal into the 36 separate rotor blade passages, and averaging across the 36 passages. This average result is shown twice, assuming periodicity, to more easily discern the applicable flow features. Also in Figure 5.1, the axial position of the utilized sensors is shown at the bottom of each figure as a series of black dots. For these initial comparisons, the data were collected at one position with respect to the upstream and downstream vane rows. However, these static pressure data were all collected at the same position with respect to the stator vanes and the measurement location was selected to ensure that the sensors were not positioned in the wake from the upstream stator vane. Further consideration is given to the variability of the tip leakage flow due to interaction with the stationary vane rows in the next section.

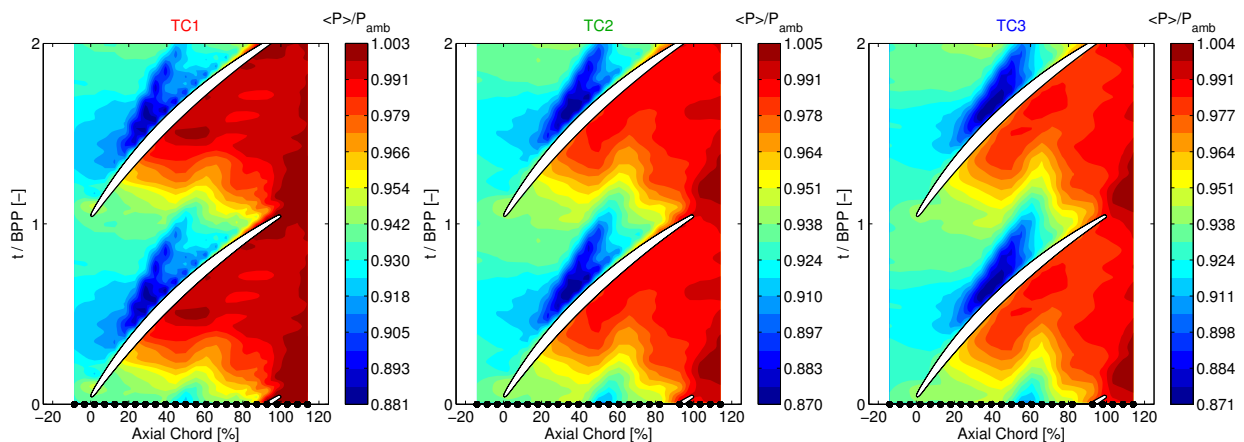


Figure 5.1: Ensemble-average static pressure field over Rotor 1 for each tip clearance configuration at NL.

The phase-locked ensemble average data in Figure 5.1 identify a low pressure region, representing the tip leakage flow. However, the leakage flow trajectory becomes less distinct downstream of approximately 60% axial chord. As an alternative method for identifying the leakage flow path, previous authors have also used the root-mean square (RMS) unsteadiness with respect to the ensemble average:

$$P_{\text{RMS}}(t_i) = \sqrt{\frac{1}{N} \sum_{k=1}^N [P(t_i) - \langle P(t_i) \rangle_k]^2} \quad (5.2)$$

This definition of RMS unsteadiness provides the ability to more definitively identify regions of pressure fluctuation. For example, the same data from Figure 5.1 (previously presented as an ensemble average) are recast in terms of the RMS with respect to the ensemble average in Figure 5.2. This figure shows that the RMS definition provides the capability to more easily distinguish the tip leakage flow trajectory up to nearly 80% axial chord.

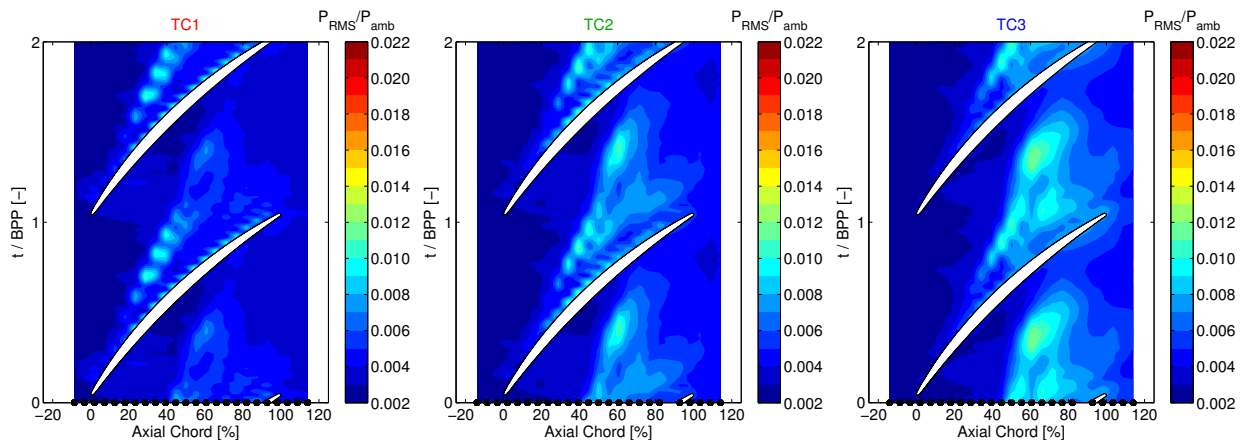


Figure 5.2: Static pressure field unsteadiness over Rotor 1, presented as an RMS with respect to the EA, for each tip clearance configuration at NL.

Similar to the data presented at NL, an ensemble-average of the static pressure field over Rotor 1 at a high loading (HL) operating condition is shown in Figure 5.3 for each tip clearance. Compared to the NL results, these HL data show that the tip leakage flow region has increased its trajectory angle across the rotor passage, as expected from the increased incidence angle on the rotor and the increased pressure difference across the blade tip. Initially, there is no discernable difference in the trajectory angle between these tip clearance configurations in Figure 5.3, although the RMS with respect to the ensemble average can again be used to more easily track the leakage flow trajectory across the rotor passage.

These RMS data, Figure 5.4, highlight flow patterns at the high loading operating condition which are not clearly observable in the ensemble average results of Figure 5.3. Of note, the trajectory angle of the tip leakage flow increases as the tip clearance height increases from TC1 to TC3. This observed trend can be attributed to the fact that the HL conditions for the three tip clearances represent positions which are at varying positions with respect to the stall point, as

discussed in Section 3.3.1. In particular for the TC3 tip clearance configuration, Figure 5.4 shows the leakage flow is approaching a tangential angle.

At the HL operating condition shown in Figure 5.4, the larger tip clearance configurations (TC2 and TC3) show regions of large unsteadiness (RMS) where the tip leakage flow disturbance impinges on the adjacent blade. These data do not provide a definitive explanation for whether or not this machine displays the “double-leakage” discussed by Khalsa (1996). However, there is reason for speculation, particularly related to the region of high flow unsteadiness on the suction side of the rotor blade in the region of 30 to 60% axial chord for TC2 and 20 to 50% axial chord for TC3. An advanced data collection campaign implementing non-intrusive measurements techniques (such as the PIV methodologies introduced in this project) inside the blade passage could provide more insight into this phenomenon.

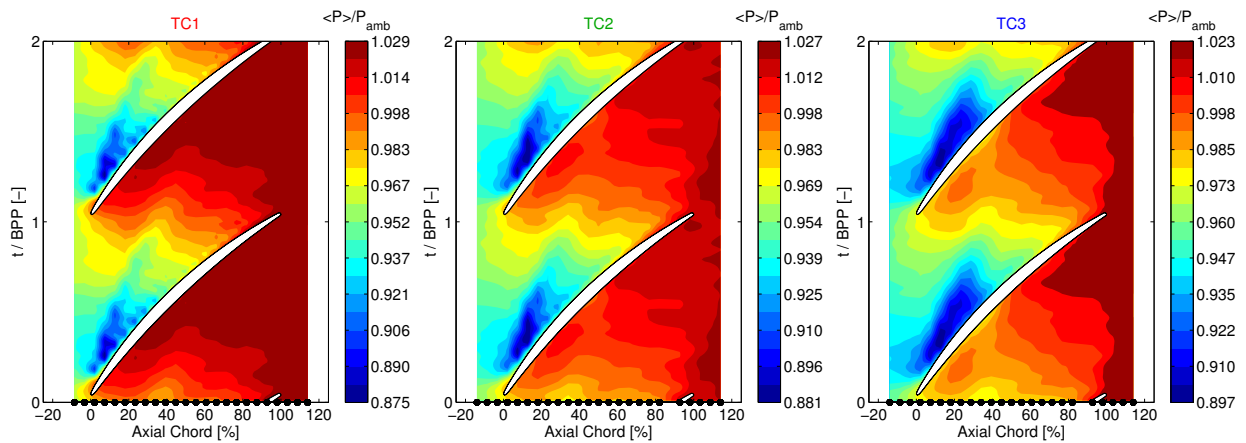


Figure 5.3: Ensemble-average static pressure field over Rotor 1 for each tip clearance configuration at HL.

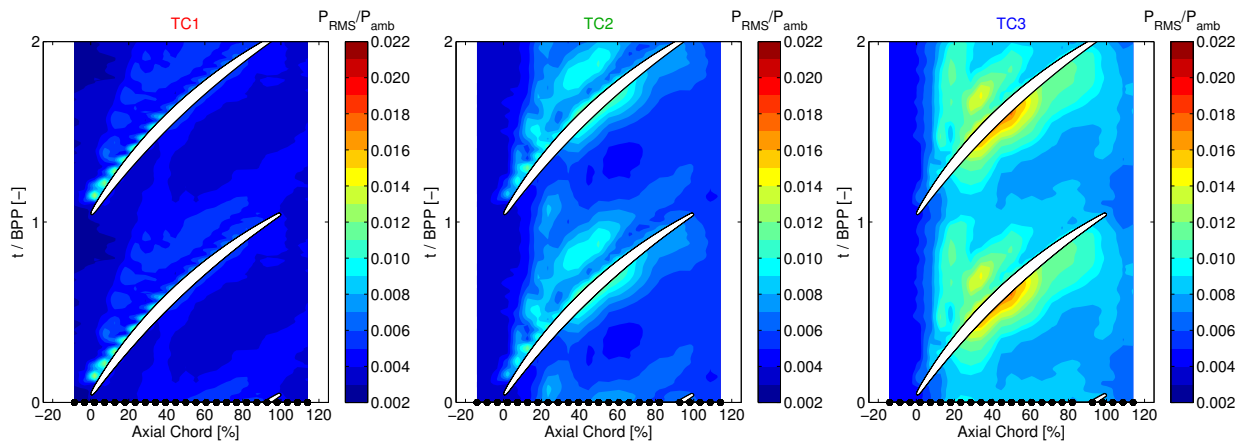


Figure 5.4: Static pressure field unsteadiness over Rotor 1, presented as an RMS with respect to the EA, for each tip clearance configuration at HL.

Using the RMS pressures shown in Figure 5.2, Figure 5.4, and a similar figure for the low loading condition, the effect of the tip leakage flow trajectory on loading condition and tip clearance height can be determined. These trajectories, shown in Figure 5.5, have been identified as the locus of the peak RMS values. The comparison for these trajectories has been specifically selected for the Rotor 1 data because they represent comparisons of tip leakage flow trajectories which are less affected by upstream flow conditions. In all cases, Rotor 1 experiences the same “clean” inlet flow exiting the IGV, whereas the rotors in the aft stages of the compressor experience more variability due to ingestion of the upstream flow disturbances.

For the two high flow rate conditions, NL and LL, Figure 5.5 shows an increase of tip clearance height has the effect of moving the leakage flow trajectory closer to the blade suction surface. This figure also more clearly reveals a non-linear (“kinked”) leakage flow trajectory, which is especially apparent for the TC3 tip clearance configuration at the high flow rate conditions, LL and NL. This observation was also noted by Yoon et al. (2006) near mid-chord, but the results shown here represent a less drastic turn of the leakage flow than was observed by those authors. Chen (1991) theoretically predicts this non-linear trajectory, but not until the end of the passage, where the image vortices required to satisfy kinematic constraints change with the absence of the blade as an effective wall.

In addition to these observed trends at high flow rate operating conditions, Figure 5.5 also depicts a noticeable change of the leakage flow trajectory concavity at the high loading condition as the tip clearance height increases. The discussion of Figure 5.4 noted the change of the flow angle between the three tip clearance configurations, but the locus of peak RMS values shows the two larger tip clearance heights turn more noticeably toward the adjacent blade. It is likely that this observed change of flow trajectory path is also due to the relative proximity of the HL points to the stall condition with different tip clearance heights.

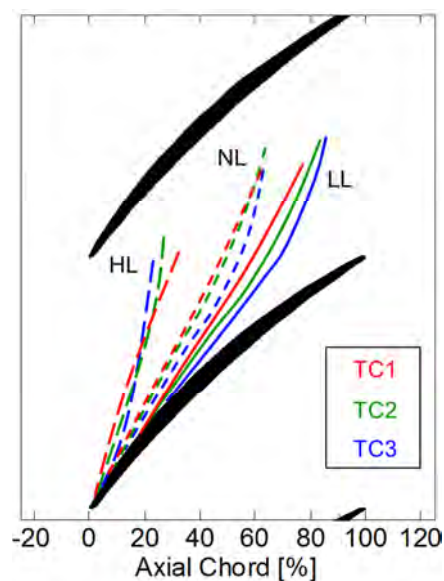


Figure 5.5: Rotor 1 tip leakage trajectories for all three tip clearance configurations at three loading conditions on the 100% corrected speedline.

The over-rotor static pressure fields presented thus far have compared the results for one rotor with three tip clearance heights. In contrast, Figure 5.6 shows the RMS unsteadiness of the static pressure field over each of the three rotor rows at the NL condition for TC2. As with the Rotor 1 results shown above, these figures represent a mean flow field, for which the data have

been separated into the number of blades in the row (36, 33, or 30 for Rotor 1, Rotor 2, and Rotor 3, respectively) and subsequently averaged. These averaged data are then repeated (assuming periodicity) to more clearly distinguish the flow features in the blade passages.

In Figure 5.6, a clear distinction can be made between the data for Rotor 1 and the data for the Rotor 2 or Rotor 3. As shown above in Figure 5.5, the trajectory of the Rotor 1 tip leakage flow is non-linear, but this is less present in Rotor 2 or Rotor 3. Furthermore, the Rotor 2 and Rotor 3 results portray a wider region of high flow unsteadiness (RMS), indicating a different shape of the leakage flow at these positions.

In the same manner, Figure 5.7 shows the RMS unsteadiness over each rotor for TC2 at HL. As with the nominal loading condition, a clear distinction can be drawn between the Rotor 1 data and the results for Rotor 2 or Rotor 3. Although the angle of the leakage flow trajectory is similar for the three rotors, a wider region of high flow unsteadiness is present for the Rotor 2 and Rotor 3 results, representing a larger leakage flow disturbance for these rotors.

The measurements in the fixed frame of reference for the data in Figure 5.6 and Figure 5.7 are nearly identical in position with respect to the upstream stator vane row and the associated low-pressure wake region. Thus, the results in these figures further emphasize the differences measured over Rotor 1, which always ingests the same clean inlet flow from the IGV, compared to the latter Rotor rows, which are subject to flow disturbance ingestion from the upstream rotor rows and, in particular, the affected flow in the outer region near the rotor tip.

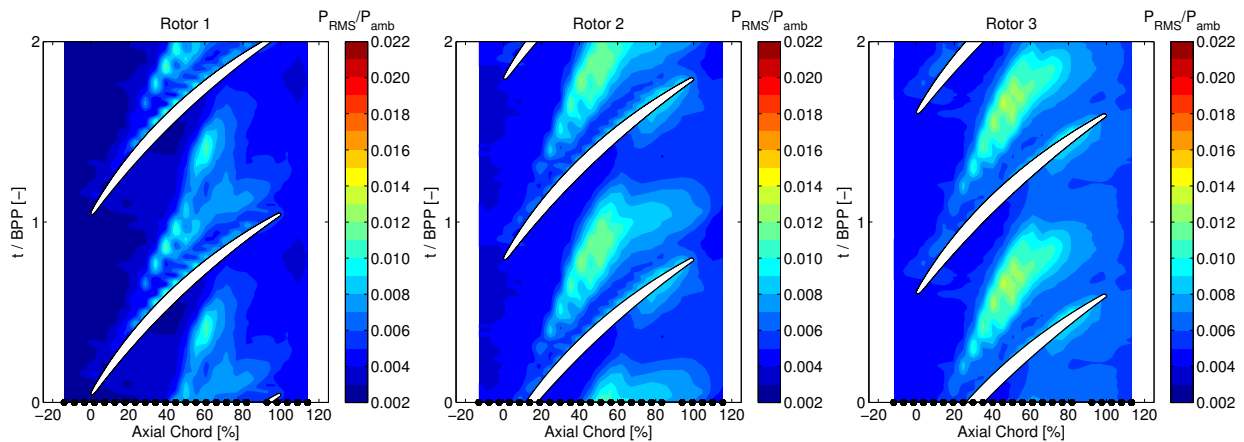


Figure 5.6: Static pressure field unsteadiness, presented as an RMS, over each rotor for TC2 at NL.

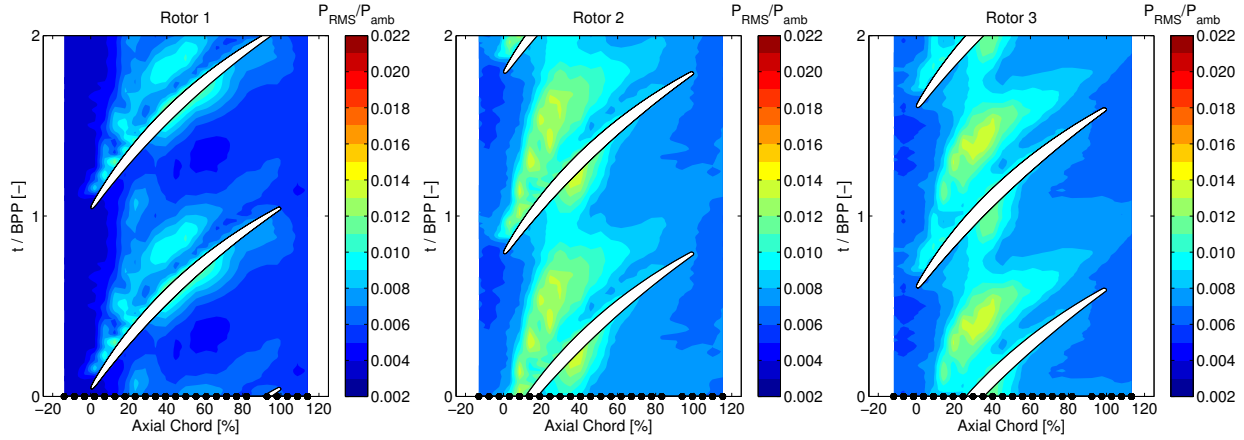


Figure 5.7: Static pressure field unsteadiness, presented as an RMS, over each rotor for TC2 at HL.

## 5.2. Influence of Stator Wakes on Leakage Flow

The wealth of data presented so far for this project have suggested the loading condition of the compressor can affect the overall influence of the tip leakage flow. In particular, the over-rotor static pressure field time series in Section 5.1 above showed the trajectory of the leakage flow through the rotor passage changes significantly as the compressor loading is increased toward stall. With this understanding, the rotor tip leakage flow can also be noticeably affected by position with respect to the upstream stator vane row.

In the wake of a stator vane (i.e., Stator 1), the absolute velocity deficit creates a corresponding increase of incidence into the downstream rotor row (i.e., Rotor 2). The local increase of incidence angle loads up the front of the rotor, affecting the strength and trajectory of the tip leakage flow. As a result, the location of the probe in the stationary frame of reference will dictate whether or not the measured flow parameter (pressure, velocity, etc.) will be affected by the rotor passing through the upstream vane wake.

This phenomenon is illustrated in Figure 5.8 with respect to the rotor passing through the upstream stator wake. In Figure 5.8(a), the rotor leading edge (Rotor 2, in this case) is positioned between stator wakes, and a corresponding velocity triangle is shown. At this location, the leakage flow propagates through the rotor passage and is measured by a series of probe locations at the rotor exit plane. In Figure 5.8(b), the rotor leading edge is located in the wake of the upstream stator, and the associated velocity triangle appears as a deficit of velocity in the absolute frame of reference. In this case, as the rotor loading increases, the leakage flow region increases in size, and the trajectory changes as its inception point moves upstream toward the rotor leading edge.

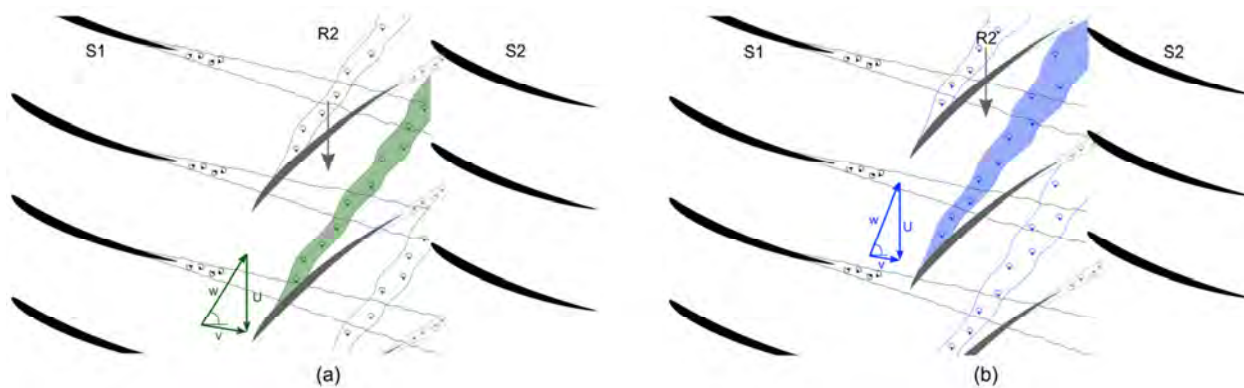


Figure 5.8: Schematic of the interaction between rotor tip leakage flow and upstream stator wake. (a) R2 passing in the middle of the S1 passage, (b) R2 passing through the S1 wake.

The modulation of the tip leakage flow due to an interaction with the upstream stator wake is exemplified qualitatively using flow visualization results on the compressor casing endwall, Figure 5.9. In this figure, the casing endwall has been photographed over each of the three rotor rows following flow visualization tests at each of three loading conditions for TC1. In this figure, the approximate axial location of leakage flow inception can be identified by the path of absent paint (near mid-chord for nominal loading, and moving forward toward the blade leading edge as the loading increases). Also in the photographs of Figure 5.9, the stator wakes can be identified by similar regions of absent paint – the wakes for Stator 1 and Stator 2 are most clearly identified at the high loading and near stall operating conditions.

As suggested by the cartoon schematic in Figure 5.8, when the rotor passes through the upstream stator wake (in the absolute reference frame), the velocity deficit causes the position of leakage flow inception to move axially upstream. The strength of this modulation is different for Rotor 1 than for Rotor 2 or Rotor 3 due to the difference of the IGV wake compared to wake of Stator 1 or Stator 2. Furthermore, the modulation pattern on the casing endwall changes as the loading condition changes. The fundamentals of this rotor-stator interaction have been documented by few authors in the past (Mailach et al., 2008; Krug et al., 2015), but these photographs motivate a more in-depth analysis. The following measurements expand upon the findings of a recent study at part-speed operating conditions in the Purdue three-stage axial compressor (Smith et al., 2015b).

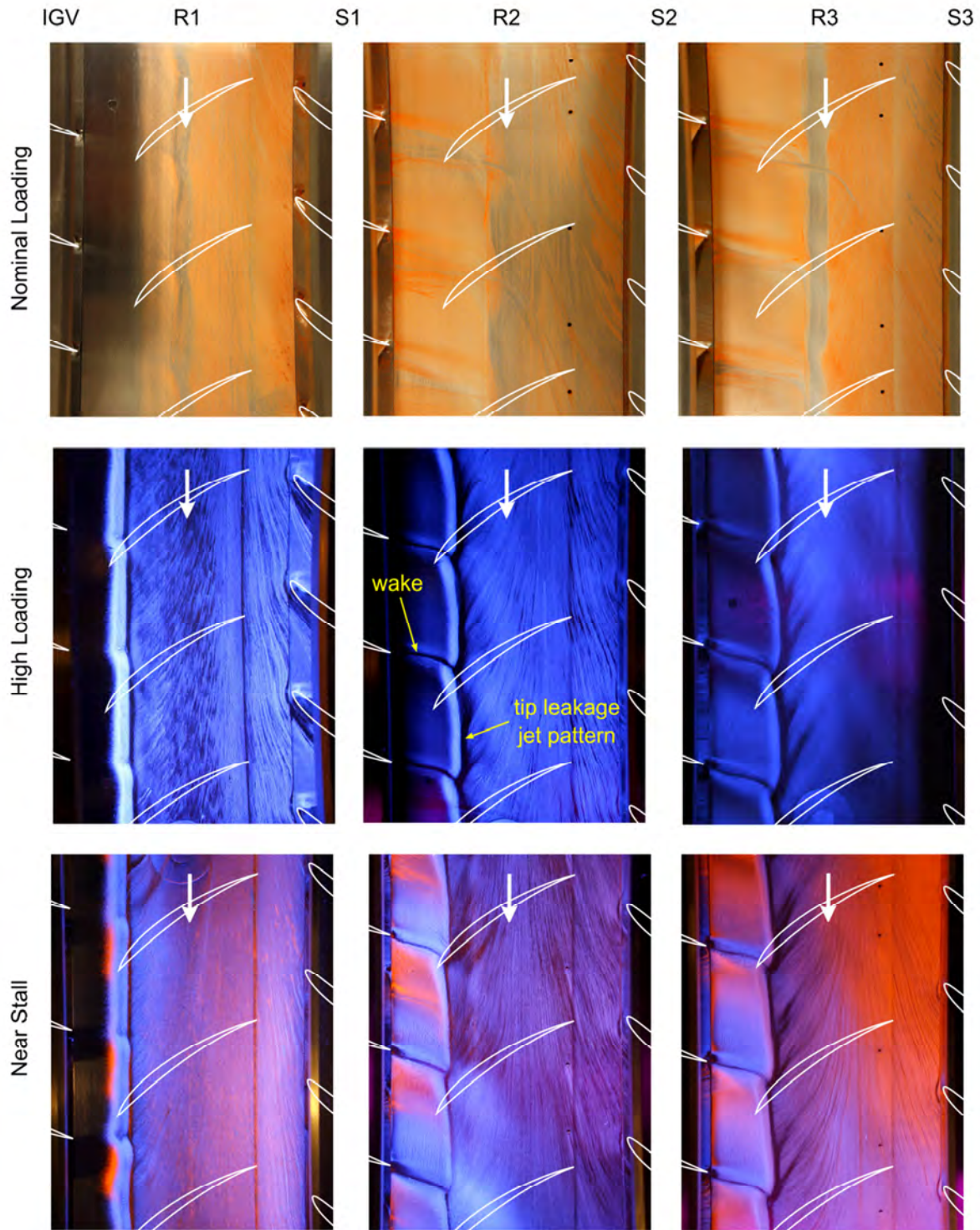


Figure 5.9: Flow visualization on the casing endwall highlighting a modulation of the tip leakage flow for TC1.

### 5.2.1. Influence of Stator Wakes on Leakage Flow Trajectory

As described in Section 5.1, the over-rotor static pressure field measurements presented above were all acquired at one fixed position with respect to the upstream and downstream vane rows. However, the interaction of the rotor tip leakage flow and the upstream stator wakes suggested by previous authors, and alluded to in the photograph of Figure 5.9, motivates additional analysis. Thus, over-rotor static pressure measurements were repeated with the baseline tip clearance, TC1, at several loading conditions for each rotor.

The cartoon schematic in Figure 5.10 outlines the measurement process conducted using the over-rotor static pressure measurement array. The sensors in this measurement system are in fixed positions in the compressor casing, but the stator vanes can be moved (either together or independently). Thus, Figure 5.10 shows representative measurements that may be measured at two vane positions with respect to the fixed measurement locations: (a) the sensors are located between the upstream stator wakes and measure the freestream flow, or (b) the sensors are approximately in the upstream stator wake. In each case, the time-resolved measurements are phase-locked with the rotor rotation, so the shaded measurement region identifies one blade passage of time-resolved static pressure data for each of the two vane positions. The cartoons in Figure 5.10 show measurements over Rotor 2 for which Stator 1 and Stator 2 are moved together, but similar measurements were collected over Rotor 1 and Rotor 3, and some data were also collected over Rotor 2 when Stator 1 and Stator 3 were moved independently from one another.

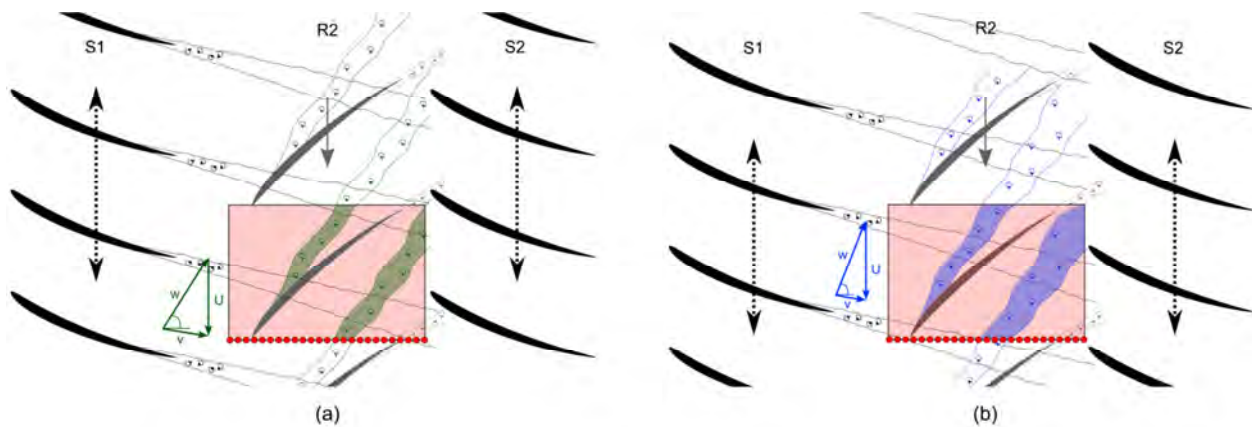


Figure 5.10: Schematic of leakage flow measurements over the rotor for two vane wake-leakage flow interaction positions, (a) and (b). A boxed region identifies a representative snapshot of the leakage flow identified by the static pressure measurements.

The first of these measurements, Figure 5.11, highlights the Rotor 1 leakage flow variations when moving all of the stator vanes simultaneously to 25 unique equally-spaced pitchwise positions with respect to the fixed dynamic pressure sensor positions for the nominal loading (NL) condition. Figure 5.11 shows the unsteadiness represented by the RMS with respect to the ensemble average. For each representation of the pressure measurements, the diagrams may be followed in a clockwise direction, as identified by the directional arrow.

To more clearly separate the modulation of the leakage flow from the 25 pitchwise positions shown in Figure 5.11, two of the pitchwise vane positions have been selected for

comparison. These positions, identified in Figure 5.11 as vpA and vpB, are approximately 50% vane passage out of phase from one another.

The RMS unsteadiness results for these two discrete vane positions are enlarged and compared in Figure 5.12(a-b). For these data, the leakage flow trajectories have been identified by connecting the locus of peak unsteadiness positions. The comparison of trajectories, Figure 5.12(c), shows a small but identifiable difference between the trajectories for the two vane positions, vpA and vpB, on the order of 1.5 degrees. This difference may seem small, but it is significant, especially compared to the effects observed for different tip clearances and loading conditions. Specifically, this modulation of the leakage flow trajectory identified in Figure 5.12(c) for the stator-rotor interaction is 50% more than the leakage flow trajectory change for the tip clearance increase from TC1 to TC2 identified in Figure 5.5.

This quantification shows that the motion of the rotor into and out of the upstream stator wake can change the leakage flow trajectory more than a doubling of the tip clearance height from 1.5% to 3.0% annulus height. To adequately study the tip leakage flow, data acquisition at one pitchwise position with respect to the stationary vane rows is insufficient. This pitchwise modulation must be carefully considered, especially when attempting to compare experimental results with CFD solutions.

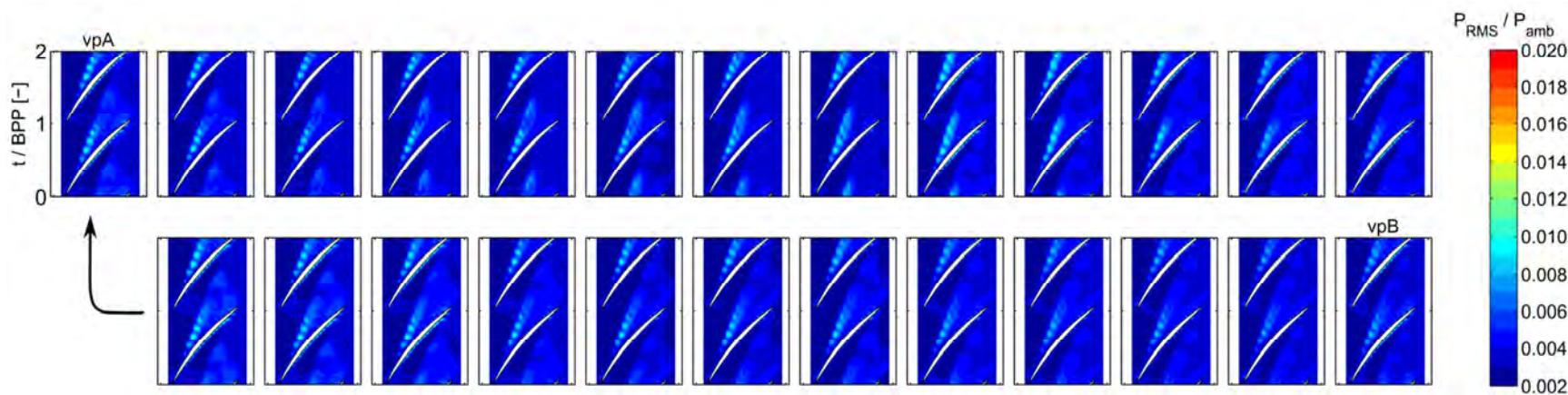


Figure 5.11: Static pressure field over Rotor 1, averaged for all 36 blades, in terms of RMS static pressure, at each pitchwise position across one vane passage (clockwise) for TC1 at NL.

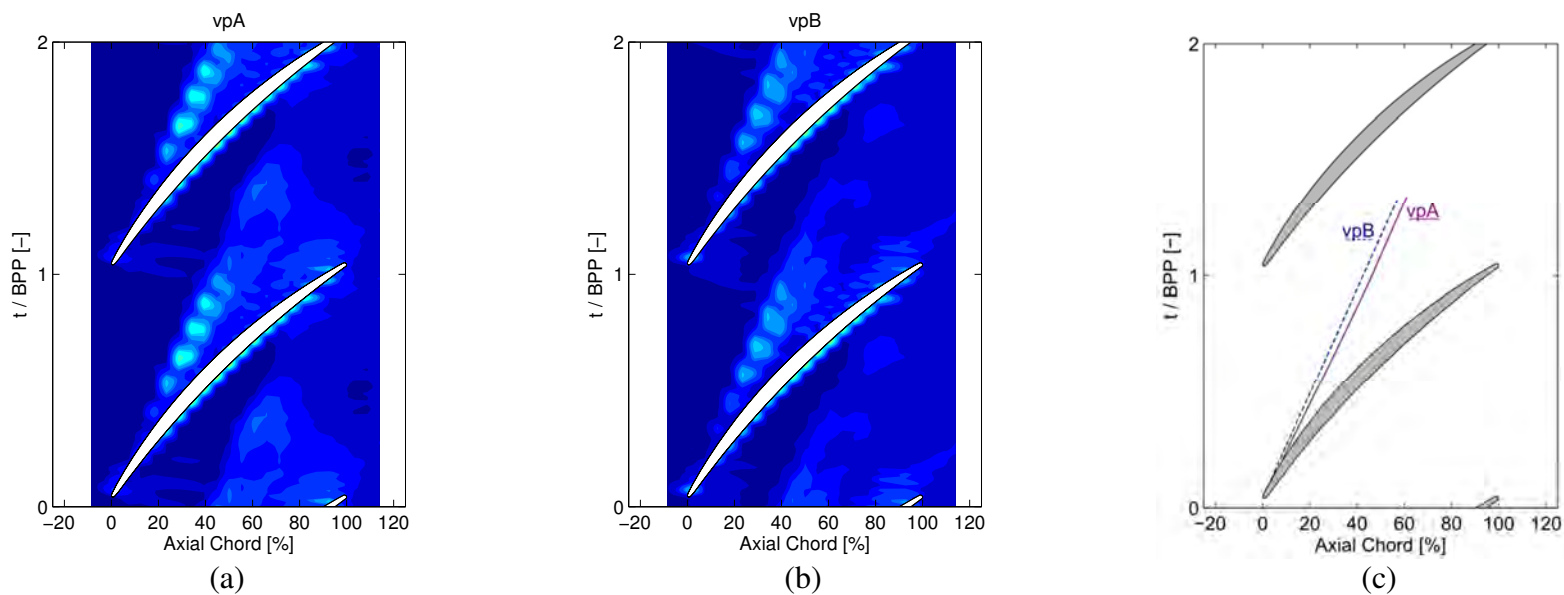


Figure 5.12: Static pressure unsteadiness (RMS) over Rotor 1 for vpA (a) and vpB (b) from Figure 5.11, and the trajectories (c).

The results from Figure 5.11 and Figure 5.12 identified a modulation of the leakage flow trajectory that agrees with the flow visualization photographs. However, the IGV wake is expected to have a smaller effect on the leakage flow for Rotor 1 than the Stator 1 or Stator 2 wakes for Rotor 2 and Rotor 3, respectively. Furthermore, it is important here to more clearly distinguish the effects of the upstream vane row from those of the downstream vane row to ensure that the downstream potential field does not significantly impact the leakage flow development. Thus, the static pressure field over Rotor 2 was chosen to investigate both of these points.

To address these questions, two separate vane movement processes were introduced – effectively clocking the position of the IGV and Stator 1 with respect to Stator 2 and Stator 3. (Recall that IGV, Stator 1, and Stator 2 all have the same vane count of 44, which allows vane clocking studies in this facility.) Specifically, the first method moved IGV and Stator 1 simultaneously to the same 25 pitchwise positions as for Figure 5.11, while Stator 2 and Stator 3 were maintained in fixed locations. In the second method, Stator 2 and Stator 3 were moved simultaneously to the 25 pitchwise positions while the IGV and Stator 1 were held fixed.

The calculated RMS unsteadiness pressure fields from this two-movement process are presented in Figure 5.13 at NL. This figure shows results for the first movement (Move IGV & S1, Fix S2 & S3) for the 25 pitchwise positions. As before, two of these positions are identified as vpA and vpB, and the results for those two vane positions are shown in Figure 5.14(a-b). Comparing the RMS unsteadiness from these two pitchwise vane positions, there is a region of high unsteadiness appearing for positions greater than 70% axial chord for vpB which does not appear for vpA. Referring to Figure 5.13, this region of high unsteadiness appears and disappears while moving clockwise around the 25 pitchwise positions. In addition, the trajectory is also compared for these two identified vane positions, in Figure 5.14(c). For this first vane movement process, the trajectory of the leakage flow modulates by approximately 1.5 degrees between vpA and vpB. In this case, the relative trajectories of vpA and vpB are opposite from the results shown in Figure 5.12(c). The positions of the IGV and Stator 1 with respect to the measurement sensors are nearly identical, but it is expected that the IGV wake will affect Rotor 1 differently than the effect of Stator 1 on Rotor 2 due the nature of the IGV as an accelerating vane row. This first vane movement process has isolated the upstream vanes from the downstream vanes for Rotor 2 to emphasize the effect of the upstream vane row on the leakage flow development.

A similar analysis of RMS unsteadiness is also presented for the second vane movement process (Move S2 & S3, Fix IGV & S1), Figure 5.15. For this case, the 25 positions in Figure 5.15 may identify a slight change of the pressure field unsteadiness near the trailing edge of the rotor blades where the downstream vane row may affect the flow, but there is no appreciable change of the leakage flow pattern or trajectory throughout the 25 positions. This becomes more apparent by selecting the same two relative positions, identified as vpA and vpB for comparison in Figure 5.16(a-b). The RMS unsteadiness for these two positions is nearly identical, and the trajectories traced in Figure 5.16(c) reinforce this invariability. Ultimately, these results in Figure 5.13 through Figure 5.16 highlight the effect that the upstream vane wakes may impose on the tip leakage flow (as suggested in the schematic of Figure 5.8), and they separate observations from the potential field associated with the downstream vane row.

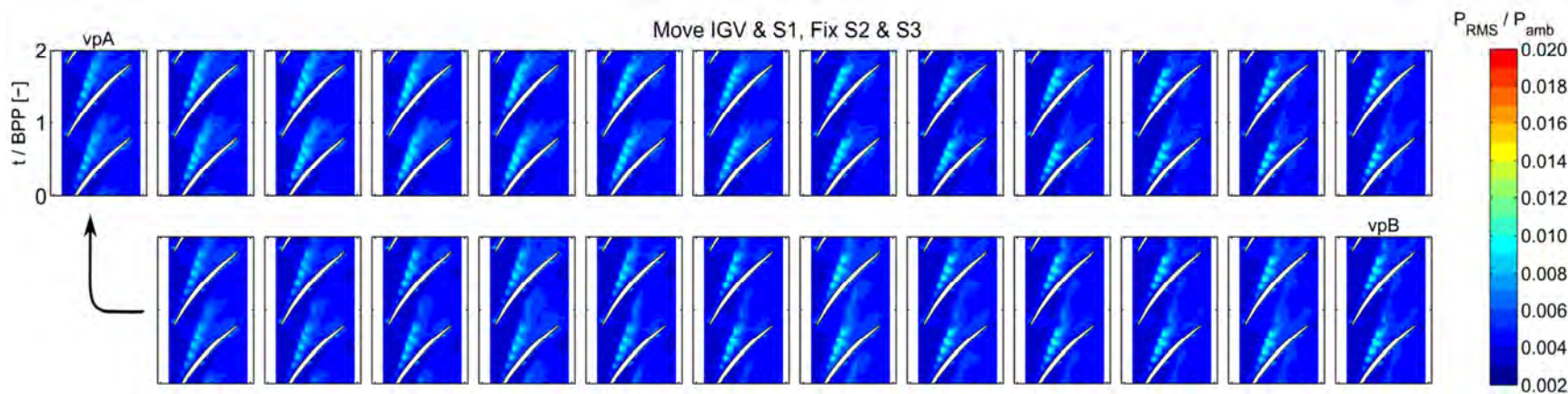


Figure 5.13: Static pressure field over Rotor 2, averaged for all 33 blades, in terms of RMS static pressure, at each pitchwise position across one vane passage (clockwise) for TC1 at NL. Only IGV and S1 are moved, S2 and S3 are fixed.

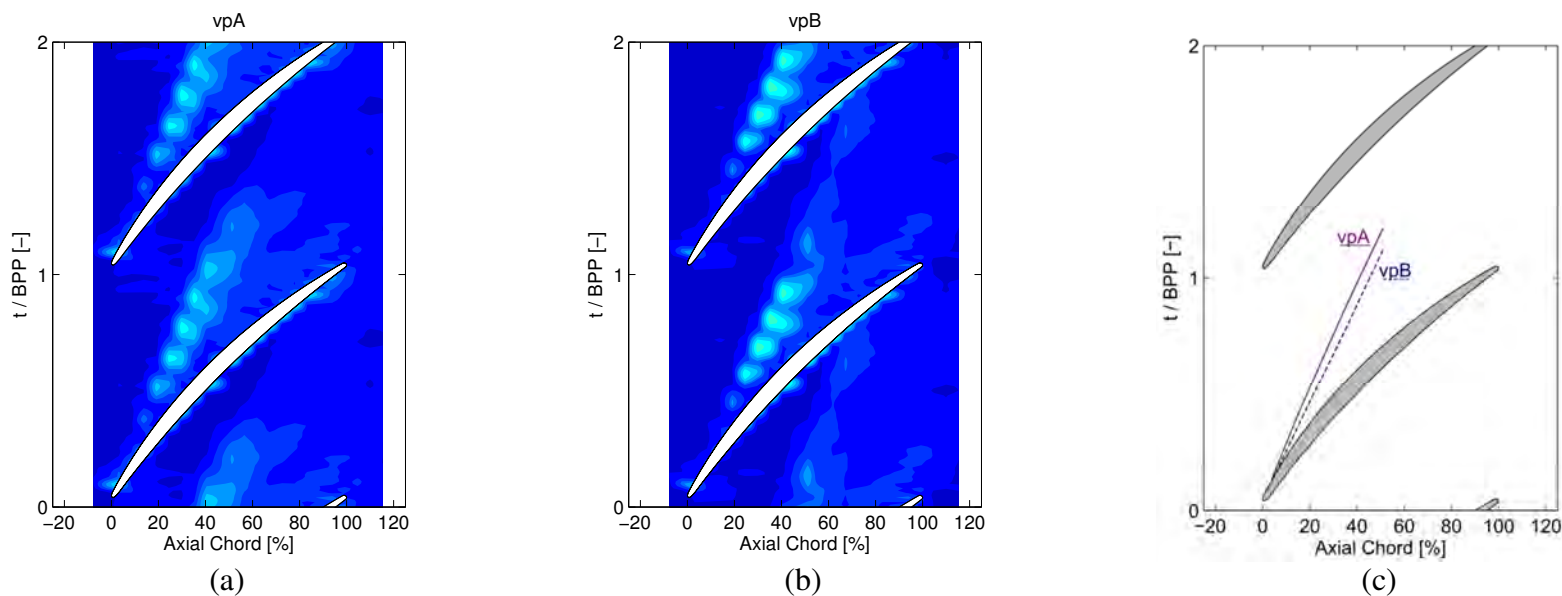


Figure 5.14: Static pressure unsteadiness (RMS) over Rotor 2 for vpA (a) and vpB (b) from Figure 5.13, and the trajectories (c).

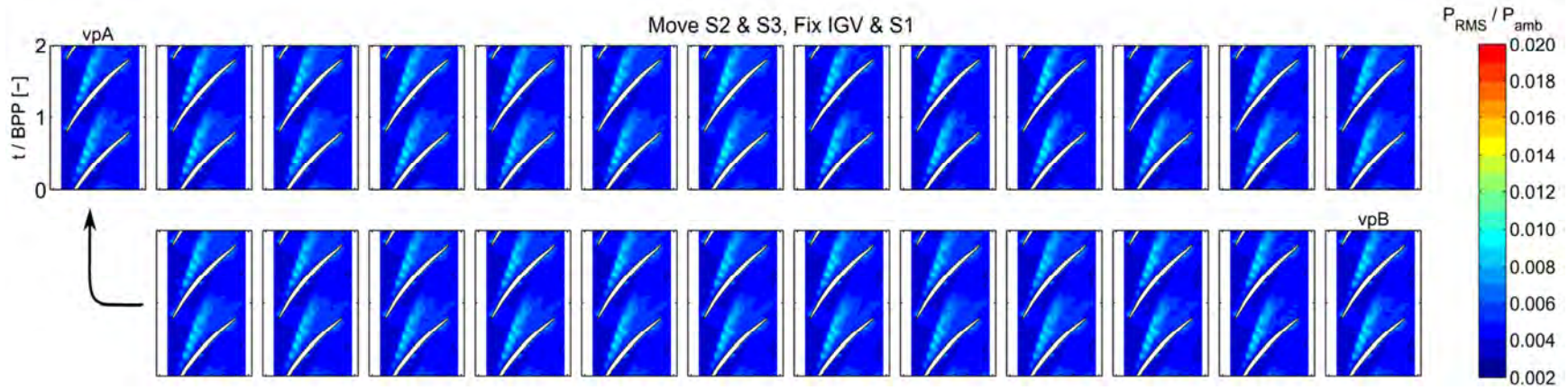


Figure 5.15: Static pressure field over Rotor 2, averaged for all 33 blades, in terms of RMS static pressure, at each pitchwise position across one vane passage (clockwise) for TC1 at NL. Only S2 and S3 are moved, IGV and S1 are fixed.

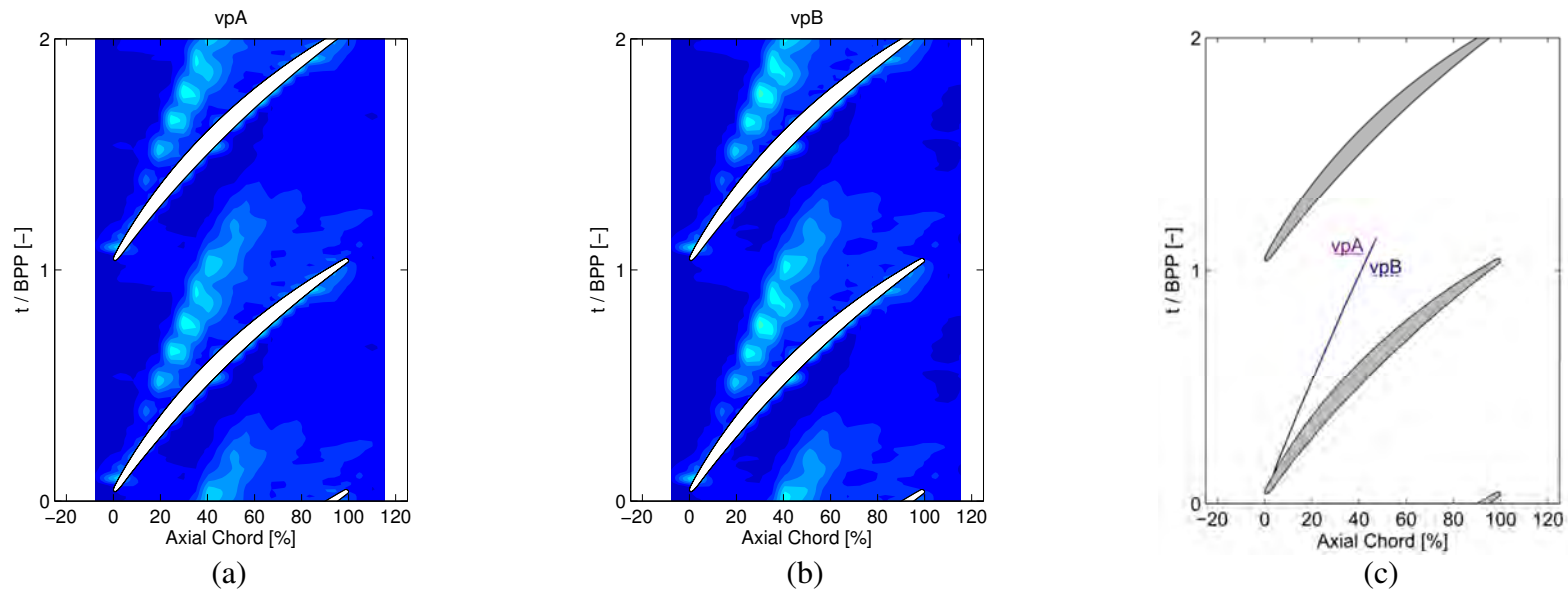


Figure 5.16: Static pressure unsteadiness (RMS) over Rotor 2 for vpA (a) and vpB (b) from Figure 5.15, and the trajectories (c).

To this point, the Rotor 1 leakage flow trajectory modulation was identified at the nominal loading condition. However, the IGV is expected to affect the Rotor 1 flow field differently than the downstream stators will affect the rotors of the latter stages. As a result, the Rotor 2 pressure field was analyzed using two separate vane movement processes to investigate the embedded stage and separate the effects of the upstream vane wakes from the downstream potential field. At this point, further analysis is warranted to evaluate the effect of changing loading condition, and Rotor 3 was selected as the vehicle for this analysis.

Figure 5.17 identifies a modulation of the leakage flow trajectory for Rotor 3 using the simultaneous movement of all vane rows described previously for Figure 5.11. In Figure 5.17, the Rotor 3 unsteadiness data at the nominal loading (NL) condition show the modulation of the leakage flow for the 25 vane positions. Considering the pitchwise position identified as vpA, highlighted in Figure 5.18(a), the locations of high RMS are identified to approximately mid-chord, and then attenuate slightly prior to reappearing as a high-intensity region at the intersection with the trailing edge of the adjacent blade. In contrast, for vpB (Figure 5.18(b)), the high RMS regions begin to attenuate further forward in the passage (near 60% axial chord), but the high-intensity region at the trailing edge also moved forward in the passage to approximately 80% axial chord. For Rotor 3 at this NL condition, the approximately trajectories identified in Figure 5.18(c) vary less than the results shown previously for Rotor 1 or Rotor 2 at the same loading condition.

At the high loading (HL) operating condition for Rotor 3 in Figure 5.19, a similar trend can also be identified. The comparison of vpA and vpB at this HL condition in Figure 5.20(a-b) shows a more dramatic difference than for the NL condition. At HL, Figure 5.20(a) shows the high unsteadiness region of the leakage flow attenuates at approximately 40% axial chord before reappearing as a region of high unsteadiness at its intersection with the adjacent blade, near 65% axial chord. In contrast, Figure 5.20(b) shows for vpB that the same attenuation occurs near 40% axial chord, but the “island” of high unsteadiness can then be identified near 55% axial chord, but not in contact with the adjacent blade. However, Figure 5.20(b) also shows a region of high unsteadiness in contact with the adjacent blade centered near 85% axial chord which does not align with the trajectory path connecting the locus of high unsteadiness for the rest of the passage. The leakage flows in Figure 5.20(a-b) are clearly different, and their approximate trajectories are traced in Figure 5.20(c).

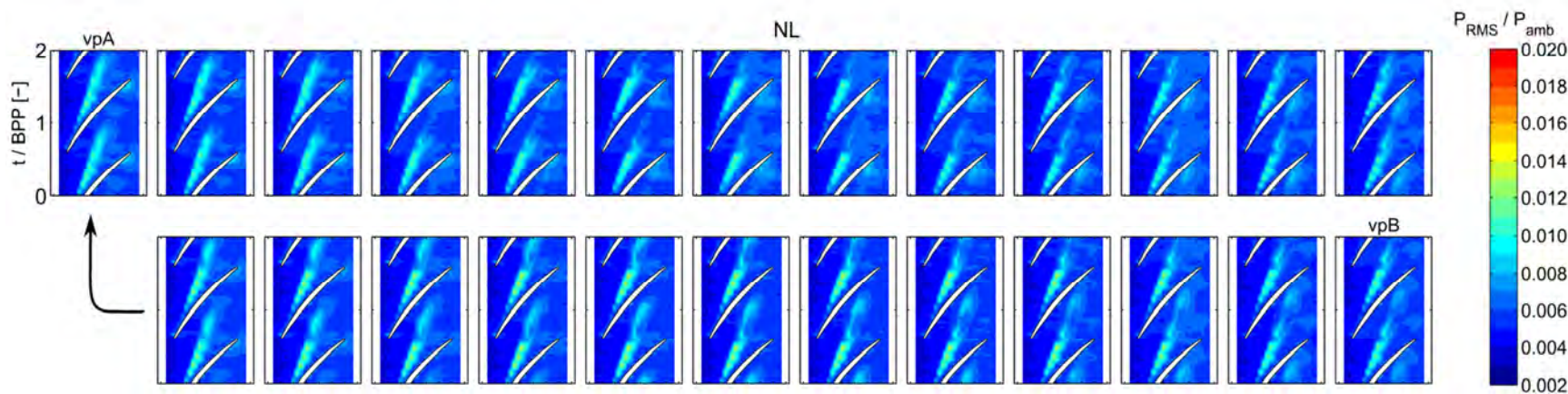


Figure 5.17: Static pressure field over Rotor 3, averaged for all 30 blades, in terms of RMS static pressure, at each pitchwise position across one vane passage (clockwise) for TC1 at NL using two separate vane movement techniques.

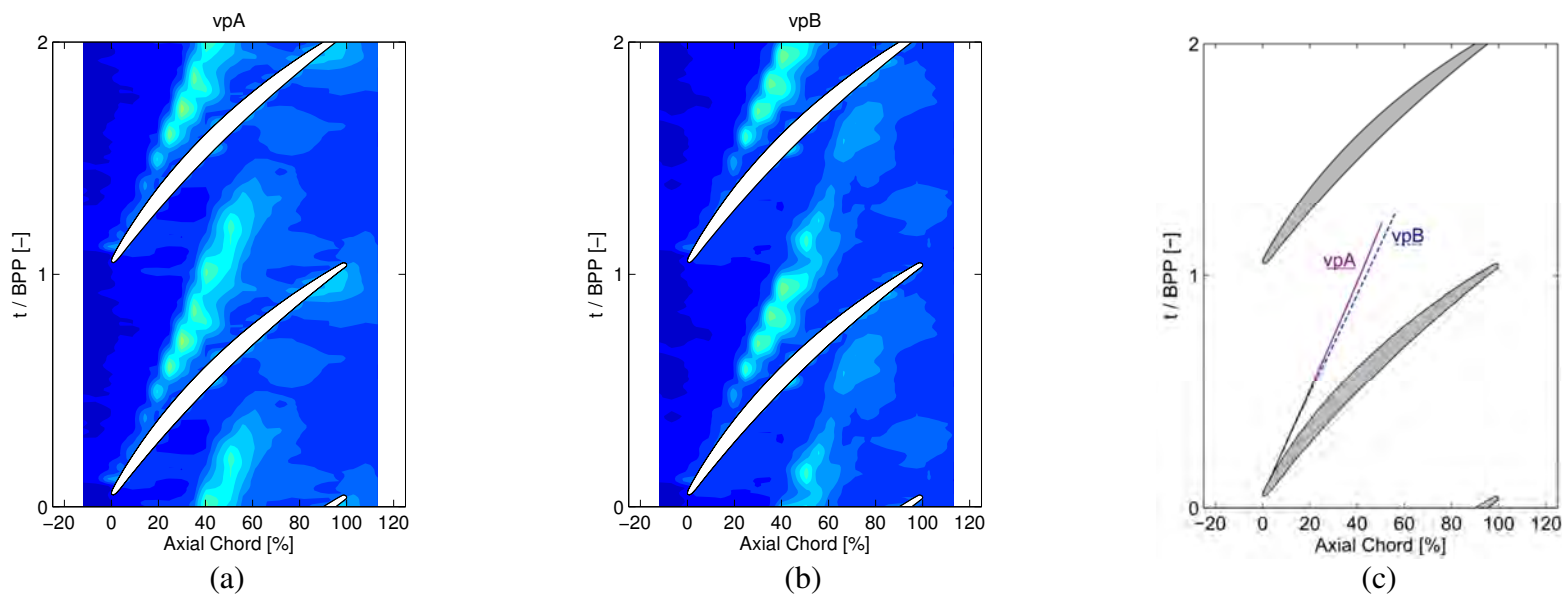


Figure 5.18: Static pressure unsteadiness over Rotor 3 for vpA (a) and vpB (b) from Figure 5.17, and the trajectories (c) (TC1, NL).

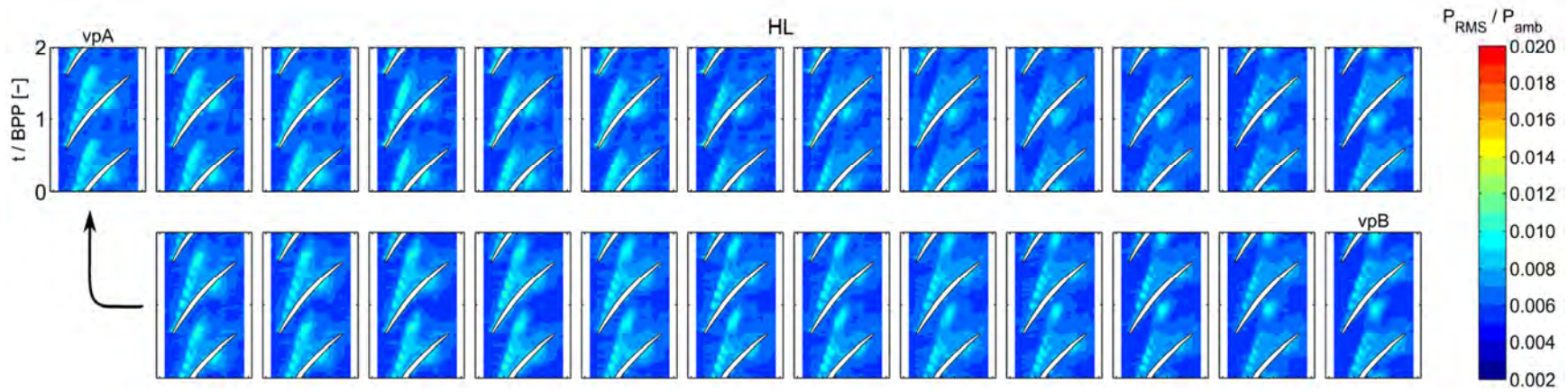


Figure 5.19: Static pressure field over Rotor 3, averaged for all 30 blades, in terms of RMS static pressure, at each pitchwise position across one vane passage (clockwise) for TC1 at HL.

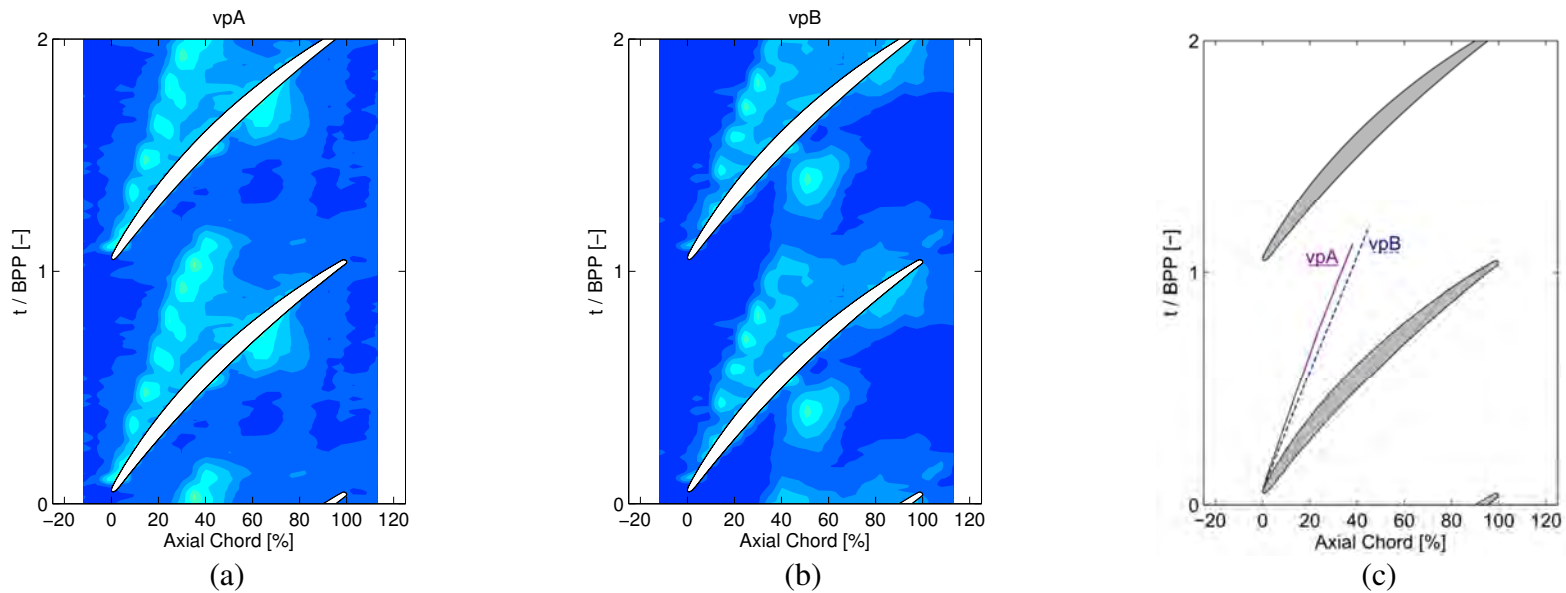


Figure 5.20: Static pressure unsteadiness over Rotor 3 for vpA (a) and vpB (b) from Figure 5.19, and the trajectories (c) (TC1, HL).

## 5.2.2. Rotor Exit Total Pressures

To further capture the effect of the upstream vane wake on the rotor tip leakage flow, the time-resolved total pressure measurements downstream of the rotor blade rows have been completed for up to 28 radial positions at each of the 26 pitchwise positions (pp) across one vane pitch. (Of these 26 positions, 25 are *unique* positions, since one pair of positions, pp1 and pp26, are periodic with respect to the vane pitch.) The cartoon schematic in Figure 5.21 shows the relative locations of the probe positions at the rotor exit plane for simultaneous movements of all vane rows as the rotor interacts with the upstream vane wake to modulate the rotor tip leakage flow.

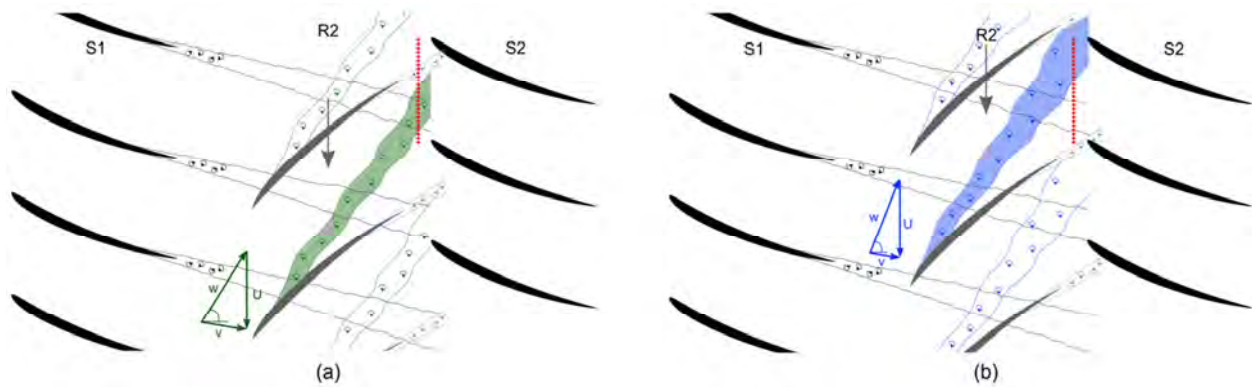


Figure 5.21: Schematic of leakage flow measurements at rotor exit planes for two vane wake-leakage flow interaction positions, (a) and (b).

The time-resolved total pressure measurements are presented here as an unsteadiness using the RMS with respect to the ensemble average, as defined in Equation (5.2). This presentation of results accommodates the identification of recirculating flow regions expected in the tip leakage flow disturbance, as well as the rotor wake. These RMS measurements are presented for the Rotor 1 exit plane at the NL and HL operating conditions in Figure 5.22 and Figure 5.23, respectively.

In these figures, the RMS with respect to the ensemble average (500 revolutions, for these data) has been calculated at each circumferential vane position, and then averaged across all rotor blades (36 blades for Rotor 1) to identify an averaged rotor passage. The IGV wake is very thin and has a minimal effect on the downstream rotor row. As a result, Figure 5.22 and Figure 5.23 show a weak modulation of the tip leakage flow disturbance across one vane pitch (following the figures in a clockwise direction, denoted by the titles pp1-pp26). However, an increased unsteadiness at the center of the leakage flow disturbance region is identifiable, particularly for the TC3 tip clearance configuration measurements at the NL operating condition in Figure 5.22. In addition to the pitchwise modulation of the flowfield exemplified by the 26 circumferential measurement positions, a mean contour represents the rotor wake averaged across one vane pitch. The PS and SS of the rotor blade are also labeled in this mean contour to orient the figure.

At the nominal loading condition, Figure 5.22, a clear distinction can be made between the tip leakage flow disturbances for each of the tip clearance configurations, TC1 and TC3. For the

smaller tip clearance, the unsteadiness due to the tip leakage flow occupies a region which extends down from the outer casing endwall to approximately 80% annulus height, whereas the larger tip clearance height shows a leakage flow region which reaches approximately 70% annulus height, as well as affecting a noticeably larger area in the pitch-wise direction.

At the same Rotor 1 exit position for the HL operating condition, Figure 5.23 shows the TC1 leakage flow region no longer has a coherent circular shape, but rather fills a corner area adjacent to the pressure side of the rotor wake. The TC3 tip clearance configuration, on the other hand, maintains a shape which closely resembles the result from the NL condition in Figure 5.22. However, its size and relatively intensity of the unsteadiness parameter are both increased at the higher loading condition. Also at the HL condition, both tip clearance configurations show a noticeable change as the hub corner separation off the suction surface previously observed at NL grows into a thick wake which extends above 50% annulus height.

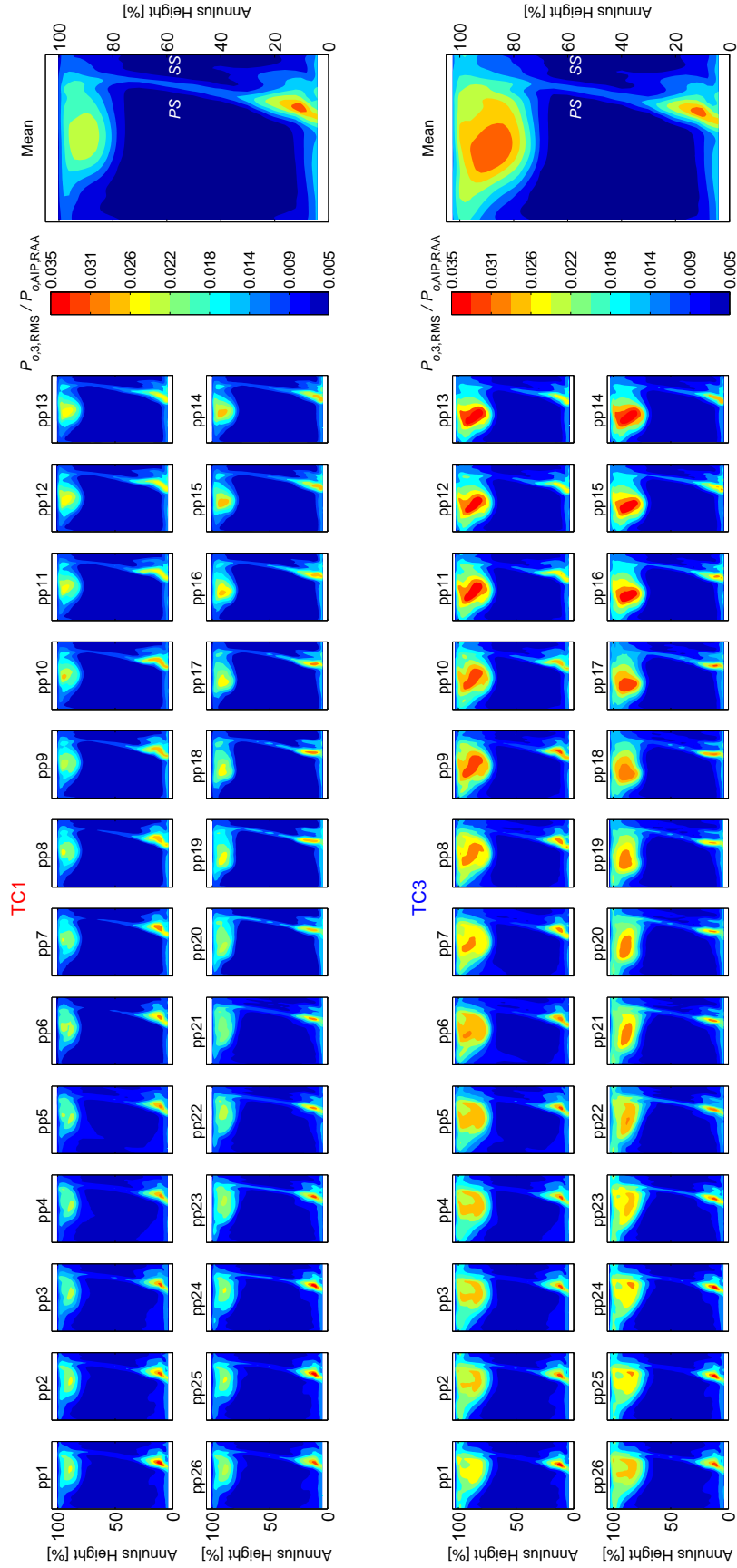


Figure 5.22: Average Rotor 1 exit flow field, in terms of RMS total pressure, at each circumferential location across one vane passage (clockwise) at NL.

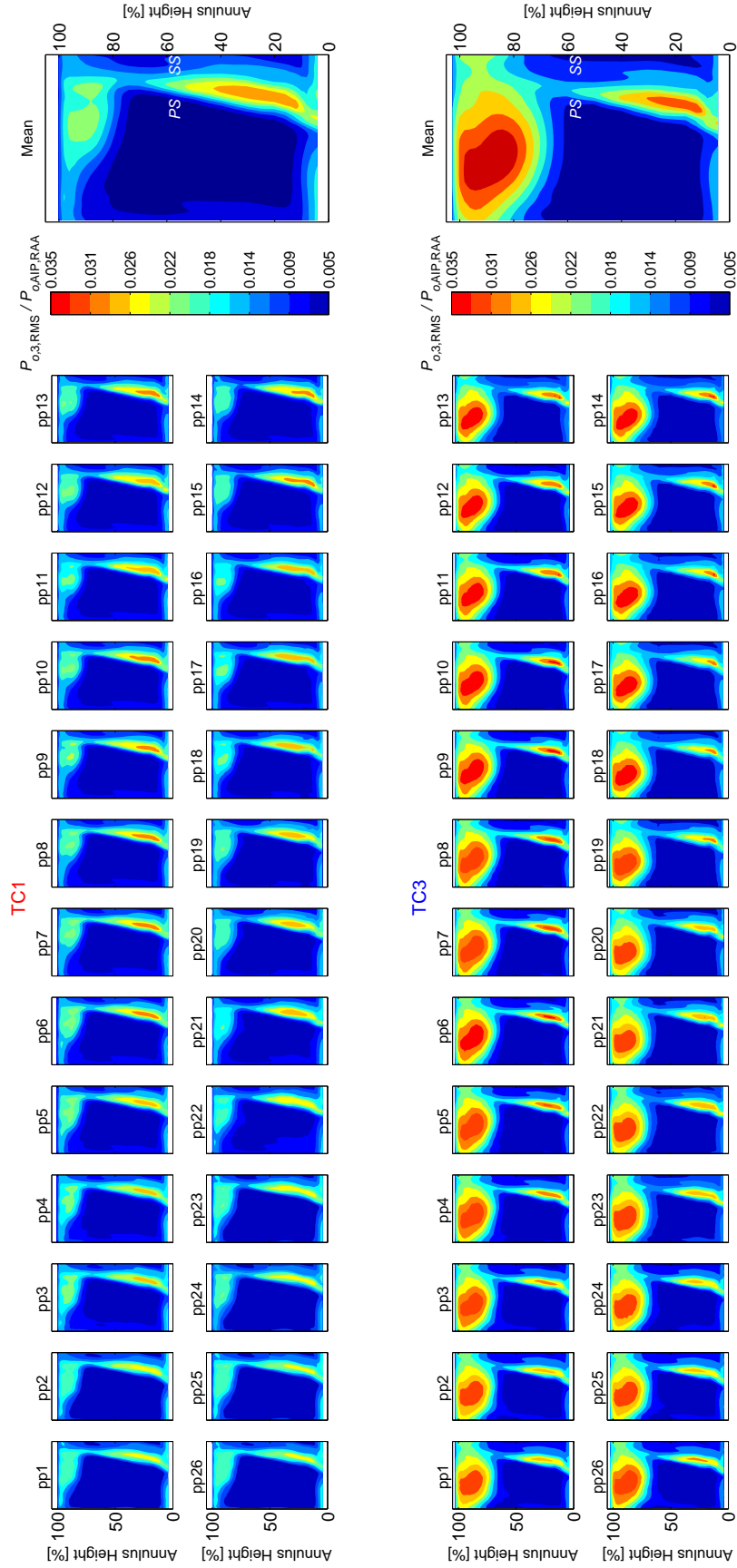


Figure 5.23: Average Rotor 1 exit flow field, in terms of RMS total pressure, at each circumferential location across one vane passage (clockwise) at HL.

Time-resolved total pressure measurements at Rotor 2 exit for the NL and HL operating conditions, Figure 5.24 and Figure 5.25, respectively, are also presented as the RMS unsteadiness with respect to the ensemble average. At Rotor 2 exit, the leakage flow modulation is more clearly distinguished by following the measurements at each position across one vane pitch. For TC1 at the nominal loading condition, two adjacent high-intensity regions of flow unsteadiness are identifiable in the outer tip region for the measurements labeled pp1–pp7. These two regions compare with the results observed in Figure 5.6 (for TC2, although the figure for TC1 is similar), which is expected based on the position of the static pressure measurements falling in this same range with respect to the stator vanes. The strength of the two high-unsteadiness regions is also sufficiently significant to persist into the circumferential mean for TC1 in Figure 5.24. The TC3 results in Figure 5.24 position the extremes of the pitchwise leakage flow modulation in the same locations as for TC1. Further, the measurements are similar to the observations for Rotor 1, such that the radial extent of the leakage flow region for TC3 extends to approximately 70% annulus height, compared to 80% for TC1.

At the high loading condition for Rotor 2 presented in Figure 5.25, the unsteadiness of the flow identified by the RMS fluctuations shows less modulation than at the nominal loading condition (the RMS of the passage represents magnitudes which exist more in the middle of the prescribed contour range), especially for TC1. However, two regions of high pressure unsteadiness are still faintly present in the mean contour for TC1. Comparing the HL condition with the NL results for Rotor 2, the circumferential probe position which yields the most intense leakage flow structure is not the same. This result is expected as the width of the upstream stator wake is significantly changed between the two conditions. Furthermore, the trajectory of the leakage flow is expected to change as the rotor loading is increased.

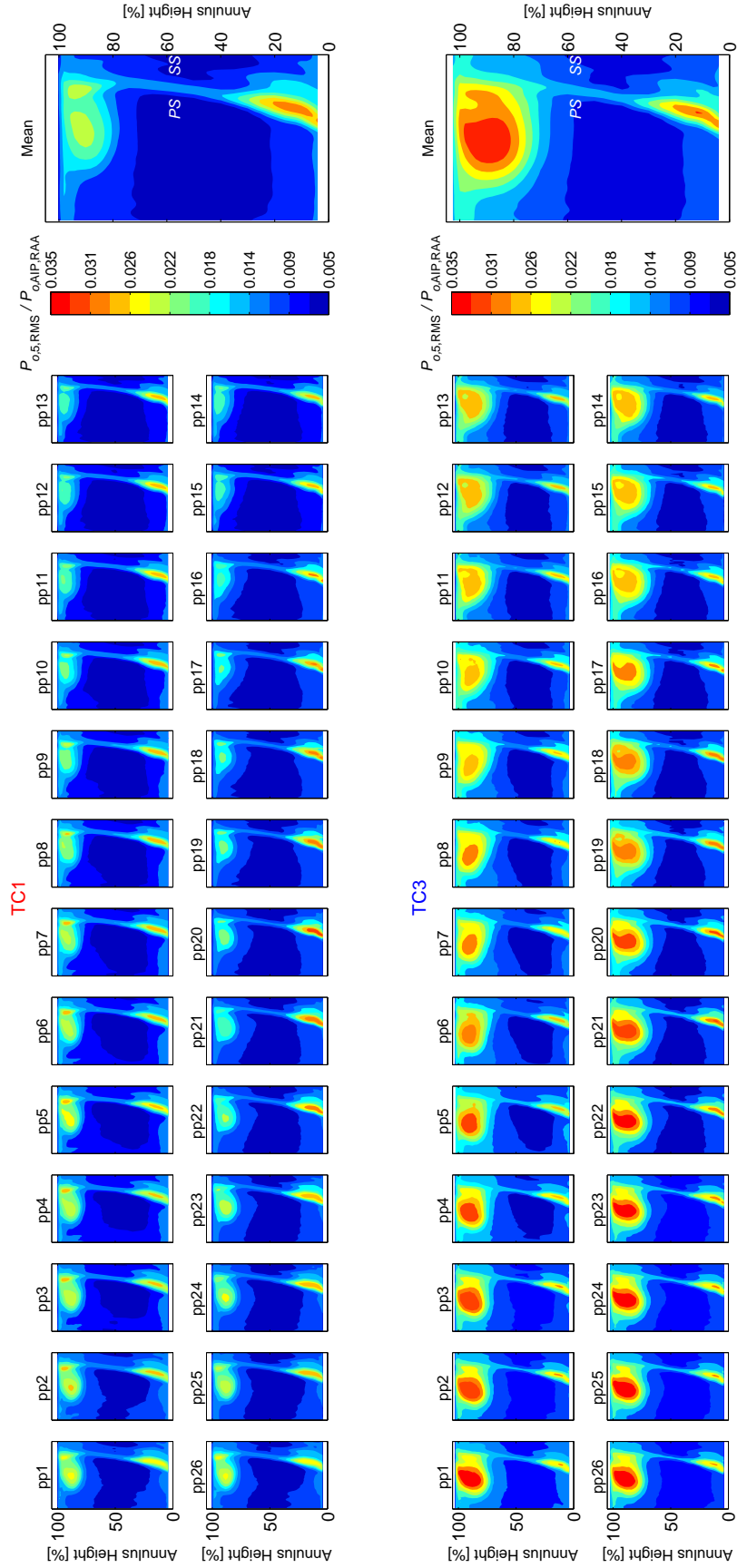


Figure 5.24: Average Rotor 2 exit flow field, in terms of RMS total pressure, at each circumferential location across one vane passage (clockwise) at NL.

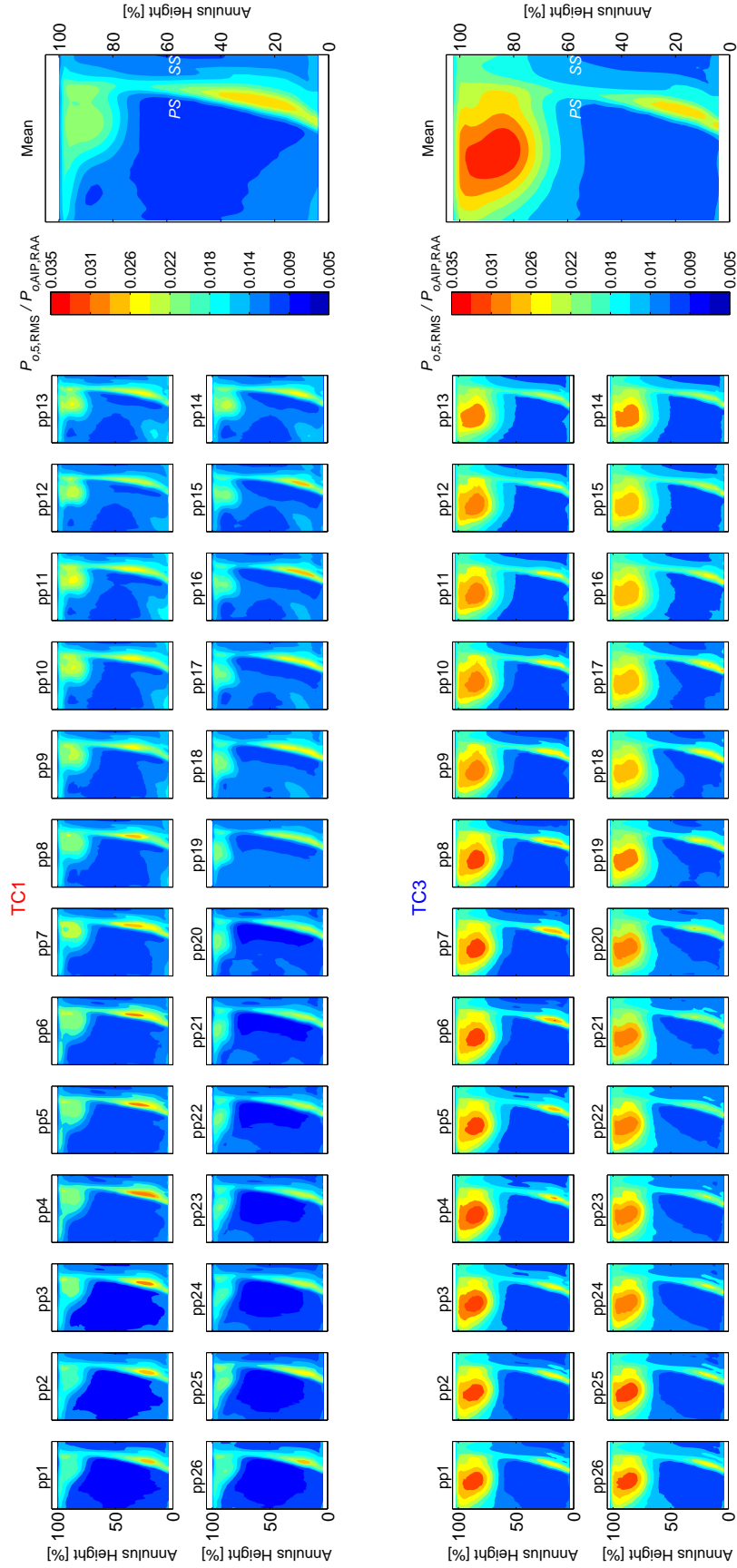


Figure 5.25: Average Rotor 2 exit flow field, in terms of RMS total pressure, at each circumferential location across one vane passage (clockwise) at HL.

Similar to the other rotor rows, the unsteadiness of the Rotor 3 exit total pressure field is shown in Figure 5.26 and Figure 5.27 for the NL and HL operating conditions, respectively. At the NL condition, the results for TC1 identify two adjacent regions of high unsteadiness (in agreement with other results in this section of the document) – one in the middle of the passage and another adjacent to the blade pressure surface. As with Rotor 2, this observation compares with the over-rotor static pressures for TC2 at the NL condition (Figure 5.6). For the TC3 configuration, the circumferential modulation of the leakage flow in Figure 5.26 is less discernable compared to the TC1 measurements. This observation suggests the leakage flow region with the large tip clearance height is less sensitive to the influence from the upstream stator vane.

For the high loading condition, Figure 5.27, the TC1 unsteadiness is dominated by the rotor wake more than the leakage flow. Comparing the pitchwise modulation results, the location with the smallest or weakest leakage flow region corresponds to the most significant rotor wake, as the decreased leakage flow blockage provides less energizing benefit to the suction surface wake separation tendencies in the lower portion of the annulus. Similarly, the positions with the largest leakage flow regions show the least suction surface separation (i.e., the thinner rotor wakes). Also at the high loading condition, Figure 5.27 shows the leakage flow region for TC3 fills nearly the entire rotor passage, with radial extent down to approximately 70% annulus height. In contrast, the region of high unsteadiness identified as the leakage flow for TC1 only affects approximately half of the rotor passage with radial extent to just below 80% annulus height but with a more significant rotor wake.

Ultimately, these rotor exit total pressure field measurements provide valuable insight into the rotor tip leakage flow disturbance as it enters the downstream vane passage. Furthermore, the influence of the upstream stator wake can play an important role in the size, shape, and trajectory of the leakage flow through the rotor passage – particularly for Rotor 2 and Rotor 3, whereas Rotor 1 is weakly affected by the IGV wake. In combination with the over-rotor static pressure field measurements, these rotor exit data can provide bounding planes which could be used to influence more focused measurements in the rotor passage using non-intrusive measurement techniques, such as the PIV methods introduced in Chapter 6.

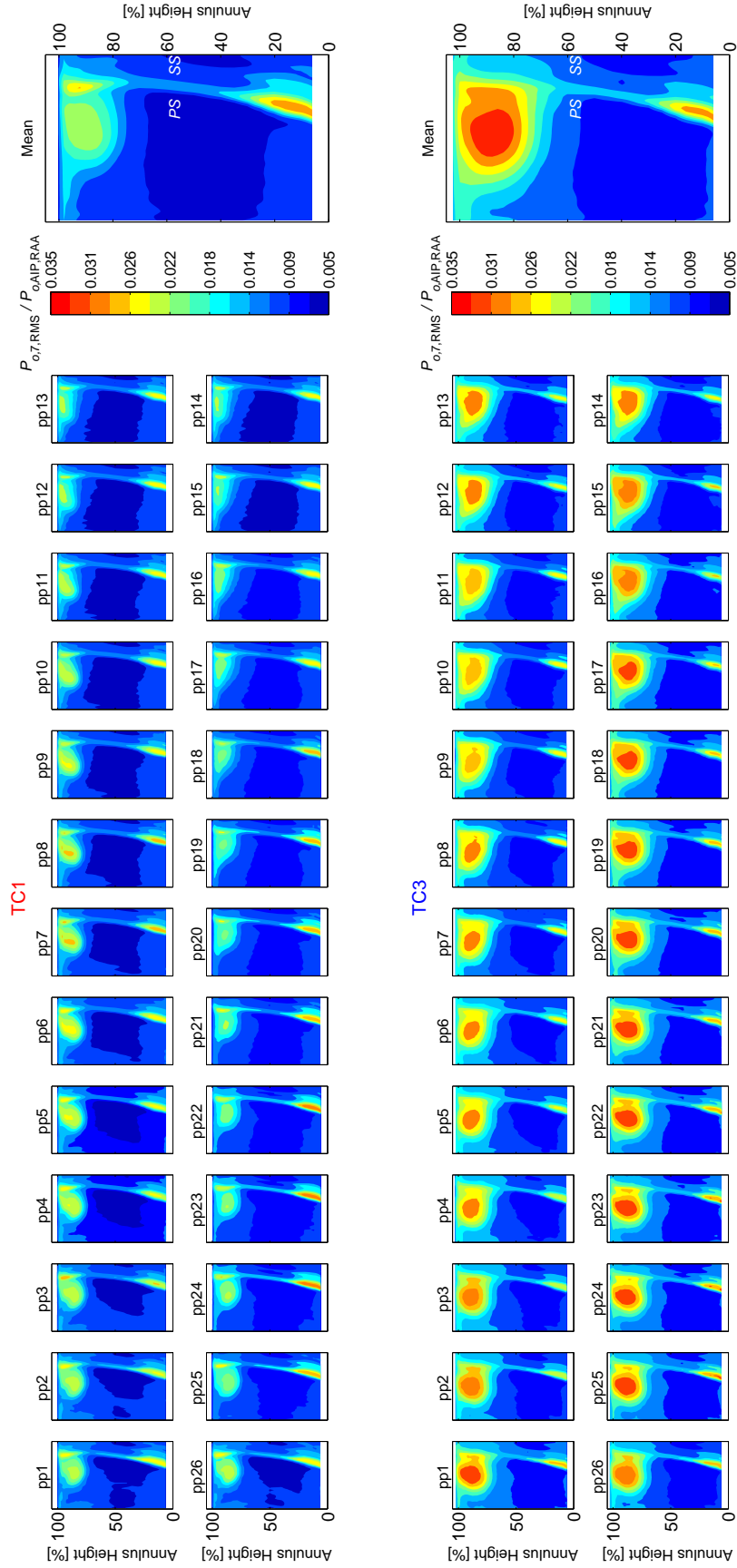


Figure 5.26: Average Rotor 3 exit flow field, in terms of RMS total pressure, at each circumferential location across one vane passage (clockwise) at NL.

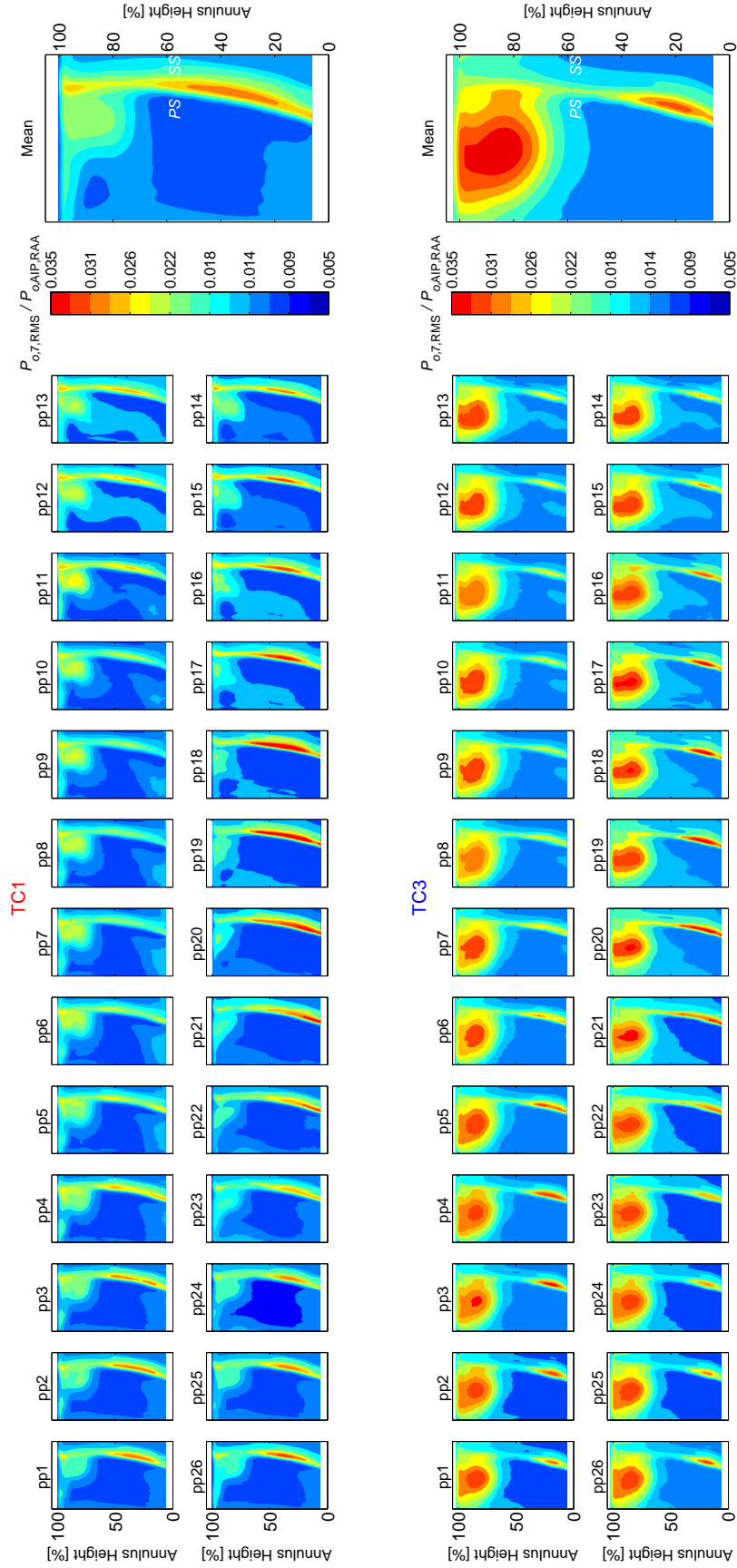


Figure 5.27: Average Rotor 3 exit flow field, in terms of RMS total pressure, at each circumferential location across one vane passage (clockwise) at HL.

### 5.2.3. Quantifying the Size of the Leakage Flow

The RMS unsteadiness of these rotor exit total pressure data provides a unique opportunity to quantify the size of the leakage flow region at the rotor exit measurement plane. Suder (1998) uses the calculation of axial velocity gradients to identify a defect region for quantifying flow blockage. A similar method has been implemented with these RMS total pressures to identify a defect region. Specifically, the gradient of RMS pressure was calculated in the radial and circumferential directions, and a cutoff value was assigned to determine the defect region, as exemplified in Figure 5.28. Once the defect region was identified, a human-guided selection tool in the plotting GUI manually separated the points from the defect region associated with the leakage flow from those associated with the rotor wake or the hub endwall boundary layer. These separated leakage flow points are also highlighted for the example in Figure 5.28. These points associated with the leakage flow disturbance region were then integrated across the passage to determine the percentage of the rotor exit flow passage which is affected by the tip leakage flow.

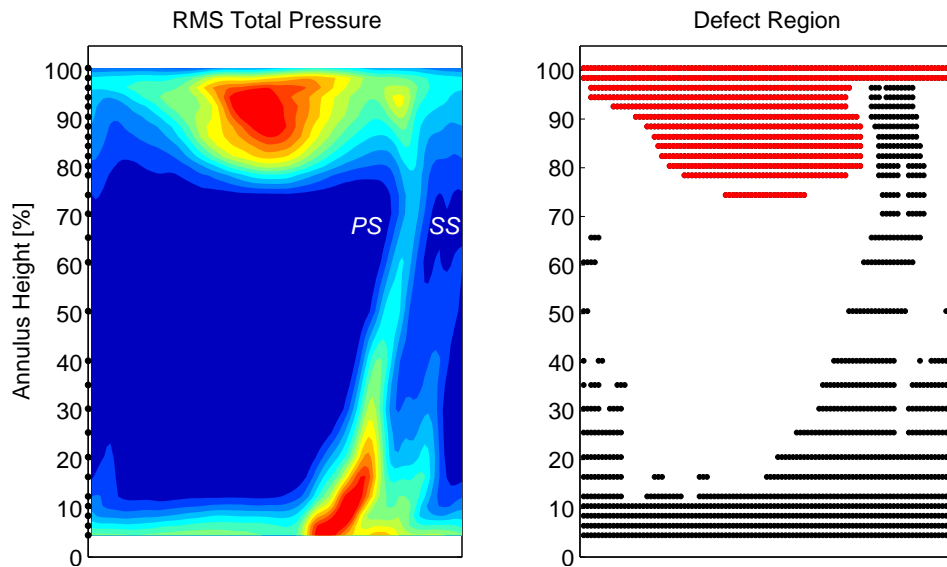


Figure 5.28: Identification of defect region associated with leakage flow unsteadiness.

This process was repeated for each of the 26 pitchwise measurement positions presented in Figure 5.22 through Figure 5.27. Because there is a potential error associated with the human-guided identification technique, the identification process was repeated three times for all of the data sets. This repetition facilitates the calculation of pertinent statistics related to human-introduced variability. The average of these leakage flow disturbed areas was then calculated at each pitchwise position for each measurement condition.

A passage-averaged value was calculated for each measurement condition, as shown by the filled bar plots in Figure 5.29. As shown in the figures above, the leakage flow region can change significantly for the different pitchwise measurement positions. Thus, the minimum affected area and maximum affected area are noted in Figure 5.29 by range bars about the passage-averaged value. For reference, and in the context of the results shown in Figure 5.29, the human-introduced variability may be represented by the standard deviation with respect to the sample

mean. The calculated disturbed areas yield a standard deviation of less than 2% of the passage area for all conditions with the TC1 configuration. The TC3 data have a standard deviation of less than 2.5% of the passage area for Rotor 1 and Rotor 2 data, but approaching 5% of the passage area for the Rotor 3 data.

The information in Figure 5.29 show the expected result of increased leakage flow disturbed area as the rotor tip clearance height is increased. Rotor 2 shows the lowest percentage of affected area for both tip clearances and both loading conditions, which is perhaps unexpected given the knowledge presented thus far about latter stages ingesting the high-loss leakage flow from the upstream rotor(s). Figure 5.29 also shows that Rotor 1 has the least pitchwise variability of the leakage flow size, which aligns with the fact that the IGV has a thinner wake than Stator 1 or Stator 2. This result can also be referred to the flow visualization photograph highlighting the leakage flow variability for TC1, Figure 5.9, which shows the significant difference of leakage flow variability for Rotor 1 compared to Rotor 2 or Rotor 3.

Figure 5.29 also shows a similarity between Rotor1 and Rotor 2 (compared to Rotor 3) which has not been identified until now. At the NL condition, the increase of leakage flow affected area between TC1 and TC3 is an identical 10.5% for both Rotor 1 and Rotor 2, whereas Rotor 3 shows a smaller increase of 7.6%. At the HL condition, the same comparison is echoed as Rotor 1 and Rotor 2 show an identical increase of 15.3% between Rotor 1 and Rotor 2, whereas Rotor 3 shows a smaller increase of 10.4%. Based on these data, Rotor 3 shows a trend of 30% less increase of leakage flow area between TC1 and TC3 compared to Rotor 1 and Rotor 2 for these loading conditions.

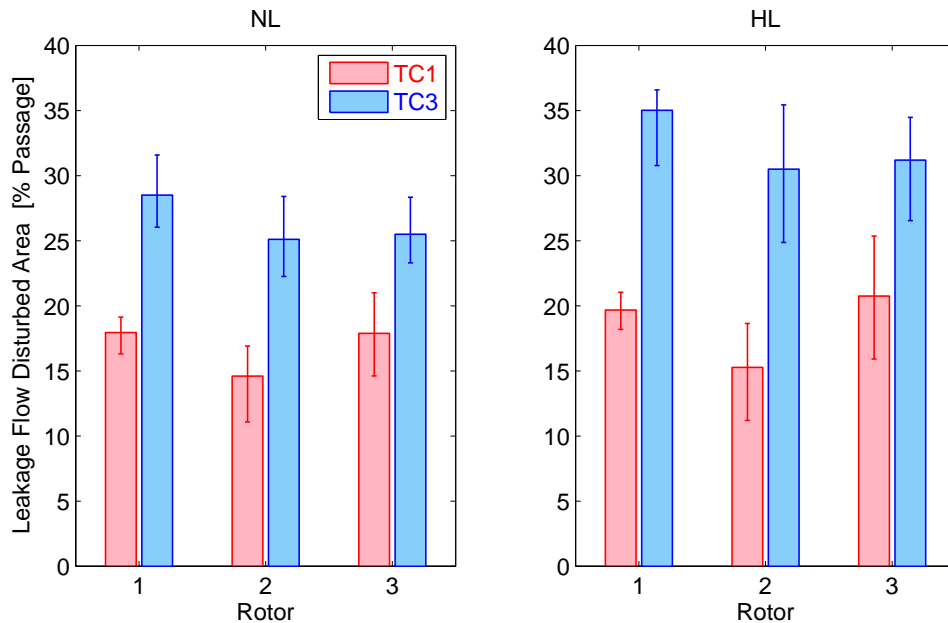


Figure 5.29: Percentage of rotor passage affected by tip leakage flow: passage-averaged value and range.

### **5.3. Thermal Anemometry**

The steady pressure and temperature measurements presented in Chapter 3, combined with the time-resolved pressure measurements above, provide valuable insight into the overall performance of the Purdue three-stage compressor, as well as the underlying flow physics governing the tip leakage flow disturbance under different rotor tip clearance conditions. However, a quantification of the flow angles provides an additional method by which to evaluate the overall effect of the rotor tip leakage flows and validate computational tools. The slanted hot-wire technique implemented for these measurements provides valuable information about the flow features in three-dimensions, as described in Section 2.5.3. At each of the axial measurement planes 2 through 8 (see Figure 2.6), hot-wire data were collected at up to 28 radial positions across the annulus height and a series of circumferential positions across one vane pitch. Data were sampled at a rate of 1 MHz for 200 rotor revolutions. Several methods for evaluating the results are presented here which feature results to complement the measurement techniques already introduced.

#### **5.3.1. Flow Angles and Velocity**

To analyze the flow angles output from the slanted hot-wire processing technique, the radial profiles at each axial measurement plane are considered for two tip clearance configurations (TC1 and TC3). For these results, the passage-averaged flow angles were calculated using data collected at several measurement positions with respect to the fixed vanes (13 circumferential positions for rotor exit planes and 20 circumferential positions for stator exit planes).

The absolute flow angles for both tip clearance configurations at the nominal loading (NL) operating condition are shown in Figure 5.30. As the tip leakage flow passes from the rotor pressure surface to the suction surface, its trajectory across the rotor passage is interpreted in the flow angles as underturning in the rotor relative frame of reference. However, the corresponding decrease of local flow velocity in the endwall region as a result of the flow blockage due to the tip leakage flow disturbance is significant enough to cause the absolute flow angles to increase in the tip region at the rotor exit (Goto, 1992). This effect is clearly observed at the rotor exit planes in Figure 5.30. As the rotor tip clearance height is increased, the increased flow blockage from the larger leakage flow region is noted as the absolute flow angle at the rotor exit planes also increases.

In Figure 5.30, the Rotor 1 exit angles are distinctly different than those for the Rotor 2 and Rotor 3 exit angles. In fact, a comparison of the Rotor 2 and Rotor 3 exit angles for either tip clearance configuration, TC1 or TC3, shows nearly identical radial profile shapes and magnitudes. This observation aligns well with the previous notes that Rotor 1 performs differently than Rotor 2 and Rotor 3 in the Purdue three-stage compressor.

At this same loading condition, the stator exit angle profiles are less affected by tip clearance height than the rotor exit profiles for these passage-averaged, time-averaged results. The Stator 1 exit results present an increase of absolute flow angle in the outer 40% annulus height as the rotor tip clearance height is increased, indicating that the decreased flow velocity in this region causes the stator loading to increase and the stator is less capable of performing the same amount of flow turning when the Rotor 1 tip clearance height is increased. At the Stator 2 and Stator 3 exit planes, the curvature of the absolute flow angle profile changes as the rotor tip clearance height is increased, and both stators (most notably Stator 3) show a slight decrease of

flow angle in the outer 15% annulus height near the tip region. Referring to the steady detailed total pressure contours for Stator 2 and Stator 3 at the NL operating condition, Figure 3.39 and Figure 3.41, respectively, this change of flow angle is due to the slight shift of the location of maximum wake thickness toward the hub.

The same passage-averaged, time-averaged radial profiles of absolute yaw angle are also considered at the high loading (HL) operating condition, Figure 5.31. Similar to the observations at the NL operating condition, these HL data also show a difference between the results at Rotor 1 exit and those at Rotor 2 or Rotor 3 exit. At all three rotor exit planes for HL, however, the shift between the two tip clearance configurations is nearly twice that observed for NL. As the leakage flow region overtakes a more significant area at the high loading condition, Figure 5.31 also shows a decrease of absolute yaw angle at Rotor 1 exit (due to the redistribution of mass flow) for the lower 70% annulus height which was less noticeable at the NL operating condition. Also at the HL condition, Figure 5.31 shows the reduction of the Stator 2 hub corner separation for TC3 compared to TC1 has a profound effect on the radial yaw angle profile in the same region occupying the lower 35% annulus height which was also identified in Figure 3.40.

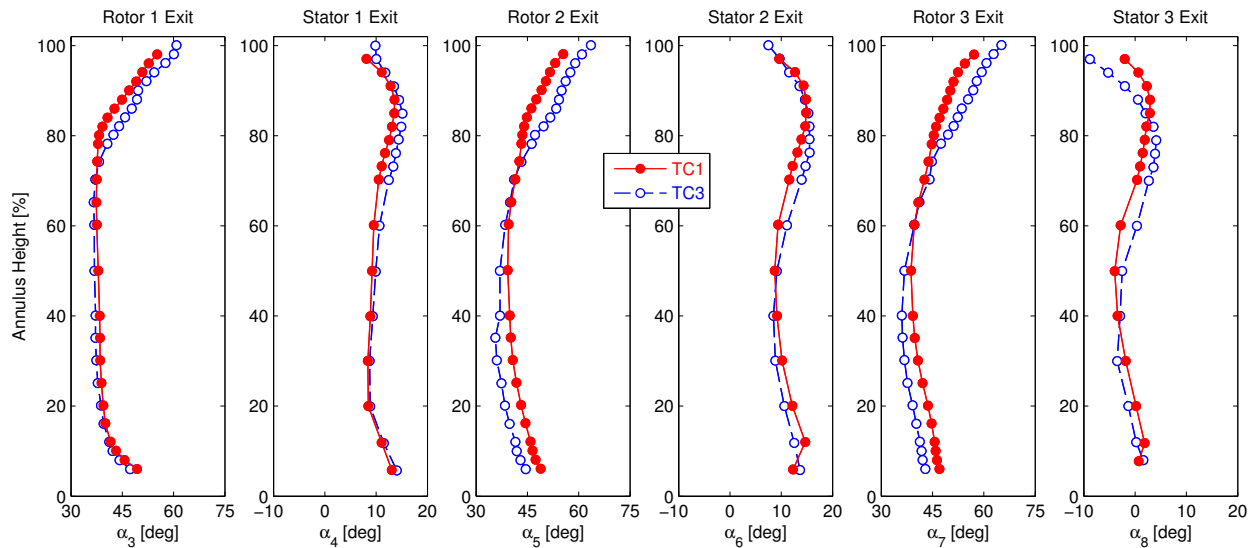


Figure 5.30: Radial profiles of absolute yaw angle at NL.

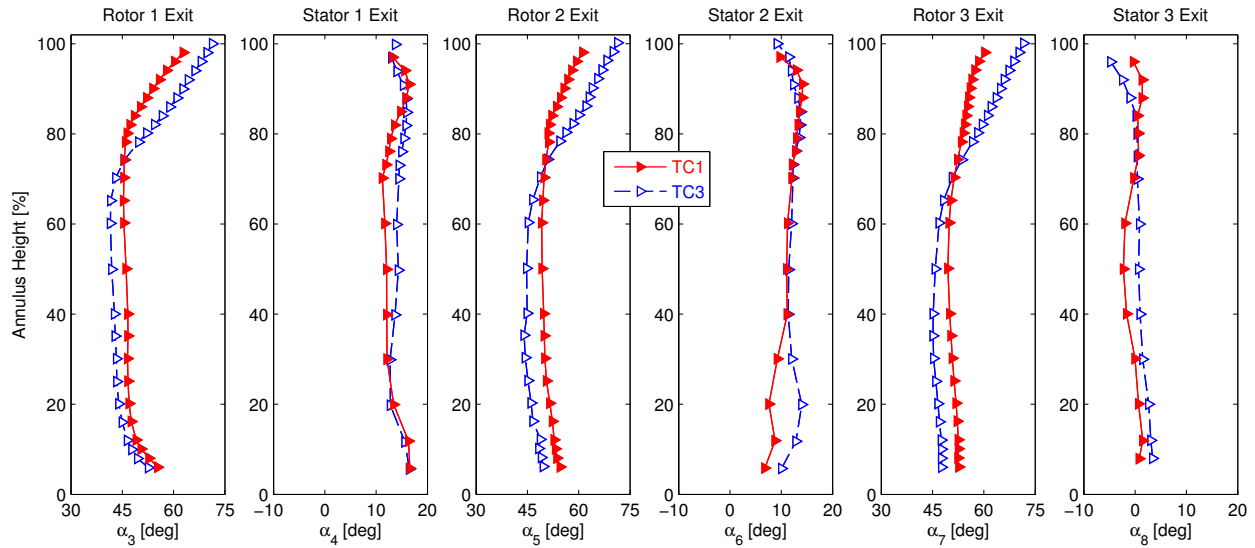


Figure 5.31: Radial profiles of absolute yaw angle at HL.

The constant annulus height of the Purdue three-stage compressor lends itself to a simplified parallel streamline assumption, thereby neglecting the need to consider substantial contributions of radial flow (i.e., pitch angles) in the flowfield. However, the centrifugal effect imparted to the fluid by the rotors has the effect of pushing fluid outward in the radial direction. As a result, the flow may be expected to have a slight positive trend of pitch angles across the annulus height. Indeed, the NL results of passage-averaged, time-averaged pitch angle profiles, Figure 5.32, show a slight positive profile across the entire annulus for TC1. Throughout this report, the explanations of results with increased tip clearance height have been based on the observation of redistributed flow from the tip toward the hub. For TC3, Figure 5.32 identifies this trend as the pitch angles in the flow regions unaffected by the leakage flow (i.e., less than 70% annulus height) decrease on the order of five degrees. This net change of pitch angles between TC1 and TC3 confirms the theory of flow distribution from the tip toward the hub.

At the stator exit planes, the sharp increase of pitch angle near the endwall has been documented by previous five-hole probe measurements in the same facility. However, this observation near the endwall may be attributable to the influence of the hole through which the measurement probe is inserted (i.e., for measurements above 95% annulus height).

At the HL operating condition, Figure 5.33, similar trends of pitch angle with annulus height are observed as the rotor tip clearance height is increased from TC1 to TC3. Especially for the Stator 2 exit results, the considerable decrease of hub corner separation with increased tip clearance height is also noted in the pitch angles.

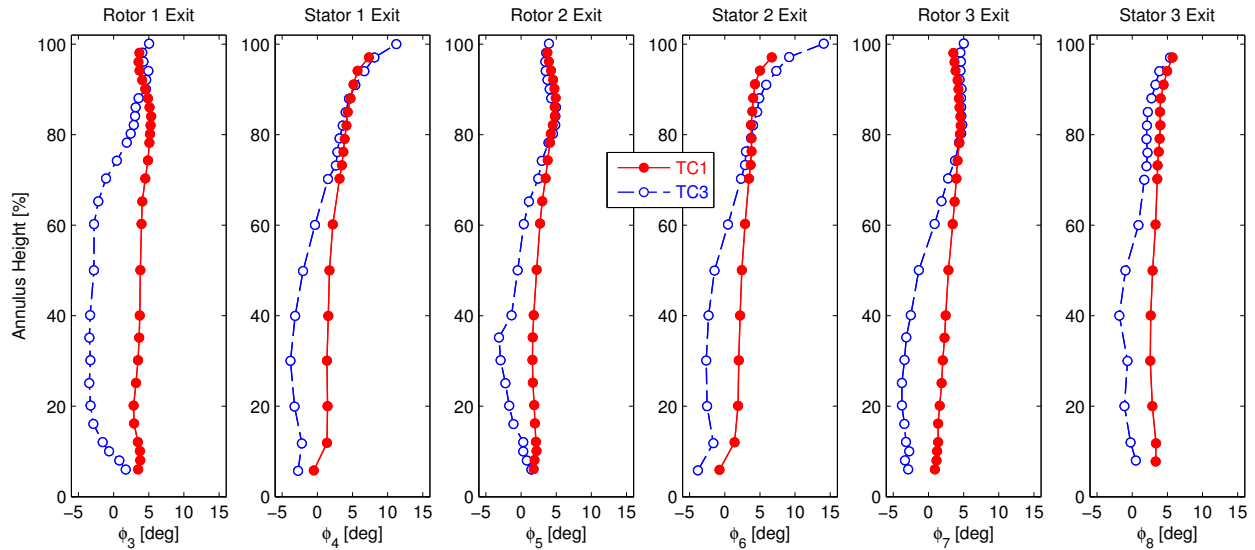


Figure 5.32: Radial profiles of pitch angle at NL.

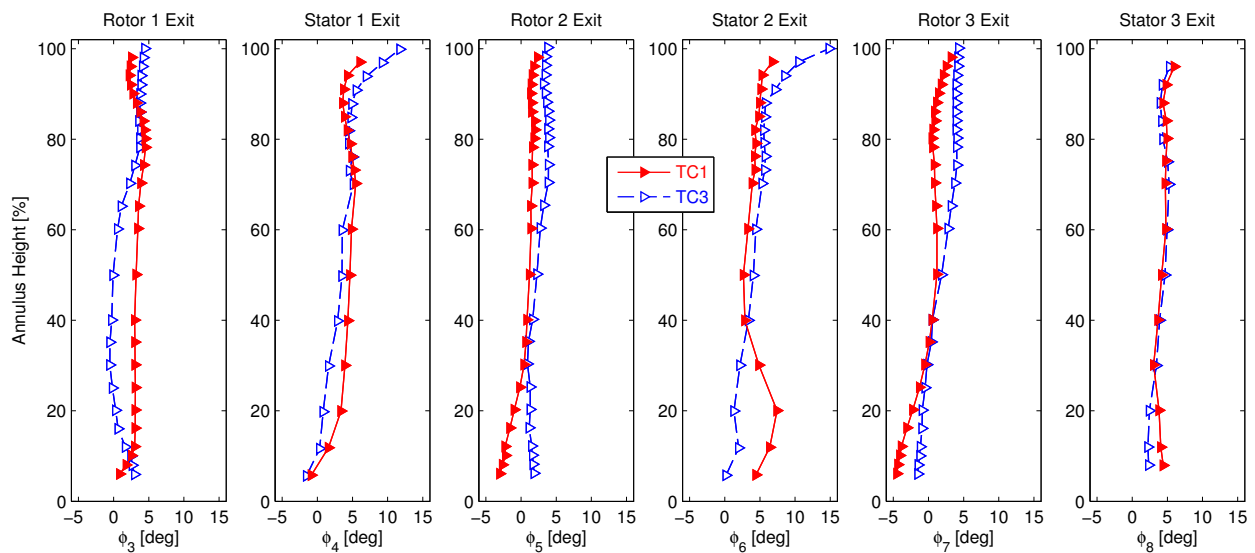


Figure 5.33: Radial profiles of pitch angle at HL.

To this point, allusion has been made to the redistribution of flow from the tip toward the hub as the tip clearance height is increased and the corresponding increase of the tip leakage flow affects the flow as increased blockage. The measured steady and time-resolved pressures have shown the redistribution of normalized pressure rise, and the flow visualization have shown the effect that the increased flow near the hub can have on the separated flow regions for the stationary vane rows. The absolute flow angles shown here in Figure 5.30 and Figure 5.31 provide further assurance of this trend. However, the axial velocity profiles can provide a more definitive representation of the mass flow rate through the machine to confirm the statements about redistributed mass flow suggested throughout this report.

These axial velocity profiles are shown in Figure 5.34 for the axial measurement planes at the exit of Rotor 2 and Rotor 3, which show the specific effect of the tip leakage flow on the rotor exit flow fields which will include the important multistage effects. The profiles in Figure 5.34(a-b) correspond to the nominal loading and high loading conditions, respectively, and the data have been normalized in all cases by the corresponding tip speed,  $U_t$ .

The results in Figure 5.34 show several interesting trends at both loading conditions. In particular, a comparison of the two rotors at NL or HL shows qualitatively similar profiles for each of the two tip clearance configurations. At the NL condition, Figure 5.34(a), there is a noticeable decrease of axial velocity in the tip region for both rotors and both tip clearances. However, the velocity profile has a profile across the span which resembles a parabolic profile. This contrasts with the HL condition, Figure 5.34(c), which shows a noticeable decrease of axial velocity near the tip (outer 20-30% span), but a more constant axial velocity profile across the lower 70-80% span. A comparison with the time-resolved total pressure measurements in Figure 5.24 through Figure 5.27 shows that this change of velocity profile is due to the thicker rotor wake at the high loading conditions, for which the separation off the suction surface of the rotor blade becomes more significant across a more substantial portion of the span.

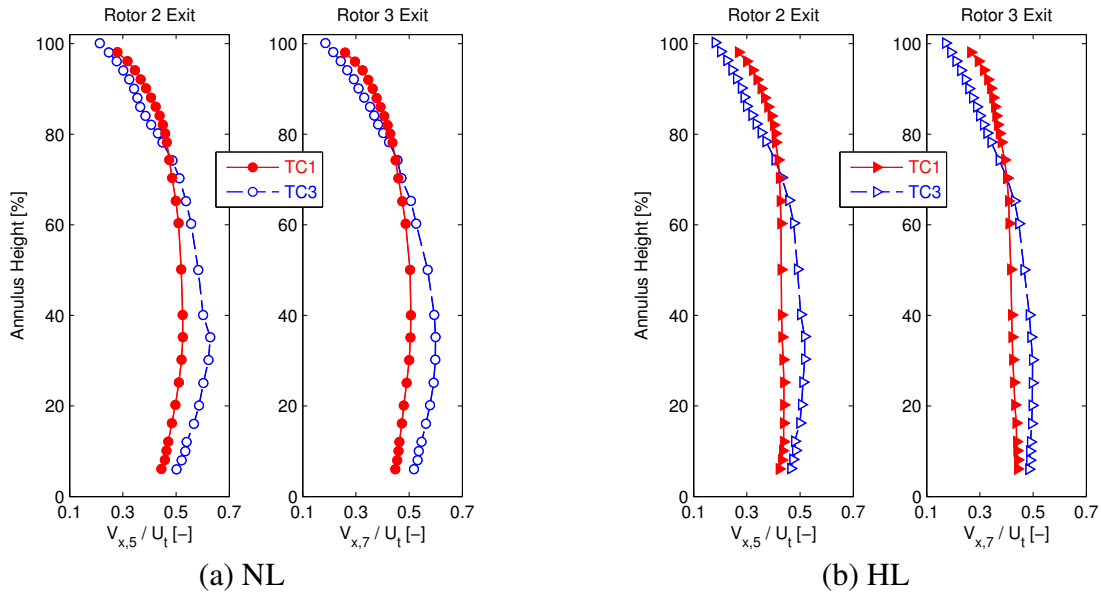


Figure 5.34: Radial profiles of normalized axial velocity at Rotor 2 and Rotor 3 exit.

### 5.3.2. Blockage

In addition to the flow angles presented in the previous section, the flow blockage at each axial measurement plane has been quantified using the method outlined by Suder (1998). As discussed in Section 2.5.3.3, the ambient temperature during hot-wire experiments has potentially introduced an additional inadvertent error in the data which prevents direct comparison of the velocity magnitudes from one test to the next. However, the blockage parameter is an alternative presentation method which relies less on the absolute magnitude of

the measurements for calculation. Thus, the blockage data presented here serve as a more meaningful method for comparing the effective flow velocities.

Suder (1998) defines the blockage quantification method as the effective reduction in flow area:

$$B = 1 - \frac{\text{effective area}}{\text{geometric area}}. \quad (5.3)$$

Equation (5.3) is further defined by evaluating the effective area as a function of the velocity-density deficit in the flow region,  $\delta^*$ :

$$B = 1 - \frac{A - \int \delta^* dr}{A}, \quad (5.4)$$

for which  $A$  represents the geometric flow area. The velocity-density deficit is analogous to the displacement thickness introduced through fundamental boundary layer theory:

$$\delta^* = \int_0^{2\pi/\text{NB}} \left( 1 - \frac{\rho u}{(\rho u)_{\text{inviscid}}} \right) r d\theta, \quad (5.5)$$

where NB is the number of blades (or vanes) in the row of interest.

For these data, the blockage can be calculated at the rotor exit planes by analyzing time-series measurements. The time series is first phase-locked ensemble-averaged, then passage-averaged across one vane pitch, and finally averaged over each of the blades in one row; this final product represents a mean rotor wake at the given measurement plane and loading condition. Similarly, the same blockage parameter can be calculated in a spatial reference frame (instead of a time series) at stator exit planes, for example. At these locations, the hot-wire signal is time-averaged and then presented as a function of pitch-wise location.

In either case, the physical method described by Suder (1998) is the same: determine a defect region via axial velocity gradients and the selection of an arbitrary cutoff value. For this study, the cutoff value was chosen to be  $3 \text{ s}^{-1}$  for all conditions. In agreement with Suder's conclusion, the arbitrary selection of the cutoff values has a negligible effect on the result (less than 5% change of calculated blockage values). Several cutoff values in the range of  $1\text{-}5 \text{ s}^{-1}$  were considered for these data. Examples of the axial velocity data and the corresponding defect region are shown in Figure 5.35 and Figure 5.36 for rotor exit data and stator exit data, respectively.

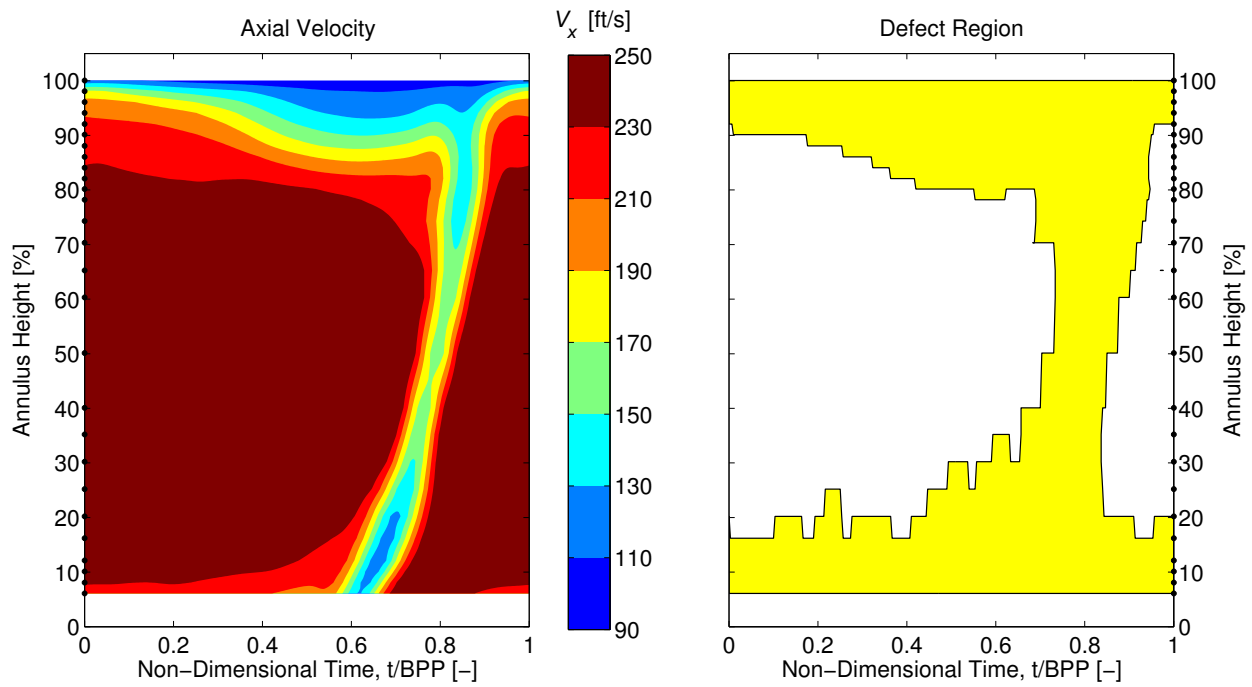


Figure 5.35: Example of defect region identification for Rotor 2 exit (TC1, NL).

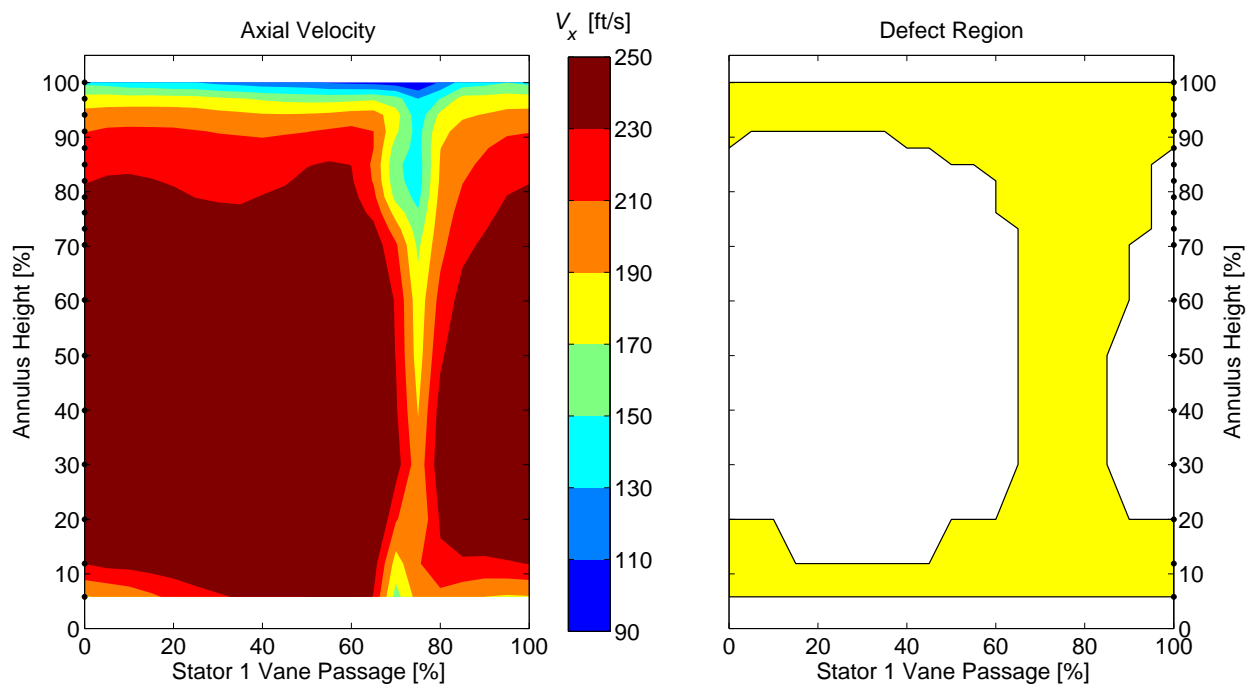


Figure 5.36: Example of defect region identification for Stator 1 exit (TC1, NL).

The calculated blockage values are presented in Figure 5.37 for the nominal loading (NL) condition and Figure 5.38 for the high loading (HL) condition. A summary of these results is also listed in Table 5.1 as a representative one-dimensional blockage value for each axial measurement position, loading condition, and tip clearance configuration. A preliminary analysis of the results in Figure 5.37 show the most significant changes in blockage are observed in the tip region at Rotor 1 exit, Stator 2 exit, and Stator 3 exit for the two tip clearance configurations investigated here (TC1 and TC3). Considering the total pressure measurements at Rotor 1 exit in Figure 5.22, it is not surprising that there is a more significant blockage region due to the increased tip leakage flow disturbance. However, it is particularly interesting that the same disturbance does not appear as significantly in the calculated blockage for the Rotor 2 and Rotor 3 exit data. Although the Rotor 2 exit data do show an increase of blockage on the order of 10% in the region from 80 to 90% annulus height, the Rotor 1 exit data are nearly 20% different between the two tip clearance configurations across the region spanning 80 to 100% annulus height.

The Stator 2 exit total pressure field, Figure 3.39, reveals that the increased blockage in the tip region at the same location in Figure 5.37 is due to largely to low pressure regions near the wall, not the wake itself. On the other hand, the Stator 3 exit total pressure field (Figure 3.41) shows a thicker wake in the outer 50% of the flow annulus between the two tip clearance configurations. However, this blockage effect is only identified for the outer 30% of the flow annulus.

As the compressor is throttled toward stall, the similarity between the observed blockage trends at each rotor exit plane increases, Figure 5.38. Of the three rotors, Rotor 3 actually shows a decrease of blockage in the tip region with increased loading for TC1, a result which is not surprising considering the difference of Rotor 3 exit measurements at the same conditions presented earlier. In Figure 5.26 and Figure 5.27, the mean wake contours of RMS total pressure show the leakage flow region is decreased at high loading, but at the expense of a very thick wake at HL which extends across a majority of the passage. Based on the calculated values in Table 5.1, the more intense fluctuating wake region extending across the blade span is significant enough to offset the blockage created by the leakage flow at NL (and more). Also at the three rotor exit planes, the blockage differences between the two tip clearance configurations approach 30% and the radial extent begins at approximately 70% annulus height for all rotors – a similarity which was not observed as clearly for the three rotors at the NL condition.

For the high loading condition, a comparison of the two tip clearance configurations at Stator 2 exit confirms the expectations from the steady total pressure traverses shown previously in Figure 3.40 and flow visualization photographs. Although the Stator 2 exit blockage in Figure 5.38 increases across the outer 60% annulus height (on the order of 10% increased blockage), the reduction of the corner separation region off the suction surface of the vane is represented by the decrease of blockage in the lower 40% annulus height (on the order of 10% decreased blockage).

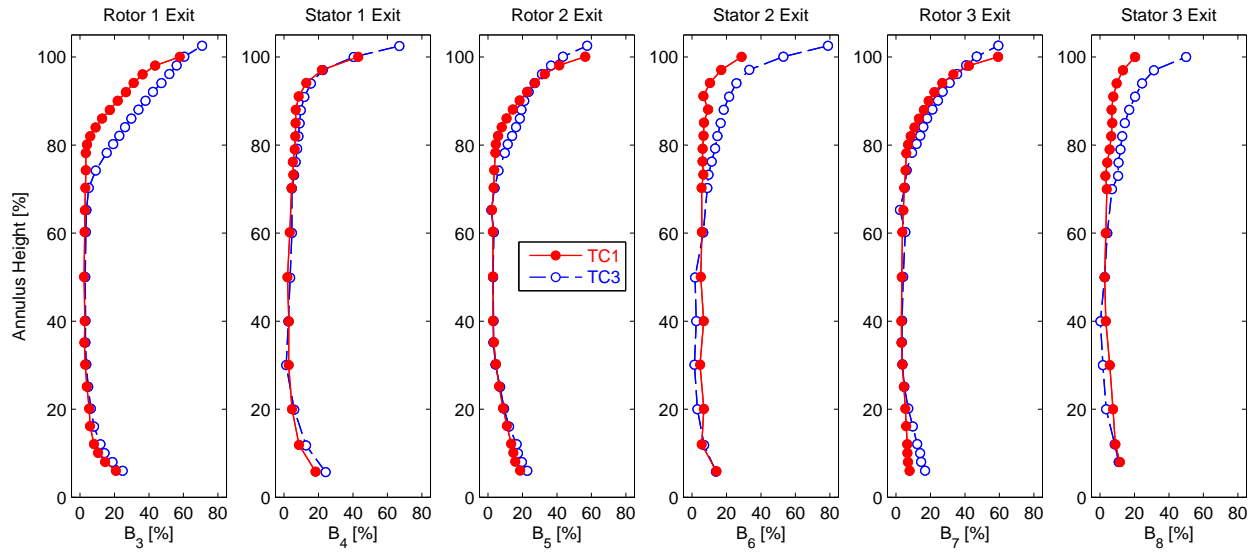


Figure 5.37: Radial profiles of blockage at NL.

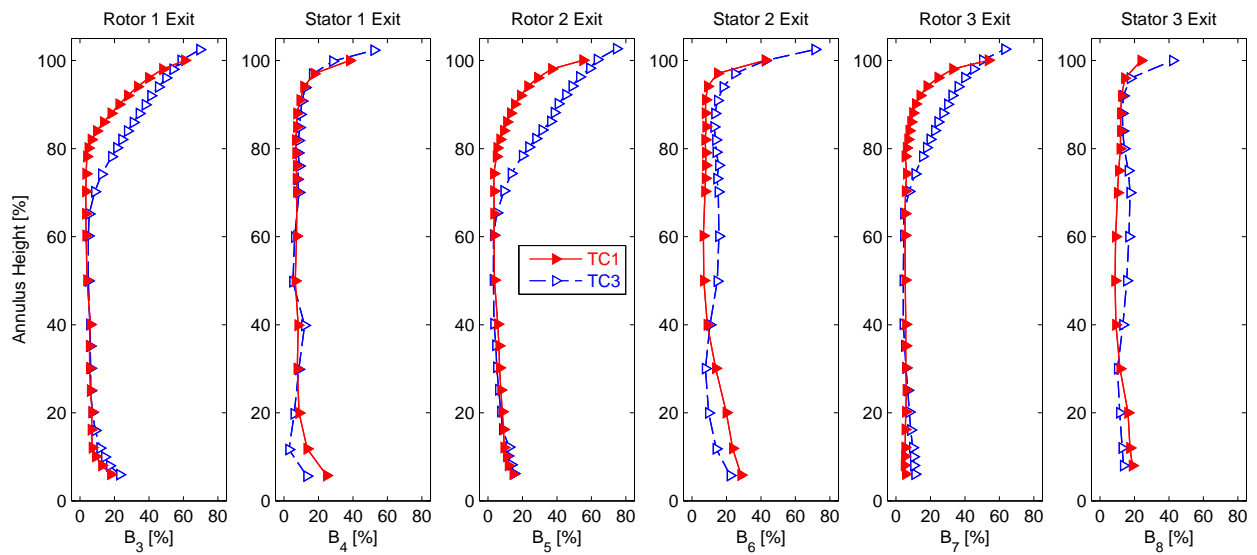


Figure 5.38: Radial profiles of blockage at HL.

Table 5.1: Summary of one-dimensional blockage parameters, listed in percent flow area.

TC Config.	Loading	R1 Exit	S1 Exit	R2 Exit	S2 Exit	R3 Exit	S3 Exit
TC1	NL	9.1	6.8	9.3	7.4	8.4	6.2
	HL	10.2	10.0	11.8	12.4	11.8	12.3
TC3	NL	15.5	9.4	9.0	10.9	7.6	8.5
	HL	16.6	9.4	16.4	15.4	13.3	14.2

### 5.3.3. Streamwise Vorticity

The streamwise vorticity provides an additional method for evaluating the leakage flow region once the three-dimensional velocity vectors are known. Because the ensemble-average technique has been used to calculate the velocity vectors, the presence of an instantaneous vortex cannot be evaluated. However, this technique can still determine the average rotational motion in the leakage flow region.

Inoue et al. (1986) define the streamwise vorticity by calculating the projection of two vorticity components on the streamwise flow direction (defined by the relative flow angle,  $\beta$ ):

$$\omega_{st} = \left[ \frac{1}{r} \frac{\partial(rV_\theta)}{\partial r} - \frac{1}{r} \frac{\partial V_r}{\partial \theta} \right] \cos \beta - \left[ \frac{1}{r} \frac{\partial V_r}{\partial x} - \frac{\partial V_x}{\partial r} \right] \sin \beta, \quad (5.6)$$

where the first bracketed terms represents the axial vorticity,  $\omega_x$ , and the second bracketed term represents the tangential vorticity,  $\omega_\theta$ . Unlike the measurements collected by Inoue et al., the data collected in this study were only captured at one axial survey plane downstream of each rotor. As a result, the gradient of radial absolute velocity,  $\partial V_r / \partial x$ , cannot be evaluated for these measurements. Future studies may build in the ability to evaluate this change in the axial flow direction. However, if the contributions from this gradient are assumed to be small with respect to the other components, they can be neglected. Under this assumption, the streamwise vorticity is simplified:

$$\omega_{st} = \left[ \frac{1}{r} \frac{\partial(rV_\theta)}{\partial r} - \frac{1}{r} \frac{\partial V_r}{\partial \theta} \right] \cos \beta - \left[ -\frac{\partial V_x}{\partial r} \right] \sin \beta. \quad (5.7)$$

The derivatives needed for Equation (5.7) were numerically calculated using a central differencing scheme, with exception to the edges of the data region, which were calculated as single-sided differences.

Figure 5.39 shows contours of streamwise vorticity, as calculated from Equation (5.7), for two different tip clearance configurations and two loading conditions at the Rotor 1 exit plane. The calculated vorticity results in Figure 5.39 are normalized by the angular velocity of the rotor,  $\Omega$ . The leakage flow structures identified in Figure 5.39 are very similar to the regions identified by the passage-averaged time-resolved total pressure measurements in Figure 5.22 and Figure 5.23. Specifically, the leakage flow for TC1 extends downward to approximately 80% span, whereas the leakage flow for TC3 extends to approximately 70% span for NL and 65% span for HL. However, Figure 5.39 also shows that the regions of high vorticity typically associated with the tip leakage vortex (recall, these data are ensemble-averaged and passage-averaged, so they do not represent an instantaneous vortex) does not stay attached to the wall, but moves radially downward into the passage. These results suggest that, although the total pressure unsteadiness (RMS) at the rotor exit plane is an adequate method for identifying the leakage flow region, those results may not sufficiently represent any true vortex structures.

Further analysis of the contours in Figure 5.39 shows the difference of the wake region for TC1 versus TC3. Inoue et al. (1986) also identified these regions of positive and negative vorticity associated with the passing rotor wake, an observation which was attributed to the radial velocities induced by the centrifugal effects of the passing rotor. However, there is a significant reduction of both the positive and negative regions of vorticity in the rotor wake as the tip clearance height is increased from TC1 to TC3. This observation can be linked to the redistribution of flow velocity toward the hub, which energizes the separation-prone fluid on the rotor suction surface and effectively reduces the strength of the wake region (although

comparisons of the yaw angle wake profiles at several spanwise locations, not shown here, suggest the width of the wake may not necessarily become narrower). Indeed, a deeper investigation of the contribution from each of the three velocity gradients in Equation (5.7) shows that the  $\partial V_r / \partial \theta$  component of the streamwise vorticity has a peak value which not only changes magnitude, but also its circumferential position, leading to the change of the wake vorticity. This observed trend is in contrast to the other two components in Equation (5.7) which have peak values that are unaffected in their circumferential position and show a change only in their magnitude.

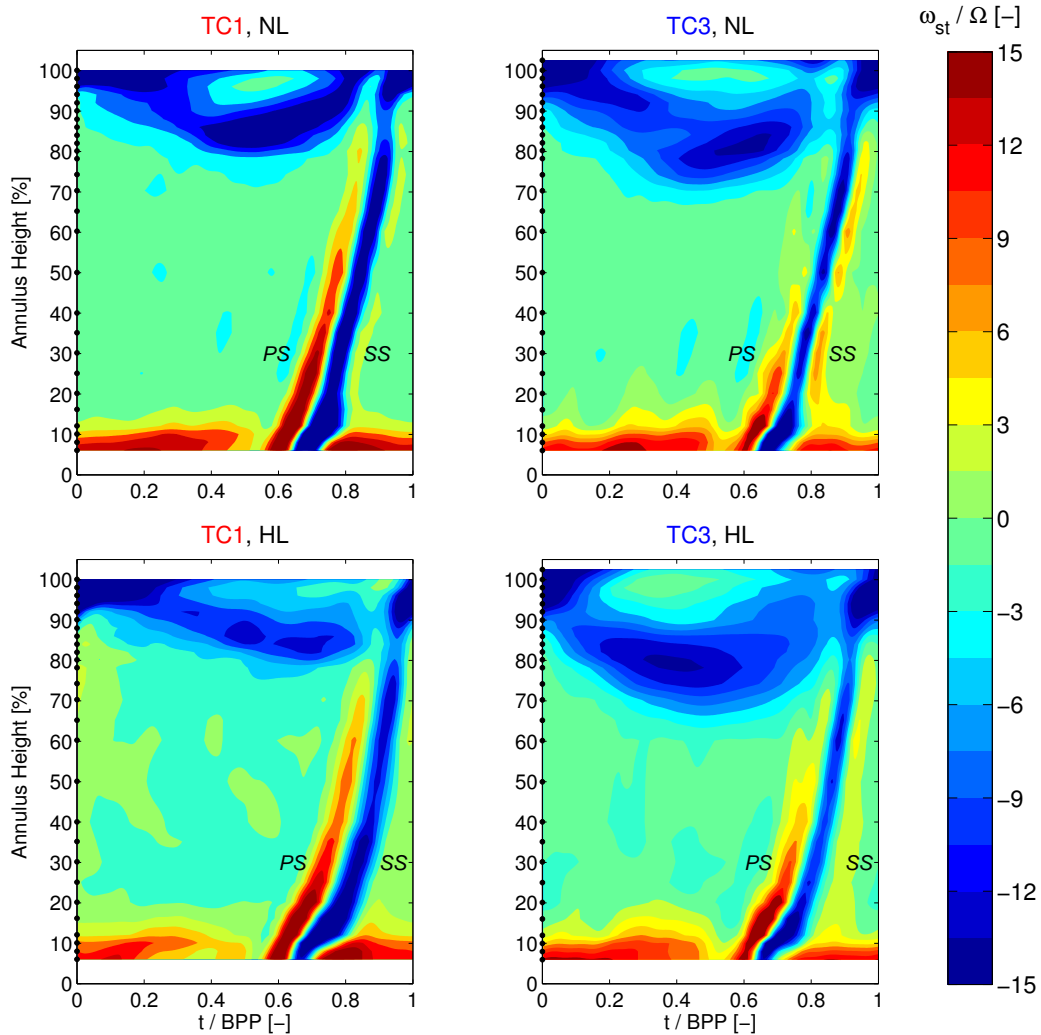


Figure 5.39: Contours of streamwise vorticity at Rotor 1 exit for TC1 and TC3.

In addition to these results for Rotor 1, the streamwise vorticity is also presented for TC1 at the exit of Rotor 2 and Rotor 3 in Figure 5.40. These results confirm many of the previous analyses suggesting the Rotor 2 and Rotor 3 may behave similarly to each other, but different from Rotor 1. In particular, a qualitative comparison of the streamwise vorticity contours in Figure 5.40 shows leakage flow vorticity structures which are similar in size and shape. A primary difference here is the results at Rotor 3 exit for both NL and HL extend downward

approximately 5% deeper into the passage than the results at Rotor 2 exit. This difference compares well with the leakage flow regions identified by high unsteadiness in the time-resolved total pressures, Figure 5.24 through Figure 5.27, and similar comparisons can be drawn between the rotor wake shapes at the two measurement locations.

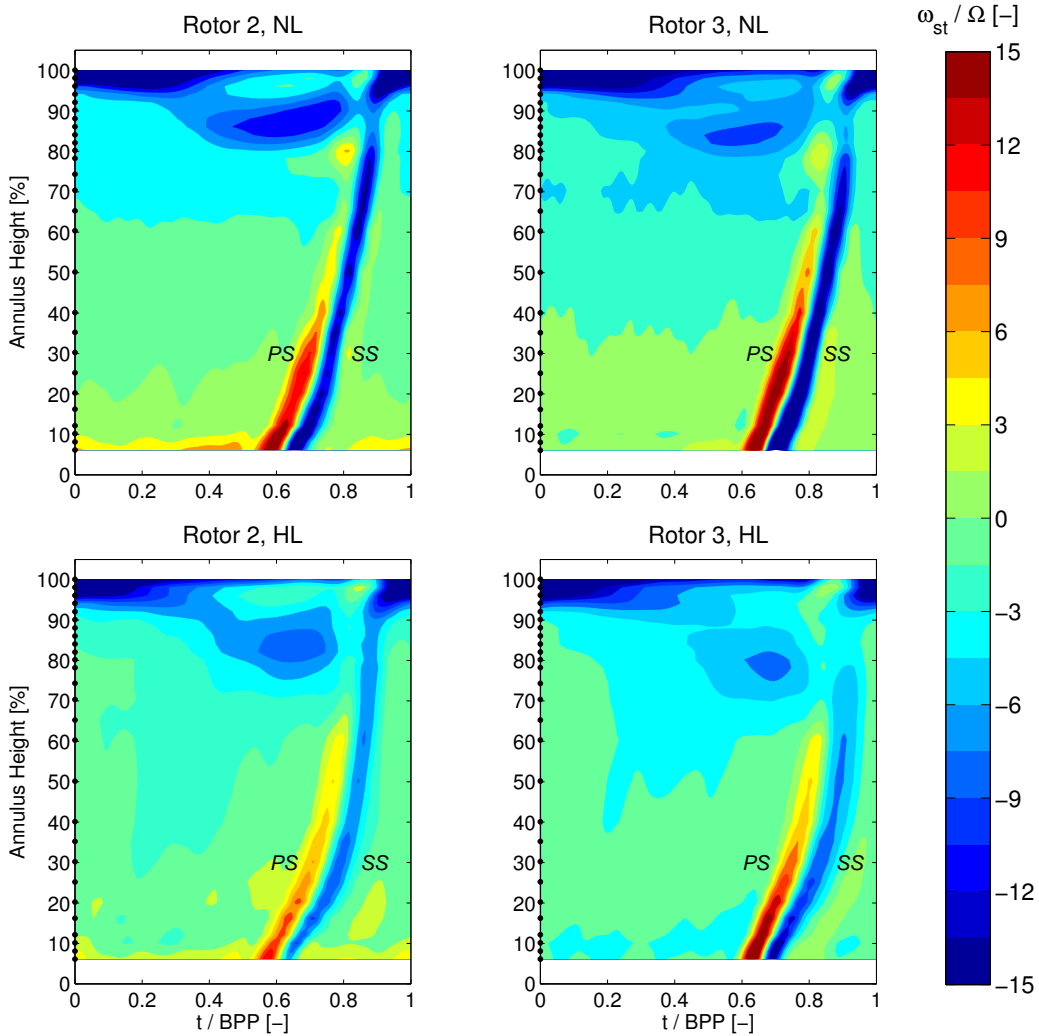


Figure 5.40: Contours of streamwise vorticity at for TC1 at Rotor 2 and Rotor 3 exit.

To supplement the streamwise vorticity contours shown here, the maximum vorticity strength has been quantified for each of the test conditions. The vorticity contour plots (e.g, Figure 5.39 and Figure 5.40) were used to locate the region of the blade passage which corresponds to the leakage flow. In this region, a search tool identified the largest negative value (based on the coordinate system in the above figures).

This information, presented in Figure 5.41, summarizes the streamwise vorticity results from all of the test conditions to one-dimensional values for comparison. These data show that as the rotor tip clearance is increased from TC1 to TC3, the maximum vorticity strength in the leakage flow region increases for Rotor 2 and Rotor 3, but decreases for Rotor 1. A comparison of the Rotor 1 vorticity contours for TC1 in Figure 5.39 shows that the change of the shape of the

high negative vorticity region identified as the leakage flow from NL to HL is more dramatic than any of the other conditions shown here. This change of the leakage flow shape may contribute to the different for Rotor 1 at NL in Figure 5.41. Finally, as the loading condition changes from NL to HL, there is a consistent decrease of maximum streamwise vorticity strength. This trend shows an inverse proportionality of leakage flow size (Figure 5.29) with maximum vorticity strength in the leakage flow region which holds for a change in loading condition, but not a change in tip clearance height. The results in Figure 5.41 have been calculated for the passage-averaged vorticity, as shown in the contour plots above, but follow-on work will analyze the change of maximum streamwise vorticity strength with the stator-rotor interaction. This future analysis will allow the identification of a range for the bars in Figure 5.41, similar to the ranges defined in Figure 5.29.

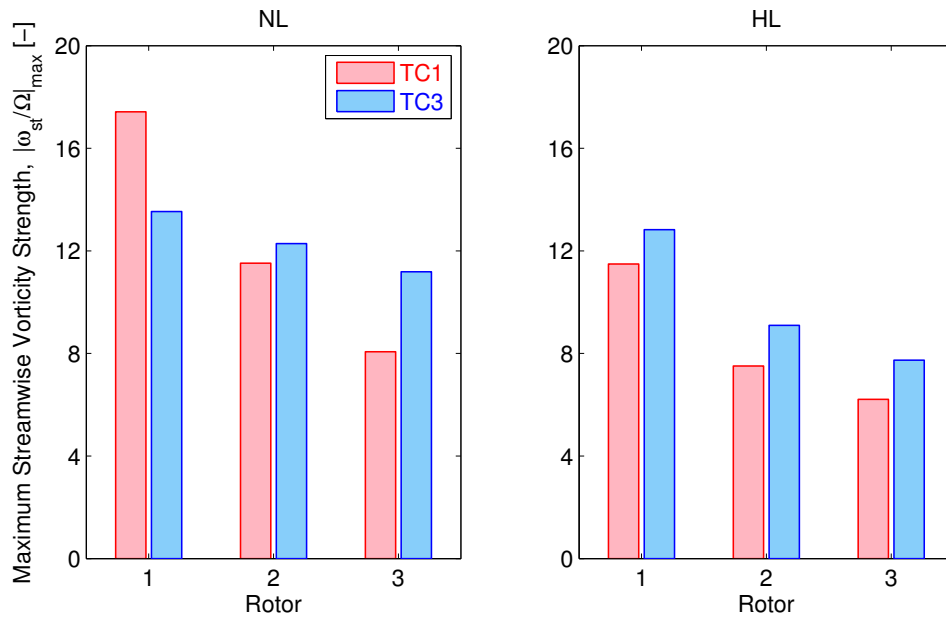


Figure 5.41: Passage-averaged maximum streamwise vorticity strength.

## CHAPTER 6: PARTICLE IMAGE VELOCIMETRY

*Sayantana Bhattacharya and Pavlos P. Vlachos*

The objective of the PIV aspect of this project was to develop a technique to acquire data in the tip flow region of an embedded rotor in a multistage compressor. The unique aspect of this work is that the same window used to acquire the images was also used to deliver the laser illumination to the flow field, thus eliminating the need for inserting a periscopic probe to the flow field. The successful implementation of this technique at two loading conditions (nominal and high loading) for the TC3 tip clearance configuration is discussed below.

The three-component vector fields obtained by generalized stereo reconstruction at each circumferential location were analyzed. The recorded stereo image coordinate system was reoriented and scaled to express the data in terms of the coordinate system defined by axial chord, span, and blade passage. The blade tip velocity was subtracted from the circumferential velocity component to change from absolute frame of reference to compressor blade coordinate system. The flow direction and the coordinate system are expressed in the following schematic (Figure 6.1).

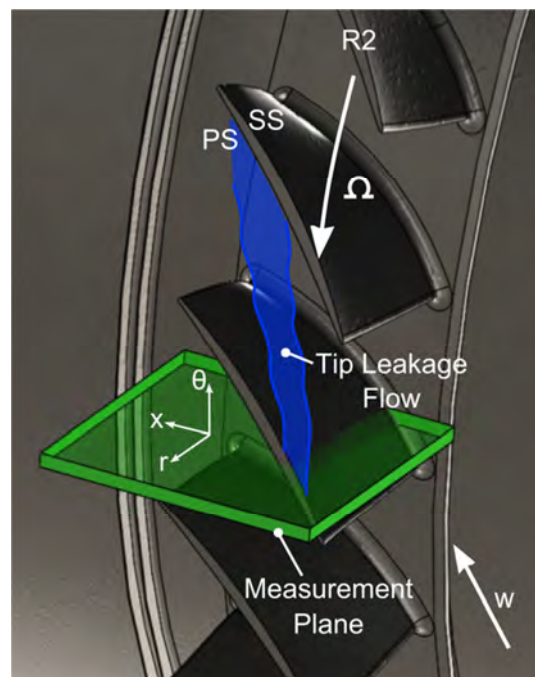


Figure 6.1: Schematic of the PIV measurement plane and corresponding coordinate system.

### 6.1. Stereo Results

The twenty measurement planes containing the three-component planar velocity fields were combined to reconstruct the volumetric vector field across the blade passage. The effective domain was 70% to 96% span, 15% to 90% axial chord and 100% blade passage. The velocity field was smoothed with a Gaussian kernel of 2 standard deviations and a window size of 7x7

grid points to reduce the noise in the flow field. The volume of data was then sliced in constant span-wise locations as shown in the following figures. Although the measurements were across one complete blade passage, for more intuitive representation the domain was periodically repeated along the blade passage direction.

The radial velocity contours in Figure 6.2 show a radial inflow and outflow represented by the blue and the red regions, respectively. For the nominal loading case, the alternating red and blue region close to the suction side of the blade is indicative of the tip leakage flow and this structure expands as the flow passes through the blade passage. A radial outflow is also observed on the pressure side close to the blade tip and within 20% axial chord, which essentially rolls up on the suction side and forms the tip leakage vortex. However, for the high loading case, little radial inflow is observed close to the tip of the blade within 20% axial chord and the radial outflow on the pressure side of the blade is more dominant throughout the passage flow at the 95% spanwise slice. At high loading, the radial inflow is observed at spanwise slices away from the tip.

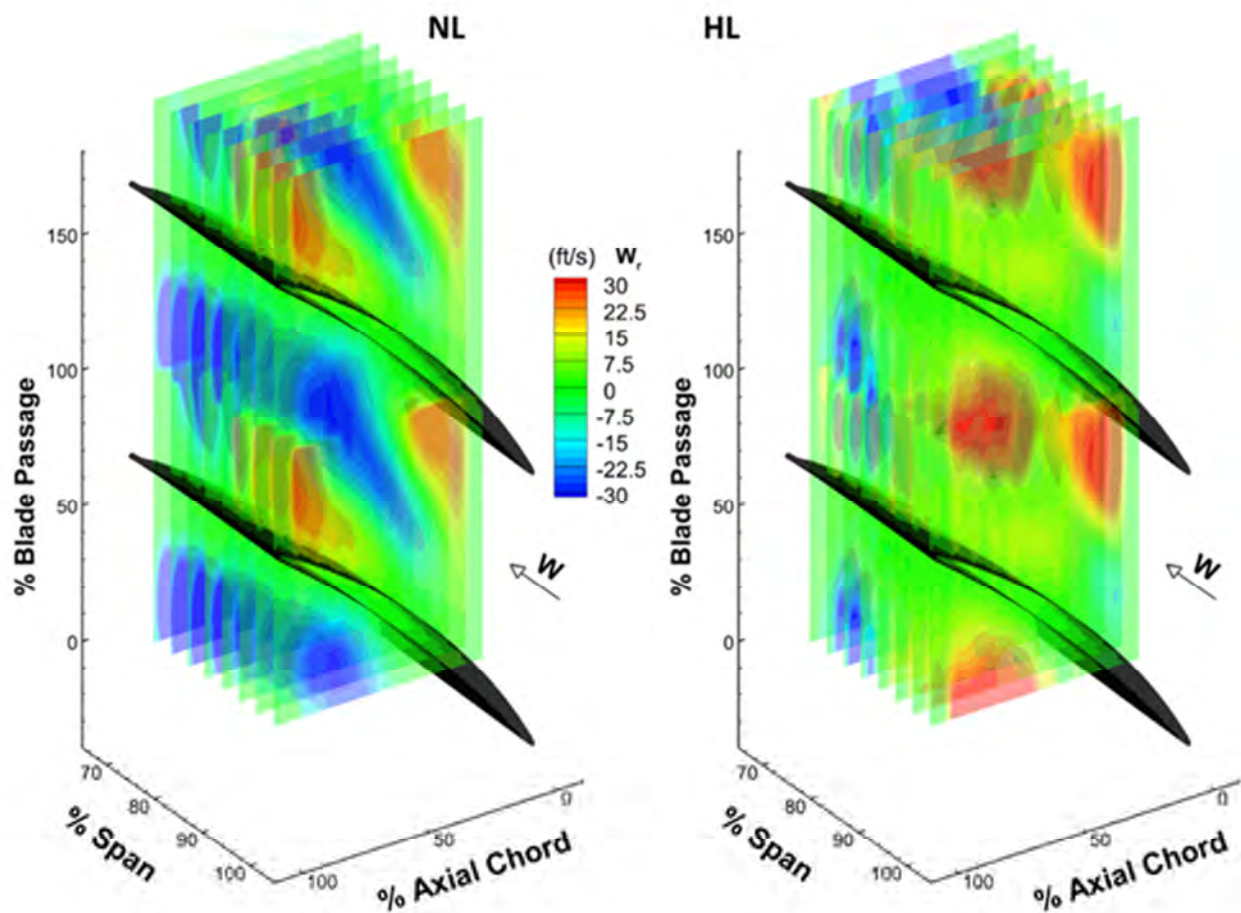


Figure 6.2: Spanwise volume slices of radial velocity for stereo reconstructed velocity field at two loading conditions.

The radial velocity at each spanwise location is examined in detail for both loading conditions. Figure 6.3 shows the spanwise slices for the nominal loading condition. The blue region with negative radial velocity is present from 95% to 75% span and extends through almost 70% of the blade passage. The consecutive red and blue region indicating the tip leakage flow is present on the suction side of the blade up to 84.5% span, and after that, the secondary flow breaks into small regions of radially inward flow. The positive relative radial velocity,  $W_r$ , near the pressure side of the blade within 20% axial chord is very strong at the 95% span location and decreases gradually towards the hub.

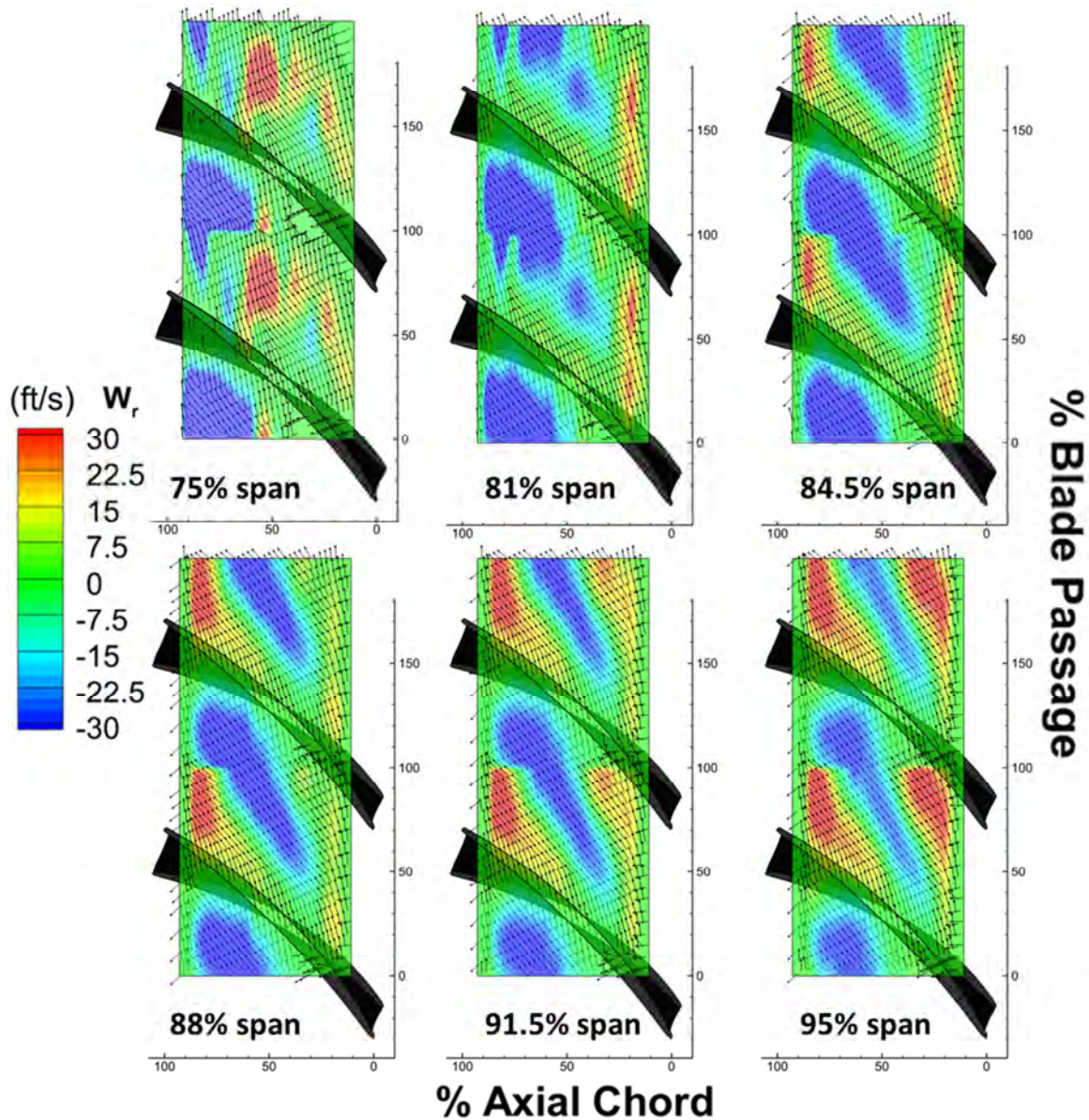


Figure 6.3: Contours of radial velocity at different span-wise location for NL. A vector field representing the projected velocity in the  $r - \theta$  plane is superimposed over the contours. Flow is from right to left.

For the high loading condition, a strong radial outflow is dominant throughout the spanwise slices on the pressure side of the blade and within first 25% of the axial chord (Figure 6.4). Also, the blade passage is dominated by a strong positive radial component (red and yellow contours) with a few blue regions in between up to 88% span. From 95% span to 75% span, the secondary flow towards the hub increases for the high loading case.

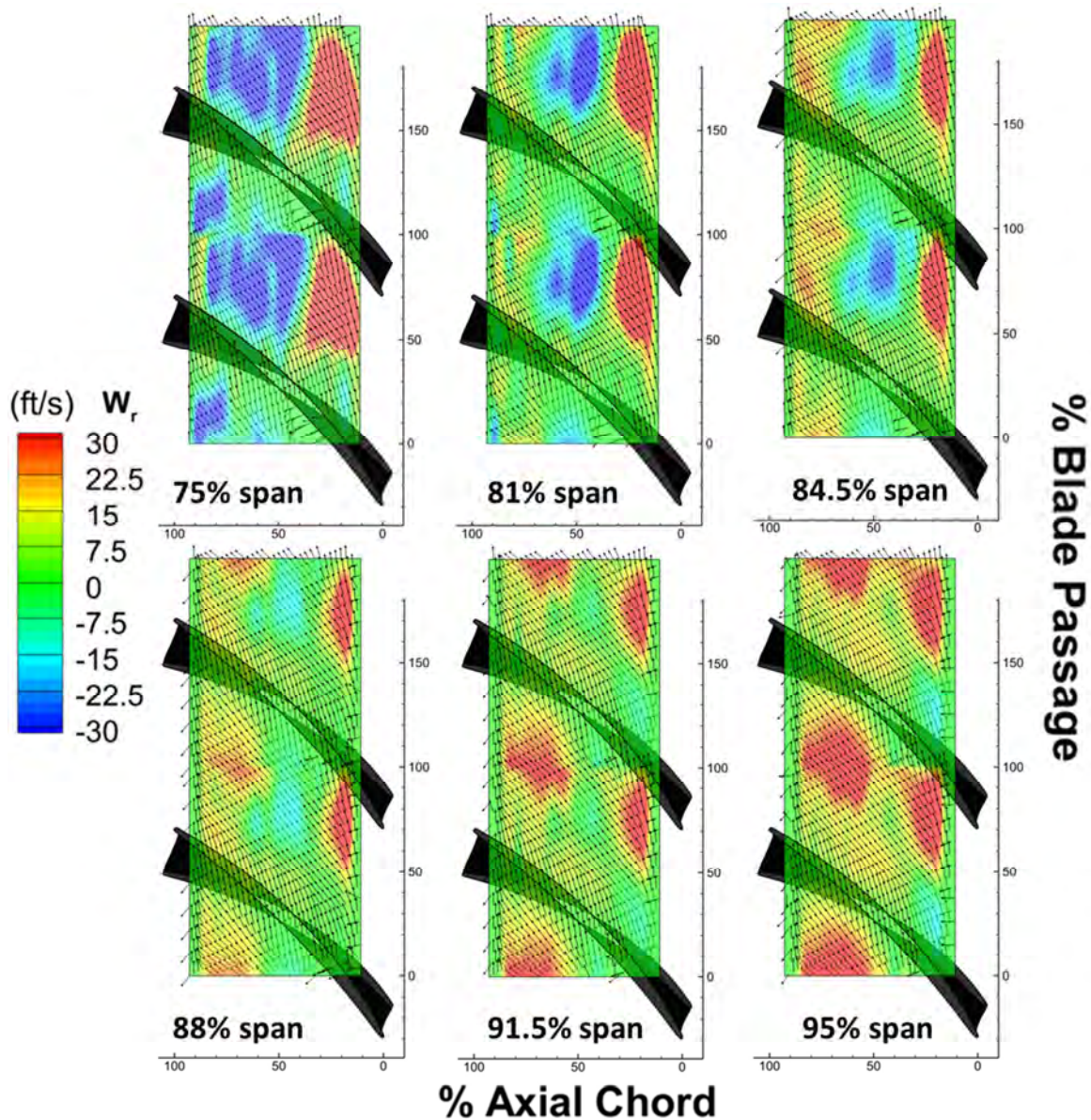


Figure 6.4: Contours of radial velocity at different span-wise location for HL. A vector field representing the projected velocity in the  $r - \theta$  plane is superimposed over the contours. Flow is from right to left.

The vectors in both Figure 6.3 and Figure 6.4 are projections of the three-dimensional velocity vector onto the  $r - \theta$  plane. The relative velocity vectors in the blade frame of reference reveal the primary flow from right to left following the staggered blade passage. The vectors are

physically consistent in the middle of the passage, except along the edge of the blades and the side of the domain of measurement. The presence of spurious vectors in this region is mainly an artifact of the smoothing operation along the blade edges where no vectors were initially present.

## 6.2. Tomographic Results

In addition to the stereo results presented above in Figure 6.2 through Figure 6.4, tomographic reconstructions were also created, as described in Section 2.6.2. The tomographic PIV vector fields were also interpolated and smoothed using Gaussian smoothing. The three dimensional vector fields were obtained for twenty phase locked positions along the circumference with a 15% overlap between the volumes. The individual volumes were stacked up to represent the flow field within the blade passage, and the spanwise slices in the measurement volume are shown in Figure 6.5.

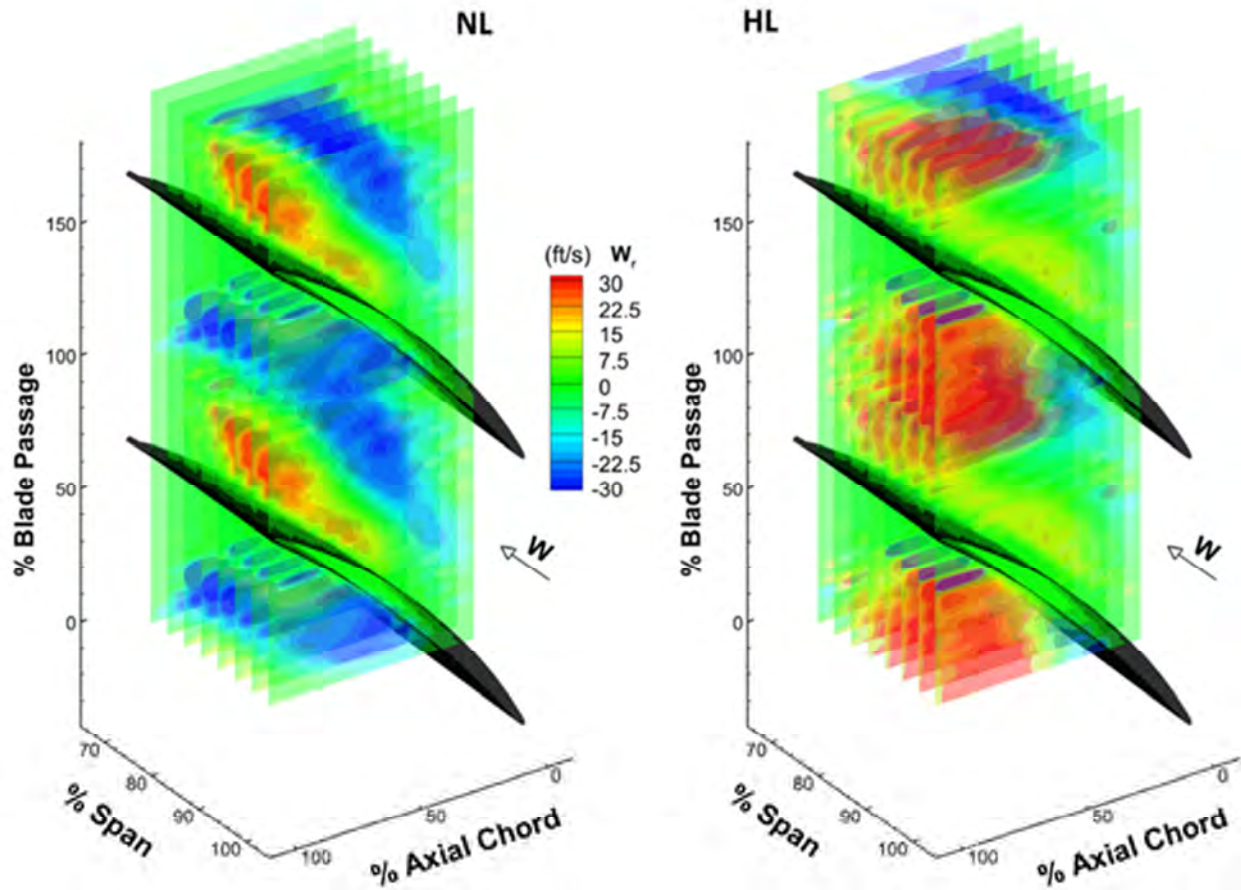


Figure 6.5: Spanwise volume slices of radial velocity for tomographic reconstructed velocity field at two loading conditions.

The results for both loading conditions show adjacent radial inflow and outflow region on the suction side of the blades and this structure extended throughout the blade passage. Comparing the results with the stereo reconstructed measurements, a few differences are

observed. First, the strong radial outflow on the pressure side of the blade within 20% axial chord, which was observed in the stereo results, is not present in the tomographic PIV results. Second, for the high loading case, although the radial outflow is still dominant in the slices towards the tip at 95% span, the radial inflow (blue) region is more prominent for this particular case even at 95% span as compared to the stereo results. Despite minor differences, overall the tomographic PIV results are similar to the ones obtain with stereo-PIV. However, the quality of the tomographic PIV solution greatly depends on the tomographic reconstruction and eliminating the “ghost” or false reconstructed particles. Thus, further efforts are necessary to achieve a more robust volumetric reconstruction and to minimize the noise in the output vector fields.

### **6.3. Summary**

These results show the capability to do three-dimensional volumetric PIV measurements in a high-speed multistage compressor without introducing any probe in the measurement volume. All the previous PIV measurements to date have introduced a light sheet probe which inevitably creates a disturbance in the downstream rotor flow region. Here, the laser sheet was introduced through a glass window on the casing and the cameras were focused on a 4mm thick laser sheet through the same window. Reflection was overcome by using fluorescent particles and filters in front of the lenses. Phase-locked measurements were taken in one complete blade passage. Using multiple camera information both stereoscopic and tomographic PIV velocity fields were obtained.

## CHAPTER 7: SUMMARY AND CONCLUSIONS

*Reid A. Berdanier and Nicole L. Key*

The effect of rotor tip clearances on axial compressor performance has been a focus of research for several decades. In general, studies have found that pressure rise capability, efficiency, and operability range all decrease as the rotor tip clearance height is increased. However, the future of gas turbine engine engineering is moving toward designs which will incorporate smaller blade heights in the rear stages of high pressure compressors. As a result, a decrease in blade heights and a corresponding increase in relative rotor tip clearances are expected in the rear stages of these next-generation compressors. Therefore, a better understanding of the fundamental flow physics and multistage performance effects related to large tip clearance heights in axial compressors is a necessity.

### **7.1. Overview of Methods and Findings**

This work has investigated the effects of large rotor tip clearances on the performance of a three-stage axial compressor at Purdue University. A series of experimental measurement techniques has been implemented to evaluate compressor performance and interrogate the tip leakage flow for three rotor tip clearances: 1.5%, 3.0%, and 4.0% based on annulus height.

Benchmark compressor performance measurements showed the pressure rise capability and isentropic compressor efficiency through the machine decrease approximately linearly with rotor tip clearance height. Measurements with seven-element total pressure and total temperature rakes inserted at inter-stage locations in the compressor showed a redistribution of flow from the tip toward the hub as the tip clearance height was increased. This effect is due to the increased blockage related to the tip leakage flow.

Stall inception evaluated using piezoresistive pressure transducers distributed circumferentially around the compressor, approximately 10% axial chord upstream of the rotor leading edges. These measurements showed the compressor stalls as a result of long length-scale modal disturbances for the 100% corrected speedline with the 1.5% tip clearance configuration. Previous research has suggested modal stall characteristics may be expected when the individual stages of a multistage compressor are well-matched. At part-speed operating conditions, or when the tip clearance height was increased, however, the compressor was more likely to exhibit spike-type stall inception mechanisms emanating from Rotor 1.

Additional time-resolved measurements of total pressure at the rotor exit planes and hot-wire measurements of three-dimensional flow velocities were collected for two tip clearance configurations at two loading conditions on the 100% corrected speedline: a nominal loading point near the peak efficiency point and a low flow rate high loading point. By casting the rotor exit dynamic total pressures in terms of an unsteadiness parameter (the RMS with respect to the ensemble average), the radial and circumferential extent of the tip leakage flow disturbance was evaluated. These measurements, in addition to flow visualization images, helped to identify a modulation of the tip leakage flow, affecting its size and depth of penetration into the main flow, as the rotor interacts with the wakes propagating from the upstream stator. Also, these time-resolved velocity data were also used to quantify the blockage at each measurement plane and

correlate the blockage with the observed tip leakage flow disturbance. Additionally, streamwise vorticity calculations were used to characterize the strength of the leakage flow from each rotor.

Finally, a novel three-dimensional PIV measurement technique has been developed for application in multistage compressors. This new technique circumvents the need to introduce intrusive probes for light sheet delivery. Instead, the laser sheet was introduced through the same optical access window used to acquire the images. Issues with reflections from the incident light were overcome through the use of fluorescent seed particles and appropriate optical filters on the cameras. Phase-locked measurements were collected using four cameras in stereo configurations to reconstruct planar velocity fields, as well as an out-of-plane component. Initial tomographic reconstructions were performed, as well.

The measurements collected for this project represent a unique data set which contributes to better understanding the tip leakage flow field and its associated loss mechanisms. These data will serve the community as a method for validating computational design tools, especially at off-design conditions. Through this process, the results presented herein will aid in the development of new blade designs which could be desensitized to rotor tip leakage flows and their associated performance decrements.

## **7.2. Recommendations for Future Research**

The results presented herein provide a wealth of data which will improve the understanding of tip leakage flow effects in axial compressors. However, there is still significant processing that can be performed to glean additional information from the collected data. For the time-resolved measurements, in particular, the results shown here have only analyzed the time domain, and further analysis of the frequency content may unveil more information, particularly relating to the multistage effects of the machine and any potential aeromechanical forcing.

The detailed flow field traverses (steady total pressure, time-resolved total pressure, time-resolved velocities) were conducted only for the smallest and largest tip clearance configurations at the nominal loading and high loading operating conditions. Thus, there is a multitude of additional data which could be collected at additional loading conditions (i.e., a negative incidence, low loading condition) or at the intermediate tip clearance height. The measurements collected from a third tip clearance could accommodate a more thorough analysis of trends associated with vorticity, leakage flow size, etc. with changing tip clearance.

The non-intrusive PIV technique implemented here is the first of its kind to introduce the laser illumination through the same optical access window as the imaging, thereby avoiding intrusive periscope methods. With this proof-of-concept, the opportunity is available to non-intrusively measure the compressor flow field in each of the three rotors for three tip clearance heights and at several loading conditions. These non-intrusive measurements help to fill in the void left by the other traditional measurement techniques by capturing data in the rotor passage, but they also provide the opportunity to validate measurements and gain additional confidence in measurements from all techniques.

Finally, the understanding of the rotor tip leakage flow field and its impact on the compressor performance developed through this study has created a unique opportunity to investigate leakage flow control techniques (such as casing treatments) and other leakage flow desensitizing design methodologies in this three-stage axial compressor. Ultimately, it is these technologies that will help to drive the future of robust compressor designs.

## LIST OF PUBLICATIONS RESULTING FROM THIS PROJECT

- [1] Berdanier, R.A., Smith, N.R., Fabian, J.C., and Key, N.L., 2015, “Humidity Effects on Experimental Compressor Performance—Corrected Conditions for Real Gases,” *Journal of Turbomachinery*, **137**(3), 031011 (10 pages).
- [2] Berdanier, R.A. and Key, N.L., 2015, “Experimental Investigation of Factors Influencing Operating Rotor Tip Clearance in Multistage Compressors,” *International Journal of Rotating Machinery*, Article ID 146272 (13 pages).
- [3] Smith, N.R., Berdanier, R.A., Fabian, J.C., and Key, N.L., 2015, “Reconciling Compressor Performance Differences for Varying Ambient Inlet Conditions,” PowerEnergy2015-49102. To be presented at the ASME Power and Energy Conference, San Diego, CA, June 26-July 2, 2015.
- [4] Berdanier, R.A. and Key, N.L., “Tip Leakage Flow Effects on Multistage Compressor Performance for Small Core Engine Applications,” In review for *Journal of Turbomachinery*.
- [5] Smith, N.R. and Key, N.L., “Flow Visualization for Investigating Stator Losses in a Multistage Axial Compressor,” In review for *Experiments in Fluids*.
- [6] Berdanier, R.A. and Key, N.L., “Data Processing Techniques for Measurements Collected from a Single Slanted Hot-Wire,” To be presented at the AIAA Fluid Dynamics Conference, Dallas, TX, June 22-26, 2015.

## LIST OF REFERENCES

- Adkins, Jr., G.G. and Smith, Jr., L.H., 1982, "Spanwise Mixing in Axial-Flow Turbomachines," *Journal of Engineering for Power*, **104**(1), pp. 97-110.
- Atkinson, C., and Soria, J., 2009, "An efficient simultaneous reconstruction technique for tomographic particle image velocimetry," *Experiments in Fluids*, **47**(4-5), pp. 553-568.
- American Society of Mechanical Engineers, 2004, "Flow Measurement," ASME PTC 19.5-2004, pp. 19-27.
- Ball, P.R., 2013, "An Experimental and Computational Investigation on the Effects of Stator Leakage Flow on Compressor Performance," Purdue University, West Lafayette, IN, Master Thesis.
- Balzani, F., Scarano, F., Riethmuller, M.L., and F.A.E. Breugelmans, 2000, "Experimental Investigation of the Blade-to-Blade Flow in a Compressor Rotor by Digital Particle Image Velocimetry," *Journal of Turbomachinery*, **122**(4), pp. 743-750.
- Berdanier, R.A. and Key, N.L., 2015a, "Experimental Investigation of Factors Influencing Operating Rotor Tip Clearance in Multistage Compressors," *International Journal of Rotating Machinery*, Article ID 146272 (14 pages).
- Berdanier, R.A. and Key, N.L., 2015b, "Data Processing Techniques for Measurements Collected from a Single Slanted Hot-Wire," To be presented at the AIAA Fluid Dynamics Conference, Dallas, TX, June 22-26, 2015.
- Berdanier, R.A., Smith, N.L., Fabian, J.C., and Key, N.L., 2015, "Humidity Effects on Experimental Compressor Performance—Corrected Conditions for Real Gases," *Journal of Turbomachinery*, **137**(3), 031011 (10 pages).
- Brossman, J.R., 2012, "An Investigation of Rotor Tip Leakage Flows in the Rear-Block of a Multistage Compressor," Purdue University, West Lafayette, IN, PhD Thesis.
- Bruna, D. and Turner, M.G., 2013, "Isothermal Boundary Condition at Casing Applied to the Rotor 37 Transonic Axial Flow Compressor," *Journal of Turbomachinery*, **135**(3), 034501 (4 pages).
- Camp, T.R. and Day, I.J., 1998, "A Study of Spike and Modal Stall Phenomena in a Low-Speed Axial Compressor," *Journal of Turbomachinery*, **120**(3), pp. 393-401.
- Chen, G.-T., 1991, "Vortical Structures in Turbomachinery Tip Clearance Flows," Massachusetts Institute of Technology, Cambridge, MA, PhD Thesis.
- Collis, D.C. and Williams, M.J., 1959, "Two-dimensional convection from heated wires at low Reynolds numbers," *Journal of Fluid Mechanics*, **6**(3), pp. 357-384.
- Courtiade, N. and Ottavy, X., 2012, "Experimental Study of Surge Precursors in a High-Speed Multistage Compressor," ASME Paper GT2012-68321, pp. 1-10.
- Cumpsty, N.A., 1986, "Annulus Wall Boundary-Layer Measurements in a Four-Stage Compressor," *Journal of Engineering for Gas Turbines and Power*, **108**(1), pp. 2-6.
- Cumpsty, N.A., 2004, *Compressor Aerodynamics*, Krieger: Malabar, FL.
- Day, I.J., 1993, "Stall Inception in Axial Flow Compressors," *Journal of Turbomachinery*, **115**(1), pp. 1-9.
- Denton, J.D., 2010, "Some Limitations of Turbomachinery CFD," ASME Paper GT2010-22540, pp. 1-11.
- Dickens, T. and Day, I., 2011, "The Design of Highly Loaded Axial Compressors," *Journal of Turbomachinery*, **133**(3), pp. 1-10.

- Dong, Y., Xinqian, Z., and Qiushi, L., 2014, "An 11-stage axial compressor performance simulation considering the change of tip clearance in different operating conditions," *Proceedings of the IMechE Part A: Journal of Power and Energy*, **228**(6), pp. 614-625.
- Eckstein, A.C., Charonko, J., and Vlachos, P., 2008, "Phase correlation processing for DPIV measurements," *Experiments in Fluids*, **45**(3), pp. 485-500.
- Eckstein, A. and Vlachos, P.P., 2009a, "Assessment of advanced windowing techniques for digital particle image velocimetry (DPIV)," *Measurement Science and Technology*, **20**(7), 075402 (9 pages).
- Eckstein, A. and Vlachos, P.P., 2009b, "Digital particle image velocimetry (DPIV) robust phase correlation," *Measurement Science and Technology*, **20**(5), 055401 (14 pages).
- Elsinga, G., Scarano, F., Wienele, B., and Van Oudheusden, B.W., 2006, "Tomographic Particle Image Velocimetry," *Experiments in Fluids*, **41**(6), pp. 933-947.
- Erwin, J.R., 1964, "Experimental Techniques," *Aerodynamics of Turbines and Compressors*, W.R. Hawthorne ed., Princeton University Press, Princeton, NJ, pp. 167-269.
- Flegg, H.G., 1974, *From Geometry to Topology*, Crane, Russak, & Co., New York, NY.
- Freeman, C., 1985, "Effect of Tip Clearance Flow on Compressor Stability and Engine Performance," VKI Lecture Series, 1985-05.
- Gallimore, S.J. and Cumpsty, N.A., 1986, "Spanwise Mixing in Multistage Axial Flow Compressors: Part I – Experimental Investigation," *ASME Journal of Turbomachinery*, **108**(1), pp 2-9.
- Goto, A., 1992, "Three-Dimensional Flow and Mixing in an Axial Flow Compressor with Different Rotor Tip Clearances," *Journal of Turbomachinery*, **114**(3), pp. 675-685.
- Gupta, A., Khalid, S.A., McNulty, G.S., and Dailey, L., 2003, "Prediction of Low Speed Compressor Rotor Flowfields with Large Tip Clearances," ASME Paper GT2003-38637.
- Heidmann, J.D., 2009, "NASA Turbomachinery Technical Working Group Technology Assessment," *Mechanical Engineering: Global Gas Turbine News*, **49**(4), pp. 5-6.
- Houghton, T. and Day, I., 2010, "Stability Enhancement by Casing Grooves: The Importance of Stall Inception Mechanism and Solidity," ASME Paper No. GT2010-22284, 9 pages.
- Hoying, D.A., Tan, C.S., Vo, H.D, and Greitzer, E.M., 1999, "Role of Blade Passage Flow Structures in Axial Compressor Rotating Stall Inception," *Journal of Turbomachinery*, **121**(4), pp. 735-742.
- Hunter, I.H. and Cumpsty, N.A., 1982, "Casing Wall Boundary-Layer Development Through an Isolated Compressor Rotor," *Journal of Engineering for Power*, **104**(4), pp. 805-817.
- Hutton, S.P., 1956, "Three-Dimensional Motion in Axial-Flow Impellers," *Proceedings of the Institute of Mechanical Engineers*, **170**, pp. 863-873.
- Inoue, M., Kuroumaru, M., and Fukuhara, M., 1986, "Behavior of Tip Leakage Flow Behind an Axial Compressor Rotor," *Journal of Engineering for Gas Turbines and Power*, **108**(1), pp. 7-14.
- Khalid, S.A., Khalsa, A.S., Waitz, I.A., Tan, C.S., Greitzer, E.M., Cumpsty, N.A., Adamczyk, J.J., and Marble, F.E., 1999, "Endwall Blockage in Axial Compressors," *Journal of Turbomachinery*, **121**(3), pp. 499-509.
- Khalsa, A.S., 1996, "Endwall Blockage in Axial Compressors," Massachusetts Institute of Technology, Cambridge, MA, PhD Thesis.

- King, L.V., 1914, “On the Convection of Heat from Small Cylinders in a Stream of Fluid: Determination of the Convection Constants of Small Platinum Wires with Applications to Hot-Wire Anemometry,” *Philosophical Transactions of the Royal Society A*, **214**, pp. 373-432.
- Krug, A., Busse, P., and Vogeler, K., 2015, “Experimental Investigation Into the Effects of the Steady Wake-Tip Clearance Vortex Interaction in a Compressor Cascade,” *Journal of Turbomachinery*, **137**(6), 061006 (10 pages).
- Lakshminarayana, B., Pouagare, M., and Davino, R., 1982a, “Three-Dimensional Flow Field in the Tip Region of a Compressor Rotor Passage—Part 1: Mean Velocity Profiles and Annulus Wall Boundary Layer,” *Journal of Engineering for Power*, **104**(4), pp. 760-771.
- Lakshminarayana, B., Davino, R., Pouagare, M., 1982b, “Three-Dimensional Flow Field in the Tip Region of a Compressor Rotor Passage—Part 1: Turbulence Properties,” *Journal of Engineering for Power*, **104**(4), pp. 772-781.
- Lemmon, E. W., Huber, M. L., and McLinden, M. O., 2013, NIST Standard Reference Database 23: Reference Fluid Thermodynamic and Transport Properties—REFPROP, Version 9.1, National Institute of Standards and Technology, Standard Reference Data Program, Gaithersburg, MD.
- Levis, W.R., 2006, “Unsteady Casewall Pressure Measurements in a Transonic Compressor,” Naval Postgraduate School, Monterey, CA, Master Thesis.
- Leylek, J.H. and Wisler, D.C., 1991, “Mixing in Axial-Flow Compressors: Conclusions Drawn from Three-Dimensional Navier-Stokes Analyses and Experiments,” *Journal of Turbomachinery*, **113**(2), pp 139-160.
- Liu, B., Wang, H., Liu, H., and Yu, H., 2003, “Experimental Investigation of Unsteady Flow Field in the Tip Region of an Axial Compressor Rotor Passage at Near Stall Condition with SPIV,” ASME Paper No. GT2003-38185, pp. 1-12.
- Lou, F., Fabian, J., and Key, N.L., 2013, “Effects of Invoking Different Gas Models on Air Compressor Efficiency Calculation,” *Journal of Engineering for Gas Turbines and Power*, **136**(1), 012601 (8 pages).
- Ma, H., 2001, “Three-Dimensional Unsteady Flow Field Due to IGV-Rotor Interaction in the Tip Region of an Axial Compressor Rotor Passage,” ASME Paper No. 2001-GT-0296.
- Mailach, R., Lehmann, I, and Vogeler, K., 2008, “Periodical Unsteady Flow Within a Rotor Blade Row of an Axial Compressor—Part II: Wake-Tip Clearance Vortex Interaction,” *Journal of Turbomachinery*, **130**(4), 041005 (10 pages).
- McDougall, N.M., 1990, “A Comparison Between the Design Point and Near-Stall Performance of an Axial Compressor,” *Journal of Turbomachinery*, **112**(1), pp. 109-115.
- McDougall, N.M., Cumpsty, N.A., and Hynes, T.P., 1990, “Stall Inception in Axial Compressors,” *Journal of Turbomachinery*, **112**(1), pp. 116-123.
- Meinhart, C.D., Wereley, S.T., and Santiago, J.G., 1999, “PIV Measurement of a Microchannel Flow,” *Experiments in Fluids*, **27**(5), pp. 414-419.
- Methel, J.C., Smith, N.R., and Key, N.L., 2015, “Vane Wake Characterization for a Multistage Compressor Including Variability,” AIAA Paper No. 2015-1341, pp. 1-11.
- Michon, G.-J., Miton, H., and Ouayhaya, N., 2005, “Unsteady Off-Design Velocity and Reynolds Stresses in an Axial Compressor,” *Journal of Propulsion and Power*, **21**(6), pp. 961–972.
- Morrison, E.S.S., 2013, “Development of a Three Dimensional Compressible Flow Calibration Facility for Thermal Anemometry,” Purdue University, West Lafayette, IN, Master Thesis.

- Müller, D., Sheard, A.G., Mozumdar, S., and Johann, E., 1997, “Capacitive measurement of compressor and turbine blade tip to casing running clearance,” *Journal of Engineering for Gas Turbines and Power*, **119**(3), pp. 877-884.
- Murray, W.L., 2014, “Experimental Investigation of a Forced Response Condition in a Multistage Compressor,” Purdue University, West Lafayette, IN, Master Thesis.
- NACA Subcommittee on Compressors, 1950, “Standard Procedures for Rating and Testing Multistage Axial-Flow Compressors,” NACA TN-1138.
- Peacock, R.E., 1982, “A review of turbomachinery tip gap effects. Part 1: Cascades,” *International Journal of Heat and Fluid Flow*, **3**(4), pp. 185-193.
- Peacock, R.E., 1983, “A review of turbomachinery tip gap effects. Part 2: Rotating machinery,” *International Journal of Heat and Fluid Flow*, **4**(1), pp. 3-16.
- Pullan, G., Young, A.M., Day, I.J., Greitzer, E.M., and Spakovszky, Z.S., 2015, “Origins and Structure of Spike-Type Rotating Stall,” *Journal of Turbomachinery*, **137**(5), 051007 (11 pages).
- Reeder, J.A., 1968, “Tip Clearance Problems in Axial Compressors (A Survey of Available Literature),” Atomic Energy Commission R&D Report K-1682.
- Sanders, A.J., Papalia, J., and Fleeter, S., 2002, “Multi-Blade Row Interactions in a Transonic Axial Compressor: Part I—Stator Particle Image Velocimetry (PIV) Investigation,” *Journal of Turbomachinery*, **124**(1), pp. 10-18.
- Sans, J., Dell-Era, G., Desset, J., Brouckaert, J.-F., and Hiernaux, S., “Time-Resolved Measurements of the Unsteady Flow Field in a Single Stage Low Pressure Axial Compressor,” ASME Paper No. GT2013-94264, pp. 1-14.
- Schmidt, D.P. and Okiishi, T.H., 1976, “Multistage Axial-Flow Turbomachine Wake Production, Transport, and Interaction,” AFOSR-TR-77-0720.
- Shin, H.-W. and Hu, Z.A., “Measurement of Swirling Flow Field Using the Single-Slanted Hot-Wire Technique,” *International Journal of Turbo and Jet Engines*, **3**(2-3), pp. 139-146.
- Shin, H.-W., Solomon, W., and Wadia, A., 2008, “Transonic fan tip-flow features revealed by high frequency response over-tip pressure measurements,” ASME Paper No. GT2008-50279, pp. 1-9.
- Sirakov, B.T. and Tan, C.-S., 2003, “Effect of Unsteady Stator Wake—Rotor Double-Leakage Tip Clearance Flow Interaction on Time-Average Compressor Performance,” *Journal of Turbomachinery*, **125**(3), pp. 465-474.
- Smith, L.H., 1970, “Casing Boundary Layers in Multistage Axial-Flow Compressors,” in: *Flow Research in Blading*, L.S. Dzung, ed., Elsevier, Amsterdam, p. 275.
- Smith, N.R. and Key, N.L., 2015, “Flow Visualization for Investigating Stator Losses in a Multistage Axial Compressor,” In review for *Experiments in Fluids*.
- Smith, N.R., Berdanier, R.A., Fabian, J.C., and Key, N.L., 2015a, “Reconciling Compressor Performance Differences for Varying Ambient Inlet Conditions,” ASME Paper No. PowerEnergy2015-49102.
- Smith, N.R., Murray III, W.L., and Key, N.L., 2015b, “Considerations for Measuring Compressor Aerodynamic Excitations Including Rotor Wakes and Tip Leakage Flows,” ASME Paper GT2015-43508, pp. 1-11.
- Soloff, S.M., Adrian, R.J., and Liu, Z.-C., 1999, “Distortion compensation for generalized stereoscopic particle image velocimetry,” *Measurement Science and Technology*, **8**(12), pp. 1441-1454.

- Storer, J.A. and Cumpsty, N.A., 1994, "An Approximate Analysis and Prediction Method for Tip Clearance Loss in Axial Compressors," *Journal of Turbomachinery*, **116**(4), pp. 648-656.
- Suder, K.L., 1998, "Blockage Development in a Transonic, Axial Compressor Rotor," *Journal of Turbomachinery*, **120**(3), pp 465-476.
- Suder, K.L. and Celestina, M.L., 1996, "Experimental and Computational Investigation of the Tip Clearance Flow in a Transonic Axial Compressor Rotor," *Journal of Turbomachinery*, **118**(2), pp 218-229.
- Talalayev, A., 2011, "On the Renovation of the Three-Stage Axial Compressor Research Facility for Compressor Performance Research," Purdue University, West Lafayette, IN, Master Thesis.
- Tschirner, T., Johann, E., Müller, R., and Vogeler, K., 2006, "Effects of 3D aerofoil tip clearance variation on a 4-stage low speed compressor," ASME Paper No. GT2006-90902, pp. 1-10.
- Van Zante, D.E., Strazisar, A.J., Wood, J.R., Hathaway, M.D., and Okiishi, T.H., 1999, "Recommendations for Achieving Accurate Numerical Simulation of Tip Clearance Flows in Transonic Compressor Rotors," *Journal of Turbomachinery*, **122**(4), pp 733-742.
- Voges, M., Willert, C.E., Mönig, R., Müller, M. W., and Schiffer, H.-P., 2012, "The challenge of stereo PIV measurements in the tip gap of a transonic compressor rotor with casing treatment," *Experiments in Fluids*, **52**(3), pp. 581-590.
- Walsh, P.P. and Fletcher, P., *Gas Turbine Performance*, Blackwell Science, Oxford, 2008.
- Weichert, S. and Day I., 2014, "Detailed Measurements of Spike Formation in an Axial Compressor," *Journal of Turbomachinery*, **136**(5), 051006 (9 pages).
- Wernet, M.P., Van Zante, D., Strazisar, T.J., John, W.T., and Prahst, P.S., 2005, "Characterization of the tip clearance flow in an axial compressor using 3-D digital PIV," *Experiments in Fluids*, **39**(4), pp. 743-753.
- Wernet, M.P., John, W.T., Park, B., Prahst, P.S., and Strazisar, A.J., 2001, "Characterization of the Tip Clearance Flow in an Axial Compressor Using Digital PIV," AIAA Paper No. 2001-00697, pp. 1-14.
- Williams, R., Gregory-Smith, D., and He, L., 2006, "A Study of Large Tip Clearance Flows in an Axial Compressor Blade Row," ASME Paper No. GT2006-90463, pp. 1-9.
- Wisler, D.C., 1985, "Loss Reduction in Axial-Flow Compressors Through Low-Speed Model Testing," *Journal of Engineering for Gas Turbines and Power*, **107**(2), pp. 354-363.
- Wisler, D.C., Bauer, R.C., and Okiishi, T.H., 1987, "Secondary Flow, Turbulent Diffusion, and Mixing in Axial Flow Compressors," *Journal of Turbomachinery*, **109**(4), pp 455-482.
- Wisler, D.C. and Beacher, B.F., 1989, "Improved Compressor Performance Using Recessed Clearance (Trenches)," *Journal of Propulsion*, **5**(4), pp. 469-475.
- Yoon, S.Y., Song, S.J., and Shin, H.-W., 2006, "Influence of Flow Coefficient, Stagger Angle, and Tip Clearance on Tip Vortex in Axial Compressors," *Journal of Fluids Engineering*, **128**(6), pp. 1274-1280.





